DEPT OF ZOOLOGY, UNIVERSITY OF OXFORD

Investigations on natural silks using dynamic mechanical thermal analysis (DMTA)

A thesis submitted for the degree of Doctor of Philosophy

Presented by
Juan Guan
Trinity Term, 2013

Supervised by

Dr. David Porter

Professor Fritz Vollrath

Abstract

Investigations on natural silks using dynamic mechanical thermal analysis (DMTA)

Juan Guan

Green-Templeton College Trinity Term, 2013

A thesis submitted for the degree of Doctor of Philosophy

This thesis examines the dynamic mechanical properties of natural silk fibres, mainly from silkworm species *Bombyx mori* (*B. mori*) and spider species *Nephila edulis*, using dynamic mechanical thermal analysis, DMTA. The aim is not only to provide novel data on mechanical properties of silk, but also to relate these properties to the structure and morphology of silk. A systematic approach is adopted to evaluate the effect of the three principal factors of stress, temperature and hydration on the properties and structure of silk. The methods developed in this work are then used to examine commercially important aspects of the 'quality' of silk.

I show that the dynamic storage modulus of silks increases with loading stress in the deformation through yield to failure, whereas the conventional engineering tensile modulus decreases significantly post-yield.

Analyses of the effects of temperature and thermal history show a number of important effects: (1) the loss peak at -60 °C is found to be associated the protein-water glass transition; (2) the increase in the dynamic storage modulus of native silks between temperature +25 and 100 °C is due simply to water loss; (3) a number of discrete loss peaks from +150 to +220°C are observed and attributed to the glass transition of different states of disordered structure with different intermolecular hydrogen bonding.

Excess environmental humidity results in a lower effective glass transition temperature (T_g) for disordered silk fractions. Also, humidity-dynamic mechanical analysis on *Nephila edulis* spider dragline silks has shown that the glass transition induces a partial supercontraction, called T_g contraction. This new finding leads to the conclusion of two independent mechanisms for supercontraction in spider dragline silks.

Study of three commercial *B. mori* cocoon silk grades and a variety of processed silks or artificial silks shows that lower grade and poorly processed silks display lower T_g values, and often have a greater loss tangent at T_g due to increased disorder. This suggests that processing contributes significantly to the differences in the structural order among natural or unnatural silks. More importantly, dynamic mechanical thermal analysis is proposed to be a potential tool for quality evaluation and control in silk production and processing.

In summary, I demonstrate that DMTA is a valuable analytical tool for understanding the structure and properties of silk, and use a systematic approach to understand quantitatively the important mechanical properties of silk in terms of a generic structural framework in silk proteins.

Acknowledgements

"Time has longer legs than me."

When I wrote this in one of my early emails to David, he commented this phrase as very funny and "GJ style". Now time has run another four years tirelessly, and GJ has become Juan, not quite as handsome as a Hispanic man, but different from the "slightly shy and timid Chinese girl". For all the changes (of course in a positive way), I would like to say: "David, thank you!"

My thanks also go to Alison, who taught me an English attitude of life and the art beyond science. I enjoyed all the museum tours you took me and was fascinated by your stories although David says you made up some of them☺

Looking back through my time in Oxford, without the help from my colleagues in Oxford Silk Group, I could never imagine my thesis being finished as such a great piece (my longest ever-written English document!). May I acknowledge you in a very personal "Juan's" style with sincere gratitude:

Chris, the genius, thank you for a "big" smile to welcome me on my first day in the lab, your training for me on DMA with such patience and care, as well as many ingenious discussions on my DMA data. Thank you for taking me to Manchester for my first conference!

Tom, the crazy funny one, thank you for guiding me in calibrating the instrument, showing me how to reel spider silks, and offering such a lively musical environment in South American or African style that I could prepare my samples much faster under such fast beats!

Fujia, another funny one, thank you for being a consultant on almost every aspect of my life in Oxford. You are like a sister, very generous, frank and open-minded. I wish you a great happy life!

Max, the one who knows a lot and is always willing to offer his knowledge to the full, thank you for being such a great friend and colleague! Sorry that I won't be able to attend your wedding. Therefore I write my very best wishes here for your wedding, for your new life, and for your great future!

Gwilym, not easy to summarize in one phrase☺, great thanks to you for taking me to experience the Christmas celebration of a British family, the Bonfire party, the bluebell search in your wood, and cycling in town with the "alleycat"! Thank you for my happiness in Oxford!

Beth, the one who is the dearest in the lab and speaks beautiful English, thank you for being a great English teacher and a great friend – because of you my English speaking has improved so much! I wish you a great, fun, scientific career!

Imke, Bjoern and Jannik, the tall Germans living way above my eye level, I look forward to seeing a grown-up Jannik – how tall will he become?

Nick, the one who does so much more than he talks, thank you for all the professional advice on operating DMA and help with handling the liquid nitrogen, it is all very much appreciated! A special “thank you” for the wonderful celebration cake you made for my viva!

Stephanie, who has become the mother of the beautiful twins, thank you for teaching me French baking and during the time I learned that baking needs to be so precise that an analytical chemist would feel shy!

I would also like to thank my colleagues Thomas, Gunnar, Miguel, Darshil and Alex! It is delightful to know you and to work with you!

I wish to give my thanks to my dear friends in Oxford for your generous friendship: Judith Boettcher, Anne van der Lingen, Linxin Li, Qian Liu, Atsuko Sato, Anna Schrade, Anna Huber, Tonya Muller.

It seems I have forgotten an important person - Fritz. How could I? May I say “thank you” for all your generous support through my time in Oxford! You are energetic, open, and so active that sometimes I think I am not as young as you are! I would like to express my love to Leslie, who introduced me to the game world of Jenga.

For the very valuable support and love from my family, I thank my mom, my fiancé Jian, my stepfather and my two brothers. For your love and my love for you, I will move on and live a brilliant life.

Juan

On a rainy morning in Oxford

Table of Contents

Chapter 1. Introduction

1.1 Polymers: synthetics and natural proteins

The name “polymer” was invented in 1830 by Swedish chemist Berzelius to describe large molecules composed of ‘many parts’. The example molecule he used was glucose, which is by no means a polymer in a modern sense. Much later in the 1920s German scientist Staudinger clarified the long molecular chains nature of polymers or macromolecules. Following this, the invention of “Nylon” as a replacement for natural silk by Carothers with DuPont established polymers as commercial industrial materials through their 1938 patent [1], alongside the development of synthetic rubber to compensate for the limited supply of natural materials during World War II. The development of many other successful synthetic polymers has brought tremendous changes to our daily life since the 1940s across all areas from engineering to medicine.

On the other hand, biological polymers have been around from the very beginning of life, and human beings have been exploiting natural polymeric materials such as wool and silk on an industrial scale for millennia. However, the diversity of natural polymers and their versatile properties and functionalities has been reemphasized since the fossil fuel-based resources have become costly and consequently the future of synthetics needs reevaluating. Also, the negative environmental impact of synthetics (processing, poor degradability and low recyclability) has driven more research and applications to consider natural polymers.

The twentieth century saw great breakthroughs in understanding complex biopolymers, such as the discovery of the double-helix structure of DNA molecules [2]. There has also been a dramatic underpinning increase in our understanding of the

'workhorse' proteins that put all the genetic information from DNA into practice. The first sequenced protein was insulin by Frederick Sanger [3, 4]. Due to the difficulties in purifying a large enough quantity for detailed X-ray structural analysis, the first experimentally resolved protein structures were hemoglobin and myoglobin in 1958 [5, 6]. However, the prediction of protein secondary structures from their primary sequences had already been done by Linus Pauling in 1951 from fundamental chemical insights into the probable configuration of proteins dominated by strong hydrogen bonding [7].

A key family of natural structural proteins include fibrous proteins such as keratin (e.g. in human hair), actin (e.g. in muscles), collagen (e.g. in tendons) as well as silk produced by silkworms, spiders and other arthropods. These proteins tend to have more regular and repetitive amino acid sequences associated with mechanical performance for their role as structural materials, rather than enzymes for metabolic functions, which require more specific configurations for specific chemical functionality. Because some of these relatively abundant structural proteins operate *ex vivo* and perform a variety of important bioengineering functions, interest has concentrated upon understanding their structure-property-function relationships from a physics and materials science perspective, instead of the more usual biological (e.g. genetic) or chemical approaches.

Specific questions often relate to how these proteins self-assemble into secondary structures in order to tune their bulk materials properties to perform specific biomechanical functions in different environments. A lot of good work has been done on collagen and its structure-property relationship, for example [8]. However, the work on silk is not as advanced, especially on developing a coherent set of structure-property-function relationships for this exciting family of biopolymers. The work presented in

this thesis aims to improve our understanding of the thermo-mechanical properties of silk by using analytical techniques developed for more 'straightforward' synthetic polymers. Understanding these issues will be very valuable in order to develop new 'bio-inspired' synthetic analogue materials for both performance and environmental benefits.

1.2 Silk: a featured biopolymer

1.2.1 Definition of "silk"

As introduced above, silks belong to a family of structural proteins that are distinct from all other synthetic and natural proteins. Natural silk solids or fibres are produced from a stored liquid-crystal gel [9-11] via a process called "spinning" controlled by animal behaviour that is often compared to the industrial fibre spinning process called drawing/pultrusion. This behavior of spinning differentiates silks from hair or wool, which is principally grown from tissue cells at a much slower rate. Compared with industrial fibre processing, natural silk spinning glands are believed to be more complicated, with fine controls on both the chemical (e.g. pH and ions [12, 13]) and physical environments [14, 15].

Furthermore, silks are produced naturally by a wide range of animals, not only the domesticated silkworms *Bombyx mori* (*B. mori*), but also the wild caterpillar species such as *Antherea pernyi* (*A. pernyi*) and all spiders (araneid) [16], as well as insects such as honey bees [17, 18] or even a few crustacean shrimp species living in sand-silk-composite homes in the sea [19]. It is also important that many silk-spinning species, primarily spiders, produce more than one type of silk and each type has a different function and use [16]. For example, *Nephila edulis* (*N. edulis* or *Nephila e.*) spider can

produce three types of silks for web-building, one type for egg-sac cocoons, and another type for wrapping prey [20, 21].

To address the chemical and biological features of silks, Craig gives a good definition of silk: “fibrous proteins, which contain highly repetitive sequences of amino acids and are stored as a liquid inside the animal, configure into fibers when sheared or ‘spun’ at secretion [16]”. We may very simply refer to it as a protein fibre spun by an animal [20].

Note that this thesis mainly concerns the structure and properties of “natural” silk fibres produced by animals or insects, rather than ‘artificial’ such as reconstituted silk fibroin (RSF). The following brief introduction to the structural aspects of natural silks is intended to outline the main features of silk structure that determine their highly attractive mechanical properties of combined toughness and strength. More importantly, the summary on structure and properties of silk aims to find out what is needed to further the understanding of silk structure and properties. This is the motivation behind my research focused on using dynamic mechanical thermal analysis to study silks.

1.2.2 Primary structures of silk proteins

All silks are made largely of proteins, by definition. The protein component in silk is called fibroin for silkworms or spidroin for spiders. Depending on the silk-spinning species, fibroins or spidroins are different in their primary structure of amino acid sequences, and the size and secondary structure morphology of the single molecules can be very different. Each silk often contains more than one protein. For example, the domesticated *B. mori* silk fibroin consists of three different proteins, namely PG25, heavy and light chain polypeptides, and the heavy and light chain polypeptides have molecular weight of over 390 kD and 25 kD respectively [22]. *Nephila clavipes* spider

major ampullate dragline (MA) silk consists of two spidroins: Spidroin 1 of 61 kD and Spidroin 2 of 54 kD [23, 24]. For most spider species the fractions of the two or more component spidroins have not been reported, thus leaving an obstacle for chemical composition based structure-property predictions. Some reported data also do not agree well. For example, the ratios of Spidroin 1 and Spidroin 2 for *Nephila clavipes* MA silk were 3:2 by [25] and 9:1 by [26].

For the four main natural silks in this thesis, namely *B. mori* silkworm silks, *Nephila e.*, *Araneus diadematus* (*Araneus d.*) and *Argiope bruennichi* (*Argiope b.*) major ampullate dragline silks, the amino acid composition of component fibroin or spidroins is shown in Table 1.1. Note that, although the major amino acid fractions in a specific fibroin/spidroin do not vary significantly, the contents of other minor amino acids vary from one reference to another. For example, the reported proline content in the silk of *Argiope* spider species disagrees significantly as highlighted as bold in Table 1.1. The characteristic sequences of the fibroins or spidroins are shown in Figure 1.1. The abbreviations are as follows: G for Glycine, A for Alanine, S for Serine and P for Proline. *B. mori* silk fibroin has a highly repetitive core with repeating –GAGAGS– segments in a stretched backbone length of 200 nm [27], and the three major amino acids, glycine, alanine and serine makes up of over 80% of the total molecular weight. The three spider silks have high glycine content but less alanine and serine compared with *B. mori* fibroin [28], and in some spidroins, the 'disorder' proline appears frequently in the forms of characteristic segments such as –GPGXX–. For example, *Araneus d.* spidroin has about 16% proline. It has been suggested that the concentration of glycine and the absence of proline in the amino acid composition of silks may be correlated to the evolution of spider silk structure and functions [28].

It has been shown that terminal groups, especially C-terminal regions of spidroins, have very different structures and functions from the rest of the protein [29]. The C-terminal regions are highly conserved in sequences among different species, and have low isoelectric point and higher hydrophobicity compared with the repeating core [29].

Table 1.1 Major amino acid compositions (weight percentage) in the five studied natural silks.

Amino acid	*B. mori* [30]	*Nephila c.* [31]	*Nephila e.* [32]	*Araneus d.* [33]	*Argiope** [34]	[32]
Alanine (A)	34.3%	21.1%	31.0%	17.6%	21.8%	-
Glycine (G)	42.6%	37.1%	41.2%	37.2%	25.9%	-
Serine (S)	16.0%	4.5%	3.7%	7.4%	11.8%	-
Glutamine/ G acid	1.7%	9.2%	8.8%	11.5%	7.8%	-
Proline (P)	0.6%	4.3%	4.2%	15.8%	**4.7%**	**9.3/10.4%**

Bombyx mori	Heavy chain	GAGAGSGAAG[SGAGAG]$_6$Y
Nephila clavipes* Major ampullate silk	Spidroin 1	AGRGGLGGQGAGAAAAAAAGGAGQGGYGGLGSQG
	Spidroin 2	GPGQQGPGGYGPGQQGPSGPGSAAAAAAAAAAGPGGYGPG QQGPGGY
Araneus diadematus Major ampullate silk	ADF-2	GGXGGXGGQGGLGSQGAGGAGQGGYGAGQGGAAAAAAAA
	ADF-3	GGYGPGSGQQGPGQQGPGQQGPGGQGPYGPGASAAAAAA
	ADF-4	GPGGYGPGSQGPSGPGGYGPGPGSSAAAAAAAAS
Argiope bruennichi Major ampullate silk	Spidroin 1	GAASAAAAAGGQGGRGGFGGLGSQGEGGAGQGGAGAAAA AAAAGADGGFGLGGYGAGRGYGAGLGGAGGA
	Spidroin 2	AAAAAAAAGGYGPGAGQQGPGSQGPGSGGQQGPGSQGPG SGGQQGPGGQGPYGPS

Coloured segments: AAA; GGX; GPG or occasionally GPX. X represents any other amino acid than G, A, or P.

*The sequence data for *Nephila edulis* is not available, therefore the sequence from the same family *Nephila clavipes* is shown instead.

Figure 1.1 Characteristic sequences from the repetitive core of silk species: *Bombyx mori* fibroin heavy chain [27]; *Nephila clavipes* major ampullate silk [23, 35]; *Araneus*

diadematus major ampullate silk [36]; and *Argiope burennichi* major ampullate silk [37]. Full sequences can be found in the ExpASY database (http://www.expasy.org/) and the entry numbers are: P05790; P19837; P46804; Q16986; Q16987; Q16988; I6XQ31; I6YNT3.

1.2.3 Morphology of silks

Because of such regularity and periodicity in the amino acid sequences of fibroins or spidroins, most silks have a morphology composed of well-defined protein secondary structures (locally folded and hydrogen bonded) such as: β-sheets associated with the –GAGAGS– motif in *B. mori* fibroin [38] or polyalanine segments in spidroins [24, 39], β-turns (usually two bulky side-chain amino acids, e.g. tyrosine, separated by flexible glycine), α-helices or other helical structures (when amino acids such as proline occur periodically in a glycine rich sequence), and other unordered structures (random coil) from the irregular motifs. Fundamentally, the local secondary structures are defined by steric hindrance of peptide side chains and strong hydrogen bonding along and between the molecular chains. Figure 1.2 shows some typical secondary structure building blocks of silks and two β-strands can organize into β-sheets with hydrogen bonding perpendicular to the chain backbones to form an H-bonding plane.

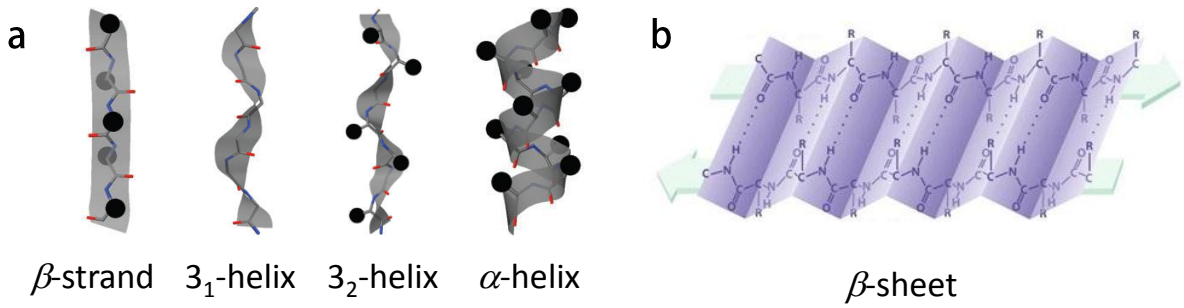

Figure 1.2 Secondary structures of silks: (a) representations taken from reference [18] on honey bee silks; (b) anti-parallel β-sheet shown with inter-chain hydrogen-bonding.

Spectroscopic techniques such as Circular Dichroism (CD) for proteins in solution, or Raman spectroscopy and Infra-Red spectroscopy for solid fibres, or nuclear magnetic

resonance (NMR) for both liquid and solid states, are able to identify the local structures of silks. However, there is certain discrepancy in the results of secondary structural assignments, partially due to the different data processing procedures and assumptions specific to each technique. For example, for *B. mori* silks, one Raman study suggested 50% β-sheet, 28% β-turn, 14% 3_1-helix and only 8% unordered (3% error range) [26]; another suggested 57% β-sheet, 23% β-turn, 13% total helix and 11% disordered (5% error range) [40]; a FTIR study suggested 49% β-sheet (3% error range) [41]; an NMR study suggested 61% total β-sheet and the rest was distorted β-turns [42] and a different NMR study [43] reported 70% β-sheet with inter-strand contacts for the silkworm species *Samia cynthia ricini*. The one consensus seems to be that *B. mori* silk contains 50-60% β-sheets.

For spidroins, due to the very fine sizes of single silk fibres, experiments are more difficult. One study [26] based on the Raman technique reported the conformation composition of *Nephila e.* and *Nephila c.* major ampullate silks to be similar: 36% β-sheet, 31% β-turn, 22% 3_1-helix; and 11% unordered; a recent IR study [44] showed *Nephila c.* contains 46% β-sheet including 27% which is D_2O accessible compared with 8% of D_2O accessible β-sheet out of 50% total β-sheet for *B. mori* silks; the van Beek NMR study on *Nephila e.* dragline silk suggested β-sheet with an angular orientation factor of 0.74 embedded in a predominant oriented structure with 3-fold symmetry [45], however, no quantitative proportions were given. Again high variability, but this is to be expected from a natural material with a wide possible range of production conditions, which will be discussed in the mechanical property section.

To briefly summarize the local morphological structures of both silks: the β-sheet content in *B. mori* silks has been quantified to a reasonably agreed value from

spectroscopic evidence although the rest of the structures are still inconsistent; however, the understanding of the secondary structures in *Nephila e.* spider dragline silks does not show consensus.

Unlike globular proteins, such as enzymes, that often impart chemical functionalities, silks do not appear to have defined quaternary structures, but rather the local secondary structures of silks organize into nano-domains. In the case of *Nephila* (*edulis* or *clavipes*) silks, for example, a minimal domain with an unfolded length of 14 nm was shown in an AFM study for synthetic spidroins [46], the crystal size is approximately 5×2×7 nm in spider silks from X-ray measurements [47-49], and 4 nm long folded "beads" are predicted from the repetitive sequences [20]. The nano-domains further organize into nano-fibrils suggested by the following studies: atomic force spectroscopy (AFM) on synthetic spidroin [46], light and electron microscopy on solid fibres [50], AFM combined with electron microscopy on domesticated and wild silkworm silks [51], AFM combined with X-ray on *B. mori* and *Nephila c.* silks [52], a neutron scattering study [53], as well as similar AFM combined with scanning electron microscopy (SEM) and X-ray on *Nephila pilipes* silks [48]. Orientation in both "crystalline" and "amorphous" phases is shown to play an important role in the structural organization of silks on the nano-scale [49, 54, 55]. Whether these fibrils are embedded in a matrix or not to form fibres is not so clear.

On slightly larger scale, spider silks are reported to possess skin-core structures [50, 55-57], and the skin of spider dragline silk has a varied thickness from 150 nm to 250 nm [50] as well as a higher crystal fraction than the core [58]. There is no doubt that silk structures are hierarchical. However, it is not obvious how this hierarchy might work energetically on both nano- and micro-scale as well as on the macro-level.

Many studies also show that silk structure and morphology is affected considerably by the processing, storage and testing conditions, including mechanical/physical, chemical and biological factors [12, 13, 15, 58]. It is because of this structural sensitivity to the environment that silk researchers sometimes have difficulties to measure the same silk structures consistently even for one type of silk. This also leads to diverse experimental observations on the properties of silks, as will be addressed in the next section.

On top of the secondary structure and the micro- and macro-structure, the silks from silkworms *B. mori* possess a composite structure: the directly spun silks or silks unravelled from cocoons are called "baves", which consist of two individual fibres (brins) made of silk fibroin and wrapped by another protein called sericin. The process to remove sericin is called degumming, and before and after the process, silks are called "raw" and degummed respectively.

1.2.4 Mechanical properties of natural silks

Among all the properties of silks, mechanical properties almost always come to the top of the list. This is reasonable since silks are structural proteins, which have evolved to perform demanding functions such as structural supports of spiders' webs with wind- and insect-impact resistance. As commented in a recent paper [59], almost every silk paper starts with strong claims such as "silk features exceptional mechanical properties such as high tensile strength and great extensibility, making it one of the toughest materials known [60]". Then the question arises: how great are these mechanical properties of natural silks? To answer this question, two aspects need to be considered, magnitude and variability. Let us start with quasi-static tensile properties, and more specifically extensibility, strength (in terms of breaking strain and stress) and modulus.

Dynamic mechanical properties of silks will be introduced in more detail in the following "dynamic mechanical analysis" section.

Reviews and summaries on the tensile properties of various silks in the context of other synthetic and natural fibres can be found in a number of references [61-63]. Figure 1.3 (a) compares the tensile properties of silks with that of more conventional materials such as glass, steel and high-strength fibres [64], and spider dragline silks are acclaimed for their high toughness. More specifically, Figure 1.3 (b) compares the tensile properties of two natural silks (*B. mori* silkworm silk and *Nephila e.* spider dragline silk) with the high performance synthetic analogs, polyethylene terephthalate (PET) and Nylon 6,6 fibres. Spider dragline silks possess superior tensile properties compared to that of silkworm silks in terms of strength and toughness. It is fair to say that the high tenacity PET fibres have better tensile performance than the *B. mori* silkworm silks. However, the strength and toughness of high tenacity Nylon and PET fibres only just approach to those of spider dragline silks.

Table 1.2 quotes a number of values for some relevant natural silks of the interest of this thesis from the large volume of literature. Variability is a main feature of Table 1.2. Firstly, variability is high for a given property from different references. For example, the modulus of raw *B. mori* cocoon silks could vary from 7 to 17 GPa, and even within the same study, the value changes from 9 to 17 GPa [65]. This large variation in tensile properties could be attributed to the lack of consistency in the experimentation from one researcher to another, such as measuring the fibre diameter for instance, or the lack of control in the conditions under which the silks were collected, stored and tested. In some cases, the hydration state of silks is not well-defined, yet this has been shown to affect the mechanical properties considerably [66, 67]. Also it has been discussed in the

previous section that silk structure is sensitive to many physical factors. Thus, it becomes crucial to examine the mechanical properties in the context of the structural changes due to the effect of independent physical factors using consistent methods and experimentation.

Secondly, the tensile properties of spider dragline silks vary from species to species (e.g. *Nephila e.* and *Nephila c.*) as shown in Table 1.2, and this inter-specific variability suggests that one has to be careful with the assumption that silks from different spider species of the same genus share similar structures and properties. The diversity of tensile properties from spider dragline silks of different species is also demonstrated in Figure 1.3 (c).

Thirdly, and perhaps more interestingly, even within one type of spider dragline silk there can be large differences in mechanical properties. As shown in Figure 1.3 (d), with different degrees of supercontraction in *Nephila e.* spider dragline silk, silks display different mechanical properties, for example, greater supercontraction gives less order and orientation for reduced stiffness and strength, but greater extensibility [20, 32, 69]. A more detailed literature study on the mechanical properties of spider dragline silks and "supercontraction" will be presented in Chapter 6 where it is of immediate relevance.

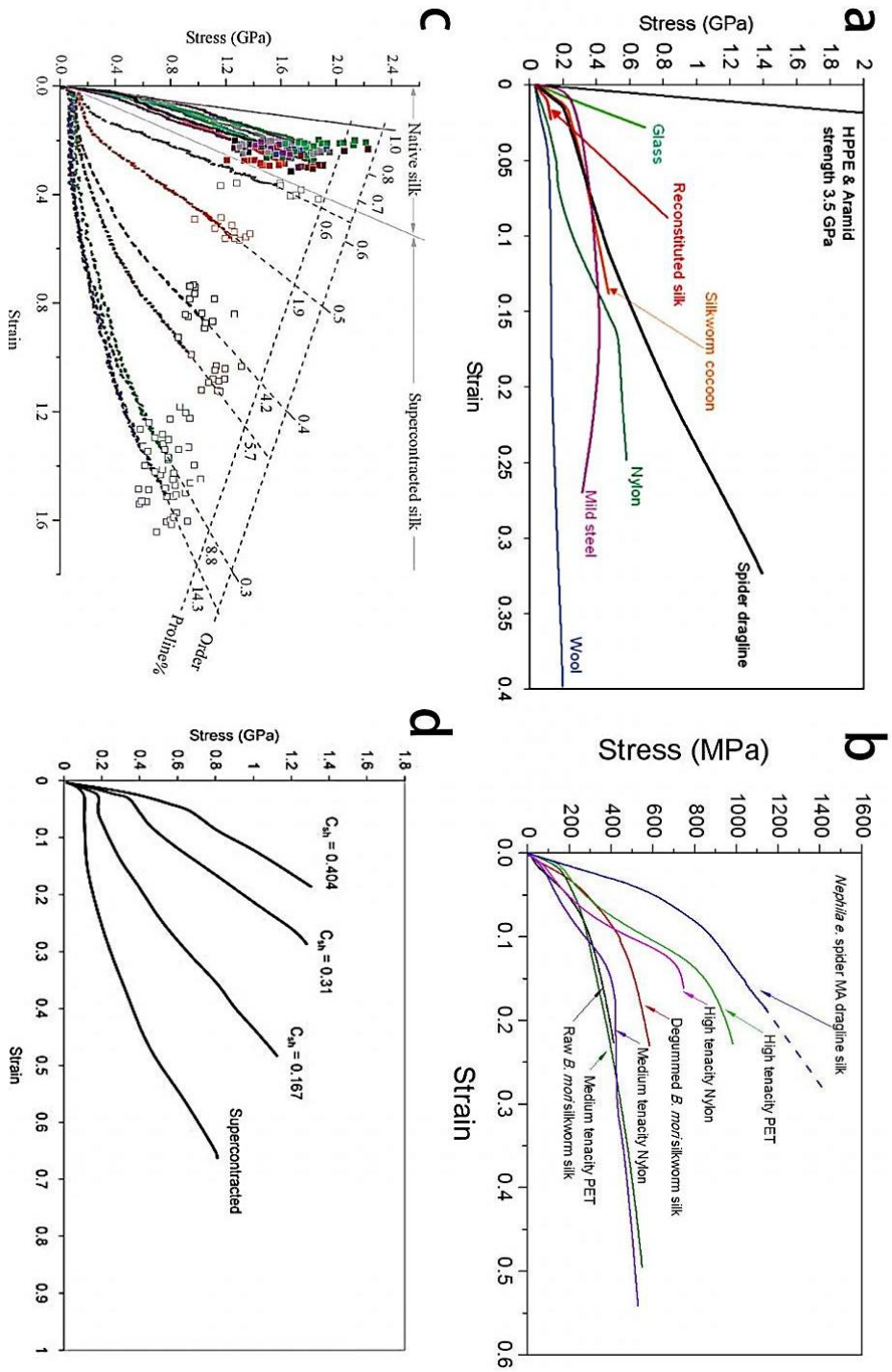

Figure 1.3 Some aspects of tensile properties of silk fibres: the magnitude of tensile properties of silks in comparison with other fibre materials including glass, mild steel and high strength polymers [64] (a); comparing tensile properties of natural silks with synthetics from the author's own work [68] (b); comparing the effect of supercontraction on tensile properties of spider dragline silks from different species (colors are designated as black for *Nephila e.*, green for *Argiope burennichi*, purple for *Araneus diadematus* [32] (c); and tensile properties of *Nephila e.* dragline silks of different controlled degrees of supercontraction, showing the wide range of properties possible in a single silk type [32] (d).

Table 1.2 Tensile properties from the literature on the subject fibres of interest to this thesis.

Fibres		Modulus /GPa	Strength /GPa	Extensibility	Toughness /MJ·m^{-3}	Ref.
Silkworm cocoon silks	*B. mori* (raw)	7	0.6	0.18	70	[61]
		9-17	0.3-0.6	0.1-0.2	-	[65]
		10	0.74	0.20	-	[70]
	B. mori (degummed)	12-17	0.45-0.70	0.12-0.24	-	[71]
Spider dragline silks	*N. edulis*	~17	1.44	~0.25	198	[32]
		7.9	1.2	0.39	215	[72]
	N. clavipes	11-13	0.88-0.97	0.17-0.18	-	[70]
		13.8	1.0	0.2	111	[73]
	Argiope argentata	8.2	1.2	0.23	116	[73]
		~11	1.91	~0.25	225	[32]
	Araneus gemmoides	8.3	1.06	0.29	141	[73]
	Araneus diadematus	2.8	1.19	0.31	-	[70]
		10.4	1.7	0.23	225	[32]
Human hair	Asian	~3.9	0.19	0.46	-	[74]
Synthetics	Nylon 6,6	5	0.95	0.18	80	[75]
	PET	6.5-19.4	0.30-0.83	0.24-0.06	-	[76]

Note that although many silk properties are available in the literature, the overall information with both correlated structures and properties for all the relevant silks remains incomplete. For example, no references could be found on the tensile properties of *Argiope bruennichi (Argiope b.)* dragline silks.

To summarize, the literature shows a need to clarify the claims on the tensile properties of natural silks using consistent experimentation in comparison with the updated performances of the synthetic polymers. It is also crucial to understand where the variability of the tensile properties of both silkworm and spider silks comes from.

1.2.5 Structural models and structure-property relationships for silks

In order to explain the properties of silks, especially those of spider dragline silks, many attempts have been made in the past to develop structure-property relations. In

Figure 1.4 the top and middle rows show examples of these models mainly concerning spider dragline silks. Note that most models tend to agree on the macro-level morphology of a skin-core morphology with nano-fibrils, while the details on the "packing" of nano structures vary.

The earliest structural model proposed by Termonia [77] based on X-ray evidence simply pictures a large number of small crystallites in an amorphous matrix of rubber-like chains. Jelinski [78] then separated the crystal phase into two components based on the crystalline orientation from NMR observations. Van Beek's NMR-based model shown in Figure 1.3 (h) [45] contained irregular β-sheet regions interleaved with predominantly 3_1-helices, and both elements were highly oriented and the sizes of both varied. The three models were aimed at all spider dragline silks, which could be referred to as "two-phase" models with orientation. Similar ideas can be found in more recent publications [48, 69, 79, 80].

More specifically, some studies [81, 82] based on the supercontraction of spider silks propose a model of crystals embedded in an initially hydrogen bonded network of random chains, and upon wetting the hydrogen bonding is disrupted by water. Along with orientation, this change in hydrogen bonding in the "amorphous" phase contributes to the order difference between virgin and supercontracted spider silks. In RSF films, it was also proposed that hydrogen bonding could be formed between amorphous chains [83]. The hydrogen bonding in the non-crystalline region clearly plays some role in enhancing the mechanical properties of silks, and recent experimental and theoretical studies from our group [59, 68] are starting to clarify this effect.

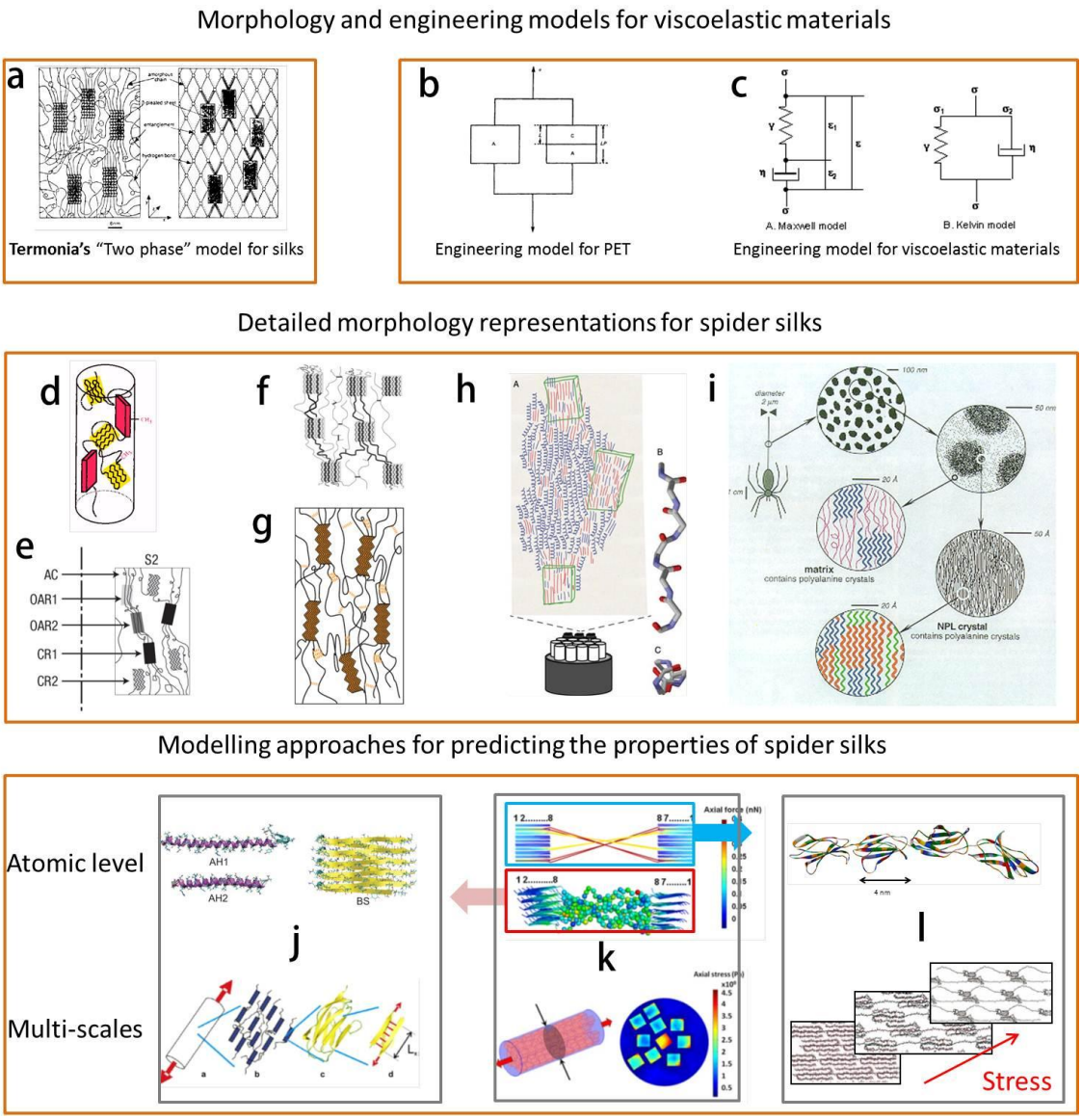

Figure 1.4 Structural representations and modelling on spider silks. Top row, simplified models: Termonia's two phase model [77] (a); engineering illustrations of Termonia's model: PET model by Ward [84] (b) and classic "viscoelastic property" models found in textbooks (c). Middle row, morphology representations for spider silks based on Termonia's model: Jelinski's [78] (d); Liu's supercontraction model [69] (e); two other models showing hydrogen-bonding between "amorphous" chains [81, 82] (f) and (g); van Beek's NMR model [45] (h); Viney's model from OXMAT (i);. Bottom row, modeling approaches for predicting the properties of spider silks: Buehler's molecular dynamics (MD) modeling [60, 85, 86] (j); Grater's combined modeling of both MD and finite element analysis (FEA) [87] (k); and Porter's 'string of beads' morphology and mean field theory [20, 88] (l).

For complex sequences of amino acid groups in polymer chains, simple ideas of crystallinity and order need to be extended to include their effect on morphology at the nanometer scale. The non-periodic lattice (NPL) concept proposed by Viney [89, 90] is illustrated in Figure 1.4 (i). Viney showed from X-ray scattering analysis that silks have a wide size distribution of β-sheet crystallites from 5 nm to 70 nm and some larger crystallites must incorporate -GGX- motifs, which were thought to most likely form helical structures. He also argued that the non-equilibrium conditions during the fibre solidification may override the role of the primary structure of spidroins so that the observed microstructural characteristics were not necessarily always consistent with the primary structure. Nevertheless, the qualitative NPL concept does not yet succeed to quantitatively bridge the nano-structures with the micro- and macro- properties.

Since the structural models for spider silks do not seem clear in details except that β-sheet crystals of uneven sizes are scattered in a non-crystalline phase, modelers would rather use a simple "two-phase" model of hard crystals embedded in a soft matrix. Conventional structure-property relationships (QSPR) methods, such as the empirical spring-and dashpot engineering methods shown in Figure 1.4 (b) and (c) have not yet produced any useful predictive equations, given the incomplete experimental evidence on both the structure and properties of silks. At the atomic level, the properties (for example the strength) of a typical β-sheet crystal of various sizes can be simulated using molecular dynamics (MD), such as examples by Buehler's group as illustrated in Figure 1.3 (j) [60, 85, 86]. The larger scale MD simulations require super-computing power, but are hindered in their usefulness without understanding the fundamental physics of such materials. Thus the properties of nanocrystalline polymeric materials cannot be

simulated beyond the mesoscales into microstructural and macroscopic levels by simply using MD simulations.

Graeter [87] recently conducted a comprehensive study on interpreting the properties of silk fibres using both MD simulations and finite element analysis (FEA), as illustrated in Figure 1.4 (k). It suggests that there is little difference between MD and FEA in predicting the strength and modulus of β-sheet crystals in an amorphous matrix. The key step is to use a good semi-empirical force field that contains a good description of hydrogen bonding to quantify the intermolecular level interactions. Another important conclusion from this study was that significantly high values of toughness can be achieved via an oriented lamellar crystal morphology with total crystallinity of about 40%.

An alternative approach is to accept the complexity of the detailed molecular structure and use a mean field method that takes ensemble average parameters of energy and dimensions for a representative peptide group in a given silk composition and morphology to predict bulk mechanical properties. For example, Porter's model [91, 92] starts with an average lattice (or a characteristic group) defined by a small number of independently calculated parameters, such as cohesive energy and thermal degrees of freedoms of the skeleton vibrations based on quantum physics, and group interaction modeling (GIM) [93] is then used to predict engineering properties. GIM has been tested successfully on over 200 different polymers, and the predicted properties agree well with the experimental observations. The advantage of this approach is that a continuous set of engineering properties through thermal transitions can be predicted for different states of matter from a limited number of basic parameters. Also, the model starts by predicting dynamic mechanical properties as a function of temperature and rate

using energy storage and dissipation at a molecular level, and then transforms these into conventional engineering properties, which is directly relevant to this thesis. The work reported in this thesis is being used to develop and validate GIM extensions for oriented semicrystalline polymers.

1.3 Dynamic Mechanical Thermal Analysis (DMTA)

Dynamic Mechanical Thermal Analysis (DMTA) is a technique to study the viscoelastic behaviour of polymers, and together with dielectric analysis, these techniques are the most important for understanding relationships between structure and properties for polymers [94]. In contrast with rheology for measuring liquid or gel materials, DMA is suitable for measuring more 'solid-like' materials and the associated structural-mechanical transitions such as the glass transition. Because of the importance of DMA in characterizing thermal properties such as the glass transition temperature (T_g), many researchers or industrial users often call it Dynamic Thermal Mechanical Analysis (DMTA). In most contexts of this thesis, DMA is used and when a thermal or temperature effect is examined (for example, in Chapter 4), DMTA is used for accuracy. This section first introduces the viscoelastic nature of polymers, then explains how DMA is able to characterize the properties of polymers, and finally reviews the literature on biopolymer characterizations using DMA, especially for silk.

1.3.1 Viscoelastic nature of polymers

The viscoelastic properties of polymers are presented in detail in many text books. For example, Vincent's book "Structural Biomaterials" [95] is particularly straightforward in discussing viscoelasticity specially targeted at biopolymers. Here I will outline briefly some basic principles that relate to the DMTA method, before more

detailed discussions on specific aspects of viscoelastic properties in silks in the main body of this thesis.

As the name suggests, "viscoelastic" is a combination of two limiting characteristics of materials, elastic and viscous. As illustrated in the creep test in Figure 1.5, elastic means an instant maximum response to a stimulus and the material structure is able to recover instantly and completely to the original state once the stimulus is removed. Viscous means that the material response to the stimulus is a function of time. In the case of a constant stress stimulus on a Newtonian liquid, the strain response in time causes a strain rate and once the deformation is made, it becomes irreversible in time (the so-called 'plastic' flow). Also in the dynamic test in Figure 1.5, when stress is applied to a material in sinusoidal forms, the resultant strain response will be sinusoidal but the phase delay is different between pure elastic, pure plastic, and viscoelastic polymers. The elastic response is perfectly in phase with the stimulus, but the pure viscous (or 'plastic') response is often a little confusing. Because the maximum strain/stress response corresponds to the maximum rate of the stimulus stress/strain, so the two signals in a dynamic test are exactly 90 degrees out of phase. For a viscoelastic polymer, the overall general strain/stress response (amplitude and phase lag) to the stress/strain stimulus could be simply the addition of the elastic and viscous responses, depending on the rate/frequency and amplitude of the stimulus, and the proportion of the elastic and viscous components.

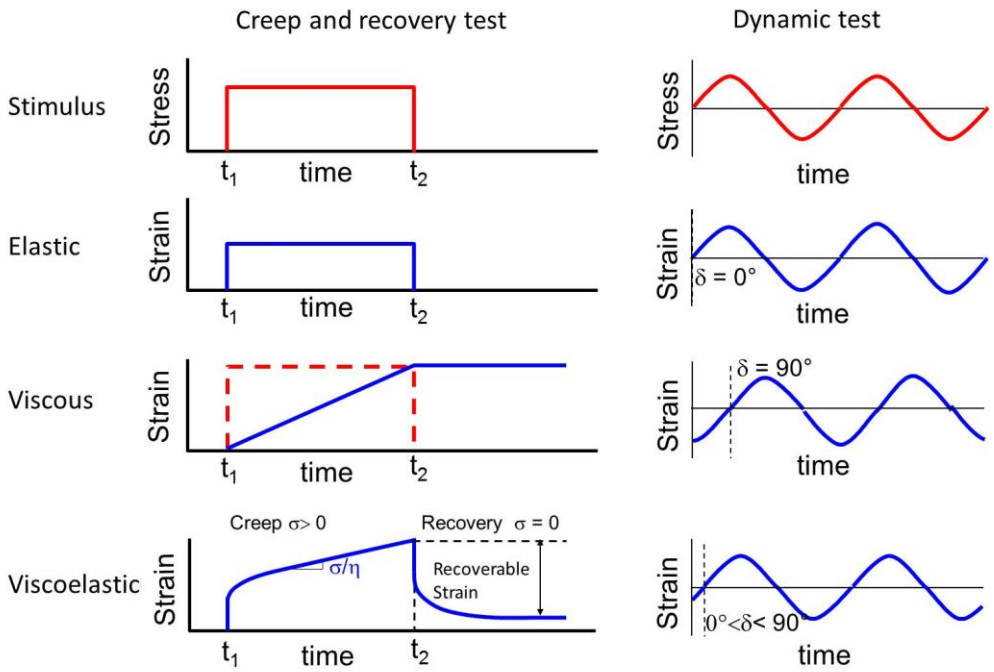

Figure 1.5 Creep and dynamic responses of elastic, viscous and viscoelastic materials.

To further extend "viscoelasticity", all polymers can be proposed to consist of four 'states of matter': three solid (largely elastic) states including ordered crystal, disordered/amorphous glass and amorphous rubber, and one liquid (largely viscous) state/melt. The crystal and glass states sustain load by changes in the bond length between molecules and have modulus values of the order GPa, directly related to the bond energy density. Rubbers have a much lower modulus of the order MPa and deform by large changes in shape, but are able to recover in shape once the force is removed. A glass changes to a rubber through the glass transition, which is observed as either a transition temperature, T_g, or a dramatic loss of modulus through yield in a stress-strain performance. The low modulus of rubbers and the viscosity of liquids are due to molecules becoming mobile above a critical separation distance for intermolecular interactions due to thermal expansion or mechanical stretching so that they can move relative to each other. The combination of rubber 'elasticity' and liquid viscosity is

classically considered to be the most important contribution to the viscoelasticity of polymers, and many fundamental properties reflect this, such as the apparent viscosity combining both the storage modulus and a characteristic relaxation time.

Semicrystalline polymers such as silk and nylon can have all the different states of matter in different combinations, depending on the chemistry, temperature, environment, morphology *etc*. This leads to great potential variability in such polymers, as discussed above in section 1.2.4. Detailed aspects of the origin of specific viscoelastic properties in silks are discussed in the body of this thesis in Chapter 3 to 6.

1.3.2 Using DMA to characterize viscoelastic polymers

The aim of DMA/DMTA is to separate the elastic and viscous components and try to relate them to structural features in a polymer. The elastic component is characterized by the storage modulus, *E'*, and the viscous component is characterized by the loss modulus, *E''*, and the relationship between the storage and the loss moduli is the loss tangent, $tan\delta = E'/E''$, measured as tangent of the phase angle between the two responses. Loss tangent also quantifies the ratio of mechanical energy stored to energy dissipated in a deformation cycle, therefore directly indicates the material composition in terms of elastic and viscous components. Here a general method of dynamic test is discussed and more specific methods using DMA are presented in Chapter 2.

The DMA dynamic mechanical test applies sinusoidal deformations through small stress/strain stimuli and captures the responses in strain/stress. The experimental set-up of DMA needs to be able to accurately apply/measure stress, strain, rate/frequency and phase lag. The deformation could be in different modes such as shear (mostly used in rheology tests), bending or tension. An ideal oscillation frequency range should be 10^{-4}-10^{4} Hz, similar to that of dielectric analysis. However, in a compromise to practicality

and accuracy, many commercial models of DMA only perform in a frequency range of 0.01-200 Hz: too low and the experiments become prohibitively long; while too fast leads to mechanical stability issues with the machine itself. Nevertheless the technique still stands distinct from "quasi-static" (strain rate < 0.01 s^{-1}) or high-rate/impact testing (> about 10^2 s^{-1}).

At present the most popular DMA model built by TA Instruments uses forced oscillation, and it applies a sinusoidal force at a prescribed frequency and measures the "strain" response from samples in the course of time and temperature. Although the sensitivity and the ease of measurement have been improved greatly, the principal mechanism behind the technique remains the same. The technical details on the controls and measurements of the instrument will be discussed in Chapter 2, methods.

DMA has been used extensively in polymer science and industry for many decades. McCrum, Read and Williams's book "Anelastic and dielectric effects in polymeric solids" was first published in 1967 [94], and still serves as an excellent polymer handbook that provides many excellent examples of DMA characterization on a large range of synthetic polymers. Historically, its fundamental use has been to characterize the glass transition of the amorphous component in polymers from glass state to rubbery state. However, DMA can be used in almost any polymer application problem. For example, DMA can help develop novel polymer products such as coatings [96]; it can also help characterize the thermo mechanical properties of polymer composites [97]. DMA is also used more and more to study biopolymers, for example, collagen [98, 99] and cellulose [100]. In biomedical applications, for example sutures, DMA is proven to be very useful [101].

1.3.3 DMA on silks

In silk research, as was introduced previously, many techniques of structural analysis and mechanical property measurement have been used extensively and a large body of experimental observations has been accumulated. However, although there is no lack in the literature on thermal or mechanical analysis alone on silks, to date, there are only a limited number of studies using DMA or DMTA to study silks. These studies include silk fibre structure-property relations [101-106], reconstituted silk fibroin (RSF) [83, 107, 108], chemical/ physical/ mechanical modifications of silk fibres or RSF [109-112], and silk composites [113-116], most of which are aimed at composite or medical materials. Moreover, DMA is used as a complementary technique to other structural analytical tools, and it is rare to see systematic DMA reports on silks, especially *natural* silk fibres.

To summarize the previous observations on characterizing silks using DMA, four aspects are discussed. Firstly, DMA is used to characterize the glass transition of the amorphous structure of silks. For *B. mori* silks, T_g ranges from 205 to 221 °C [101, 105], and this temperature decreases when the fibres are chemically modified, e.g. by alkaline treatment [110]. For RSF films, the amorphous isotropic T_g is about 177 °C reported by [83], and depending on the treatments, it could shift to either higher temperatures when ethanol treatment, stretching and heat is applied or lower temperatures when only ethanol treatment is applied [83]. The magnitude of T_g peak for RSF is much greater than natural silk fibres. For *Nephila* spider major ampullate dragline silks, T_g is reported to be 160 °C by [102] and 198 °C by [104].

Secondly, DMA is used to characterize the glass transition of silk composites. In the all-silk composite, for example, silk fiber-reinforced RSF film [117], the thermo

mechanical properties of the RSF could be improved by adding silk fibres. In other silk composites, depending on the blending materials, the composite T_g could be raised [116] or lowered [115]; and the mechanical properties of composites could outperform that of pure RSF [116].

Thirdly, DMA is used to probe the mechanical properties of silks in terms of structure-property relations. For example, the high toughness of spider silks at low temperatures was studied and the -70 °C peak was suggested to correlate to the mechanical toughness of spider silks [104]. In another study on RSF films, applying uni-axial tension to different ratios was proved to enhance the toughness of these films based on the DMA evidence [112]. Using CDA (Continuous Dynamic Analysis), a dynamic technique similar to DMA but with strain-control, Blackledge *et al.* [103]examined the dynamic mechanical properties of two types of silks from the black widow spider, however, without establishing all the links between structures, properties and functions, it aimed to provide insights into the evolution of cob-web spiders and their silks.

Lastly, DMA is used to examine the relaxation behavior of silks for practical applications. For example, to test the suitability of silks for medical suture applications, dynamic mechanical properties of silks were studied in a temperature range of -125 to 250 °C and a frequency range of 1 to 20 Hz in order to discuss the viscoelastic characteristics and the stress relaxation behavior of silks [101]. Another study [106] showed that dielectric thermal analysis (DETA) proved to be more sensitive in low temperature and high frequency range, while DMTA was more useful in characterizing T_g at high temperatures.

1.4 Overview of this thesis

1.4.1 Defining the research scope

The first three sections of the introduction summarize the literature concerning the topics that are of interest in this thesis: silk, silk structure and morphology, silk mechanical properties, DMA and why DMA is useful for understanding silk structure-property relationships. To conclude from the previous introduction, although there is a scatter of varied experimental observations from separate structural or property testing of silks, there is no consistent or coherent understanding of natural silks as structural biomaterials, specifically the vital link between their structures and properties. Moreover, no systematic DMA/DMTA study has been conducted on natural silks, in spite of its widespread use as perhaps the most important single analytical technique for synthetic polymers. Therefore, the broad aim of this thesis is to investigate the structure-property relationships for natural silks using DMA/DMTA. Furthermore, new systematic DMTA results on natural silks would contribute to advances in the subject and to provide underpinning framework to explain the intrinsic differences in natural silks. These can be interpreted in terms of how structural differences have evolved to allow silk to perform such a wide range of different biological functions.

Silks are known to vary from species to species and from type to type. Therefore, in the choice of diversity or generality for silk types, I chose the latter and focus specifically on two most studied silks: *B. mori* silkworm silks and *Nephila* spider dragline silks to explore general features of dynamic mechanical properties of silks. Additionally, synthetic polymers are included in this work for establishing methods as well as direct and consistent comparison with silks. Many synthetic polymers have been characterized using DMTA as introduced earlier, and because their structures are much

simpler compared with natural polymers, the structure-property relationships are more straightforward commensurately. For direct and consistent comparison with silks, two popularly used synthetic polymer fibres, nylon and PET, are chosen. This follows a general trend of comparing natural and synthetic materials in biopolymer research on the basis that they are all essentially polymers.

1.4.2 Evaluating the three principal factors

As discussed in previous sections, the factors affecting silk structure and properties are highly complex, and structure is particularly complex and diverse in natural silks. Therefore, to take a more physical approach to this work, I chose to study the synergistic effects of three physically fundamental factors on dynamic mechanical properties of silks: force/load (Chapter 3), temperature (Chapter 4), and water (Chapter 5 and 6). Force or load means mechanical stress since the biological functions of silks are to help the animals cope with external "stress" to fulfill a biological function. Temperature provides critical information on physical-chemical interactions at the molecular level. Lastly, water is a key contribution to most properties of biomaterials, and silk has specific interesting hydration effects such as supercontraction, for which DMTA would be an ideal tool.

1.4.3 Outlining the thesis body chapters

Chapter 2. Methods: Quasistatic and dynamic mechanical analysis on natural silks

This chapter describes the methods on calibrating the instrument, evaluating the experimental set-up, and measuring both the quasi-static and dynamic mechanical properties of silks and other fibres. In the last section of this chapter, preliminary tests on PET fibres are presented to demonstrate the methods, data presentations and experimental analyses.

Chapter 3. Dynamic mechanical properties of silks under load

This chapter examines and compares the effect of mechanical stress on the dynamic mechanical properties of *B. mori* silks, *Nephila edulis* silks, nylon 6,6 fibres and human hair. Quasi-static tensile tests, cyclical tensile tests and creep tests are also conducted to complement the dynamic mechanical testing. Quasi-static tensile modulus and dynamic storage modulus are discussed in relation to mechanical stress.

Chapter 4. Thermal and thermal history effect on the dynamic mechanical properties of silks

This chapter examines the dynamic mechanical properties of *B. mori* silks and *Nephila edulis* silks through a wide temperature range from -100 °C to +250 °C, and the changes due to thermal history. Fundamental mechanisms are discussed such as denaturation and glass transition in order to explain these structural changes.

Chapter 5. Humidity effect on mechanical properties of B. mori silkworm silks

This chapter examines the effect of excess humidity on both the quasi-static tensile properties and dynamic mechanical properties of *B. mori* silks. Humidity-temperature induced glass transition is attributed to the changes in modulus of silks subjected to combinations of high humidity and temperature.

Chapter 6. Supercontraction of spider dragline silks

This chapter examines the supercontraction in spider dragline silks in light of the glass transition induced changes from the previous chapter. Instead of just full supercontraction, a partial contraction is captured in *Nephila edulis* dragline silks under the conditions of high humidity at 50 °C. This observation is examined in detail and mechanisms are proposed for supercontraction in *Nephila edulis* dragline silks.

Chapter 7. The "quality" of silkworm silks

This chapter examines and compares the mechanical properties, especially dynamic mechanical properties in a temperature profile of various kinds of natural and unnatural *B. mori* silks. Factors such as ageing and artificial processing conditions are discussed to account for the differences in the structures of these silks. Dynamic mechanical thermal analysis is found to be sensitive to the structural differences in silks and therefore proposed as a potential Quality Control tool.

Chapter 8. Concluding remarks

This chapter contains three sections. The first section summarizes previous observations and findings in an alternative order that these discoveries were made chronologically. The second section discusses a general idea for modeling the structure of silks. The last section provides a short outlook of the work and some future experiments that can be followed from this work.

1.4.4 Concerns on ethics and animal rights

This study uses animal silks and often involves a process of collecting silks directly from the animals, especially spiders. This example process of spider silk collection is documented in various TV programs, and the video filmed in our lab can be found on the following website: http://www.theguardian.com/science/video/2013/jan/12/fritz-vollrath-spider-silk-video. The concerns arose out of ethics or animal rights. One reason some people feel offended while watching the video is that they believe it is not natural for the spider to be "forced" to spin by humans, or some think the spider is under "pain". To make sure the minimal possible damage to the spider, the protocol of spider silk collection/reeling defines the exact length in time for the spider to be anesthetized under CO_2, the way to immobilize the spider, to start reeling only after the spider wakes

up, and to use a reeling speed that is close to its natural spinning speed under normal conditions. More importantly, the spider will be returned to the web where it was.

According to the Animals (Scientific Procedures) Act 1986 (newly revised to act from January 2013), the animal testing regulation for research in the UK, the protected species include "all living vertebrates, other than man, and any living cephalopod". Therefore spiders under the phylum of *Anthropoda* are not protected by this regulation. Many people are, perhaps, similarly concerned by the use of large quantities of the fruit fly species Drosophila melanogaster in other research carried out by British Universities. These flies are also not protected under this regulation.

1.5 References

[1] Carothers, W. H. Linear polyamides and their production. US 2,130, 523, 20 September, 1938.

[2] Watson, J.; Crick, F. A structure for deoxyribose nucleic acid. *Nature* **1953,** *421* (6921), 397-398.

[3] Sanger, F.; Tuppy, H. The amino-acid sequence in the phenylalanyl chain of insulin. 1. The identification of lower peptides from partial hydrolysates. *Biochem. J.* **1951,** *49* (4), 463.

[4] Sanger, F.; Thompson, E. The amino-acid sequence in the glycyl chain of insulin. 1. The identification of lower peptides from partial hydrolysates. *Biochem. J.* **1953,** *53* (3), 353.

[5] Fanelli, A. R.; Antonini, E.; Caputo, A. Studies on the structure of hemoglobin I. Physicochemical properties of human globin. *Biochim. Biophys. Acta* **1958,** *30* (3), 608-615.

[6] Kendrew, J. C.; Bodo, G.; Dintzis, H. M.; Parrish, R.; Wyckoff, H.; Phillips, D. A three-dimensional model of the myoglobin molecule obtained by x-ray analysis. *Nature* **1958,** *181* (4610), 662-666.

[7] Pauling, L.; Corey, R. B. Configurations of polypeptide chains with favored orientations around single bonds: two new pleated sheets. *Proc. Natl. Acad. Sci. U. S. A.* **1951,** *37* (11), 729.

[8] Eyre, D. R. Collagen: molecular diversity in the body's protein scaffold. *Science* **1980,** *207* (4437), 1315-1322.

[9] Knight, D. P.; Vollrath, F. Liquid crystals and flow elongation in a spider's silk production line. *Proc. R. Soc. Lond. Ser. B-Biol. Sci.* **1999,** *266* (1418), 519-523.

[10] Vollrath, F.; Knight, D. P. Liquid crystalline spinning of spider silk. *Nature* **2001,** *410* (6828), 541-548.

[11] Willcox, P. J.; Gido, S. P.; Muller, W.; Kaplan, D. L. Evidence of a cholesteric liquid crystalline phase in natural silk spinning processes. *Macromolecules* **1996,** *29* (15), 5106-5110.

[12] Knight, D. P.; Vollrath, F. Changes in element composition along the spinning duct in a Nephila spider. *Naturwissenschaften* **2001,** *88* (4), 179-182.

[13] Terry, A. E.; Knight, D. P.; Porter, D.; Vollrath, F. PH induced changes in the rheology of silk fibroin solution from the middle division of Bombyx mori silkworm. *Biomacromolecules* **2004,** *5* (3), 768-772.

[14] Dicko, C.; Knight, D.; Kenney, J. M.; Vollrath, F. Secondary structures and conformational changes in flagelliform, cylindrical, major, and minor ampullate silk proteins. Temperature and concentration effects. *Biomacromolecules* **2004,** *5* (6), 2105-2115.

[15] Dicko, C.; Knight, D.; Kenney, J. M.; Vollrath, F. Structural conformation of spidroin in solution: a synchrotron radiation circular dichroism study. *Biomacromolecules* **2004,** *5* (3), 758-767.

[16] Craig, C. Evolution of arthropod silks. *Ann. Rev. Entomol.* **1997,** *42*, 231-267.

[17] Weisman, S.; Haritos, V. S.; Church, J. S.; Huson, M. G.; Mudie, S. T.; Rodgers, A. J. W.; Dumsday, G. J.; Sutherland, T. D. Honeybee silk: recombinant protein production, assembly and fiber spinning. *Biomaterials* **2009,** *31* (9), 2695-700.

[18] Sutherland, T.; Young, J.; Weisman, S. Insect Silk: One Name, Many Materials. *Ann. Rev. Entomol.* **2009,** *55*, 171-188.

[19] Kronenberger, K.; Moore, P. G.; Halcrow, K.; Vollrath, F. Spinning a Marine Silk for the Purpose of Tube-Building. *Journal of Crustacean Biology* **2012,** *32* (2), 191-202.

[20] Vollrath, F.; Porter, D. Spider silk as an archetypal protein elastomer. *Soft Matter* **2006,** *2*, 377-385.

[21] Vollrath, F. Strength and structure of spiders' silks. *J Biotechnol* **2000,** *74* (2), 67-83.

[22] Takei, F.; Kikuchi, Y.; Kikuchi, A.; Mizuno, S.; Shimura, K. Further Evidence for Importance of the Subunit Combination of Silk Fibroin in Its Efficient Secretion from the Posterior Silk Gland-Cells. *J. Cell Biol.* **1987,** *105* (1), 175-180.

[23] Xu, M.; Lewis, R. V. Structure of a protein superfiber - spider dragline silk. *Proc. Natl. Acad. Sci. U. S. A.* **1990,** *87* (18), 7120-7124.

[24] Hinman, M. B.; Lewis, R. V. Isolation of a clone encoding a second dragline silk fibroin. Nephila clavipes dragline silk is a two-protein fiber. *J. Biol. Chem.* **1992,** *267* (27), 19320-4.

[25] Sponner, A.; Schlott, B.; Vollrath, F.; Unger, E.; Grosse, F.; Weisshart, K. Characterization of the protein components of Nephila clavipes dragline silk. *Biochemistry* **2005,** *44* (12), 4727-4736.

[26] Lefevre, T.; Rousseau, M.; Pezolet, M. Protein Secondary Structure and Orientation in Silk as Revealed by Raman Spectromicroscopy. *Biophys. J.* **2007,** *92* (8), 2885-2895.

[27] Zhou, C.-Z.; Confalonieri, F.; Medina, N.; Zivanovic, Y.; Esnault, C.; Yang, T.; Jacquet, M.; Janin, J.; Duguet, M.; Perasso, R.; Li, Z.-G. Fine organization of Bombyx mori fibroin heavy chain gene. *Nucleic Acids Res.* **2000,** *28* (12), 2413-2419.

[28] Dicko, C.; Porter, D.; Bond, J.; Kenney, J. M.; Vollrath, F. Structural disorder in silk proteins reveals the emergence of elastomericity. *Biomacromolecules* **2007,** *9* (1), 216-221.

[29] Beckwitt, R.; Arcidiacono, S. Sequence conservation in the C-terminal region of spider silk proteins (spidroin) from Nephila clavipes (Tetragnathidae) and Araneus bicentenarius (Araneidae). *J. Biol. Chem.* **1994,** *269* (9), 6661-3.

[30] Schroeder, W. A.; Kay, L. M.; Lewis, B.; Munger, N. The amino acid composition of *Bombyx mori* silk fibroin and of Tussah silk fibroin. *J. Am. Chem. Soc.* **1955,** *77* (14), 3908-3913.

[31] Lombardi, S. J.; Kaplan, D. L. The amino acid composition of major ampullate gland silk (dragline) of *Nephila clavipes* (Araneae, Tetragnathidae). *J. Arachnol.* **1990,** *18* (3), 297-306.

[32] Liu, Y.; Sponner, A.; Porter, D.; Vollrath, F. Proline and processing of spider silks. *Biomacromolecules* **2008,** *9* (1), 116-121.

[33] Andersen, S. O. Amino Acid Composition of Spider Silks. *Comp. Bioc.* **1970,** *35* (3), 705-&.

[34] Zhang, Y.; Zhao, A. C.; Sima, Y. H.; Lu, C.; Xiang, Z. H.; Nakagaki, M. The molecular structures of major ampullate silk proteins of the wasp spider, Argiope bruennichi: A second blueprint for synthesizing de novo silk. *Comp. Bioc. B.* **2013,** *164* (3), 151-158.

[35] Hinman, M. B.; Lewis, R. V. Isolation of a clone encoding a second dragline silk fibroin - *Nephila clavipes* cragline silk is a 2-protein fiber. *J. Biol. Chem.* **1992,** *267* (27), 19320-19324.

[36] Guerette, P. A.; Ginzinger, D. G.; Weber, B. H. F.; Gosline, J. M. Silk properties determined by gland-specific expression of a spider fibroin gene family. *Science* **1996,** *272* (5258), 112-115.

[37] Ayoub, N. A.; Garb, J. E.; Tinghitella, R. M.; Collin, M. A.; Hayashi, C. Y. Blueprint for a high-performance biomaterial: full-length spider dragline silk genes. *PLoS One* **2007,** *2*, e514.

[38] Lotz, B.; Colonna Cesari, F. The chemical structure and the crystalline structures of Bombyx mori silk fibroin. *Biochimie* **1979,** *61* (2), 205-214.

[39] Simmons, A.; Ray, E.; Jelinski, L. W. Solid-State 13C NMR of Nephila clavipes Dragline Silk Establishes Structure and Identity of Crystalline Regions. *Macromolecules* **1994,** *27* (18), 5235-5237.

[40] Gillespie, D. B.; Viney, C.; Yager, P. Raman-Spectroscopic Analysis of the Secondary Structure of Spider Silk Fiber. *ACS Symp. Ser.* **1994,** *544*, 155-167.

[41] Boulet-Audet, M.; Lefèvre, T.; Buffeteau, T.; Pézolet, M. Attenuated total reflection infrared spectroscopy: An efficient technique to quantitatively determine the orientation and conformation of proteins in single silk fibers. *Appl. Spectrosc.* **2008,** *62* (9), 956-962.

[42] Asakura, T.; Yao, J. M.; Yamane, T.; Umemura, K.; Ultrich, A. S. Heterogeneous structure of silk fibers from Bombyx mori resolved by C-13 solid-state NMR spectroscopy. *J. Am. Chem. Soc.* **2002,** *124* (30), 8794-8795.

[43] van Beek, J. D.; Beaulieu, L.; Schafer, H.; Demura, M.; Asakura, T.; Meier, B. H. Solid-state NMR determination of the secondary structure of Samia cynthia ricini silk. *Nature* **2000,** *405* (6790), 1077-1079.

[44] Paquet-Mercier, F.; Lefevre, T.; Auger, M.; Pezolet, M. Evidence by infrared spectroscopy of the presence of two types of beta-sheets in major ampullate spider silk and silkworm silk. *Soft Matter* **2013,** *9* (1), 208-215.

[45] van Beek, J. D.; Hess, S.; Vollrath, F.; Meier, B. H. The molecular structure of spider dragline silk: Folding and orientation of the protein backbone. *Proc. Natl. Acad. Sci. U. S. A.* **2002,** *99* (16), 10266-10271.

[46] Oroudjev, E.; Soares, J.; Arcdiacono, S.; Thompson, J. B.; Fossey, S. A.; Hansma, H. G. Segmented nanofibers of spider dragline silk: Atomic force microscopy and single-molecule force spectroscopy. *Proc. Natl. Acad. Sci. U. S. A.* **2002,** *99*, 6460-6465.

[47] Riekel, C.; Vollrath, F. Spider silk fibre extrusion: combined wide- and small-angle X-ray microdiffraction experiments. *Int. J. Biol. Macromol.* **2001,** *29* (3), 203-210.

[48] Du, N.; Xiang, Y. L.; Narayanan, J.; Li, L.; Lim, M. L. M.; Li, D. Design of superior spider silk: From nanostructure to mechanical properties. *Biophys. J.* **2006,** *91* (12), 4528-4535.

[49] Grubb, D. T.; Jelinski, L. W. Fiber morphology of spider silk: The effects of tensile deformation. *Macromolecules* **1997,** *30* (10), 2860-2867.

[50] Augsten, K.; Muhlig, P.; Herrmann, C. Glycoproteins and skin-core structure in Nephila clavipes spider silk observed by light and electron microscopy. *Scanning* **2000,** *22* (1), 12-15.

[51] Putthanarat, S.; Stribeck, N.; Fossey, S. A.; Eby, R. K.; Adams, W. W. Investigation of the nanofibrils of silk fibers. *Polymer* **2000,** *41* (21), 7735-7747.

[52] Miller, L. D.; Putthanarat, S.; Eby, R.; Adams, W. Investigation of the nanofibrillar morphology in silk fibers by small angle X-ray scattering and atomic force microscopy. *Int. J. Biol. Macromol.* **1999,** *24* (2), 159-165.

[53] Sapede, D.; Seydel, T.; Forsyth, V. T.; Koza, M. A.; Schweins, R.; Vollrath, F.; Riekel, C. Nanofibrillar structure and molecular mobility in spider dragline silk. *Macromolecules* **2005,** *38* (20), 8447-8453.

[54] HernandezCruz, D.; Rousseau, M.-E.; West, M. M.; Pezolet, M.; Hitchcock, A. P. Quantitative Mapping of the Orientation of Fibroin Fibers by Scanning Transmission X-ray Microscopy. *Biomacromolecules* **2006,** *7* (3), 836-843.

[55] Rousseau, M. E.; HernandezCruz, D.; West, M. M.; Hitchcock, A. P.; Pezolet, M. Nephila clavipes Spider Dragline Silk Microstructure Studied by Scanning Transmission X-ray Microscopy. *J. Am. Chem. Soc.* **2007**.

[56] Sponner, A.; Vater, W.; Monajembashi, S.; Unger, E.; Grosse, F.; Weisshart, K. Composition and hierarchical organization of a spider silk. *PLoS One* **2007,** (10), e998.

[57] Frische, S.; Maunsbach, A. B.; Vollrath, F. Elongate cavities and skin-core structure in Nephila spider silk observed by electron microscopy. *J. Microsc.-Oxf.* **1998,** *189*, 64-70.

[58] Knight, D. P.; Knight, M. M.; Vollrath, F. Beta transition and stress-induced phase separation in the spinning of spider dragline silk. *Int. J. Biol. Macromol.* **2000,** *27* (3), 205-210.

[59] Porter, D.; Guan, J.; Vollrath, F. Spider Silk: Super Material or Thin Fibre? *Adv. Mater.* **2013,** *25* (9), 1275-1279.

[60] Keten, S.; Xu, Z.; Ihle, B.; Buehler, M. J. Nanoconfinement controls stiffness, strength and mechanical toughness of [beta]-sheet crystals in silk. *Nat. Mater.* **2010,** *9* (4), 359-367.

[61] Gosline, J.; Guerette, P.; Ortlepp, C.; Savage, K. The mechanical design of spider silks: from fibroin sequence to mechanical function. *J. Exp. Biol.* **1999,** *202* (23), 3295-3303.

[62] Agnarsson, I.; Kuntner, M.; Blackledge, T. A. Bioprospecting finds the toughest biological material: extraordinary silk from a giant riverine orb spider. *PLoS One* **2010,** *5* (9), e11234.

[63] Fu, C.; Porter, D.; Chen, X.; Vollrath, F.; Shao, Z. Understanding the Mechanical Properties of Antheraea Pernyi Silk—From Primary Structure to Condensed Structure of the Protein. *Adv. Funct. Mater.* **2011,** *21* (4), 729-737.

[64] Vollrath, F.; Porter, D. Silks as ancient models for modern polymers. *Polymer* **2009,** *50* (24), 5623-5632.

[65] Perez-Rigueiro, J.; Viney, C.; Llorca, J.; Elices, M. Silkworm silk as an engineering material. *J. Appl. Polym. Sci.* **1998,** *70* (12), 2439-2447.

[66] Plaza, G. R.; Guinea, G. V.; Perez-Rigueiro, J.; Elices, M. Thermo-hygro-mechanical behavior of spider dragline silk: Glassy and rubbery states. *J. Polym. Sci. Pol. Phys.* **2006,** *44* (6), 994-999.

[67] Fu, C. J.; Porter, D.; Shao, Z. Z. Moisture effects on *Antheraea pernyi* silk's mechanical property. *Macromolecules* **2009,** *42* (20), 7877-7880.

[68] Guan, J.; Porter, D.; Vollrath, F. Silks cope with stress by tuning their mechanical properties under load. *Polymer* **2012,** *53* (13), 2717-2726.

[69] Liu, Y.; Shao, Z. Z.; Vollrath, F. Relationships between supercontraction and mechanical properties of spider silk. *Nat. Mater.* **2005,** *4* (12), 901-905.

[70] Cunniff, P. M.; Fossey, S. A.; Auerbach, M. A.; Song, J. W.; Kaplan, D. L.; Adams, W. W.; Eby, R. K.; Mahoney, D.; Vezie, D. L. Mechanical and thermal properties of dragline silk from the spider Nephila clavipes. *Polym. Adv. Technol.* **1994,** *5* (8), 401-410.

[71] Perez-Rigueiro, J.; Elices, M.; Llorca, J.; Viney, C. Effect of degumming on the tensile properties of silkworm (Bombyx mori) silk fiber. *J. Appl. Polym. Sci.* **2002,** *84* (7), 1431-1437.

[72] Vollrath, F.; Madsen, B.; Shao, Z. Z. The effect of spinning conditions on the mechanics of a spider's dragline silk. *Proc. R. Soc. Lond. Ser. B-Biol. Sci.* **2001,** *268* (1483), 2339-2346.

[73] Swanson, B. O.; Blackledge, T. A.; Beltran, J.; Hayashi, C. Y. Variation in the material properties of spider dragline silk across species. *Appl. Phys. A-Mater. Sci. Process.* **2006,** *82* (2), 213-218.

[74] Franbourg, A. Current research on ethnic hair. *Journal of the American Academy of Dermatology* **2003,** *48* (6), S115.

[75] Gosline, J. M.; Guerette, P. A.; Ortlepp, C. S.; Savage, K. N. The mechanical design of spider silks: From fibroin sequence to mechanical function. *J. Exp. Biol.* **1999,** *202* (23), 3295-3303.

[76] Kunugi, T.; Suzuki, A.; Hashimoto, M. Mechanical properties and superstructure of high-modulus and high-strength PET fiber prepared by zone annealing. *J. Appl. Polym. Sci.* **1981,** *26* (6), 1951-1960.

[77] Termonia, Y. Molecular Modeling of Spider Silk Elasticity. *Macromolecules* **1994,** *27* (25), 7378-81.

[78] Simmons, A. H.; Michal, C. A.; Jelinski, L. W. Molecular orientation and two-component nature of the crystalline fraction of spider dragline silk. *Science* **1996,** *271* (5245), 84-87.

[79] Papadopoulos, P.; Solter, J.; Kremer, F. Hierarchies in the structural organization of spider silk-a quantitative model. *Colloid and Polymer Science* **2009,** *287* (2), 231-236.

[80] Eisoldt, L.; Smith, A.; Scheibel, T. Decoding the secrets of spider silk. *Materials Today* **2011,** *14* (3), 80-86.

[81] Blackledge, T. A.; Boutry, C.; Wong, S.-C.; Baji, A.; Dhinojwala, A.; Sahni, V.; Agnarsson, I. How super is supercontraction? Persistent versus cyclic responses to humidity in spider dragline silk. *J. Exp. Biol.* **2009,** *212* (13), 1981-1989.

[82] Ene, R.; Papadopoulos, P.; Kremer, F. Combined structural model of spider dragline silk. *Soft Matter* **2009,** *5* (22), 4568-4574.

[83] Yuan, Q. Q.; Yao, J. R.; Huang, L.; Chen, X.; Shao, Z. Z. Correlation between structural and dynamic mechanical transitions of regenerated silk fibroin. *Polymer* **2010,** *51* (26), 6278-6283.

[84] Thistlethwaite, T.; Jakeways, R.; Ward, I. M. The crystal modulus and structure of oriented poly(ethylene terephthalate). *Polymer* **1988,** *29* (1), 61-69.

[85] Ackbarow, T.; Chen, X.; Keten, S.; Buehler, M. J. Hierarchies, multiple energy barriers, and robustness govern the fracture mechanics of alpha-helical and beta-sheet protein domains. *Proc. Natl. Acad. Sci. U. S. A.* **2007,** *104*, 16410-16415.

[86] Buehler, M. J.; Keten, S.; Ackbarow, T. Theoretical and computational hierarchical nanomechanics of protein materials: Deformation and fracture. *Progress in Materials Science* **2008,** *53* (8), 1101-1241.

[87] Cetinkaya, M.; Xiao, S.; Markert, B.; Stacklies, W.; Gräter, F. Silk fiber mechanics from multiscale force distribution analysis. *Biophys. J.* **2011,** *100* (5), 1298-1305.

[88] Porter, D.; Vollrath, F. Silk as a Biomimetic Ideal for Structural Polymers. *Adv. Mater.* **2009,** *21* (4), 487-492.

[89] Thiel, B. L.; Guess, K. B.; Viney, C. Non-periodic lattice crystals in the hierarchical microstructure of spider (major ampullate) silk. *Biopolym.* **1997,** *41* (7), 703-719.

[90] Thiel, B. L.; Viney, C. Spider major ampullate silk (drag line): Smart composite processing based on imperfect crystals. *J. Microsc.-Oxf.* **1997,** *185*, 179-187.

[91] Porter, D.; Vollrath, F.; Shao, Z. Predicting the mechanical properties of spider silk as a model nanostructured polymer. *The European Physical Journal E* **2005,** *16* (2), 199-206.

[92] Vollrath, F.; Porter, D. Spider silk as a model biomaterial. *Appl. Phys. A-Mater.* **2006,** *82* (2), 205-212.

[93] Porter, D., *Group Interaction Modelling of Polymer Properties*. Marcel Dekker: New York, 1995.

[94] McCrum, N. G.; Read, B. E.; Williams, G., *Anelastic and dielectric effects in polymeric solids*. John Wiley & Sons: London, 1967.

[95] Vincent, J. F., *Structural biomaterials*. Princeton Univ. Press: Princeton, NJ, 1990.

[96] Crawford, D. M.; Escarsega, J. A. Dynamic mechanical analysis of novel polyurethane coating for military applications. *Thermochim. Acta.* **2000,** *357–358* (0), 161-168.

[97] Papadopoulou, C. P.; Kalfoglou, N. K. Comparison of compatibilizer effectiveness for PET/PP blends: their mechanical, thermal and morphology characterization. *Polymer* **2000,** *41* (7), 2543-2555.

[98] Cucos, A.; Budrugeac, P.; Miu, L.; Mitrea, S.; Sbarcea, G. Dynamic mechanical analysis (DMA) of new and historical parchments and leathers: Correlations with DSC and XRD. *Thermochim. Acta* **2011,** *516* (1-2), 19-28.

[99] Wu, C. C.; Ding, S. J.; Wang, Y. H.; Tang, M. J.; Chang, H. C. Mechanical properties of collagen gels derived from rats of different ages. *J. Biomater. Sci.-Polym. Ed.* **2005,** *16* (10), 1261-1275.

[100] Paes, S. S.; Sun, S. M.; MacNaughtan, W.; Ibbett, R.; Ganster, J.; Foster, T. J.; Mitchell, J. R. The glass transition and crystallization of ball milled cellulose. *Cellulose* **2010,** *17* (4), 693-709.

[101] Vonfraunhofer, J. A.; Sichina, W. J. Characterization of Surgical Suture Materials Using Dynamic Mechanical Analysis. *Biomaterials* **1992,** *13* (10), 715-720.

[102] Guess, K. B.; Viney, C. Thermal analysis of major ampullate (drag line) spider silk: the effect of spinning rate on tensile modulus. *Thermochim. Acta.* **1998,** *315* (1), 61-66.

[103] Blackledge, T. A.; Swindeman, J. E.; Hayashi, C. Y. Quasistatic and continuous dynamic characterization of the mechanical properties of silk from the cobweb of the black widow spider Latrodectus hesperus. *J. Exp. Biol.* **2005,** *208* (10), 1937-1949.

[104] Yang, Y.; Chen, X.; Shao, Z. Z.; Zhou, P.; Porter, D.; Knight, D. P.; Vollrath, F. Toughness of spider silk at high and low temperatures. *Adv. Mater.* **2005,** *17* (1), 84-88.

[105] Tsukada, M.; Freddi, G.; Nagura, M.; Ishikawa, H.; Kasai, N. Structural-changes of silk fibers induced by heat-treatment. *J. Appl. Polym. Sci.* **1992,** *46* (11), 1945-1953.

[106] Um, I. C.; Kim, T. H.; Kweon, H. Y.; Ki, C. S.; Park, Y. H. A Comparative Study on the Dielectric and Dynamic Mechanical Relaxation Behavior of the Regenerated Silk Fibroin Films. *Macromolecular Research* **2009,** *17* (10), 785-790.

[107] Tsukada, M.; Freddi, G.; Kasai, N.; Monti, P. Structure and molecular conformation of tussah silk fibroin films treated with water-methanol solutions: Dynamic mechanical and thermomechanical behavior. *J. Polym. Sci. Pol. Phys.* **1998,** *36* (15), 2717-2724.

[108] Tsukada, M.; Freddi, G.; Gotoh, Y.; Kasai, N. Physical and chemical properties of Tussah silk fibroin films. *J. Polym. Sci. Pol. Phys.* **1994,** *32* (8), 1407-1412.

[109] Tsukada, M.; Freddi, G.; Ishiguro, Y.; Shiozaki, H. Structural-analysis of methacrylamide-grafted silk fibers. *J. Appl. Polym. Sci.* **1993,** *50* (9), 1519-1527.

[110] Freddi, G.; Kato, H.; Tsukada, M.; Allara, G.; Shiozaki, H. Physical-properties and dyeability of naoh-treated silk fibers. *J. Appl. Polym. Sci.* **1995,** *55* (3), 481-487.

[111] Tsukada, M.; Gotoh, Y.; Shiozaki, H.; Freddi, G.; Crighton, J. S. Physical Characteristics of Silk Fibers Modified with Dibasic Acid Anhydrides. *J. Appl. Polym. Sci.* **1994,** *51* (2), 345-352.

[112] Yin, J.; Chen, E.; Porter, D.; Shao, Z. Enhancing the Toughness of Regenerated Silk Fibroin Film through Uniaxial Extension. *Biomacromolecules* **2010,** *11* (11), 2890-2895.

[113] Cheng, C.; Shao, Z. Z.; Chen, X. COMPOSITE MATERIAL MADE OF REGENERATED SILK FIBROIN AND SILICA SOL. *Acta Polym. Sin.* **2008,** (10), 974-978.

[114] Anumolu, R.; Gustafson, J. A.; Magda, J. J.; Cappello, J.; Ghandehari, H.; Pease, L. F. Fabrication of Highly Uniform Nanoparticles from Recombinant Silk-Elastin-like Protein Polymers for Therapeutic Agent Delivery. *ACS Nano* **2011,** *5* (7), 5374-5382.

[115] Lee, S. M.; Cho, D.; Park, W. H.; Lee, S. G.; Han, S. O.; Drzal, L. T. Novel silk/poly(butylene succinate) biocomposites: the effect of short fibre content on their mechanical and thermal properties. *Comp. Sci. Technol.* **2005,** *65* (3-4), 647-657.

[116] Park, S. J.; Lee, K. Y.; Ha, W. S.; Park, S. Y. Structural changes and their effect on mechanical properties of silk fibroin/chitosan blends. *J. Appl. Polym. Sci.* **1999,** *74* (11), 2571-2575.

[117] Yuan, Q.; Yao, J.; Chen, X.; Huang, L.; Shao, Z. The preparation of high performance silk fiber/fibroin composite. *Polymer* **2010,** *51* (21), 4843-4849.

Chapter 2. Methods: Quasi-static and dynamic mechanical analysis on thin fibres using DMA Q800

2.1 Introduction to TA instrument: DMA Q800

The Dynamic mechanical analyser model Q800, purchased in 2007 by Oxford Silk Group from TA Instruments, is the main instrument for mechanical testing in this thesis. Figure 2.1 shows the external appearance and the internal mechanics of the instrument. It can operate in not only dynamic or oscillatory mode, but also quasi-static tensile mode. Q800 has the following key features: (1) stress or force control through a magnetic drive motor; (2) low-friction air bearing design for the drive therefore enhanced sensitivity for measuring weak samples; (3) wide temperature range from -150 °C to 600 °C; (4) optical decoder for precise position or length measurement (resolution of 1 nm).

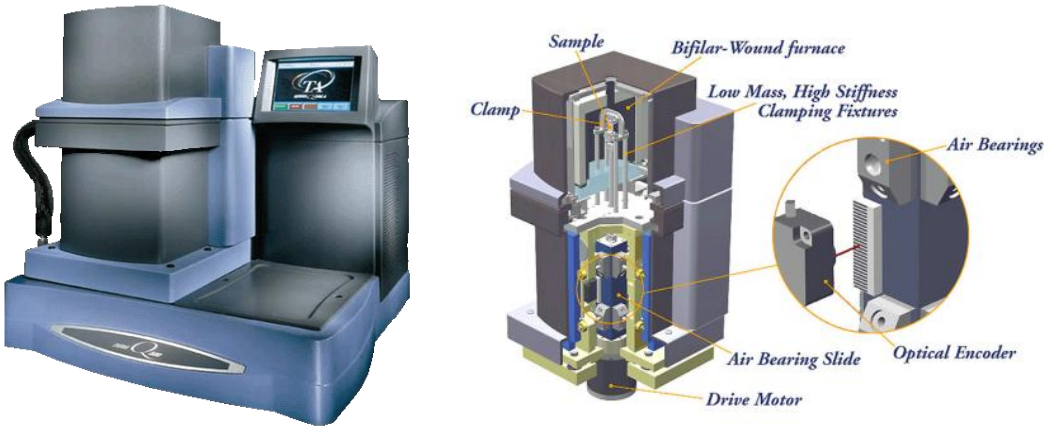

Figure 2.1 External appearance and schematic view of the internal mechanics of the instrument DMA Q800 (pictures taken from TA Instrument product brochure).

2.1.1 The measuring principles of DMA Q800

DMA Q800 has two operating modes, depending on whether the electronic control for dynamic measurements is switched on or not. It is also noted here that the

force/stress control only makes a difference from the strain control for large deformations of the samples, e.g. the quasi-static tensile test and under the static loadings for the static-dynamic test in Chapter 3. For small deformations, for example, 0.1% strain which is the dynamic oscillatory strain I use, it is assumed the strain and stress are interchangeable within the elastic limit. In the non-oscillatory mode, e.g. controlled force mode for measuring quasi-static tensile properties, the operation is relatively straightforward: force is controlled as a function of time or temperature and length is measured accordingly as an output. Quasi-static tensile tests, cyclical tensile tests and relaxation experiments such as creep are operated in this mode.

In the dynamic oscillatory mode, setting up a test involves both "static" and "dynamic" parameters including frequency, dynamic strain, static loading (pre-force), temperature range and temperature ramp rate. The basic function of the dynamic mode is to apply a small periodic deformation and to measure the dynamic mechanical response as a function of time or temperature as shown in Figure 2.2. In a dynamic test, the control variables usually are time (t), temperature (T), frequency (f), static force (F), dynamic stimulus force (F') or amplitude (A'); and the measureable parameters are length (L), dynamic response and phase lag (δ). Sample cross-sectional area (A) is needed for stress and modulus calculation. The properties derived from the above raw signals are calculated as follows:

Stiffness (K): $K= F'/A'$

Geometric factor (GF): $GF=L/A$

Storage modulus (E'): $E'= K\times GF$

Loss modulus (E''): $E''= K\times GF\times Tan\delta$

Loss tangent: $Tan\delta$

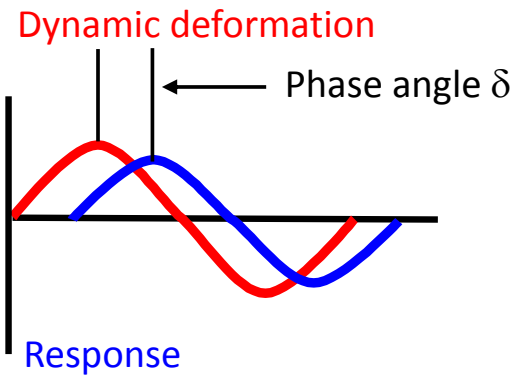

Figure 2.2 Illustration of one complete cycle of the dynamic measurement.

2.1.2 Calibrating the instrument

To ensure reliable control and measurements of the raw signals, instrument calibration needs to be performed every month or each time a new type of clamps is installed or the electronics platform of the instrument is disturbed. The lab technician or myself calibrated the instrument every month and every calibration report is recorded in the log-book.

The complete instrument calibration process includes three steps:

Electronics: a fixed shipping bracket is installed to ensure the mechanical rigidity of the drive, and a residual error due to the performance of the electronics is reported;

Force: a force gain as a function of drive slide position is measured under two conditions of unloaded and 100 g weight, and mathematically fitted and compared with a standard cubic spline, and the goodness of fit is given;

Dynamics, a set of steel samples with known stiffness and loss properties is measured over a range of force and frequency, and a residual value is reported after comparing with the standards.

If all the reported values are within range, the instrument is successfully calibrated. The next step is to install and calibrate the clamps for sample measurements. Here, I only show the calibration for tension (film/fibre) clamps, as most of the tests in this thesis were done using these clamps. The calibration includes three steps:

Clamp mass: the clamp is weighed and compensated to ensure the accuracy of force measurements;

Length: a standard gauge-block is measured in length using a micrometer and is loaded to ensure accurate measurement of sample length;

Compliance: a steel specimen of measured size and known stiffness is loaded to calibrate the flexibility of the clamps and to ensure accurate measurements on stiff samples.

To compensate the thermal lag due to clamp mass and heating rate, temperature calibration needs to be performed. There are two thermocouples in the DMA furnace, the reference thermocouple (which compares the furnace temperature with the sample temperature) and the sample sensor thermocouple (which gives the raw signal and control of temperature). There are two types of temperature calibrations: absolute or iso-thermal and dynamic temperature calibration. At least two sets of temperature offset points (true values and observed values on the DMA respectively) are needed to provide temperature correction. Here, only the temperature calibration for the tension clamps is described.

For the absolute temperature calibration, room temperature and the melting point of indium are measured and compared with the reference or "true" values. The true value of room temperature is taken as the average of three measurements from different thermometers in the testing room and compared with the temperature measured on the

DMA. For the second point, the reference value is 156.7 °C as specified in the supplier's information, and is compared with the measured value of 157.2 °C from a temperature ramp test at low rate of 0.3 °C/min, as shown in Figure 2.3. The melting point of indium in the test is identified as the turning point of the length. The negligible difference between the "true" and measured values of temperatures demonstrates the instrument DMA Q800 provides precise absolute temperature measurement.

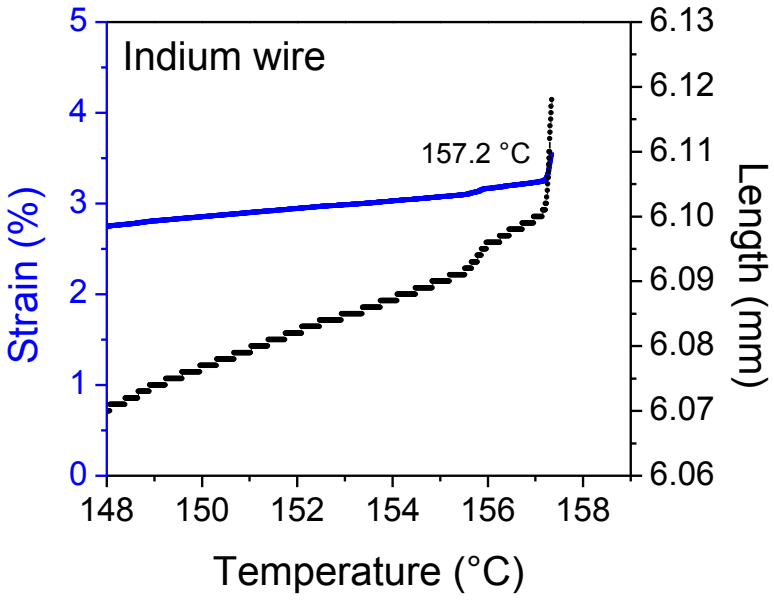

Figure 2.3 Measurement of the melting point of Indium at 0.3 °C/min heating rate in controlled force mode for absolute temperature calibration.

For dynamic temperature scans, both clamp mass and heating rate need to be compensated for the accurate temperature report. I used water and indium as standard materials for dynamic temperature calibrations under conditions of 3 °C/min heating rate on tension (film) clamps: the observed values of 4.9 °C and 167.4 °C compared with "true" values of 0 °C and 156.7 °C. It is found that dynamic heating makes a temperature difference of about 11 °C. Based on the calibration and the offset points, the measured temperature values in a dynamic temperature scan become comparable with the reported values in the literature, and consistent between different tests.

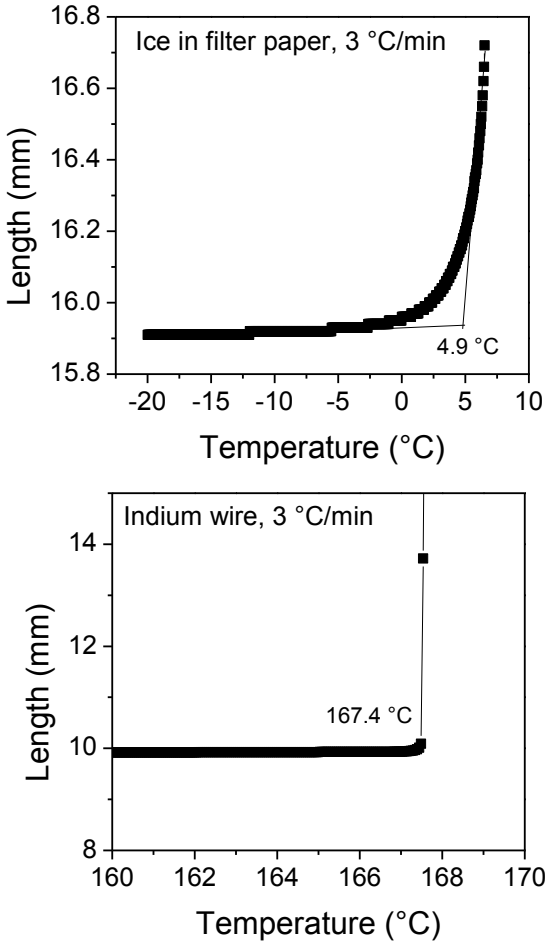

Figure 2.4 Measurement of the melting point of water and indium at 3 °C/min heating rate in controlled force mode for dynamic temperature calibration.

2.1.3 Evaluating different clamps

To suit different sample geometries and levels of stiffness, more than one type of clamps are supplied with DMA Q800. As an interesting learning process on how to operate the instrument, thin sheets of amorphous polystyrene (PS) were made from granules (molecular weight of 300 kD), and tested on three clamps: tension film/fibre, cantilever, and powder clamps. The mode of deformation of the samples in each set of clamps is different, which is important for engineering applications. For example, as shown in Figure 2.5, tension clamps with thin samples applies mainly tensile deformation; cantilever clamps apply a combination of tensile, compression and shear deformation. The powder clamp is designed as a metal pocket to sandwich the powder

or film samples, and it couples with the dual cantilever fixture; although it is sensitive to the transition temperatures, the thermo-mechanical properties cannot be quantified from the powder clamps.

Figure 2.6 compares the loss tangent results from the three clamps for PS glass transition. Because the temperature calibration references were not set up and only default temperatures were used, the absolute temperature measurements are not valid for comparison. The two loss tangent peaks from the tension and cantilever clamps agree well, and as discussed above, the transition temperature from the powder clamp is comparable with the other two, but the loss tangent peak appears much smaller and cannot be used for quantification. Taking the measured T_g from the tension clamp measurement, and subtracting the temperature calibration offset of about 11 °C, the transition temperature becomes 101 °C, almost the same as the consensus reference of 100 °C [1]. The area of loss tangent peaks between tension and cantilever clamps seems consistent and in agreement with reported values in [2], and therefore it can be used for quantification of structural properties. There was some speculation after these tests that the powder clamp measures a small volumetric loss tangent, but this hypothesis needs to be validated with a range of different polymer samples.

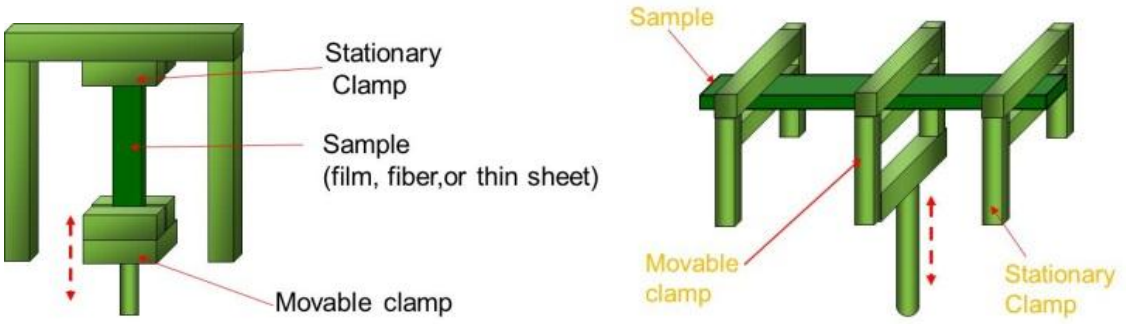

Figure 2.5 Illustrations of tension and cantilever clamps.

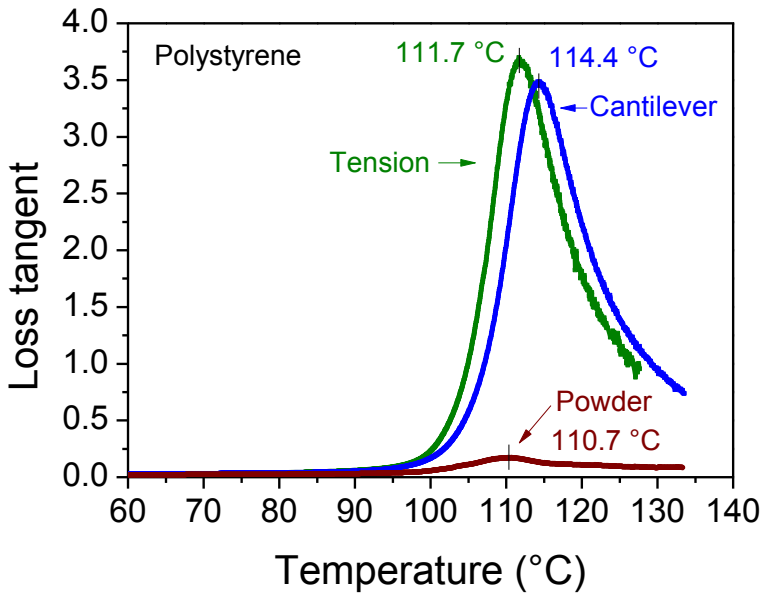

Figure 2.6 Loss tangent profiles of polystyrene (PS) sample in dynamic mechanical temperature scan in tension, dual cantilever, and powder clamps.

2.2 Sample mounting and clamping

2.2.1 Mounting fibre samples

Various fibres are used throughout this thesis. Natural *B. mori* silks are prepared from cocoon shells; and natural spider dragline silks are reeled at a "natural" drawing speed from live spiders, as will be described in section 3.2.1 of Chapter 3. Synthetic fibres including Polyethylene terephthalate (PET, both medium and high tenacity) and nylon 6,6 (both medium and high tenacity) are purchased from Goodfellow Cambridge Ltd. Specific details on each fibre will be given in later chapters where relevant. Here, only the sample mounting technique is discussed.

As shown in Figure 2.7, in order to be protected from damage during storage and to be easily loaded onto the DMA tension clamps for test, the fibre sample is fixed at the two ends on a paper-card frame. After being loaded correctly, the paper card is cut open and the fibre is left on the drive to bear the load. Loctite superglue (gel or liquid) is used

for sticking the fibre and paper-card together. When the fibre is very fine (e.g. spider silks), the mounting is handled under a microscope with LED lighting.

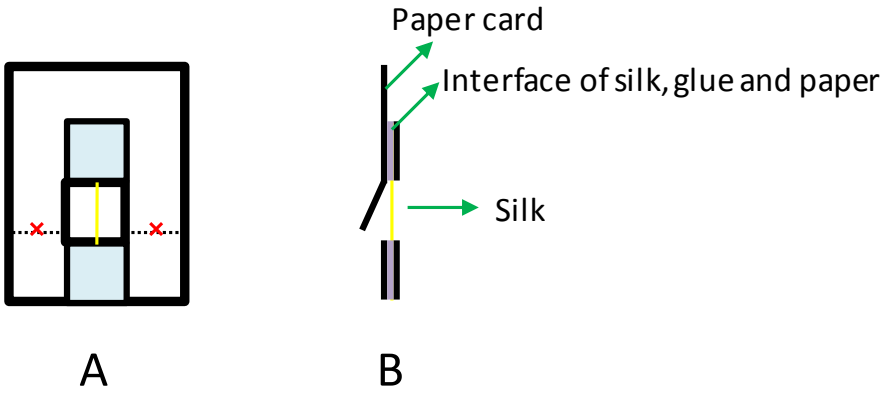

Figure 2.7 Front and side view of the sample holder (paper card frame) and the fibre sample fixture.

The default gauge length is chosen to be 5 mm based on the following considerations: first, the ratio of fibre thickness to length needs to be over 20 to ensure tensile deformation only; second, the stiffness of the sample needs to be over 100 N/m as required for accurate signal strength; and third, the total travel range of the drive is 2-25 mm. In the supercontraction Chapter 6, due to the large shrinkage of length, a larger gauge length of 10 mm is used. Note here the gauge length is the distance between the top and bottom edges of the sample window, and the gluing was made sure to align with the edges of the frame when the sample was prepared.

2.2.2 Evaluating the sample fixture system

As shown in Figure 2.7, our sample holder system involves not only the fibre but also paper card and glue. Before evaluating any real effects from the samples, it is needed to look at the thermal and mechanical responses of the paper card and the glue through the temperature (and also humidity in some cases) range, and it is best to perform a control fibre test.

Three control experiments were run as dynamic mechanical temperature scans from room temperature to 300 °C, as shown in Figure 2.8: (A) paper card, (B) paper card+glue and (C) metal wire with paper card+glue. Ideally, a lower temperature range should be covered in these tests. However, screening tests did not suggest any problems compared with higher temperature ranges. A clamping pressure of 3 psi (about 20.7 kPa) was applied when loading the samples. For (A) and (B), a static tension force of 1 N (~100 MPa) was applied and a dynamic strain of 0.2%; for (C) and (D), the static force was 0.01 N and 0.001 N with the same dynamic strain.

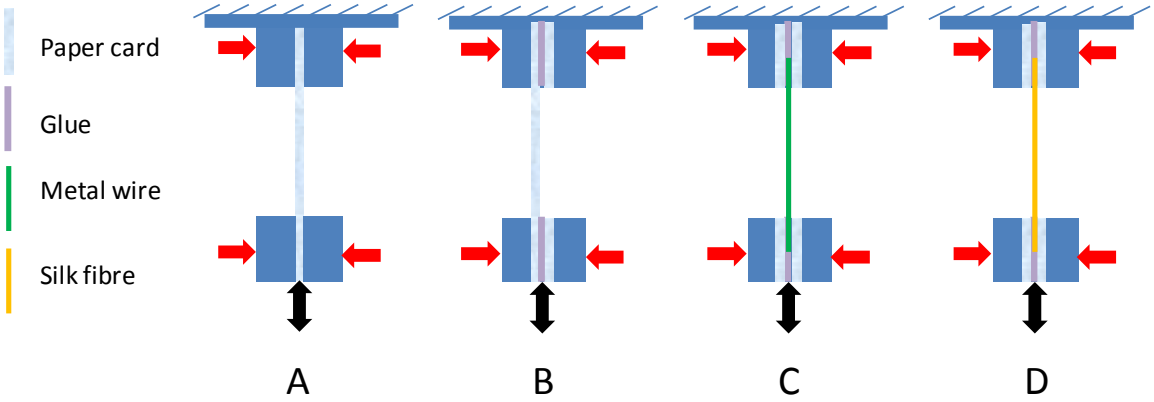

Figure 2.8 Illustrations of control experiments for testing the sample fixture materials and technique.

Figure 2.9 shows the dynamic mechanical properties of the paper card as a function of temperature: storage modulus shows a linear gradual decrease with increasing temperature, and length changes very little throughout the temperature range. The modulus reduction may be caused by two reasons: the composite network of short cellulose fibres gradually breaks down due to the combination of heat, static and dynamic loading; and the cellulose fibres soften as the temperature rises. However, it does not show any transitional change from the paper card which might interfere with the sample responses. More importantly, the paper frame is not directly under tensional load in the fibre test, therefore it is reasonable to say that the paper card used for sample

holder frames is thermally and mechanically “stable” through the testing temperature range.

Figure 2.10 compares the loss tangent profiles from the three control tests and one silk test. First, comparing (A) and (B) of paper card with or without glue between the clamps, the loss tangent starts to diverge above 125 °C, which may be caused by the softening and melting of the glue. But again, no transitional events are observed until 290 °C when the glue melts and the sample clamping collapses in (B). Second, comparing (C) and (D) of metal wire versus silk fibre, the loss tangent of metal wire shows a gradual increase as the temperature increases, which may imply either a bad adhesion between the glue and the wire or gradual softening of the glue; also, there is no apparent transition with the metal wire whereas the silk shows a transition by a clear loss tangent peak at around 217 °C.

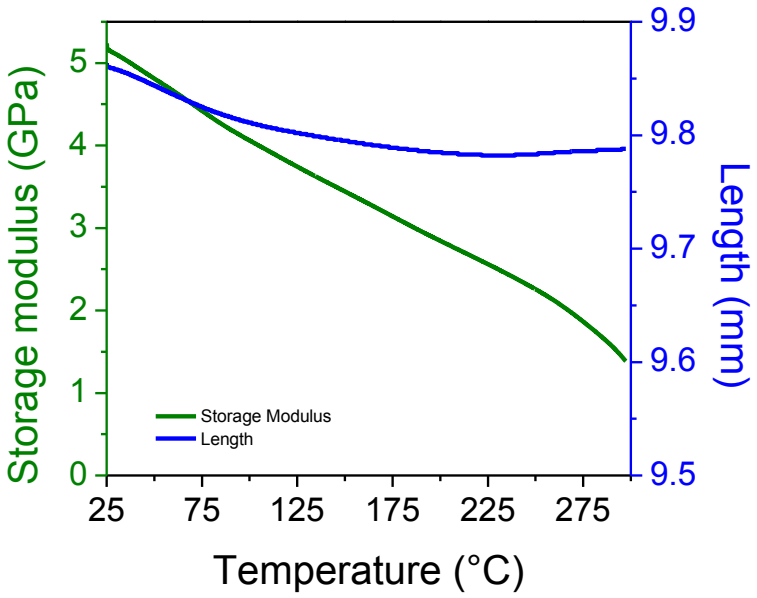

Figure 2.9 Modulus (green) and length (blue) profiles of paper card as a function of temperature in a dynamic mechanical temperature scan.

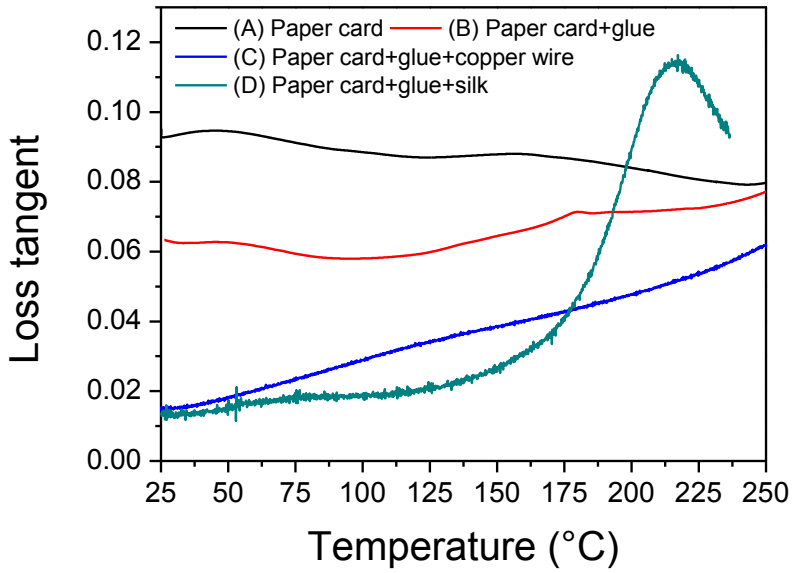

Figure 2.10 Loss tangent as a function of temperature for the four tests demonstrated in Figure 2.8.

To summarize, our sample fixture system is validated and it does not interfere with the thermal and mechanical effects on the polymeric fibres that are of interest.

2.3 Quasi-static mechanical testing

2.3.1 Slack behavior in the tensile performance of silkworm silks

In the beginning of the tensile testing on *B. mori* silks, a "J"-shaped stress-strain behavior was noticed, as shown in Figure 2.11, where the stress response is too small to be taken as the real fibre resistance. After analyzing the silks under a microscope, it is found that the 'bendy' or 'wavy' morphology of silks from the figure "8" spinning habit of a silkworm causes the "J" slack behavior, which is also seen in the tensile behaviors of soft and hydrated biopolymers such as tendon [3]. It is also found that the fibre only becomes straight at a stress above 50 MPa. In the processing of stress strain curves, the slack strain is usually removed and the extrapolated elastic fibre response offset to 0%, e.g. the strain of 8% in Figure 2.11.

One problem related to this initial nonlinear behavior of stress-strain is that the initial tensile modulus by strict engineering definition cannot be obtained at low strains (e.g. below 1%). However, also at strains larger than 1%, some molecular structures in silks may yield and the tensile modulus becomes lower. In order to be consistent in comparing the tensile moduli between samples, I take the gradient of stress over strain at around 50 MPa, where the fibre just becomes straight, as the initial tensile modulus of naturally wavy *B. mori* silks.

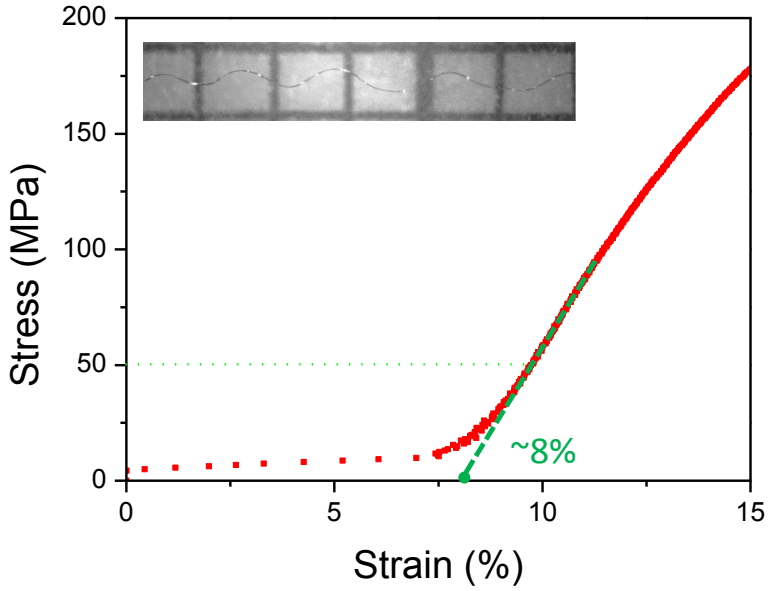

Figure 2.11 The "J"-shape stress-strain behaviour of a *B. mori* silk fibre and the correlated 'wavy' morphology of the silk (inset). Each square in the inset image measures 1 mm by 1 mm.

2.3.2 The rate dependence of stress-strain performance

The standard rate for quasi-static tensile testing used in the thesis is 0.01 s^{-1}, which is in the middle of the range most commonly used in the literature [4-7]. As only one strain rate will be used later, the strain rate effect is explored and discussed briefly here. Tensile tests at three strain rates (0.1/0.01/0.001 s^{-1}) on *B. mori* cocoon silks were conducted on a tensile tester Instron 5542 under lab conditions (25 °C, 40 % relative humidity). About ten samples for each rate were tested.

As shown in Figure 2.12 and Table 2.1, the rate effect upon the stress-strain performances is clear. In the range of 0.001-0.1 s^{-1}, as the strain rate increases, the initial modulus and the breaking stress increases, but the breaking strain does not decrease. Therefore, the breaking energy increases. It is interesting to notice that *B. mori* silks seem to respond better at a higher rate in terms of breaking energy, which suggests the potential interesting aspects of my colleagues' work of high rate or impact tests on silks [8]. Due to the data collection speed limit of the instrument, it was not possible to conduct any strain rates higher than 0.1 s^{-1}.

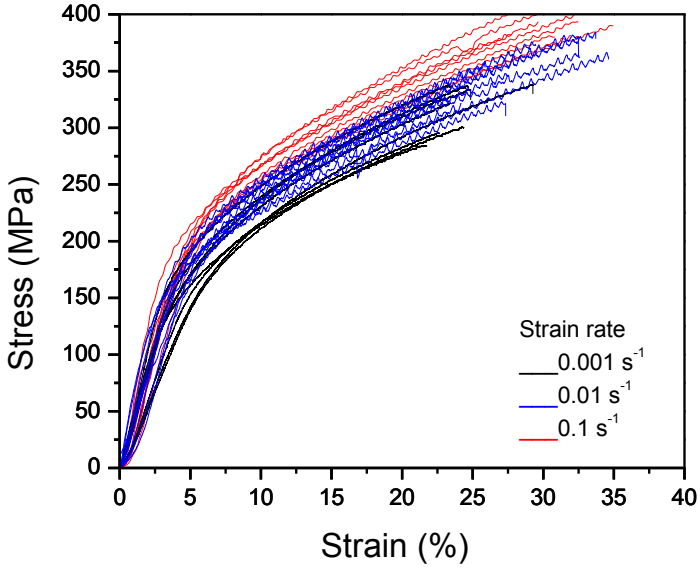

Figure 2.12 Stress-strain curves of natural *B. mori* cocoon silks at different strain rates.

Table 2.1 Tensile properties of *B. mori* silks at different rates

Strain rate (s^{-1})	Initial modulus (MPa)	Post yield modulus* (MPa)	Maximum stress (MPa)	Strain at maximum stress (%)	Breaking energy (J/cm^3)
R1 (0.1)	5660±280	564±15	398±6	32±1	91±4
R2 (0.01)	4910±300	530±16	352±8	28±1	78±4
R3 (0.001)	4190±290	593±18	318±8	24±1	59±3

*: All the values are shown as Mean±SE. Post yield modulus are taken between 300 MPa and breaking point for R1 and R2, 250 MPa and breaking point for R3.

2.3.3 Strain control versus force control

As introduced previously, DMA Q800 has a force-control basis. For reference, the force-ramp rate for tensile testing used in this thesis for *B. mori* cocoon silks is 0.1 N/min. Tensile test results on the same silks from Instron (strain rate of 0.01 s^{-1}) and DMA Q800 are compared in Figure 2.13. Below the yield strain at 5%, the two groups of curves overlap very well, although after yield the force-controlled curves show higher post-yield modulus, as if a relatively high strain rate were applied due to the lower modulus. Force ramp rates for samples with different cross-sectional areas and initial modulus are calculated roughly to match a consistent strain rate of 0.01 s^{-1}, and specific details will be given in Chapter 3.

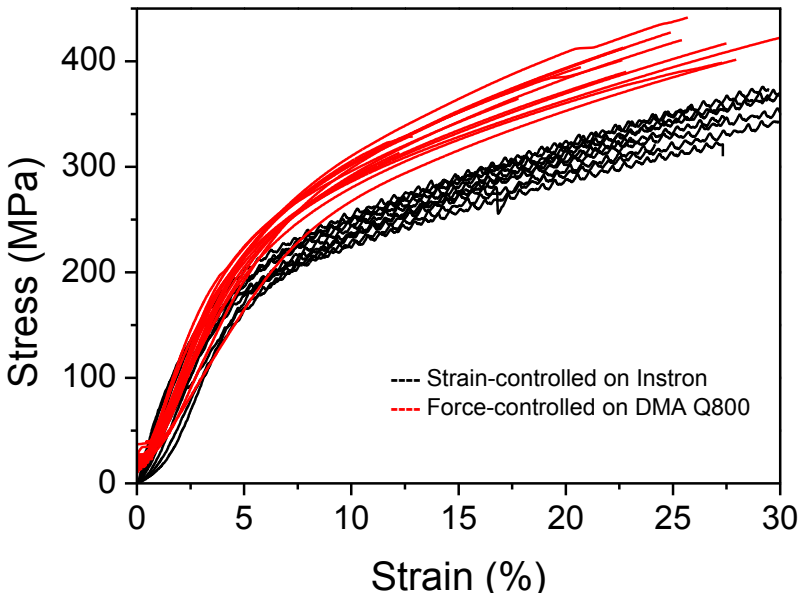

Figure 2.13 Stress-strain results from tensile tests of raw *B. mori* silks on Instron and DMA Q800 to compare strain- and force-controlled testing respectively.

2.3.4 Cyclical tensile testing

On DMA Q800 with force-control basis, cyclical loading and unloading tensile tests can be set up easily. Instead of using increased strain for each loading cycle, a series of force values are defined. Within each cycle, the maximum force, force-ramp rate

(during both loading and unloading) and relaxation time between the two cycles can be set up. In Chapter 3, more details of this test on different fibres will be discussed.

2.4 Relaxation experiments

Creep and stress relaxation experiments are useful for understanding the mechanical properties of viscoelastic polymers. Creep applies a constant stress and measures the strain response as a function of time; and stress relaxation applies a constant strain and measures the stress response as a function of time. A characteristic parameter, relaxation time, can be determined, which quantifies the viscoelastic structure in a material (e.g. purely elastic materials would have an ideal relaxation time of zero). In Chapter 3, creep tests are conducted in dynamic mechanical testing mode and will be discussed in the context of exploring the relationships of dynamic modulus with time and static loading.

2.5 Dynamic mechanical testing

Dynamic mechanical testing (the measurement of dynamic mechanical properties, mainly storage modulus and loss tangent) in this thesis applies to all the tests performed in the dynamic/oscillatory mode, which can be a time scan, a temperature scan or a humidity scan depending on the control variable.

Table 2.2 gives an overview of the parameters for setting up a dynamic test and the instrument specifications for range and resolution of each parameter.

Table 2.2 Parameters on DMA Q800 with specified range and resolution

Parameter	Range	Resolution
Temperature	-150 to 600 °C	±0.1 °C
Heating rate	0.1 to 20 °C/min	-
Force	0.0001 to 18 N	0.00001 N
Frequency	0.01 to 200 Hz	-
Dynamic deformation	± 0.5 to 10,000 μm	1 nm

2.5.1 Evaluating the parameters

a) Heating rate

In a dynamic temperature scan, the dynamic mechanical properties of samples are measured through a temperature range at a given heating rate. This heating rate affects the observations on the thermal events, especially the transition temperatures [2]. Due to the viscoelastic nature of polymers, slower heating rates result in lower observed T_g values. Figure 2.14 shows the results of temperature scans at three rates on a semi-crystalline polymer, polyethylene terephthalate (PET) film, and illustrates that higher rate does give slightly higher T_g. However, this parameter is not considered to be an important effect within the studied range of heating rates in this thesis, therefore a standard rate of 3 °C/min [9] is chosen as a defined parameter in later temperature scans on silks. It is also noted that the default temperature calibration is to compensate this heating rate (refer to section 2.1.2).

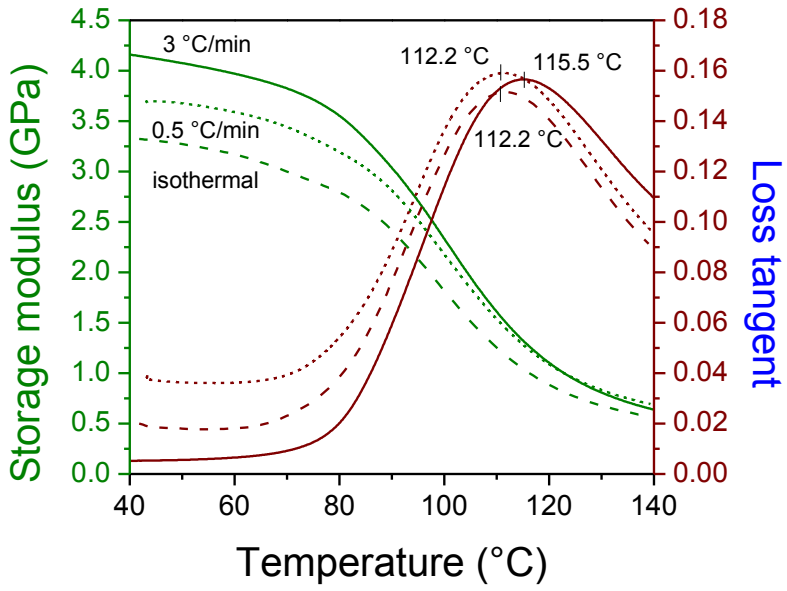

Figure 2.14 Temperature scan measurements on the glass transition of PET films at three heating rates: 0.3 °C/min, 0.5 °C/min, and 3 °C/min.

b) Frequency

The strain rate effect was studied in the previous section 2.3.2. Rate effect on the tensile tests and frequency effect on dynamic mechanical tests are linked in terms of characterizing the viscoelasticity of polymers. Here the frequency dependence of dynamic mechanical properties of *B. mori* silkworm silks is studied.

Although the instrument is advertised to operate up to high frequency of 200 Hz, it was found that the dynamic tests on thin fibres such as silks at frequency of >50 Hz became unreliable (showing negative loss tangent). Also, 0.01 Hz was too slow to be tolerated by the heating rate and a reasonable experimental length of time. Therefore, only frequencies of three decades (0.1, 1 and 10 Hz) were tested in dynamic mechanical time scans at room temperature on degummed *B. mori* silks. The lower bound of frequency 0.1 Hz meets the high bound of strain rate 0.1 s^{-1} in the tensile tests.

As shown in Figure 2.15, the storage modulus and the log(frequency) appear to have a linear relationship, although the slope is different depending on the polymer type: the

storage modulus of Polycarbonate (PC) is the least affected by the increase in frequency; epoxy resin and poly(methyl methacrylate) (PMMA) show slight increases when comparing frequency of 0.1 and 10 Hz, e.g. epoxy resin's storage modulus changes from 4.5 GPa to 5.0 GPa; and silk's modulus appears to be affected too, although the trend is not very clear given the variability of the data. Percentage-wise, the change in silk modulus from 0.1 to 10 Hz is less than 10%.

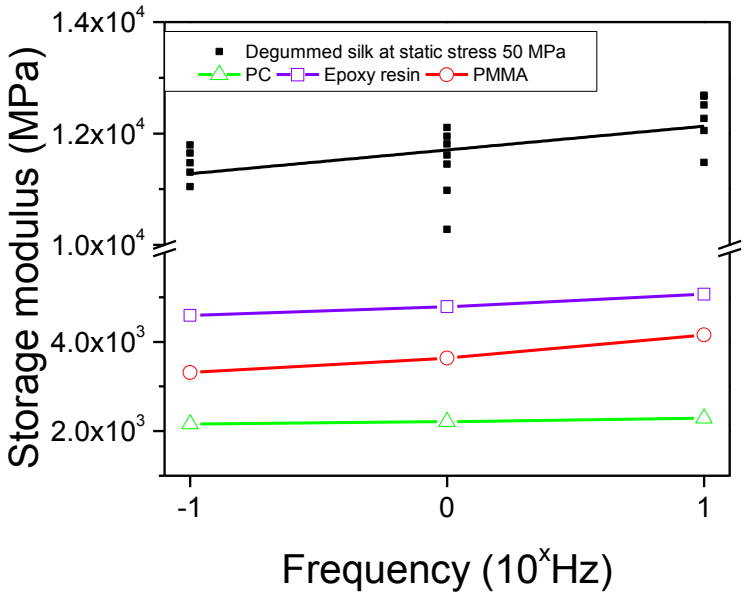

Figure 2.15 Frequency dependence of storage modulus of silks compared with synthetic materials at 25 °C. Data for PC, epoxy resin and PMMA are taken from literature [1].

Whether the dynamic mechanical properties have a frequency dependence would suggest whether the structures have transient loss events closer to the testing temperature, as illustrated in Figure 2.16. If a material is an ideal solid or liquid, its properties should not have a frequency or rate dependence at a given temperature. However, when a material is viscoelastic, and as it is going through a structural transition or loss event (shown by the loss peak), the viscoelastic structures tend to appear more "solid" at a higher frequency or higher rate in response to external stimuli such as stress. Therefore the observed transition tends to appear at a higher temperature.

The observation that silk's storage modulus increases slightly at 10 Hz frequency at room temperature compared to 0.1 Hz might suggest that: part of the silk structures cannot relax at the higher frequency of 10 Hz.

Taking together the results from the rate effect and the frequency effect, it is found that the modulus of *B. mori* silks (initial tensile modulus in the tensile tests or storage modulus in the dynamic mechanical tests) does increase with increasing rate/frequency, which implies that there is a transition close to room temperature.

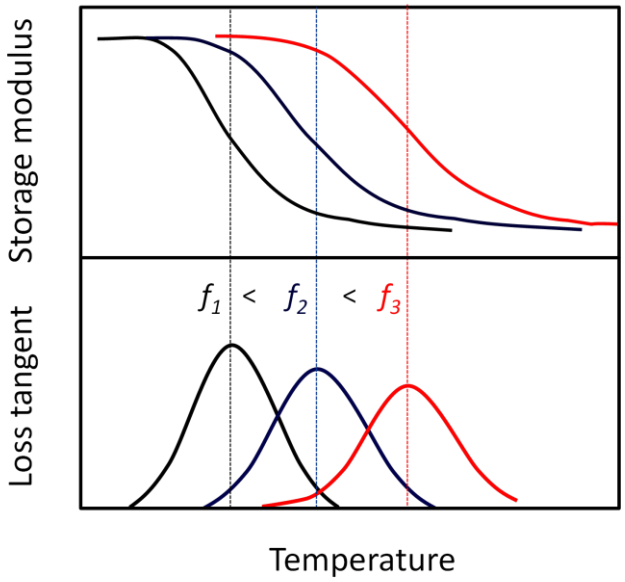

Figure 2.16 Illustration of frequency effects on the dynamic mechanical properties of viscoelastic polymers in a temperature scan.

Frequency would also have an effect on the observations of the glass transition temperatures in temperature scans, e.g. T_g for disordered silk at about 210 °C. However, it is not chosen as a priority parameter effect in this study. 1 Hz is set as a defined value for the dynamic mechanical tests, as is commonly used in other studies [9-11].

c) Dynamic strain/stress

Either dynamic strain or stress can be used as the oscillatory stimulus, and dynamic strain is chosen in this method. An appropriate dynamic strain is chosen to best

compromise the data quality (dynamic force response needs to be large enough to be measured) and as minimal as possible deformation of the sample (ideally within the "elastic" region). 5-10 microns is recommended for better resolution by TA Instruments. Considering the 5 mm gauge length, 0.1% or 0.2% dynamic strain is used for all the dynamic tests.

2.5.2 Setting up and analyzing the dynamic mechanical test

After establishing the defined parameters including heating rate, frequency and dynamic strain, I now introduce the three principal physical parameters, static force, temperature and humidity for humidity tests. The investigations on these three principle variables will form the basis of the following chapters:

Chapter 3- Dynamic mechanical properties of silks under **load**

Chapter 4- Dynamic mechanical properties of silks through **temperature**

Chapter 5 and 6- **Humidity** effect on *B. mori* silks and **Supercontraction** in spider silks

The experiments for evaluating each principal variable are, respectively: static-dynamic time scans at room temperature on the effect of mechanical loading; dynamic temperature scans at constant loading on the thermally induced changes; and dynamic humidity scans. As the details of each experiment will be given in the relevant chapters, only one example of setting up a dynamic temperature scan is given here, as illustrated in Figure 2.17. DMA Q800 has a software control panel, and in the panel the user can choose the operating mode, input the sample information e.g. geometry, set up a method and review parameters and methods.

After a test has been run successfully, the output results include all the raw signals (time, temperature, force, dynamic response, phase angle) and the derived properties (storage/loss modulus and loss tangent). The storage modulus and loss tangent at 1Hz can be analyzed as a function of temperature or loading or time, and structural features such as the glass transition can be quantified from the property changes. Length is often checked to validate the changes in the dynamic mechanical properties.

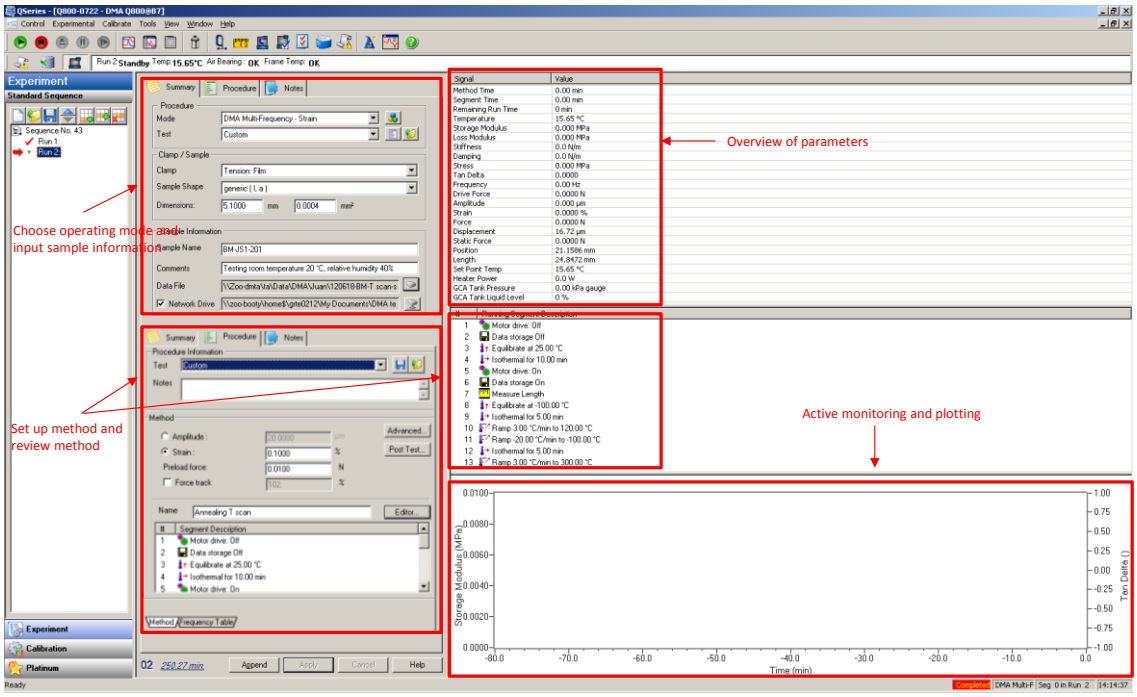

Figure 2.17 Instrument interface of DMA Q800 for users to set up an experiment, for example, here it shows setting up a dynamic temperature scan on a silk fibre.

2.5.3 Strain-controlled dynamic test

One interesting experiment was conducted on another DMA model developed by TA Instruments with built-in strain-control, as a comparison with the dynamic test on the stress controlled DMA Q800 used mainly in this thesis. A quasi-static tensile test was programmed at a low strain rate of 0.01 s^{-1} with a dynamic strain of 0.2% at 10 Hz frequency superimposed upon this to measure the strain-controlled dynamic response from the sample (see the formula below). The first part of the formula simulates the

linear strain rate, and the second part simulates the dynamic strain with a periodicity of 10 Hz.

$$\varepsilon \text{ (strain)} = -(0.01*(t) + 0.002*\sin(62.8*(t))$$

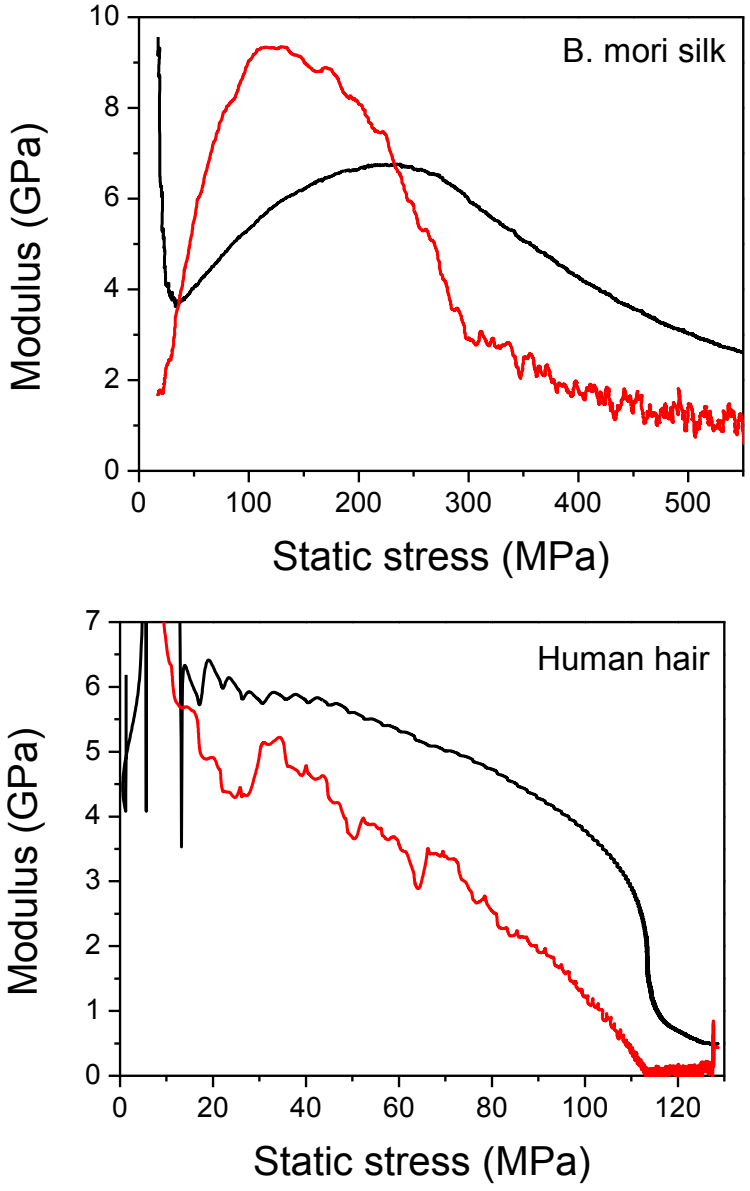

Figure 2.18 Derived "dynamic" modulus (black lines) and static modulus (red lines) measured from strain-controlled static-dynamic tests on degummed *B. mori* silk and human hair.

However, the results in Figure 2.18 show that the "derived" dynamic modulus follows the same trend of change as the static modulus (decreasing with increasing

stress), which is different from what will be reported later in Chapter 3. The difference between strain and stress controls on the sample response is worth exploring, but the aim here is simply to show that a strain controlled tensile test with superimposed dynamic strain is probably unable to measure the detailed dynamic mechanical properties of silks and their structural origins.

2.6 Other complementary techniques

2.6.1 Scanning Electron Microscopy (SEM)

In order to convert the raw force signal to stress and dynamic modulus, accurate area measurement is required, which is difficult for silk samples with irregular shapes or small sizes. For both raw and degummed silkworm silks, cross-sectional areas are measured by SEM and the average value from the sample is applied for all the stress and dynamic modulus calculation.

It was discussed whether it is appropriate to use an average value of the cross-sectional area for all individual samples. One study suggested even for force-reeled silkworm silks, the effective diameter and the shape change easily within short distance due to the spinning control of the silkworm [5, 12]. The morphology of silks by forced-reeling is presumably less varied along the length than the naturally spun silks due to the restrictions to the figure "8" head movement of the worm. Since for natural spun silks it probably makes only limited difference using the average value of a larger sample or a particular individual, I used one average value for all the silks of the same type. In the meantime one needs to bear in mind the variability of the cross-sectional areas. In this case, raw *B. mori* JS1 silks have 25% variation in cross-sectional areas, and this might contribute to the measured effects such as stress and modulus changes.

SEM is also used to provide more morphological information of the fibre samples. The measurement details and representative images will be shown in Chapter 3 as well as Chapter 7.

2.6.2 Thermo-gravimetric analysis (TGA) and differential scanning calorimetry (DSC)

Thermo-gravimetric analysis (TGA) is used to show the mass of a silk sample as a function of temperature or time in a dry air/nitrogen atmosphere, and useful information such as water content and decomposition temperature can be obtained. TGA results of silks will be discussed in Chapter 4.

Differential scanning calorimetry (DSC) is often used for characterizing thermal properties and structures of polymers. However, in this thesis, DSC is not the main analytical technique although DSC studies from the literature are often used for such analysis. In the next section, DSC is used for characterizing a semi-crystalline polymer.

2.7 Introductory experiments on Poly(ethylene terephthalate) (PET) fibres

Before moving forward to the main chapters on silks, I summarize and illustrate here the methods on both the quasi-static and dynamic mechanical analysis methods by testing an important synthetic semi-crystalline fibre, poly(ethylene terephthalate) (PET). The aim is to demonstrate how to link both the quasi-static tensile properties and the dynamic mechanical properties of a semi-crystalline polymer with its structure, and to propose useful structure-property relationships.

The PET fibres were purchased from Goodfellow Cambridge Ltd. The high tenacity PET fibre is 17 μm thick in diameter and the medium tenacity PET fibre is 14 μm. The

fibre samples were prepared with the same paper card frames of 5mm gauge length as introduced above in section 2.2.1.

2.7.1 Quasi-static tensile tests

Tensile tests on all the interested fibres in this thesis are usually conducted first and evaluated prior to any dynamic mechanical tests. Figure 2.19 shows two representative stress-strain curves for both high and medium tenacity PET. The difference between engineering stress and true stress is whether to take the area change during stretching into account. The two can be exchanged easily from the locus strain (assuming a constant volume and pure tensile deformation, for example). In this thesis, only engineering stress is used for simplicity and consistency.

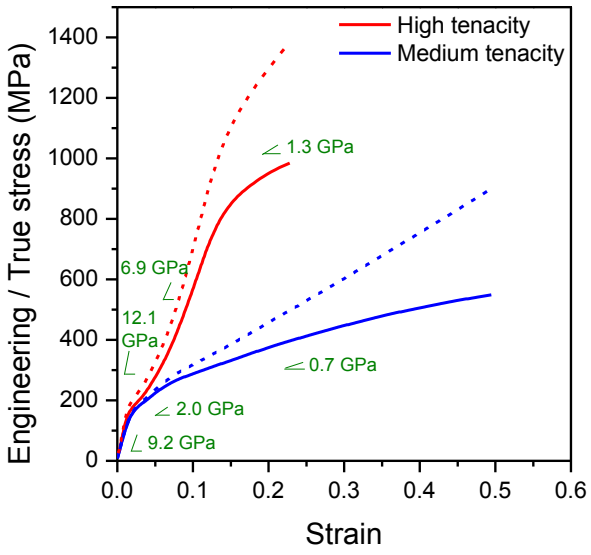

Figure 2.19 Tensile stress-strain behaviours of high and medium tenacity PET fibres with engineering stress in solid lines and true stress in dashed lines.

Comparing the tensile performances of the high and medium tenacity PET, the high tenacity has greater initial tensile modulus of 12.1 GPa than that of the medium (9.2 GPa), and higher breaking stress (1.0 GPa) at lower breaking strain (0.22). The high tenacity PET appears to go through three stages separated by two yields at ~0.02 and

0.1 strain, which suggests interesting structural changes that are different from the medium tenacity PET.

2.7.2 Cyclical tensile tests

Cyclical tensile tests tell how the tensile properties of a material change as a function of loading history. Figure 2.20 shows that cyclical stress-strain curves for both high and medium tenacity PET stay within the envelope of the tensile stress-strain curves in Figure 2.19. However, as the cyclical loading and unloading progresses above yield, the relaxation modulus increases after the load is reduced. This suggests an increased degree of order or crystallinity as more mechanical work is input into the structure. Later in Chapter 3, detailed discussions on evaluating the elastic and plastic components in silk structures from cyclical tensile test results will be presented.

2.7.3 Static-dynamic test

Static-dynamic tests measure the dynamic storage modulus as a function of static loading by superimposing a dynamic test on top of a static loading. As shown in Figure 2.21, the storage modulus increases with static loading. Although the apparent tensile modulus appears lower at high strain and stress, the elastic storage modulus does not decrease but rather increases.

It is noted that the dynamic storage modulus at 1 Hz at higher static stress (800 MPa for high tenacity PET) is 26 GPa, which is between the observed quasi-static tensile modulus and the X-ray crystal modulus of PET in the chain direction (110 GPa) [13]. Therefore, we infer that the dynamic test at 1 Hz is measuring a dynamic elastic modulus that could help quantify changes in the polymer structure under load, such as increased orientation or crystal fraction.

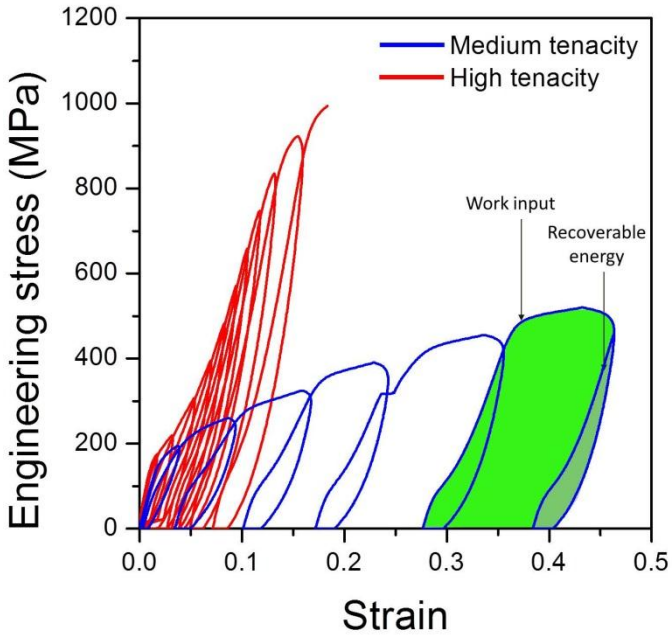

Figure 2.20 Cyclical stress-strain behaviours of high and medium tenacity PET fibres.

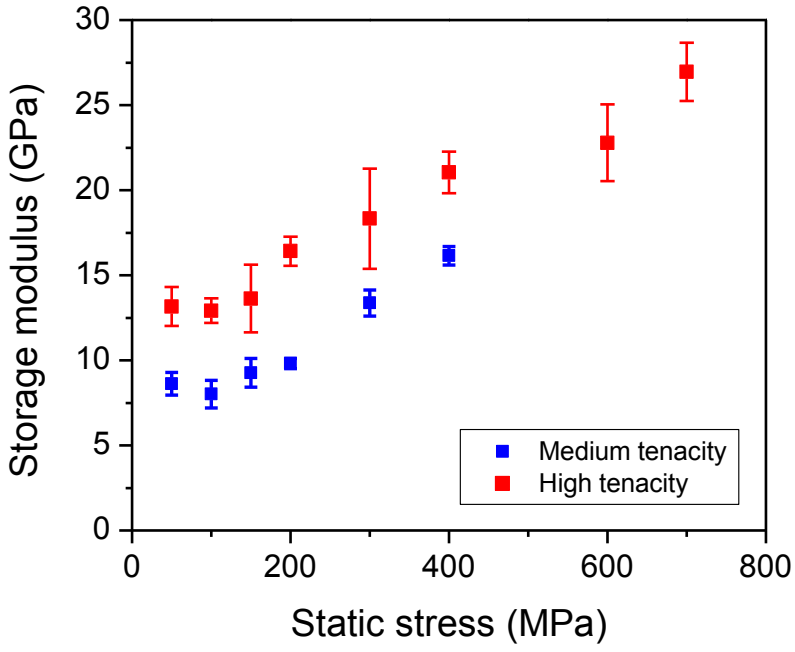

Figure 2.21 Dynamic storage modulus as a function of static loading for PET fibres.

2.7.4 Temperature scan: DMA and DSC

The dynamic storage modulus and loss tangent of both high and medium tenacity PET fibres as a function of temperature were measured in dynamic temperature scans. The results are shown in Figure 2.22. The dynamic storage modulus decreases with increasing temperature, and a faster decrease in modulus is accompanied by higher values of loss tangent, where the structural relaxations take place. A low temperature loss peak centered at about -55 °C and a high temperature at 113 °C for medium tenacity and 133 °C for high tenacity are observed. The low temperature peak is attributed to β-relaxation processes, and is not affected by the crystallinity [1]; and the high temperature peak is attributed to the glass transition, which is affected in both position and shape by the crystallinity [1]. The small shoulder peak below the main glass transition peak for the high tenacity was suspected to be due to orientation [1].

DMA measurements give the changes of dynamic mechanical properties of semi-crystalline polymers with temperature. However, more importantly, by measuring the magnitude of the properties through a thermal transition (in this case, the glass transition), the degree of disorder or the amorphous fraction in the polymer structure can be *quantified* by using relationships suggested by GIM [2] and equation 2.1. The area under the loss tangent peak of a glass transition is directly proportional to the fraction of disordered/amorphous material, and the reference value for 100% disorder can be calculated from the structure, so the disordered fraction can, in principle, be quantified.

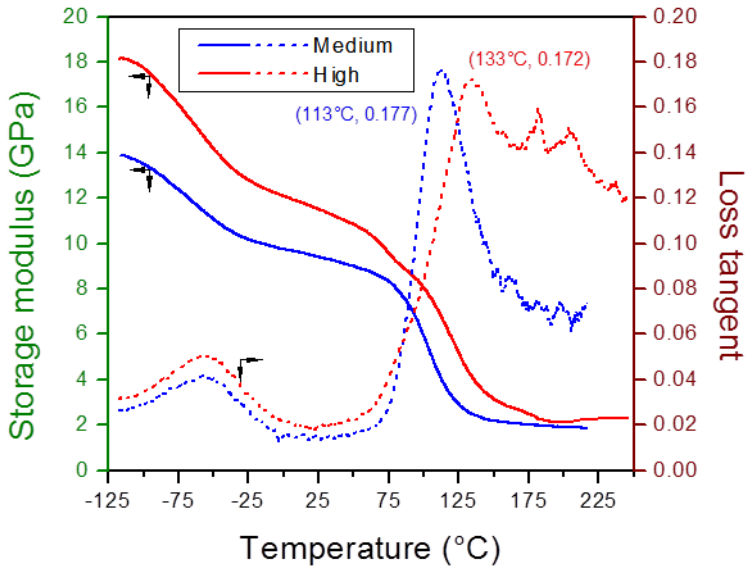

Figure 2.22 Dynamic mechanical properties, storage modulus and loss tangent, in a dynamic mechanical temperature scan for high and medium tenacity PET fibres.

In the case of comparing the properties of high and medium tenacity PET, DSC is very useful, as for both fibres we observed distinct crystal melting peaks in Figure 2.23, which can be used for quantifying the crystal type and fraction using the heat of fusion from the area under the transition peaks. Here, only qualitative comparisons are intended: the medium tenacity appears to contain two different types of crystals, but the total crystal peak is smaller than the high tenacity. Although the crystal fraction can be quantified from this result, it is not the aim of practice here. Also from Figure 2.23 (b), the glass transition can be recognized from the reverse heat flow in the modulated DSC tests.

To summarize the test methods and results on PET fibres, we demonstrate not only how to conduct mechanical testing on fibre materials, but also how to analyze and compare different properties in different types of tests (e.g. quasi-static tensile modulus and dynamic storage modulus). More importantly, from a structural point of view, we

also demonstrate how to build a structural model upon the measured mechanical properties.

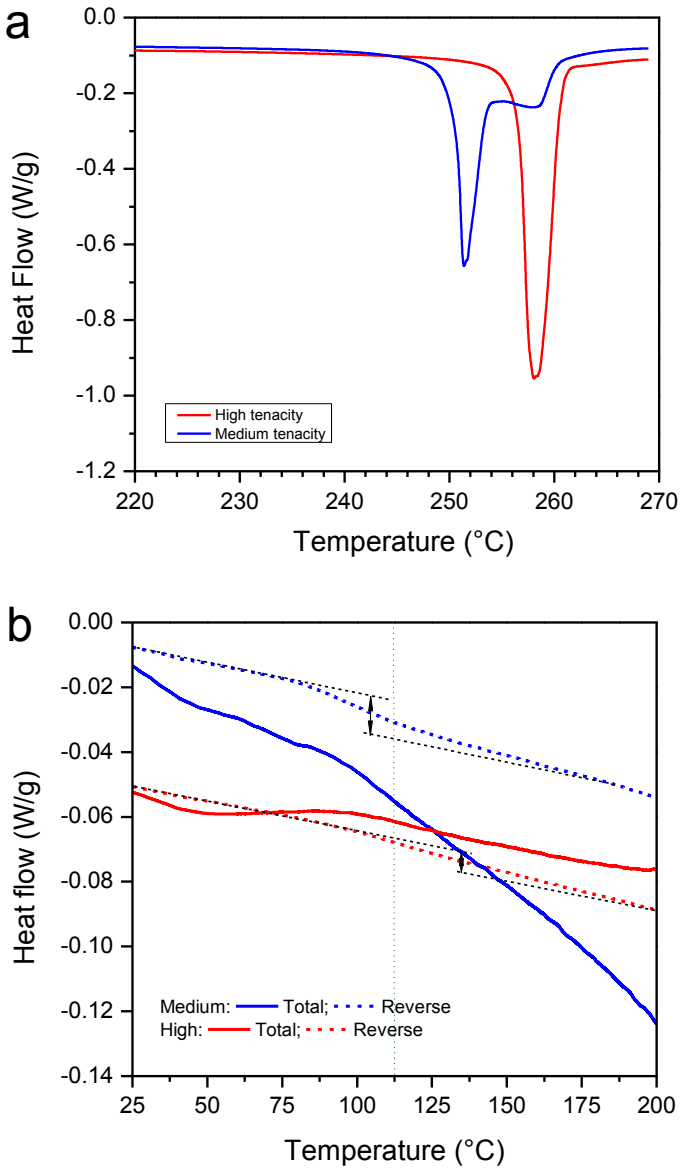

Figure 2.23 Modulated DSC tests on high and medium tenacity PET fibres: total heat flow in the main crystal melting region (a); and total (solid lines) and reverse heat flow (dashed lined) in the glass transition region (b).

2.8 References

[1] McCrum, N. G.; Read, B. E.; Williams, G., Anelastic and dielectric effects in polymeric solids. John Wiley & Sons: London, 1967.

[2] Porter, D., Group Interaction Modelling of Polymer Properties. Marcel Dekker: New York, 1995.

[3] Vincent, J. F., Structural biomaterials. Princeton Univ. Press: Princeton, NJ, 1990.

[4] Griffiths, J. R.; Salanitri, V. R. The strength of spider silk. J Mater Sci 1980, 15, 491-496.

[5] Perez-Rigueiro, J.; Elices, M.; Llorca, J.; Viney, C. Tensile properties of silkworm silk obtained by forced silking. J. Appl. Polym. Sci. 2001, 82 (8), 1928-1935.

[6] Jiang, P.; Liu, H.; Wang, C.; Wu, L.; Huang, J.; Guo, C. Tensile behavior and morphology of differently degummed silkworm (Bombyx mori) cocoon silk fibres. Materials Letters 2005, In Press, Uncorrected Proof.

[7] Liu, Y.; Shao, Z. Z.; Vollrath, F. Relationships between supercontraction and mechanical properties of spider silk. Nat. Mater. 2005, 4 (12), 901-905.

[8] Drodge, D. R.; Mortimer, B.; Holland, C.; Siviour, C. R. Ballistic impact to access the high-rate behaviour of individual silk fibres. J. Mech. Phys. Solids 2012, 60 (10), 1710-1721.

[9] Yuan, Q. Q.; Yao, J. R.; Huang, L.; Chen, X.; Shao, Z. Z. Correlation between structural and dynamic mechanical transitions of regenerated silk fibroin. Polymer 2010, 51 (26), 6278-6283.

[10] Yin, J.; Chen, E.; Porter, D.; Shao, Z. Enhancing the Toughness of Regenerated Silk Fibroin Film through Uniaxial Extension. Biomacromolecules 2010, 11 (11), 2890-2895.

[11] Yang, Y.; Chen, X.; Shao, Z. Z.; Zhou, P.; Porter, D.; Knight, D. P.; Vollrath, F. Toughness of spider silk at high and low temperatures. Adv. Mater. 2005, 17 (1), 84-88.

[12] Perez-Rigueiro, J.; Viney, C.; Llorca, J.; Elices, M. Silkworm silk as an engineering material. J. Appl. Polym. Sci. 1998, 70 (12), 2439-2447.

[13] Thistlethwaite, T.; Jakeways, R.; Ward, I. M. The crystal modulus and structure of oriented poly(ethylene terephthalate). Polymer 1988, 29 (1), 61-69.

Chapter 3. Dynamic mechanical properties of silks under load

3.1 Motivation/introduction

Silk from silkworm cocoons has a well established pedigree as a high quality natural fibre for textiles [1] and spider dragline silks are of great topical interest for their outstanding combination of strength and toughness as potential engineering materials [2-4]. However, for both materials there is a lack of reliable, consistent and specific empirical observations on their nonlinear mechanical properties under load, while at the same time there is no shortage of general attempts at describing the behaviour or of simplistic models based on generic observations of material properties. Moreover, there are few direct comparisons between the detailed engineering properties of natural silk fibres and standard commercial polymeric fibres. While the environmental credentials of silk as a future structural material are without doubt, we now need to look in detail at the fundamentals of their engineering properties at the chemical and morphological level. Only this will allow us to formulate structure-property relations that in turn will allow us either (i) to produce suitable forms of natural silk or (ii) use the mechanisms that have been optimised in the evolution of silks in order to develop improved synthetic analogues for commercial exploitation.

The two particular silks studied here are cocoon silks of the *Bombyx mori* silkworm (*B. mori* silk) and dragline threads of the golden silk spider *Nephila edulis* spider (*N. edulis* silk). Both silks are well-known, but for different reasons. *B. mori* silk has been used for human textiles for thousands of years, and is the most commercially abundant and most extensively studied among all silks [5]. *N. edulis* dragline silk has superb mechanical properties and is often taken as a reference standard of all silks, not least because of all spider silks only these fibres are substantial enough for property

measurement using standard equipment [6-8]. In addition, I also examined Nylon filaments as a successful synthetic industrial 'silk' replacement, for comparison (and as control) using the same methods and data analysis, largely because the nylon used here has mechanical properties remarkably similar to those of silkworm silk. Finally, and as a biological 'outlier' fibre, I also tested human hair, which is a naturally grown protein fibre (rather than a spun fibre, like the silk), which is the other main natural protein fibre that is considered also to have good strength and operates ex vivo, but has a very different morphological structure to silk.

The mechanical tests developed in this work applied tensile stress to the fibre samples and measured strain as the dimensional response. The biological reason to choose stress rather than strain as the control variable was based on biological function: when a spider falls or when prey impacts a web, then the radial/dragline threads have to take up the load, rather than respond to an applied dimensional strain. Indeed, many natural processes are often driven by 'stress', and it is believed that stress might be more important as an evolutionary driver for the structure and properties of natural materials.

A number of analytical tools have been used to study the secondary structure and morphological changes in silks in response to tensile deformation. An early study by wide-angle X-ray diffraction proposed that *N. edulis* dragline silk contains a well-oriented crystal fraction and an oriented amorphous fraction; as the fiber is stretched, no observable change in crystallinity was detected, but there was an increase of crystal orientation and a small reduction in the lateral crystal size [9-11]. A following XRD study drew very similar conclusions on the structure of spider dragline silk as it is stretched: crystal size perpendicular to the strain direction decreases and the crystal

orientation along the fiber increases [12]. An NMR study suggested that the proposed 'amorphous matrix' in fact has a preferred (helical) secondary structure with strong orientation [13]. Other studies using Raman spectroscopy focused on the orientation of different secondary structures in silks and seemed to demonstrate that *N. edulis* dragline silk contains highly-oriented beta-sheet and slightly-oriented other secondary structures [14]. Comparative Raman spectroscopy studies [15, 16] on silkworm and spider silks (from *B. mori* and *N. edulis* spp) showed a linear relationship of the Raman band shift (associated with 'random' conformation) and the applied mechanical stress, which was also found in other high-performance polymers (e.g. Poly(ethylene-terephthalate), PET) [17]. Finally, time-resolved FTIR and dynamic mechanical measurement were combined to study the structure-property relations of spider silk [18]. In principle, this combination of FTIR and mechanical tests would be a powerful combination of structural and property tools to possibly make the missing link of structure-property relations for spider silk). However, no further conclusions were drawn, apart from silk being a classic two-phase semi-crystalline polymer. The consensus from the structural analysis is that the crystalline phase is highly oriented in both original and stretched states of spider dragline silk. However, there is no consensus on the structural composition or changes in the non-crystalline phase during deformation.

While it is important to understand the structural and morphological changes in silk under load, it is equally important to have an accurate quantitative knowledge of the change under load of the mechanical properties of silks if we aim to understand and reproduce the desirable properties of silks. Tensile modulus is the focal property in this paper as the values reported in the literature are extremely diverse, even for one type of silk. This large variation in tensile properties could be attributed to the lack of consistency in the experimentation from one researcher to another, such as measuring

fibre diameter for instance, or the lack of control in the conditions under which the silks were collected, stored and tested. In some cases, the hydration state of silks is not well-defined, yet this has been shown to affect the mechanical properties considerably [19, 20].

Tensile properties of silks have been reported extensively, and tensile tests are usually conducted at a quasi-static strain rate of 0.01 s^{-1} and below [8, 21, 22]. The main conclusion states that apparent modulus reduces, often significantly, through yield. However, there is only a limited amount of data available on the dynamic mechanical properties of silks. Cunniff *et. al.* [23] first reported dynamic thermal mechanical properties of spider dragline silk. Later Blackledge [24] conducted a more careful and complete study on quasi-static and dynamic mechanical properties of various cobweb silks, which is the most important reference of relevance to our paper. The continuous dynamic mechanical testing using a frequency of 50 Hz showed a continuous change in dynamic mechanical properties of silks under quasi-static stretching. An increase in storage modulus was first observed as the strain increased. This was suggested to be due to an increase in orientation of molecules within the fibre. Instead of exploring the structure-property relations of silks, Blackledge's study focused more on the implications of different mechanical properties of silks on the biological functions of spiders. In a different study, Ene reported the same trend of dynamic modulus increase as a function of strain [18]. It is noted that high frequencies (i.e. 50 Hz) were used in both studies. In our study, I use 1 Hz for dynamic mechanical testing, which could bridge the gap between 0.01 s^{-1} from quasi-static tests and 50 Hz from continuous dynamic tests. In a different project of our group, pre-stress effect on the mechanical properties of *B. mori* silks is investigated at high-rate, which, together with other studies

at lower rates, would complete the whole regime of rate effect on structure-property relations of silks [25].

Here we consider in detail the mechanical properties of silk fibres under load from quasi-static to dynamic mechanical tests over the full stress-strain profile to break. We explored the apparently contradictory observation that silk modulus decreases through yield under quasi-static loading, but increases in dynamic tests. In addition, we investigated the reversibility of the modulus changes and their time dependence by testing the four fibre types using a static-dynamic procedure. This allowed us to measure the local dynamic modulus at increasing quasi-static loads through yield as a function of time and subject the fibres to cyclical loads in order to obtain complementary data on modulus and recoverable and non-recoverable strain under load. All the fibres were in their natural state and were tested dry in order to avoid complex, confounding variables such as hydration effects.

3.2 Experimental section

3.2.1 Materials

Nylon 6,6 (medium tenacity, Product No. 325710/1) was purchased from Goodfellow Cambridge Limited. Single filaments of nylon were separated from the yarn and mounted and stuck onto sample holders using Loctite superglue. The filaments are circular fibres with a diameter of 25 μm and the diameter was shown to be very consistent (variation within 1 μm) under the scanning electron microscope, SEM.

Raw/degummed *B. mori* silks: *B. mori* cocoons (grade 1, production period June 2010) from Jiangsu Province (China) were used. One cocoon was selected, and half was kept as it is and the other half was degummed. The degumming process was to soak and

stir the raw silks in sodium carbonate at 70 ^{o}C for 1 hour, then to wash three times in cold water and twice in warm water before drying at room temperature. The detailed degumming procedure can be found elsewhere [26]. Raw silk fibres (silk baves with sericin coating) were manually gently pulled out from the middle layer of the cocoon. Single degummed fibres were carefully unravelled from the dry degummed thread. Both were then carefully mounted onto the same sample holders before testing. The cross-sectional area for each was measured as described in the following SEM section.

N. edulis spider dragline silk was forcibly reeled described as follows: a medium size spider was first anesthetized by CO_2 to an extent that the spider fell "asleep" and became inactive, and then it was immobilized onto a platform. Dragline threads were then identified under a microscope. After the spider woke up, the double threads of spider dragline silk were forcibly reeled at 10 mm/s speed onto a spool with horizontal spaces and automatic advance. Silks were kept under tension and stored in a dark drawer under lab conditions (20 °C, rH 40 %). Segments of silks were then transferred from the spool to sample-holders and tension was carefully maintained. Silks from two individual spiders were used for the following tests as the first collection of silk from one spider was found not sufficient for all the tests. No difference was shown with the silks in the tensile properties apart from different dimensions. The diameter of spider silk was measured by SEM.

The hair sample was taken from the author J. G. Her hair is Asian type: dark brown in colour, straight, and with oval/circular cross-sections. The morphological features such as scales will be presented later in the results section. More information on this type of hair can be found in the references [27-29]. The diameter of hair was measured from the longitudinal view in the SEM images as the hairs were fairly circular.

Sample-holders are laser-cut paper card frames with gauge length of 5 ± 0.1 mm to allow individual fibres to be loaded onto the tension fibre clamps of TA Q800 easily. All the fibre samples in this thesis are fixed onto these sample holders using Loctite super glue (liquid) unless a different type of sample holder is mentioned.

3.2.2 Methods: SEM Characterization

Micrographs of the morphology of both cross-sections and surfaces of *B. mori* silks, *N. edulis* silk and hair were taken on an SEM (Jeol Neoscope JCM-5000). Typical micrographs for each type of fibre can be found later in the results section. *B. mori* silks have irregular shape in cross-section and wavy morphology along the fibre length, and for both raw and degummed *B. mori* silks the cross-sectional area was taken from about 30 measurements to get the average (the image processing and measurement are demonstrated in Figure 3.2); *N. edulis* spider silk is difficult to take cross-sectional images, but assuming a circular cross-section, the diameter was taken from the longitudinal images, and the average was calculated from about 10 samples randomly from the spool from the beginning to the end and 3 measurements for each sample); hair has scales on the surface from the longitudinal view, and the diameter was again measured from the longitudinal images. The dimensions and statistics for each fibre can be found in Table 3.1.

Table 3.1 Fibre information

Fibre	Cross-sectional area (± SD) (μm^2)	(Effective) diameter (± SD) (μm)	Sample size (N)
Nylon 6,6	491	25.0 ± 0.4	25
Raw *B. mori* silk	401 ± 50	22.6	33
Degummed *B. mori* silk	132 ± 16	13.0	30
N. edulis Spider silk	27.3	5.9 ± 0.4	8
	22.9	5.4 ± 0.2	11
Human hair	5.2×10^3	81 ± 2	7

Note: The diameter of nylon, *N. edulis* spider silk and human hair was measured by SEM and the cross-sectional area was calculated from the measured average diameter; the cross-sectional area of raw and degummed *B. mori* silk was measured by SEM and the diameter was calculated effectively assuming a circular cross-section. Statistics are applied only to the measured quantities in the table.

3.2.3 Quasi-static tensile and cyclical tensile tests

Dynamic Mechanical Thermal Analysis or DMTA (TA Q800) was used for all mechanical testing. Quasi-static tensile tests were conducted in force-control mode at room temperature ~25 °C, and length and force were actively monitored. 15-30 minutes dry nitrogen purge was applied after the sample was loaded to the clamps to remove the excess moisture. The force-ramp rate for each subject fibre was: 0.1 N/min for nylon and raw *B. mori* silk; 0.05 N/min for degummed *B. mori* silk; 0.025 N/min for *N. edulis* spider silk; 1 N/min for hair. The stress-strain curves with force/stress-control are comparable with those from strain-controlled tensile tests (strain rate of 0.01 s^{-1}), especially in the region before yielding.

Cyclical tensile tests used the same rates for each fibre as the quasi-static tests, and the unloading was done using controlled force ramp. The force interval between each loading cycle was chosen to obtain sufficient cycles for the analysis. The recovery time between unloading and the next loading was 3 minutes. More tests on different recovery times (3-30 mins) were done, but the recovery time on a scale of minutes was shown to have negligible effect on the recoverable behaviour, for instance, recoverable strain.

3.2.4 Dynamic mechanical test under load

Isothermal dynamic mechanical tests were performed in multiple-frequency-strain-control mode. The principle is to superimpose a dynamic test on top of increasing static load through the full stress-strain range to record the dynamic mechanical properties of

each fibre, as illustrated in Figure 3.1. Each test was conducted as a time scan of maximum 5 minutes at a frequency of 1 Hz and amplitude of 10 μm (or strain of 0.2%) at different static stress levels. During each test, length, static force, storage modulus and loss tangent were recorded as a function of time. The stress was converted to static force as an input variable on the instrument.

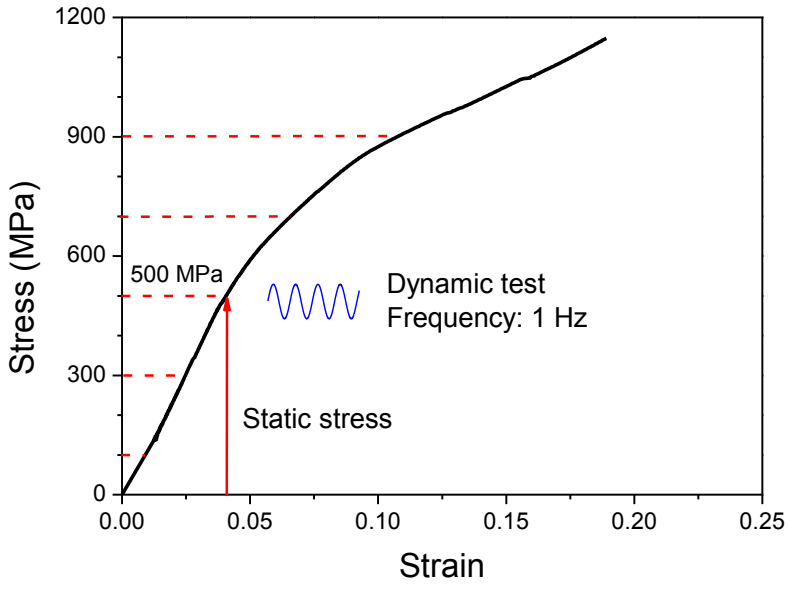

Figure 3.1 Illustration of the dynamic mechanical test of fibres under static loads through the full stress-strain profile. *N. edulis* spider silk's stress-strain and a static stress of 500 MPa are shown here.

3.2.5 Creep test

Raw *B. mori* silk was tested in a classical 'creep' experiment: loading at 100 MPa for 10 mins and relaxing for 20 mins with zero stress and monitoring the strain change over time.

3.2.6 Reversibility

For the reversibility test, only nylon and raw *B. mori* silk were tested. The concept was to repeat loading and unloading at two different loads, one low (below the yield stress) and one high (above the yield stress), to see the change in storage modulus and

length. Two sets of tests for either fibre: 50 MPa+200 MPa and 50 MPa+300 MPa for *B. mori* silk; 50 MPa+200 MPa and 50 MPa+400 MPa for nylon. Each loading lasted for 5 minutes and the fibre relaxed for 5 minutes. After the reversibility test, the specimens were tested again for stress-strain.

For consistency in all tests, engineering stress is used instead of true stress and the cross-sectional area is taken as constant through each deformation cycle. However, dynamic modulus was calculated using the cross sectional area at each applied static load.

3.3 Results

3.3.1 SEM morphology of the subject fibres

Figure 3.2 shows typical morphologies of the fibres of interest in this thesis, named as *Nephila e.* (or *N. edulis* for the later Chapter 6) spider dragline silk, raw and degummed *B. mori* silkworm silks, medium tenacity nylon 6,6 fibre, and human hair.

Nephila dragline silks have very even, smooth and round surfaces, and in this study the fibres have an average diameter of 5-6 μm. Raw *B. mori* silks have an oval or peanut shape cross-section with two silk fibroin brins wrapped by a layer of sericin glue, and the fibroin and sericin can be clearly distinguished in the digested fibre (sericin was lost) as well as the multi-cross-sections. The transverse shape of a degummed fibre was described as triangular in some *B. mori* silk studies, however, we see more diverse shapes and lack of fine control in the spinning apparatus of silkworms could be attributed. Comparing the cross-sectional areas of the raw and degummed silks, the fraction of sericin in raw silks is estimated to be 34%.

The other two fibres are medium tenacity nylon fibre and human hair. Nylon fibres have very consistent fibre diameters and the surfaces are even, smooth and round like spider silks except that these industrial fibres are much thicker. The human hair in this study shows fairly circular cross-sectional shape, and scales on the surface can be seen on the longitudinal views.

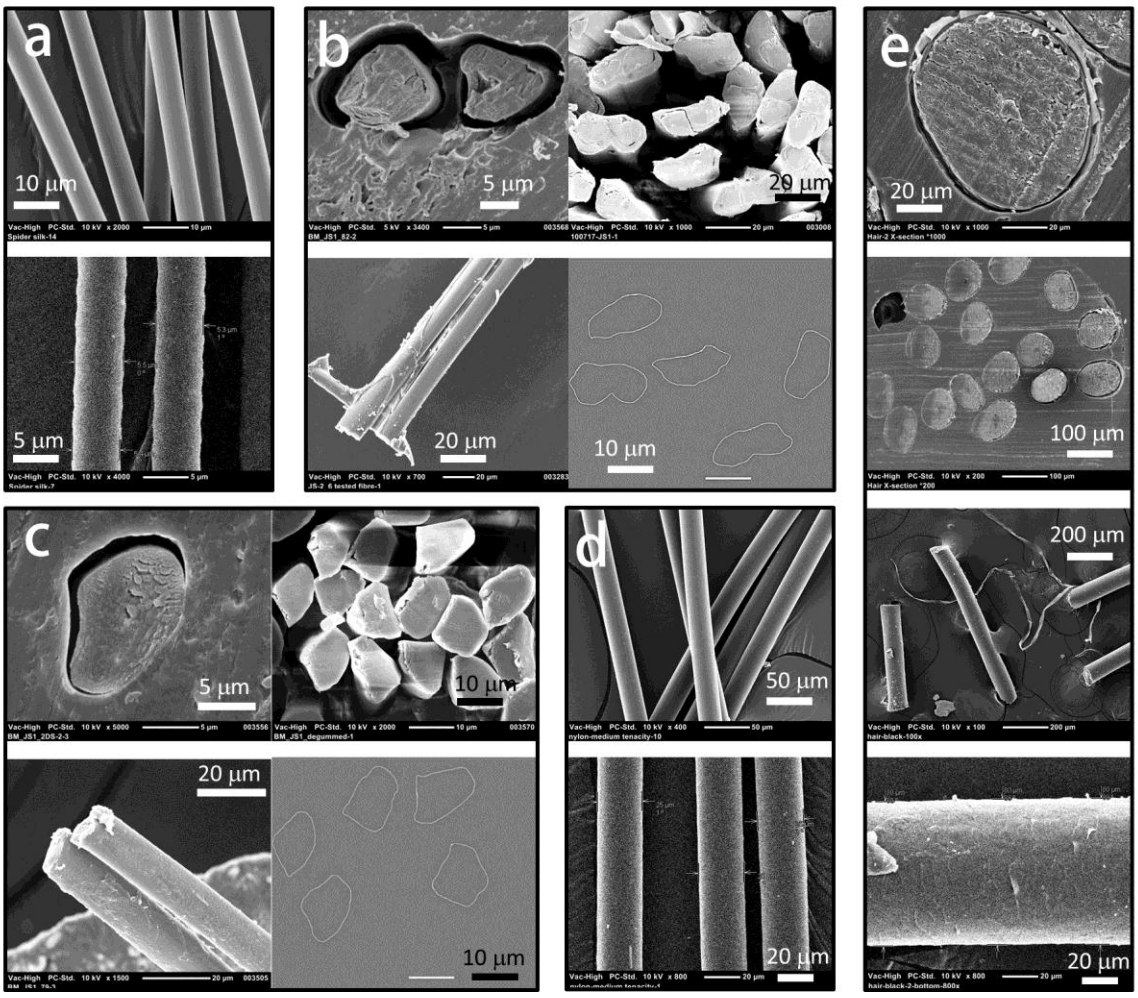

Figure 3.2 SEM images of five subject fibres: *Nephila edulis* dragline major ampulate silk (a); (raw) *Bombyx mori* silkworm silk (b); degummed *Bombyx mori* silkworm silk (c); medium tenacity nylon 6,6 fibre (d); human hair (Asian type) (e). Within (b), (c) and (e), three views were shown for a single fibre cross-section (embeded in epoxy resin and in the case of raw silkworm fibres, sericin was digested by a proteinase), cross-sections of multiple fibres and longitudinal view. The images for dimensional analysis are also shown. The scale bars are shown within each figure.

3.3.2 (Quasi-static) modulus from tensile tests

As outlined in the introduction, stress-control was used in our tensile tests. Although different for each fibre, the force-ramp rate induced a strain rate of about 0.01 s^{-1} for the initial stage before the yield and of about 0.1 s^{-1} after the yield, both of which are taken here to be quasi-static. In Figure 3.3, *Nephila* spider silk shows the highest initial modulus (11 GPa), strength (1.1 GPa) and toughness; the raw and degummed silkworm silks show the second highest initial modulus, followed by medium tenacity nylon, which has a higher breaking strain; and lastly, hair has a similar initial modulus of 5 GPa but yields at 0.03 strain and 100 MPa stress, and undergoes large plastic deformation with a relatively low post-yield modulus of 200 MPa to a high strain at break. In quasi-static tests, the five types of fibres all experienced an initial stage with high modulus and a post-yield stage with an order of magnitude lower modulus before failure.

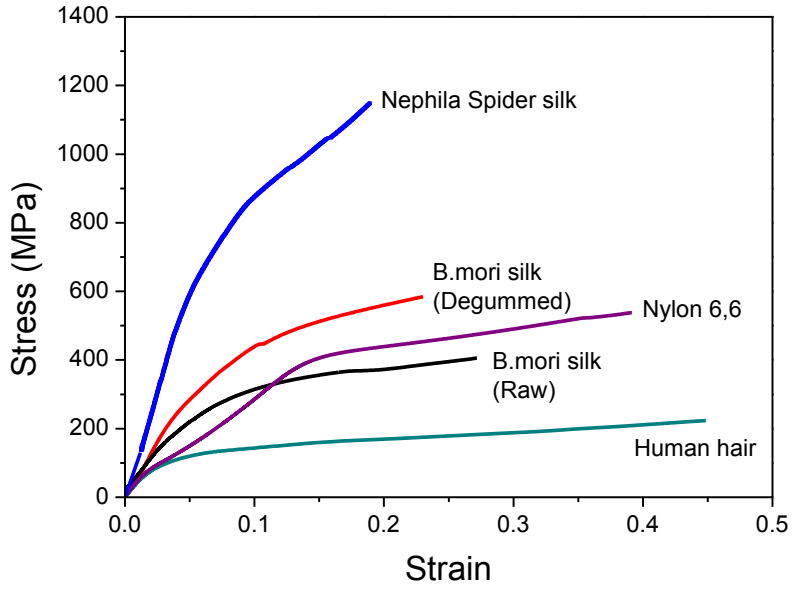

Figure 3.3 Typical stress-strain curves for the five subject fibres from tensile tests (DMTA force-controlled mode) at quasi-static rates. The force-ramp rate and cross-sectional area for each fibre can be found in the methods section.

3.3.3 Dynamic/Storage modulus with increasing static load

As described in section 3.2.4, isothermal dynamic mechanical tests using static stress as a variable were conducted to study the properties of the fibres under load at 1 Hz frequency. In this section, we only look at the storage modulus. Figure 3.4 plots the storage modulus of each fibre immediately after the application of stepwise increases in static load. Under quasi-static loading, the tensile modulus decreased in all cases as the fibre is deformed further, as shown in Figure 3.3. However, instead of decreasing, the dynamic storage modulus of nylon and both silks showed a clear trend of increasing as the load increases, particularly above the yield stress. In contrast, the dynamic storage modulus of hair decreased with increasing load. Note that the data for *B. mori* silks below stress values of about 75 MPa are not appropriate here due to the wavy morphology of the fibres; below a static stress of about 75 MPa, the measured stress response is mainly due to straightening the fibre.

The storage modulus of degummed *B. mori* silks increased from an extrapolated low stress value of about 14 GPa to 19 GPa as the static stress increased to 500 MPa. For the raw *B. mori* silks, the modulus increased from about 9 GPa to 13 GPa. The difference between raw and degummed *B. mori* silks is the sericin coating. If we take a typical fraction of 0.66 for fibroin in the whole raw fibre, we can deduce that the measured dynamic response is mainly due to the fibroin. Hence the sericin contributed very little to the load-bearing capability of the silk fibres in our experiments, which is a very different conclusion from a recent study [30].

For nylon, the modulus of 17 GPa at high stress (500 MPa) was nearly three times the value of 5 GPa at low stress (50 MPa). For *Nephila* spider silk, the modulus increased from 13 GPa to 28 GPa as the static stress changed from 50 MPa to 1100

MPa. For hair, storage modulus decreased from 4.7 GPa to 3.5 GPa with increasing static load.

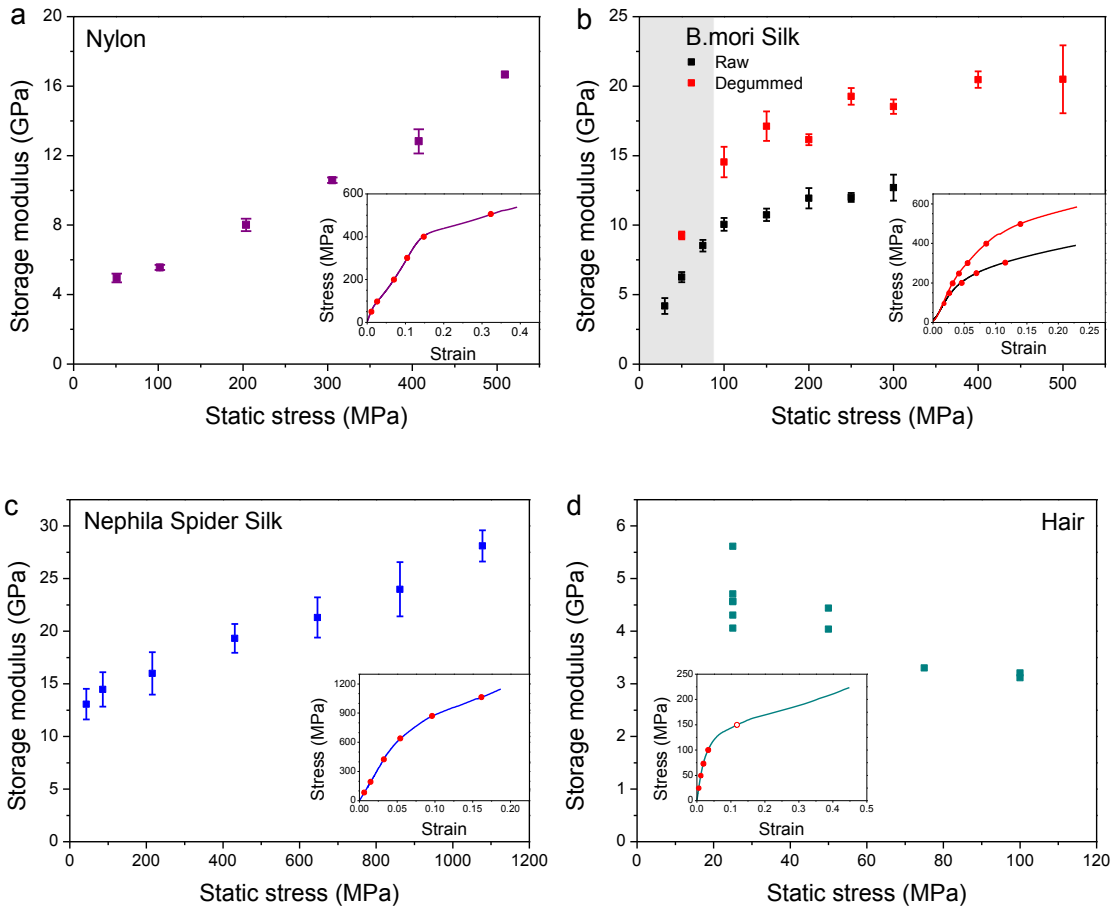

Figure 3.4 Storage modulus of the subject fibres as a function of static stress. Applied static stresses for the dynamic tests are highlighted as points in the inserted stress-strain curves.

3.3.4 Dynamic modulus under stress as a function of time: 'Creep'

Figure 3.4 shows the storage modulus increase as a response to higher static stress for silks. But, how do the modulus and other properties change as a function of time under a constant load? Figure 3.5 (a) shows the example of *B. mori* silk. With all other fibres tested (including nylon, spider silk and hair), the same trend was observed: modulus increased and loss tangent decreased in a complementary way within the observation time. Because the length/strain also increased (data not shown), following a

similar trend to the modulus increase in the dynamic test, it is logical to link to and compare with a classical creep test.

Figure 3.5 (b) shows the result of a creep test on *B. mori* silk. We propose two different relaxations in the silk structure. For example, after the load is removed, the strain relaxed by 0.016 almost instantly, and this was followed by a second slower relaxation in a similar time scale to that of the dynamic tests. An exponential decay model with a reference time constant of 36 seconds [31] was used to fit the second slower relaxation of the experimental data for both dynamic and static creep tests, as shown in dashed or red lines. The model fits both sets of experimental data well, which suggests the strain and modulus increase and the loss tangent decrease with time in the dynamic test probably have some common structural origin with the slower relaxation in the 'creep' test. Nylon showed similar results and has a best-fit creep relaxation time of 1 minute at 100 MPa static stress, of the same order of magnitude of time as *B. mori* silk.

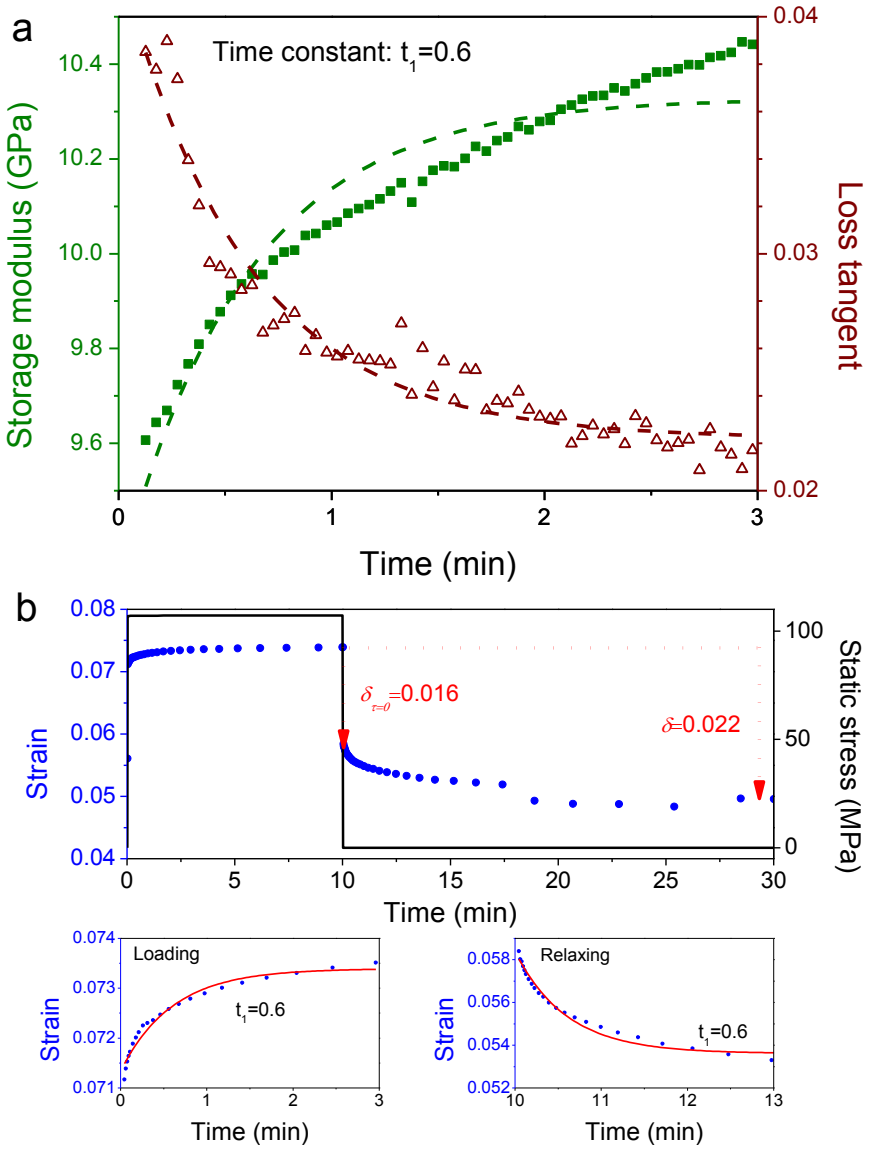

Figure 3.5 (a) Isothermal dynamic mechanical test (1 Hz) time scan on raw *B. mori* silk at a static stress of 100 MPa; **(b)** Classic creep experiment on raw *B. mori* silk using a stress 100 MPa (below are details of the slower relaxation of strain during loading and relaxing). Exponential fits with a time constant of 0.6 minutes (30 seconds) are shown in both graphs.

3.3.5 Reversibility of dynamic modulus change through loading history

As shown in Figures 3.4 and 3.5, the storage modulus increased in response to increased static stress for both *B. mori* silk and nylon, and under a constant load the modulus remained high with a gradual increase with time. This small increase of modulus under constant load is suggested to have the same structural origin as the

'creep' effect. The next question is whether the modulus retains the new higher value after the load is removed and reapplied at lower and higher values?

Figure 3.6 shows the loading history of two fibres for raw *B. mori* silk and nylon during repeated load-unload steps. Storage modulus and static strain were measured with time as a function of static stress. The low load for silk and nylon was set at 50 MPa; two high loads were taken for silk (200 and 300 MPa) and nylon (200 and 400 MPa), respectively, to reflect the loading capability of the two fibre types. The stress and 'creep' effects on storage modulus during individual loading validated the results shown in the two previous sections: higher stress resulted in higher storage modulus; and modulus increased a little with time under constant load. However, the detailed changes of modulus and strain with stress diverged between silk and nylon.

For silk, the low-load modulus increased irreversibly from 7.4 to 8.5 GPa after loading to 200 MPa and increased again irreversibly to 10.0 GPa after a high-load stress of 300 MPa, as shown in Figure 3.6. Simultaneously, the static strain at low-load increased irreversibly after higher loads, and the non-recoverable strain increased with higher loading. This suggests that the non-recoverable strain after high-load is in some way associated with the changes in dynamic modulus in *B. mori* silk. Figure 3.6 also shows how the stress-strain profile changes after high loading.

For nylon at 200 MPa, the increased static strain or non-recoverable strain after high load does not seem to make a difference to the storage modulus at 50 MPa. However, after the high load of 400 MPa, the storage modulus even decreased with increased non-recoverable static strain.

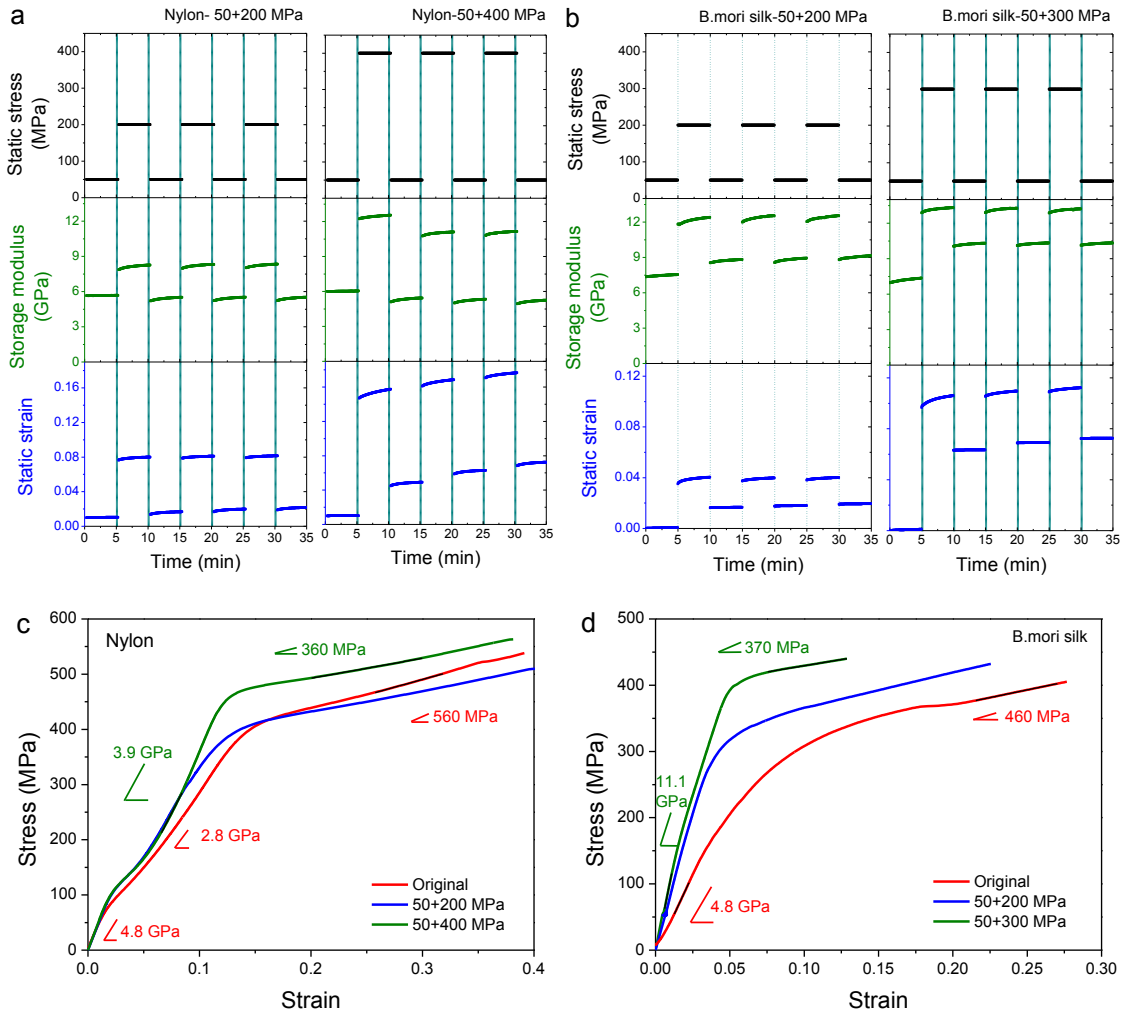

Figure 3.6 Repeated steps of low- and two different high-load conditions for (a) nylon and (b) *B. mori* silk fibres: dynamic storage modulus and non-recoverable strain in response to static stress. (c) and (d) show the change in stress-strain profile after repeated low- and high-load cycles.

Clearly, high-load history gives silk higher initial modulus and higher yielding stress in the stress-strain performance, as shown in Figure 3.6 below. But the breaking strain became lower with increased high-loading. In the case of nylon, it is complicated because of the two-yield-point stress-strain profile. High-load history enhanced the modulus after the first yield, but decreased the modulus after the second yield. The overall breaking strain did not change significantly.

3.3.6 Modulus from cyclical tensile tests

After looking at the non-recoverable properties induced by high stress loading on fibres, it was natural to look in more detail at the properties of each fibre under cyclical loading, which combines loading history and the result in the engineering performance together. There has been some data available on cyclical tensile tests on silks [31]. However, this is the first time to compare the performance of cyclical loading and unloading of both silks with nylon and hair.

In Figure 3.7 (Left), we compare the stress-strain profiles in cyclical tensile tests with normal quasi-static tensile tests for each of the four fibre types. The stress-strain profiles from the cyclical tests for nylon, *Nephila* silk and hair all fall inside the envelopes of the normal stress-strain curves; only the performance of *B. mori* appears to increase a little as the maximum loading goes beyond the yielding stress.

Figure 3.7 (Right) shows modulus as the derivative of stress as a function of strain for each of the cyclical stress-strain profiles. For all the fibre types, the relaxing modulus started from very high values at maximum load (an artefact of the curved shape of the change from loading to relaxation) and decreased as the load was gradually released, which allowed the structure to relax.

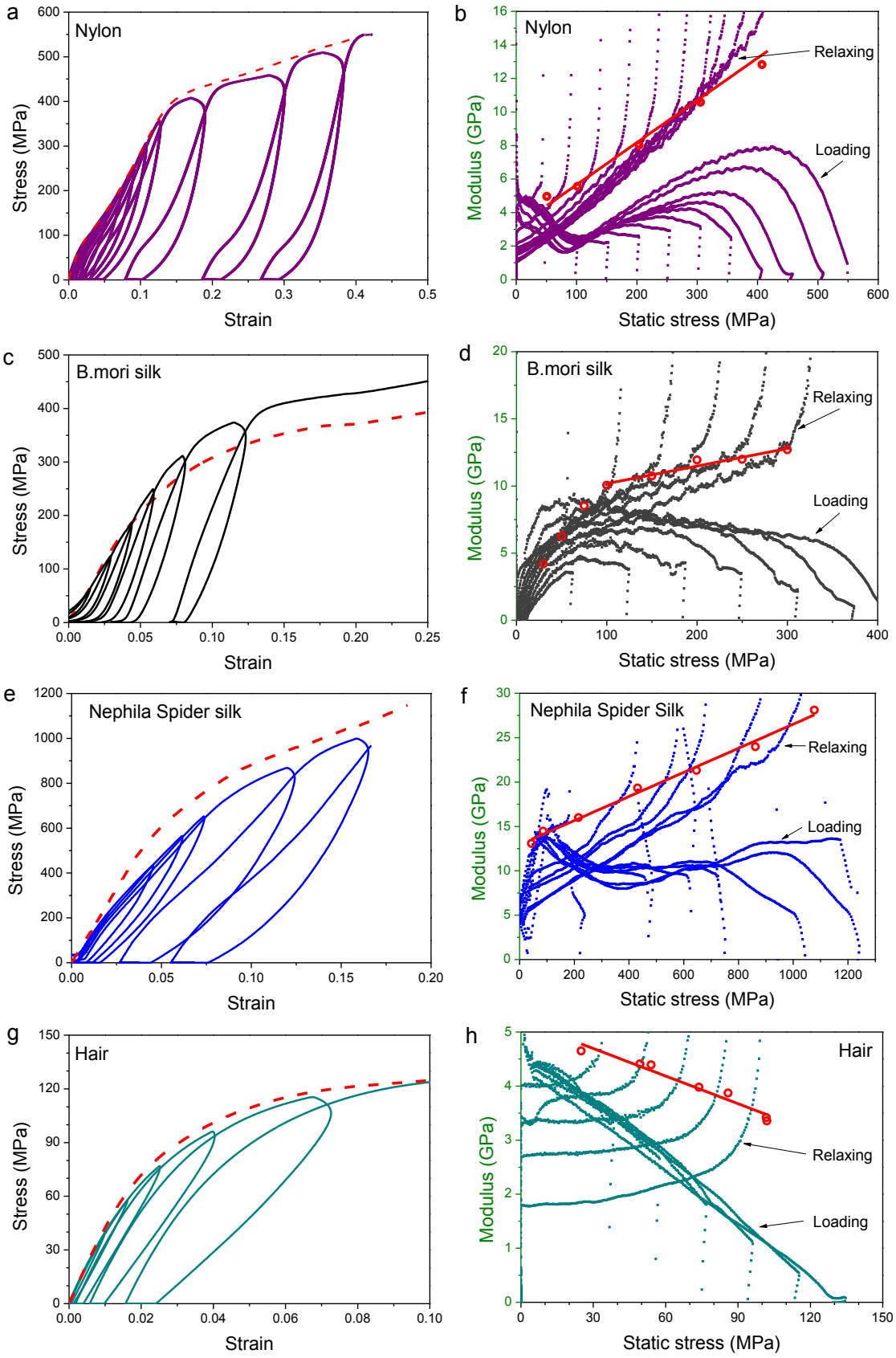

Figure 3.7 (Left) Stress-strain profiles of the cyclical loading and unloading on the four subject fibres with the original stress-strain curves in red dashed lines. The relaxation time before the next loading was 3 minutes. (Right) The derivative of stress/strain (so-

called derivative modulus) from the cyclical curves on the left, is plotted against the local stress, and the red data points are taken from Figure 3.4 with best-fit straight lines in red.

The function of relaxing modulus with stress followed the trend of the dynamic modulus against static stress (shown as red circles with red linear fit), which again validated the observation from dynamic tests: high load resulted in high local modulus for nylon and two silks, and the opposite effect for hair. The loading modulus and relaxing modulus appeared to converge at low load within the elastic region.

The one observed difference in loading modulus for the four fibres was that the loading modulus increased for nylon with increasing load, whereas it stayed constant or reduced for the other three fibres. This appears to reflect structural changes in the strain hardening section of the stress-strain curves between the two yield points in nylon.

3.3.7 Static strain from cyclical tensile tests

The observations in the reversibility tests suggested that there is a link between the non-recoverable strain and the increase in dynamic modulus. Therefore, we examined the components of recoverable and non-recoverable strain as a function of loading in the cyclical tests. In general, the maximum in the recoverable strain was different for each fibre, and if the strain exceeded this maximum recoverable value, then the non-recoverable strain increased linearly with higher loading until the fibre breaks.

Looking first at the non-silk fibres (Figure 3.8 (a) and (d)), nylon recovered fully in strain when the maximum loading strain was below 0.1, but the recoverable strain remained constant at 0.1 for higher maximum loading strain. The non-recoverable strain seemed to increase linearly with maximum loading strain beyond 0.1. This suggested a growth of elastic recoverable strain up to 0.1, and that all subsequent strain was plastic, non-recoverable deformation. Hair can recover fully in strain when the maximum

recoverable strain is below 0.03, but beyond 0.03 both the recoverable and the non-recoverable strain increased. Due to the limited data points, it was hard to derive any conclusions of the limit of both recoverable and non-recoverable strain for hair. But for nylon, it was evident that at break the non-recoverable strain reaches 0.3 and the total strain reached 0.4.

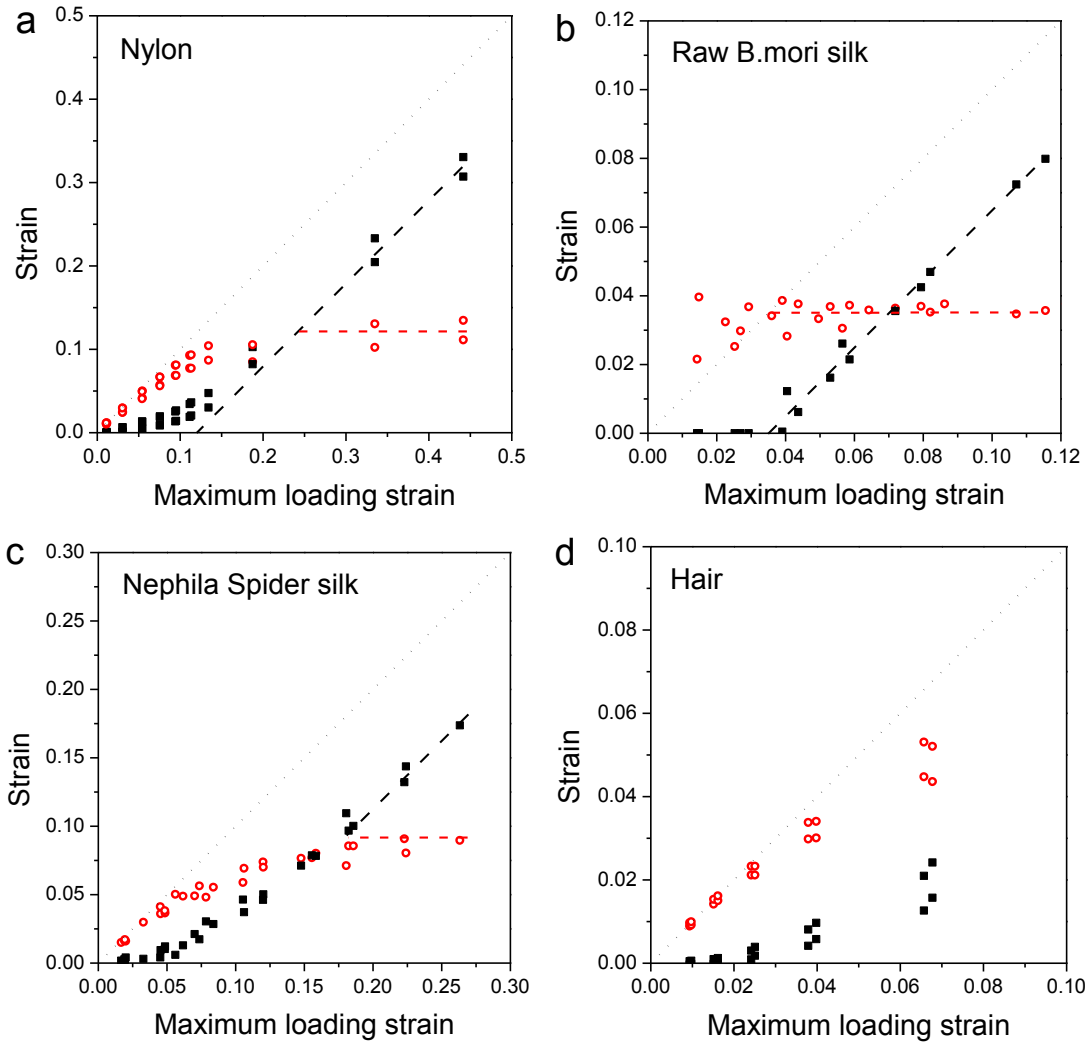

Figure 3.8 Recoverable (open circles) and non-recoverable (filled squares) strain as a function of maximum loading strain from cyclical tensile tests. The non-recoverable strains were taken soon after the load first became free or after relaxation for 3 minutes. The recoverable strain was the difference of the maximum loading strain and the non-recoverable.

In Figure 3.8 (b), *B. mori* silks gave a maximum recoverable strain of only 0.03, while the non-recoverable strain increased linearly with increased maximum loading

strain, in a similar way to the nylon. When the total strain reached 0.25 and the non-recoverable strain reached 0.22, the silk reached its strain limit and breaks. For *Nephila* silk, the trends were less clear, but it looked like recoverable strain increased to a limit of about 0.08 and the non-recoverable strain increased linearly above 0.08, but the transition from recoverable to non-recoverable was less definite.

3.4 Discussion

3.4.1 Quasi-static and dynamic moduli

We observed different trends in the change of modulus between quasi-static tensile tests and dynamic mechanical tests for Nylon and silk, both from the *B. mori* silkworm and the *Nephila* spider. In the quasi-static test, the apparent tensile modulus decreased significantly after yielding, whereas in the dynamic test, the storage modulus increased linearly with load through yield to failure. These observations are supported by the cyclical loading tests, where the relaxing modulus in particular displayed the same increase as observed in the dynamic tests under load. For hair, the loss of modulus under increasing load may probably be attributed to the breakdown of different parts of the hair structure under load, bearing in mind that the hair samples used would probably have been exposed to chemical treatments that degrade the protein structure over long period of time [27].

The quasi-static post-yield reduction in modulus in polymers has been explained and predicted quantitatively as the onset of mobility in the amorphous structure at the elastic instability point that is equivalent to the glass transition condition [32-34]. In brief, the reduced quasi-static modulus is due to dissipation of elastic energy density at the onset of mobility of the polymer chain segments at the instability point, which translates to a

plastic strain deformation under load. A larger amorphous fraction gives greater energy dissipation, and thus higher plastic flow, and commensurately lower apparent post-yield modulus. An empirical observation by Seitz is useful to quantify the yield stress as a fraction 0.028 of the initial low strain tensile modulus [35], which is predicted in more fundamental detail by the models. For example, Nylon's yield stress would be 140 MPa if calculated by the Seitz model using an initial tensile modulus of 5 GPa, and *Nephila* spider silk's yield stress would be 308 MPa by the Seitz model using an initial tensile modulus of 11 GPa.

Previous models have not highlighted the increase in dynamic (rather than quasi-static) modulus post-yield, simply because researchers would not have been aware of the details of the effect reported here. Quasi-static strain hardening is included in some polymer models, and also explicitly for silk [34, 36, 37], by the conversion of disordered to ordered states by the mechanical work done by the post-yield strain against load, and other models focus upon microfibrillar orientation [38]. Qualitatively, our results suggest that a polymer hardens under post-yield strain until the new local value of elastic modulus is reached, because at that stage the increased fraction of order would be high enough to sustain the applied load elastically without further plastic strain.

3.4.2 Structural changes through deformation

Figure 3.9 (a) compares the gradient and values of storage modulus against tensile stress for the two silks. It is evident that the two silks have the same storage modulus-static stress gradient, but different degrees of order as suggested by the different values of storage modulus at low stress. Figure 3.9 (b) replots the data from Figure 3.4 in the form of maximum applied stress as a function of the increased dynamic modulus for

nylon and the silk fibres without the sericin coating. Starting with nylon, the Seitz rule can be translated directly into a prediction of modulus under load for a classic semi-crystalline polymer with an amorphous fraction, since the polymer will strain harden (probably by increased crystallinity and orientation) until the modulus can sustain the load elastically without further yielding. The line adjacent to the nylon data points is the Seitz model with a gradient 0.028 and a starting modulus of 5 GPa and fits the observations quite well.

The silk points in Figure 3.9 show a higher gradient of about 0.07 between maximum applied stress and storage modulus. This suggests that a different activation condition for elastic instability applies to silk than for the nylon. From our introduction on silk structure the hypothesis could be taken that the 'disordered' phase in silk consists more of helix structures, rather than random coiled chains, and that these helix structures require a higher activation energy in either temperature or strain to become mobile and reconfigure to the more rigid beta-sheet ordered form. However, the hardening starts even at low loading, suggesting that the disordered fraction could be modified even at low loads.

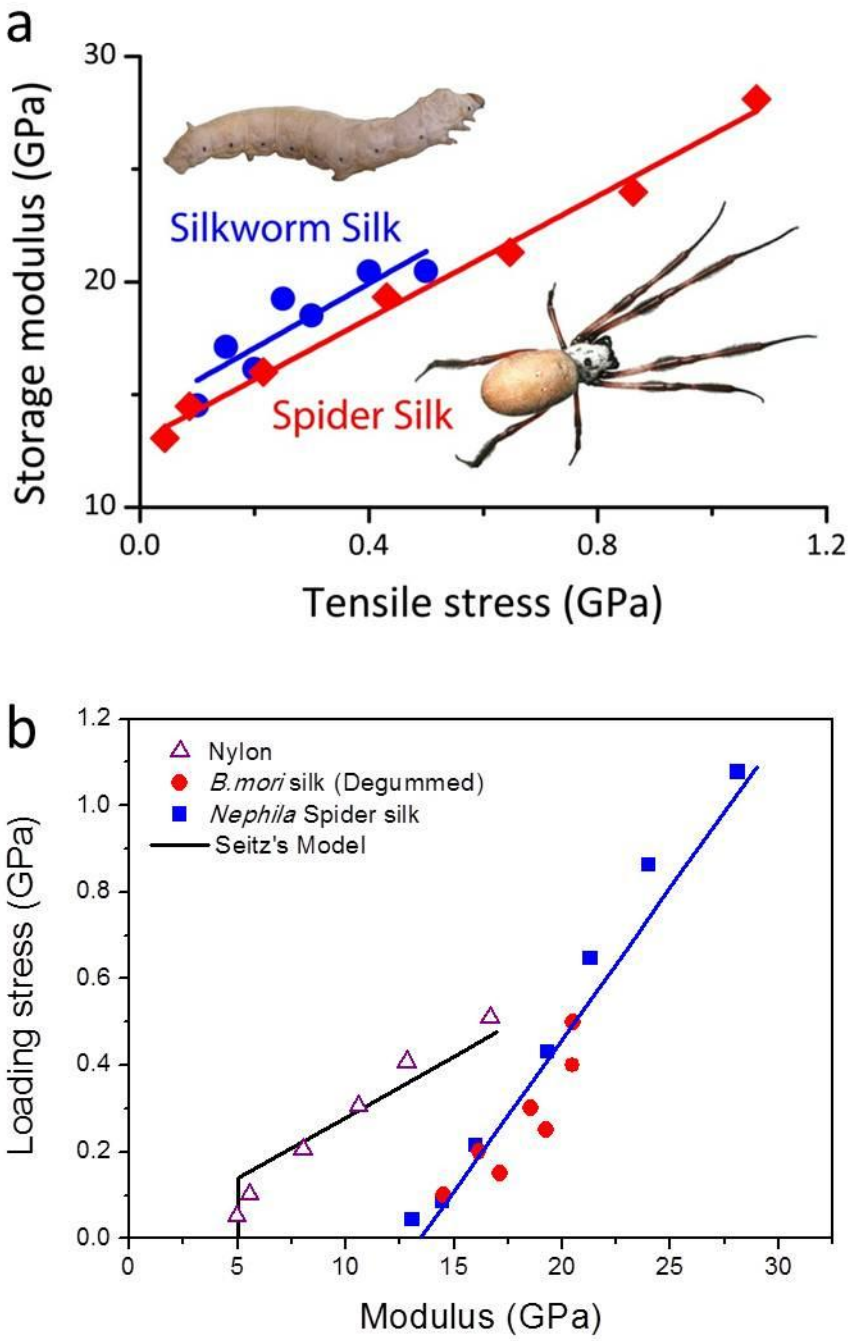

Figure 3.9 Storage modulus against static tensile stress for the two silks studied: *B. mori* silk and *Nephila* silk (a); modulus-static stress relationships for silks and nylon (b). Points are experimental data, the left hand line is the Seitz model, and the right hand line is a trendline to fit the silk data.

The elastic modulus of crystalline silk fractions has been measured by X-ray scattering tests, for example to be about 29 GPa [39], which is the upper limit measured in the *Nephila* silk at the failure stress, so a possible mechanism for our observations is

gradual conversion of helix to ordered under load until such a point that the silk polymer becomes brittle due to the high fraction of order before a sufficiently high stress is reached to unfold the ordered beta-sheets, however, the “order” here does not equal to crystalwhich could be explained by the non-periodic lattice idea of Viney [40] and the order-disorder argument of Porter and Vollrath [34]. Conversely, in nylon, the crystal structure breaks down and unfolds at high stress for a second yield point prior to break.

This concept of ‘helix to beta-sheet transformation under load’ will be pursued in future experimental work (probably by the action of selective solvents to soften the different secondary structure types), as well as in the ongoing modelling work on detailed structure-property relations in silk. The energy source for this conversion is most probably the non-recoverable plastic strain under load as the helix structures unfold and stretch. The experimental data presented here on hair will also be useful to understand the more general role of protein secondary structure and morphology on mechanical properties, which are very different from those of silk.

3.4.3 Impact of this chapter

The novel static-dynamic test, which superimposes a dynamic frequency test on top of different static loadings through the deformation to failure, enables us to measure the “pure” elastic component and hence to separate the elastic/dynamic and plastic contributions to the engineering response; the strength and toughness of the material, respectively. In addition, the change to using “stress” (a measure of mechanical work input) as a control variable instead of “strain” (a measure of morphology) to monitor the modulus and strain responses changes the modelling solutions to predicting polymer mechanical properties.

For example, I have discussed with Dr. Porter the improved GIM methods developed on the basis of these static-dynamic observations. The implication that the elastic modulus does not degrade through deformation, but rather increase due to the increase in orientation or order, means a relatively constant value of elastic modulus can be used to calculate (elastic) stress and the total strain can be calculated then by combining the elastic and plastic contributions, as shown in Figure 3.10. In fact, the modelling of stress-strain performance can be reduced to the calculation of elastic modulus prior to the yield and "plastic strain" after the yield, and the prediction of the yield or glass transition event. Fundamentally, these calculations can be established based on a limited number of fundamental parameters that define structural characteristics of the mer unit group of atoms and relationships defined by energy storage and dissipation. Particularly, plastic strain is a result of mechanical energy dissipated by the yielded disordered structures (since yield is simply the mechanically activated form of T_g), and this can be quantified by calculating the loss tangent peak of the glass transition. The following chapter will focus on the mechanical properties of silks under thermal metrics, which as we already see here is fundamentally important to silk modelling.

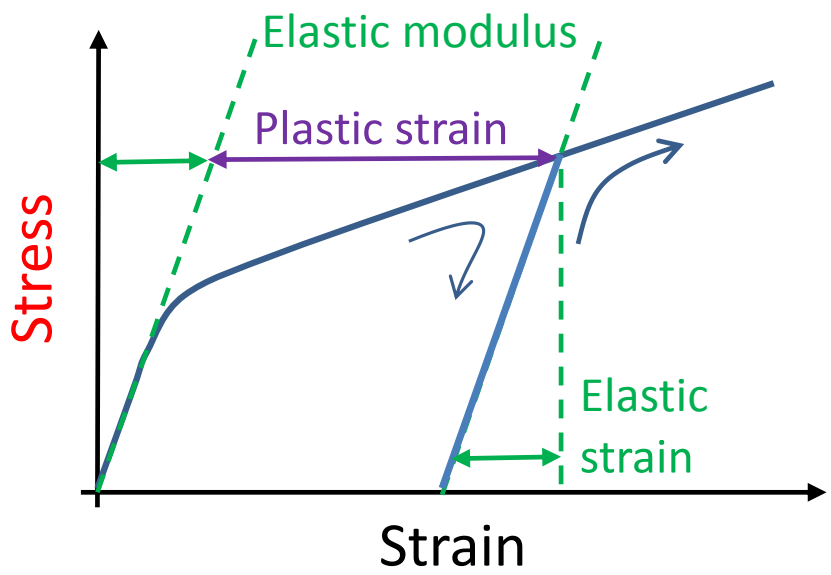

Figure 3.10 Illustration of the GIM modelling approach on predicting the stress-strain behaviour of polymers.

The structural differences between silks and nylon suggest possibilities to develop new silk-mimic structures and to improve the performance of the synthetics. One major difference is that all silks possess certain amounts of helical structures [13, 41] while nylon is semi-crystalline but is shown to perhaps only possess β-sheet structures [42]. Helical structures (α-helix or 3_1 helix) are a more hydrogen-bonded form of silk with a higher intermolecular binding energy-density than the random coils, which also means it requires more energy to unravel. This structure is found in collagen from animal skins and resilin from insect wings. There have been a few attempts to "incorporate" the helical structure into polymers with other dominant secondary structures [43, 44]. However, simply "blending" the helices into other structures does not prove to be successful to enhance engineering performance. How the functional motifs interact at nano-scales is not yet clear, and how to build a hierarchical structure from nano-scale to the engineering meso-scale, like the way natural spinners make their silk threads, remains a challenge. However, the goal of the work is to produce an engineering performance similar to spider silks at a low energy cost in its production.

3.5 Conclusions

Both silks and nylon under load/stress are shown to have reduced modulus through yield in the quasi-static tensile tests, but linearly increasing storage modulus against static load in the dynamic mechanical tests. The increase in the storage modulus of silks due to high-load is partially reversible, while nylon's storage modulus increase is reversible. The modulus-stress relationship and non-recoverable strain suggest silks are able to dissipate more strain energy through structural transformation when subjected to mechanical stress; silk possibly changing from helical to more ordered beta sheet under load. The modulus of hair decreases under load, and may be due to degradation of morphology under load.

3.6 References

[1] Kaplan, D.; Adams, W. W.; Farmer, B.; Viney, C. Silk: biology, structure, properties, and genetics. *ACS Symp. Ser.* **1994,** *544* (Silk Polymers), 2-16.

[2] Simmons, A. H.; Michal, C. A.; Jelinski, L. W. Molecular orientation and two-component nature of the crystalline fraction of spider dragline silk. *Science* **1996,** *271* (5245), 84-87.

[3] Vollrath, F.; Knight, D. P. Liquid crystalline spinning of spider silk. *Nature* **2001,** *410* (6828), 541-548.

[4] Porter, D.; Vollrath, F. Nanoscale toughness of spider silk. *Nanotoday* **2007,** *2* (3), 6.

[5] Asakura, T.; Kaplan, D. L., Silk production and processing. In *Encyclopedia of Agricultural Science*, Arntzen, C. J.; Ritter, E. M., Eds. Academic Press: London, 1994; Vol. 4, pp 1-11.

[6] Griffiths, J. R.; Salanitri, V. R. The strength of spider silk. *J Mater Sci* **1980,** *15*, 491-496.

[7] Work, R. W.; Emerson, P. D. An Apparatus and Technique for the Forcible Silking of Spiders. *J. Arachnol.* **1982,** *10* (1), 1-10.

[8] Liu, Y.; Shao, Z. Z.; Vollrath, F. Relationships between supercontraction and mechanical properties of spider silk. *Nat. Mater.* **2005,** *4* (12), 901-905.

[9] Mcnamee, S. G.; Ober, C. K.; Jelinski, L. W.; Ray, E.; Xia, Y.; Grubb, D. T., Toward single fiber diffraction of spider dragline silk from nephila clavipes. In *Silk Polymers*, ACS: 1993; Vol. 262.

[10] Grubb, D. T.; Jelinski, L. W. Fiber morphology of spider silk: The effects of tensile deformation. *Macromolecules* **1997,** *30* (10), 2860-2867.

[11] Yang, Z.; Grubb, D. T.; Jelinski, L. W. Small-angle X-ray scattering of spider dragline silk. *Macromolecules* **1997,** *30* (26), 8254-8261.

[12] Glisovic, A.; Vehoff, T.; Davies, R. J.; Salditt, T. Strain dependent structural changes of spider dragline silk. *Macromolecules* **2008,** *41* (2), 390-398.

[13] van Beek, J. D.; Hess, S.; Vollrath, F.; Meier, B. H. The molecular structure of spider dragline silk: Folding and orientation of the protein backbone. *Proc. Natl. Acad. Sci. U. S. A.* **2002,** *99* (16), 10266-10271.

[14] Rousseau, M. E.; Lefevre, T.; Pezolet, M. Conformation and Orientation of Proteins in Various Types of Silk Fibers Produced by Nephila clavipes Spiders. *Biomacromolecules* **2009,** *10* (10), 2945-2953.

[15] Sirichaisit, J.; Young, R. J.; Vollrath, F. Molecular deformation in spider dragline silk subjected to stress. *Polymer* **2000,** *41* (3), 1223-1227.

[16] Sirichaisit, J.; Brookes, V. L.; Young, R. J.; Vollrath, F. Analysis of structure/property relationships in silkworm (Bombyx mori) and spider dragline (Nephila edulis) silks using Raman Spectroscopy. *Biomacromolecules* **2003,** *4* (2), 387-394.

[17] Young, R. J.; Yeh, W. Y. Chain stretching in a poly(ethylene-terephthalate) fiber. *Polymer* **1994,** *35* (18), 3844-3847.

[18] Ene, R.; Papadopoulos, P.; Kremer, F. Combined structural model of spider dragline silk. *Soft Matter* **2009,** *5* (22), 4568-4574.

[19] Plaza, G. R.; Guinea, G. V.; Perez-Rigueiro, J.; Elices, M. Thermo-hygro-mechanical behavior of spider dragline silk: Glassy and rubbery states. *J. Polym. Sci. Pol. Phys.* **2006,** *44* (6), 994-999.

[20] Fu, C. J.; Porter, D.; Shao, Z. Z. Moisture effects on *Antheraea pernyi* silk's mechanical property. *Macromolecules* **2009,** *42* (20), 7877-7880.

[21] Blackledge, T. A.; Boutry, C.; Wong, S.-C.; Baji, A.; Dhinojwala, A.; Sahni, V.; Agnarsson, I. How super is supercontraction? Persistent versus cyclic responses to humidity in spider dragline silk. *J. Exp. Biol.* **2009,** *212* (13), 1981-1989.

[22] Guinea, G. V.; Elices, M.; Real, J. I.; Gutierrez, S.; Perez-Rigueiro, J. Reproducibility of the tensile properties of spider (Argiope trifasciata) silk obtained by forced silking. *J. Exp. Zool.* **2005,** *303A* (1), 37-44.

[23] Cunniff, P. M.; Fossey, S. A.; Auerbach, M. A.; Song, J. W.; Kaplan, D. L.; Adams, W. W.; Eby, R. K.; David, M.; Vezie, D. L. Mechanical properties and thermal properties of dragline silk from the spider *Nephila clavipes*. *Polym. Adv. Technol.* **1994,** *5*, 401 - 410.

[24] Blackledge, T. A.; Swindeman, J. E.; Hayashi, C. Y. Quasistatic and continuous dynamic characterization of the mechanical properties of silk from the cobweb of the black widow spider Latrodectus hesperus. *J. Exp. Biol.* **2005,** *208* (10), 1937-1949.

[25] Drodge, D. R.; Mortimer, B.; Holland, C.; Siviour, C. R. Ballistic impact to access the high-rate behaviour of individual silk fibres. *J. Mech. Phys. Solids* **2012,** *60* (10), 1710-1721.

[26] Greving, I.; Dicko, C.; Terry, A.; Callow, P.; Vollrath, F. Small angle neutron scattering of native and reconstituted silk fibroin. *Soft Matter* **2010,** *6* (18), 4389-4395.

[27] Robbins, C. R.; Crawford, R. J. Cuticle damage and the tensile properties of human hair. *J. Soc. Cosmet. Chem.* **1991,** *42* (1), 59-67.

[28] Robbins, C. R., *Chemical and physical behavior of human hair*. *Fourth edition*. Springer-Verlag GmbH and Co. KG, Heidelberger Platz 3, D-14197, Berlin, Germany; Springer-Verlag New York Inc., 175 Fifth Avenue, New York, NY, 10010-7858, USA: 2002; p i.

[29] Franbourg, A. Current research on ethnic hair. *Journal of the American Academy of Dermatology* **2003,** *48* (6), S115.

[30] Jauzein, V.; Bunsell, A. Bio-composite aspects of silk: the sericin sheath acting as a matrix. *J Mater Sci* **2012,** *47* (7), 3082-3088.

[31] Vehoff, T.; Glisovic, A.; Schollmeyer, H.; Zippelius, A.; Salditt, T. Mechanical properties of spider dragline silk: Humidity, hysteresis, and relaxation. *Biophys. J.* **2007,** *93* (12), 4425-4432.

[32] Porter, D., *Group Interaction Modelling of Polymer Properties*. Marcel Dekker: New York, 1995.

[33] Porter, D.; Gould, P. J. Predictive nonlinear constitutive relations in polymers through loss history. *International Journal of Solids and Structures* **2009,** *46* (9), 1981-1993.

[34] Vollrath, F.; Porter, D. Spider silk as a model biomaterial. *Appl. Phys. A-Mater.* **2006,** *82* (2), 205-212.

[35] Seitz, J. T. The estimate of mechanical properties of polymers from molecular structure. *J. Appl. Polym. Sci.* **1993,** *49* (8), 1331-1351.

[36] Vollrath, F.; Porter, D. Spider silk as an archetypal protein elastomer. *Soft Matter* **2006,** *2*, 377-385.

[37] Du, N.; Yang, Z.; Liu, X. Y.; Li, Y.; Xu, H. Y. Structural Origin of the Strain-Hardening of Spider Silk. *Adv. Funct. Mater.* **2011,** *21* (4), 772-778.

[38] Planas, J.; Guinea, G. V.; Elices, M. Constitutive model for fiber-reinforced materials with deformable matrices. *Phys. Rev. E* **2007,** *76* (4).

[39] Becker, M. A.; Mahoney, D. V.; Lenhert, P. G.; Eby, R. K.; Kaplan, D.; Adams, W. W., X-ray moduli of silk fibers from *Nephila clavipes* and *Bombyx mori*. In *Silk Polymers: Materials Science and Biotechnology*, Kaplan, D.; Adams, W.; Farmer, B.; Viney, C., Eds. American Chemical Society: Washington, 1994; Vol. Symposium Series 544, pp 185-195.

[40] Thiel, B. L.; Guess, K. B.; Viney, C. Non-periodic lattice crystals in the hierarchical microstructure of spider (major ampullate) silk. *Biopolym.* **1997,** *41* (7), 703-719.

[41] Rousseau, M. E.; Lefèvre, T.; Beaulieu, L.; Asakura, T.; Pézolet, M. Study of protein conformation and orientation in silkworm and spider silk fibers using Raman microspectroscopy. *Biomacromolecules* **2004,** *5* (6), 2247-2257.

[42] Cooper, S. J.; Atkins, E. D. T.; Hill, M. J. Temperature-Induced Changes in Lamellar Crystals of Monodisperse Nylon 6 and Nylon 6,6 Oligoamides. *Macromolecules* **1998,** *31* (25), 8947-8956.

[43] Omenetto, F. G.; Kaplan, D. L. New opportunities for an ancient material. *Science* **2010,** *329* (5991), 528-31.

[44] Rabotyagova, O. S.; Cebe, P.; Kaplan, D. L. Self-Assembly of Genetically Engineered Spider Silk Block Copolymers. *Biomacromolecules* **2009,** *10* (2), 229-236.

Chapter 4. Thermal and thermal history effect on the dynamic mechanical properties of silks

4.1 Introduction

Dynamic mechanical thermal analysis (DMTA) has been applied extensively in polymer science and engineering since the 1950s and it is arguably the most important analytical tool to bridge between the micro-structure and macro-level properties for amorphous or semi-crystalline polymers [1]. However, the technique is far less used and developed for biopolymers such as silks, due mainly to the practical difficulty of testing individual fibres (limitations of instrument sensitivity and reliable and reproducible sample preparation). Hence, there are neither established methods to quantitatively analyse the thermo-mechanical properties of single silk fibres, nor sufficient published experimental observations on samples with clearly documented thermal and mechanical processing history to be able to deduce useful structure-property relations. Previous work on DMTA analysis of silk usually shows just a single result such as a temperature scan and leaves open questions about the structural origin of dynamic mechanical effects, such as loss tangent peaks or changes in storage modulus as a function of temperature [2-5].

In Chapter 3 and the published paper [6], the effect of stress on the dynamic mechanical properties of silks was studied and a direct comparison with nylon fibres was made, which showed that the stress history causes irreversible changes in silk dynamic modulus. These changes must be caused by changes to the macromolecular structure and morphology, such as increased degree of order and orientation under increased stress loading. These structural effects can then partly explain the variability in silk properties subject to different stress histories, and have important implications

for how mechanical properties should be tested, due to factors such as the static load during dynamic mechanical tests.

This chapter looks at the effect of temperature and thermal history upon dynamic mechanical properties of natural silks, since changes in these properties as a function of temperature are valuable for the interpretation of structural changes in any polymer and will be important tools for understanding natural silk structures as well as for evaluating their potential for future applications. However, it is important from the start to realize that the variability of natural silk fibres can be large, due mainly to different production conditions, and any investigation such as this must start by looking for generic trends in property changes, rather than absolutes.

There is no lack of thermal analysis on various forms of silk fibroins, although most studies have been focused on reconstituted silk fibroin (RSF) films [7-9], rather than native silks that have been produced by silkworms or spiders. As a broad summary, the thermal properties of silk are due to the chemical structure and morphology of the silk itself and also to the effect of water in various forms and interactions with the silk macromolecules, and have been discussed in detail by Hu [8, 9]. Differential scanning calorimetry (DSC) is used methodically to study the thermal properties of silks [7]. When combined with temperature modulated DSC, glass transition effects could be differentiated from other irreversible changes. Hu proposed a water-induced glass transition mechanism for the heat capacity changes of RSF at 60 °C and, by applying heating cycles, all the bound water was successfully removed and a proposed pure silk glass transition temperature, T_g, was captured at 178 °C [8].

At temperatures below 100 °C (the atmospheric boiling point of water), water seems to contribute significantly to variations in silk thermal properties. The first question is:

how much water is there in silk? Thermogravimetric analysis (TGA) suggests RSF usually takes between 5 and 10% (w/w) water without excessive humidity treatment [8, 10]. Our own TGA analyses suggest ~5% water within native silk fibres: see Figure 4.6. The second question is: how does the water affect silk properties? There are two generic mechanisms associated with the effect of water on proteins in this temperature region: the peptide-water glass transition of the disordered structure at about 200 K (-73 °C) and denaturation at about 333 K (60 °C), both of which have been modelled previously [11, 12]. Doster [13] has reviewed the peptide-water glass transition, and scattering studies on silk suggest that such a transition occurs in hydrated silk [14].

While the transition discussed by Hu at about 333 K (~60 °C) coincides with the protein denaturation temperature, the observed transition usually occurs over a much broader temperature range than denaturation [11], and these observations by Hu do not have the same detailed relations between water content and bulk glass transition temperature reported a number of times in literature, where the water fraction-T_g relation follows a linearly decreasing trend from 200 °C down to about -60 °C [15-17]. We believe this broad transition effect between 25 and 100 °C can be simply attributed to water evaporation kinetics. A generic model for water evaporation kinetics in proteins in the range of 20 to 100 °C has been suggested by a quantitative study on reconstituted soy protein films [18]. As the water evaporates from the disordered structural components, this transition response eventually disappears as all the water associated with the disordered structure is removed. So far, no quantitative link has been established between the two low temperature transition processes, and will be considered in this work.

At higher temperatures (above 100 °C), the structure and morphology of silk itself dominates thermal properties. The upper temperature of interest here is defined by the onset of thermal degradation in proteins at about 250 °C and has been shown to be directly related to the activation energy for fission of the covalent bonds in the protein chain backbone [19]. This means that the crystal melt temperature of proteins is unlikely to be reached without prior degradation, and so attention must focus on the T_g of silks as the main source of changes in thermal or mechanical properties. DSC studies by Nakamura and Magoshi [20, 21] on native silk fibroin from the glands of silkworms showed that the T_g of silk fibroin from various species of silkworms ranges from 160 °C to 210 °C. Indeed any study of thermal properties of silks and proteins in general observes T_g values in this range, but so far without identifying any mechanisms to explain different values.

Recently, Hu [22] and Yuan [23] both used infrared spectroscopy to characterize the conformational changes in RSF structure induced by heat or chemicals (e.g. methanol), and both reported the same dry RSF glass transition temperature of 178 °C. Moreover, the temperature-modulated DSC results suggest the heat capacity of RSF decreases linearly with the increase of order/crystallinity. From DMTA observations, Yuan proposed a mechanism of a structural split of the amorphous (peak loss tangent at 177 °C) to a more disordered amorphous structure (155 °C) and more ordered forms (190 and 205 °C). Porter used models for synthetic polymers to suggest that the upper value of T_g at about 200 °C can be attributed to the strong hydrogen bonds between amide groups in adjacent protein chains, which implies that lesser degrees of hydrogen bonding in more disordered structures might lead to lower values of T_g through a direct proportionality between bonding energy and T_g [24, 25].

This DMTA study on native silks complements previous thermal studies, and more explicitly reports the dynamic mechanical properties of native silks as a function of temperature and thermal history. In particular, and following the guidelines from previous work outlined above, this work looks specifically at effects that can be attributed to water interactions with silk at lower temperatures (T < 100 °C) and to different molecular structures in the silk that lead to different values or a range of values for T_g at higher temperatures above about 150 °C and prior to degradation. To do this, the DMTA methodology for testing individual silk fibres is first outlined, and then measurements on *B. mori* silkworm silk and spider dragline silk of *Nephila edulis* are then reported and compared as a basis for suggesting structural mechanisms to explain thermal effects in silk.

In the previous chapter, in order to give a fair comparison of silks with its synthetic companion, we included medium tenacity nylon for both quasi-static and dynamic mechanical tests. It was shown that the medium tenacity nylon is nearly as strong as the degummed silkworm silk and is much tougher than silkworm silk. Here in this chapter, we will introduce the thermal effects from the results of the thermal dynamic mechanical properties of medium tenacity nylon before further analysing the silk thermal mechanical properties and structures.

4.2 Experimental section

4.2.1 Sample preparation

B. mori silkworm silks: cocoons of three commercial grades (pupae removed) from Province Jiangsu in China were kindly provided by Dr. Yaopeng Zhang from Donghua University (Shanghai, China). The three cocoon grades are named as JS1, JS2 and JS3

in order of decreasing "quality". These three types of *B. mori* silk were chosen on the basis of having clear differences in cocoon size and colour and fibre properties such as diameter (see Table 4.1 below) that might show interesting differences in dynamic mechanical properties.

Since this chapter looks for thermally induced structural differences in silks that manifest themselves in the dynamic mechanical properties, some extreme examples of poor *B. mori* silks with potential for showing poor dynamic mechanical properties would be helpful on top of the poor-grade silks. Previous publications [26] and parallel work on manipulated silkworm silks in the laboratory that controls rearing conditions or forced reeling conditions show processing could influence the silk mechanical properties, thus two of these lab-produced silks provided by Dr. Chris Holland were chosen to show interesting loss tangent features as seen in Yuan's RSF silks [23]. Since only dimensionless loss tangent was of interest in that part of the work, no details such as diameter measurements were required.

As described in the methods section of Chapter 3, *B. mori* silks glued with paper frames (the effect of glue was evaluated in Chapter 2, methods) were manually gently prepared for thermo-mechanical testing. The procedure requires care so that any unnatural damage or the effect of loading history could be minimized.

Nephila e. spider dragline silk: the collection of spider silks can be found in Section 3.2.1 of Chapter 3; herein only the procedure of preparing virgin and supercontracted silk samples is introduced.

Virgin silks: The dragline silks directly transferred from the spool to sample holders are categorized as virgin silks.

Supercontracted silks: Virgin silks were firstly transferred carefully from the segments of a spool to dividers with a dividing distance of 25 mm. The restraining length on the dividers was then adjusted from 25 mm to 19 mm to loosen the silk before the silk was immersed in water at room temperature. The silk shrank and became tensioned under water. Further measurement of the shrinkage was conducted in a 1 mm-stepwise manner. When the silk no longer shrank in water (observed as loss of tension under an optical microscope), the silk was marked as fully supercontracted and the shrinkage was noted down. On average, all silks have a shrinkage of 6-8 mm out of 25 mm (ratio: 24%-32%). The supercontracted silks were mounted on the paper holders without tensioning soon after the supercontraction (they were still wet). Both natural and supercontracted silks were kept restrained on paper holders in the testing room (temperature 20 °C, relative humidity < 40%) until the test starts.

Both medium and high tenacity nylon 6,6 were purchased from Goodfellow Cambridge Ltd. Similar to the procedure described in Chapter 3, single filaments of nylon 6,6 fibres were separated, mounted, and fixed using superglue onto paper frames for various DMTA temperature scans. As provided by the supplier, the diameters of the two nylon fibres are: 25 μm for medium tenacity and 19 μm for high tenacity. I have verified the dimensions of these fibres using SEM.

4.2.2 Dimensional measurements

SEM (Jeol Neoscope JCM-5000) was used to characterize the dimensions of silks, and full details of the method can be found in Section 3.2.2 of Chapter 3. Table 4.1 shows the relevant sample dimensional information for later sections in the results and discussions. Since only the dimensionless loss tangent is discussed for *N. edulis*

supercontracted silks as well the two lab-produced *B. mori* silks, the SEM measurements upon these silks are not required here.

Table 4.1 Silk fibre information

Fibre		Cross-sectional area (± SD) (μm^2)	Sample size (N)
B. mori silk	JS1	401 ± 50	33
	JS2	334 ± 31	25
	JS3	270 ± 34	29
N. edulis Virgin silk		22.9 ± 1.7	11

4.2.3 Tensile testing

Quasi-static tensile tests (strain rate below 0.01 s^{-1}) were performed on TA Q800 in controlled-force mode at room temperature ~25 °C. Length and force were both directly measured. 15-30 minutes dry nitrogen purge was applied after the sample was loaded to the clamps to remove the excess moisture. The force-ramp rate for each subject fibre was: 0.1 N/min for *B. mori* silk and nylon 6,6 medium tenacity fibre, and 0.025 N/min for *Nephila* dragline silk.

4.2.4 Dynamic mechanical thermal analysis (DMTA)

All the dynamic mechanical thermal tests were performed on TA Q800 under DMA multi-frequency strain mode. The parameters kept as constants are: temperature ramp rate 3 °C/min; frequency 1 Hz; and dynamic strain 0.1%. Preload force equivalent to 50 MPa stress was applied to keep the testing fibre in tension to make sure of the dynamic oscillation not falling out of tension. The rehydration test was performed with the set-up of Q800 humidity accessory. The dynamic mechanical test through a temperature range is called "temperature scan" here.

Three DMTA procedures were developed: (1) full-range temperature scan from -100 °C to 270 °C; (2) cyclical temperature scans with the first ramp up to 120 °C or 180 °C, or abbreviated as 120 °C annealing and 180 °C annealing, respectively; (3) two temperature scans up to 90 °C with rehydration (80% relative humidity for 2 hours) in between. Both *B. mori* silk (JS1) and *Nephila* dragline silks were tested on full-range temperature scan and cyclical temperature scan to 120 °C. The full-range temperature scans on three graded *B. mori* silks (JS1, JS2 and JS3) were compared; *B. mori* silk (JS3) were then tested on cyclical temperature scan with first ramp to 180 °C; the rehydration test was performed on *B. mori* (JS1) only.

4.2.5 Loading DMTA

For the temperature scans and annealing tests, a static stress of 50 MPa was applied to keep the fibre in tension. Increased static loadings (71, 100, 200, 300, 350 MPa) were applied on nylon 6,6 fibres to study the loading effect on the thermal dynamic mechanical properties of fibres. Before starting each loading temperature test, the fibre length was measured at 50 MPa static stress and recorded as the initial length. A number of static loadings were also applied in the silk tests. However, due to the fine sizes of the silk fibres and the complex interactions of loading with silks, many tests showed very noisy results.

The calculation of the cross-sectional areas for silks or nylons under different loadings was to assume a constant volume between loadings at room temperature. For example, for nylon, the initial unloaded length was first measured when 50 MPa static stress was applied, then the loaded length of the fibre at higher static stresses would be measured, and by assuming a constant volume rule through deformation, the area of the loaded fibre was calculated by dividing the initial area by the ratio of stressed

length/initial length. The thermal expansion effect on the areas is not compensated; however, thermally induced dimensional changes of static strain or length will be discussed.

4.3 Results

4.3.1 Thermal dynamic mechanical properties of nylon 6,6

Nylon was compared with silks in the previous chapter on the mechanical properties (static and dynamic moduli) under load. Nylon showed superiority over *B. mori* silks in toughness and the ability to recover from strain. In this chapter, before presenting the silk results, I first present the results of nylon fibres using various thermal dynamic methods to demonstrate the general thermal effects as the nylons are much thicker fibres and tend to give clearer signals and less noise. Nylon and silks have very different molecular structures, however, and so the results for nylon do not necessarily suggest the same mechanisms for the thermally-induced structural changes in silks.

First, what are the dynamic mechanical properties of nylon 6,6 through the full temperature range? In Figure 4.1 (a) the storage modulus of medium tenacity nylon fibre starts from 8.7 GPa at -100 °C and decreases with increasing temperature, finally reaches a low modulus of 1.6 GPa before failure at above 250 °C. As shown in the loss tangent profile, the nylon fibre experiences two major structural transitions, a lower relaxation at -52 °C and most likely a glass transition peaked at 94 °C. Note here, there are also mechanisms proposing that the changes over the glass transition temperature range could be due to the transformation of crystal forms in nylon 6,6 [27, 28]. The observed T_g is close to the reported values for nylon 6,6 [1]. However, the literature reported two low-temperature relaxations at -110 °C (probably -CH_2- in gauche conformer) and -20 °C (probably -CH_2- in trans conformer) [1]. This will be explained

in the next paragraph for the annealing test. Figure 4.1 (b) shows the stress-strain curves of nylon 6,6 go through three stages and two yields as discussed in the previous chapter. The initial tensile modulus of 5 GPa is comparable to the dynamic modulus of 5.8 GPa at 25 °C.

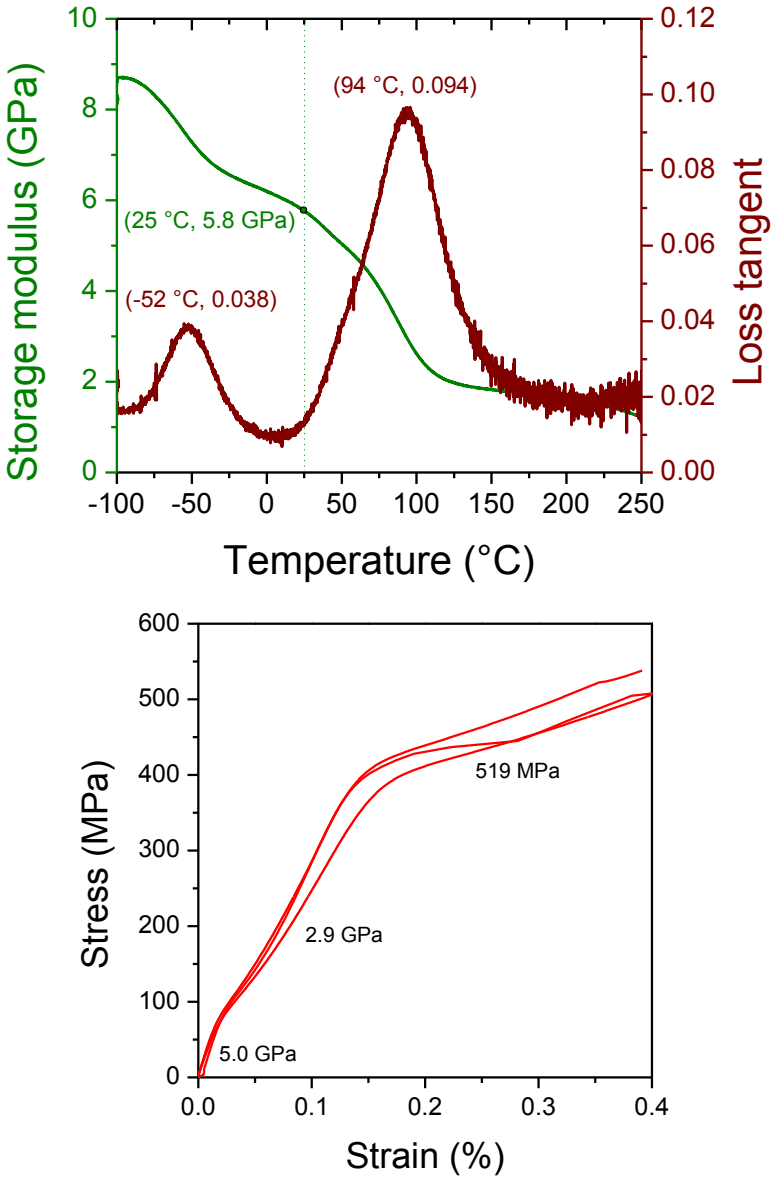

Figure 4.1 DMTA plot (a) and stress-strain curves at room temperature (b) of medium tenacity nylon.

To further explore the nature of nylon's low temperature transitions, the temperature annealing test was conducted, as shown in Figure 4.2. The high temperature for

annealing in the first scan was chosen to be the onset temperature for glass transition (about 40 °C), which should allow some molecular motions to "adjust" the structure. As a result of annealing, the low temperature transition disappeared and split into two peaks at below -100 °C and -30 °C in the second scan. The two new peaks agree with the reported low-temperature transitions for nylon 6,6 despite that the peak heights here are less. Interestingly, the starting modulus at -100 °C became lower (from 9.0 GPa to 7.8 GPa) and the room temperature storage modulus didn't seem to change after the first scan. This may suggest that the original commercial nylon 6,6 has randomly mixed group interactions from trans- and gauche conformers, and after the annealing the two structures become more resolved. Although nylon experiences transitions under thermal or mechanical conditions respectively in the dynamic measurement and the tensile test, the same "glass transition" is observed in the storage modulus reduction accompanied by a loss tangent peak and the tensile modulus reduction through the first yield in the tensile test.

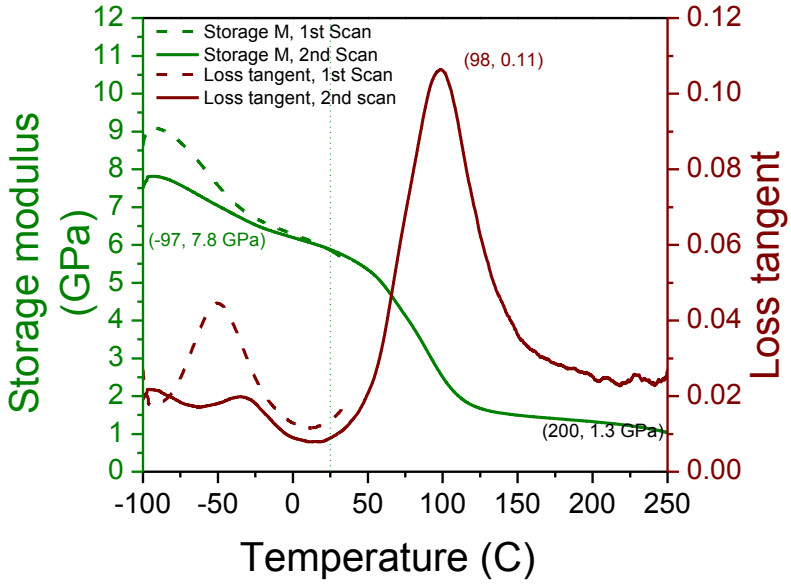

Figure 4.2 Annealing cyclical temperature scans on medium tenacity nylon.

The temperature scans with various static loadings were also conducted on these nylon fibres. Figure 4.3 (a) shows that as the loading increases, the storage modulus increases in a manner similar to that shown in the previous chapter (storage modulus change with load), and when the loading exceeded 300 MPa, the fibres were unable to reach the glass transition and failed at above 100 °C. The loss tangent profiles in Figure 4.3 (b) show more information on the molecular structures of nylon in different loading-temperature scans. The low temperature relaxation became smaller as the loading increased to 200 MPa, whereas any further higher loading did not seem to decrease the peak further; and the glass transition peak started losing its Gaussian shape with the further increased load above 300 MPa, where the peak seemed to plateau with increasing temperature before the fibre finally broke. The increase in storage modulus and the decrease in loss tangent at the glass transition confirm that the structural order in nylon 6,6 increases as the loading increases. By comparing the peak areas of loss tangent at 50 MPa and 200 MPa, the change in the structural disorder at high loading could be estimated to be ~30% less. Figure 4.3 (c) offers information on the thermal expansion of nylon, and the steep change in the gradient of static strain over temperature indicates the glass transition.

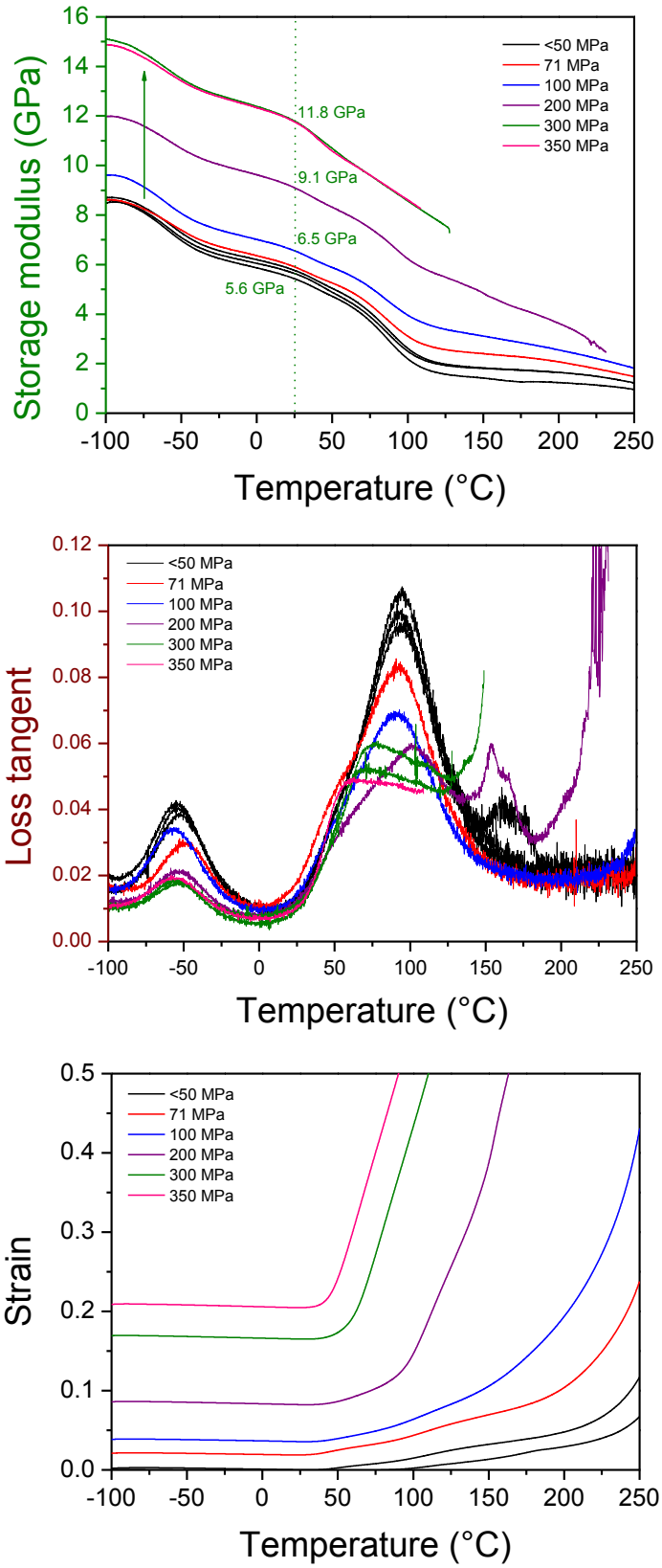

Figure 4.3 Dynamic mechanical properties of medium tenacity nylon under various static loadings through DMTA temperature scans: storage modulus (a); loss tangent (b); and static strain (c).

4.3.2 Overview of DMA temperature scans on silk

Figure 4.4 shows a typical DMTA plot of native *B. mori* silk with two dynamic mechanical properties (storage modulus and loss tangent) and static length changes as a function of temperature. For convenience, the full temperature range is divided into three regions: (1) Storage modulus decreases with increasing temperature from -100 °C to 25 °C; (2) modulus increases with increasing temperature from 25 to 120 °C; (3) modulus drops significantly from 170 to 250 °C. Increases in loss tangent are associated with temperature gradients of storage modulus, as expected on a roughly linear proportionality basis [24, 25, 29], and significant static length increases occur as the modulus decreases significantly through the upper T_g under constant static load in region (3).

As discussed in the introduction, regions (1) and (2) are explored together in the next section, since water plays the major role in the mechanisms for property changes in both regions. Region (3) is the glass transition of silk fibroin and is discussed in more detail separately, since it potentially offers most in our exploration of silk structure-property relations. Finally, we look for mechanisms that operate over all the regions and try to identify common features that may allow all the different effects to be understood in terms of structural changes that are activated by temperature.

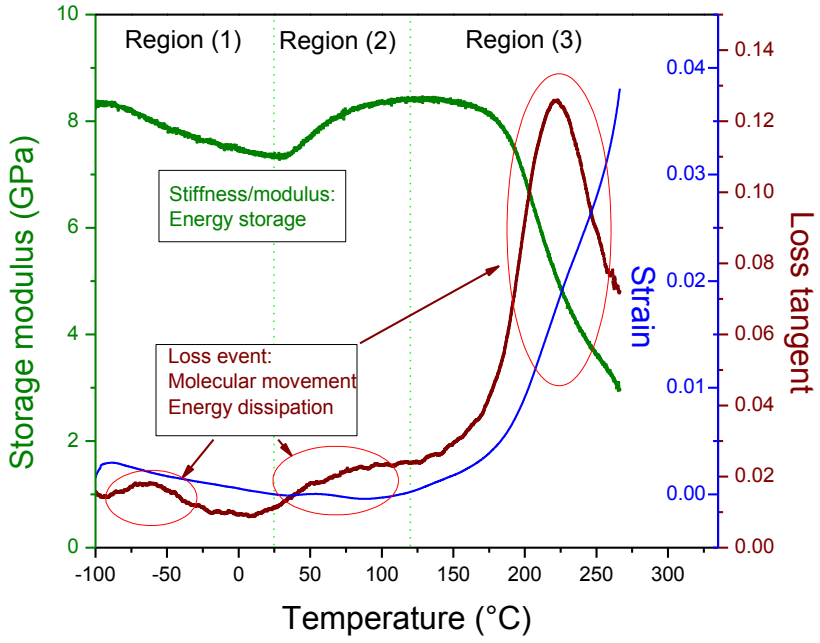

Figure 4.4 Typical Dynamic Mechanical Thermal Analysis (DMTA) profile of native *B. mori* silks showing three properties (storage modulus, loss tangent and static strain) as a function of temperature.

4.3.3 Property changes induced by water loss: 120 °C annealing

In this section, the results of cyclical temperature scans of 120 °C annealing are reported and the dynamic mechanical properties of both *B. mori* and *N. edulis* dragline silks before and after the first heating up to 120 °C are compared. Figures 4.5 (a) and 4.5 (c) show the dynamic mechanical property-temperature profile of both silks and Figures 4.5 (b) and 4.5 (d) show the stress-strain performances of both silks before and after the 120 °C annealing.

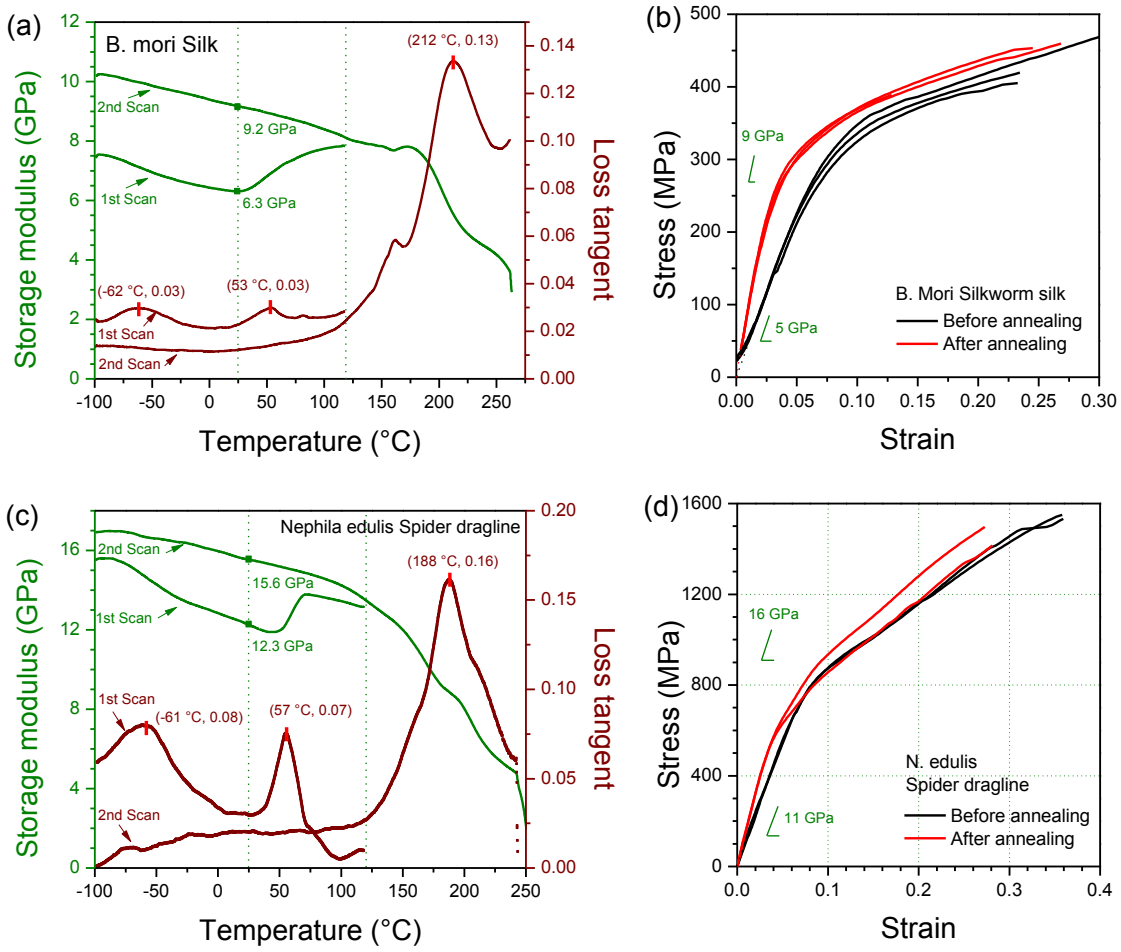

Figure 4.5 Dynamic mechanical property-temperature profile of 120 °C annealing on *B. mori* silk (a) and *N. edulis* dragline silk (c); Stress-strain curves before and after 120 °C annealing: *B. mori* silk (b) and *N. edulis* dragline silk (d).

Starting from the dynamic profiles in Figures 4.5 (a) and 4.5 (c), in the first scan both *B. mori* and *N. edulis* silks have a broad loss peak centered at -60 °C in region (1), which is conventionally assigned as the β-relaxation of silk fibroin by most literature, without specifying the structural origin of the transition [3, 30]. Since this loss peak disappeared in the second ramp after water has been removed, it seems clear that the peak must be associated with water-protein interactions, and most probably with the peptide-water glass transition [11-13]. When water is lost through the 120 °C annealing process, the peptide-water complex structure is replaced by peptide-peptide interactions

with T_g in region (3) being at much higher temperatures. Therefore, in the second ramp the relaxations related to the water-protein complex structure are not present.

In temperature region (2) from 25 °C to 120 °C, the dynamic modulus of both silks increases. Interestingly, this modulus increase is accompanied by a higher level of loss tangent similar to those in region (1), which suggests increased molecular mobility. In the dynamic heating test, *B. mori* silk's modulus increases gradually within this region from about 25 to 100 °C, whereas *N. edulis* spider silk's modulus increase and loss peak occur over a narrower temperature range between 50 and 70 °C, which may indicate a more specific molecular relaxation process than simply evaporation of water, such as denaturation [11, 12]. Note here that the difference between simple evaporation and denaturation is that, evaporation involves only the plasticiser type of water while denaturation involves hydrogen-bonded water to peptide chains. At a reference temperature of 25 °C, *B. mori* raw silk's modulus changed from 6.3 GPa in the first scan to 9.2 GPa in the second scan, which is very similar to the increase in initial modulus in the stress-strain curves (Figure 4.5 b) after annealing. Similarly, *N. edulis* dragline silks show a clear increase in both dynamic modulus (Figure 4.5 c) and initial modulus from the quasi-static tensile tests (Figure 4.5 d).

The modulus increase in this region has been observed previously and was also attributed rather vaguely to water loss [3, 29], without being explained quantitatively. Our TGA results for *B. mori* silk show about 6% w/w water (see Figure 4.6). The challenge here is to relate this relatively small water loss with the significant increase in storage modulus, and will be discussed later.

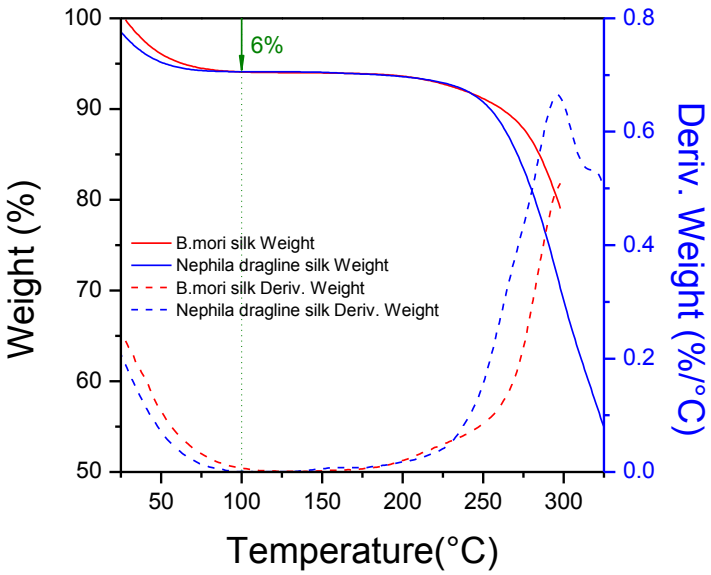

Figure 4.6 TGA results on *B. mori* and *N. edulis* dragline silks (heating rate: 3 °C/min; Nitrogen purge 100 cc/min), showing 6% water loss due to water evaporation.

Note that both low temperature loss peaks are removed simultaneously as the water is lost, together with the associated fall and increase in storage modulus. This supports our hypothesis that the ~60 °C events are simply evaporation of water from the sample after it has become mobile at the peptide-water T_g around 200 K.

4.3.4 Rehydration of the heated silks

To further test the reversibility and rate of the dehydration and possible rehydration processes, a combined temperature and humidity cyclical test was developed, as shown in Figure 4.7 for degummed *B. mori* silk, which uses the full range of conditions possible on the DMTA humidity accessory. First, the sample is exposed to a 0 to 90 °C temperature cycle at zero humidity to induce dehydration and increase the storage modulus. This is followed by exposure to high (80%) relative humidity at 30 °C for two hours to rehydrate the sample, and finally another heating cycle at zero humidity for dehydration.

The results in Figure 4.7 show an initially fast response to changes in humidity over the first 10 minutes for both modulus and loss tangent, followed by a more gradual equilibration. These combined changes suggest that relatively fast water loss and gain in the fibroin is accompanied by a gradual decrease in the fraction of disordered states available to interact with water as interchain hydrogen bonding develops with chain reconfiguration under the static loading applied to the sample during tests.

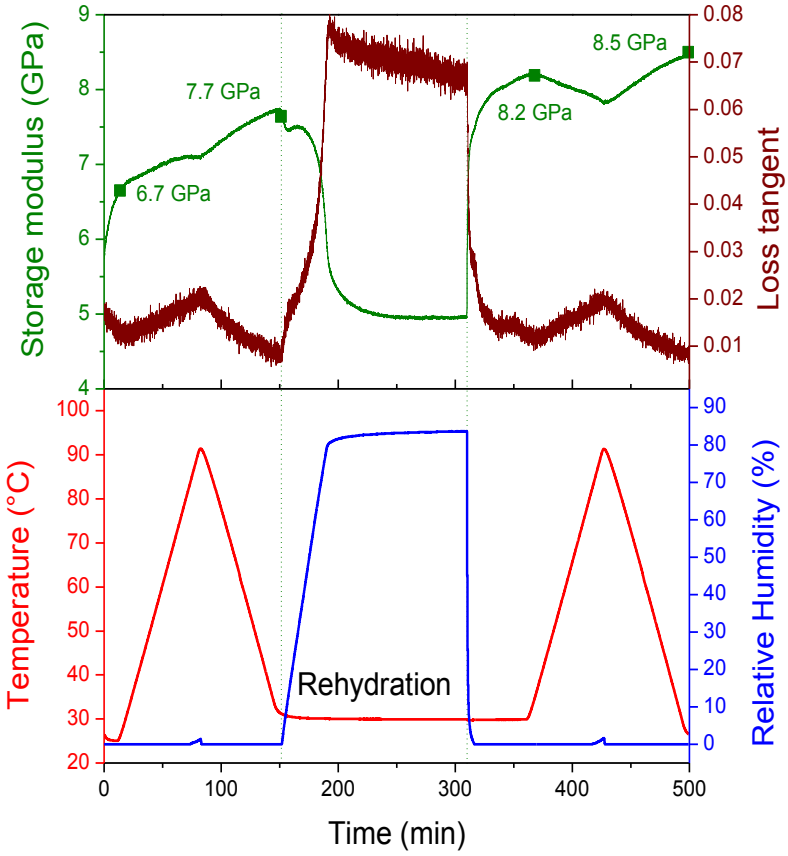

Figure 4.7 Rehydration test on *B. mori* silk at 30 °C at 80% relative humidity for 120 mins between two annealing cycles from 25°C to 90 °C at 0% relative humidity.

4.3.5 Glass transition of dry silk

While the hydration state of silks or water-silk interactions causes a great degree of variability in silks, as shown in the last section, the removal of water gives stiffer silks and induces the reformation of dry silk structures that have themselves an intrinsic

variability. In this section, the variability of dry silk structures in the high temperature region (3) (the glass transition zone) is investigated. As mentioned previously, the observed glass transition temperature ranges from 150 to 250 °C for silk fibroin [20, 21]. Yuan specifically discussed four different discrete T_g values in RSF with characteristic loss tangent peaks at 155, 177, 190, and 205 °C, relative to native silk fibres with T_g at about 220 °C, and suggested that different hydrogen bonded structures might be associated with each [23]. Here in native silks, numbers of different discrete T_g peaks are also observed below the more consistent defined T_g peak at 210 °C to 217 °C, as shown in Figure 4.8. Since the absolute value of storage modulus through the glass transition zone is less important here than the position of T_g as an indicator of structural differences, Figure 8 presents different aspects of loss tangent through T_g with different types of *B. mori* silk fibres that might intuitively be expected to have different molecular structures due to their different commercial grade classification or means of production.

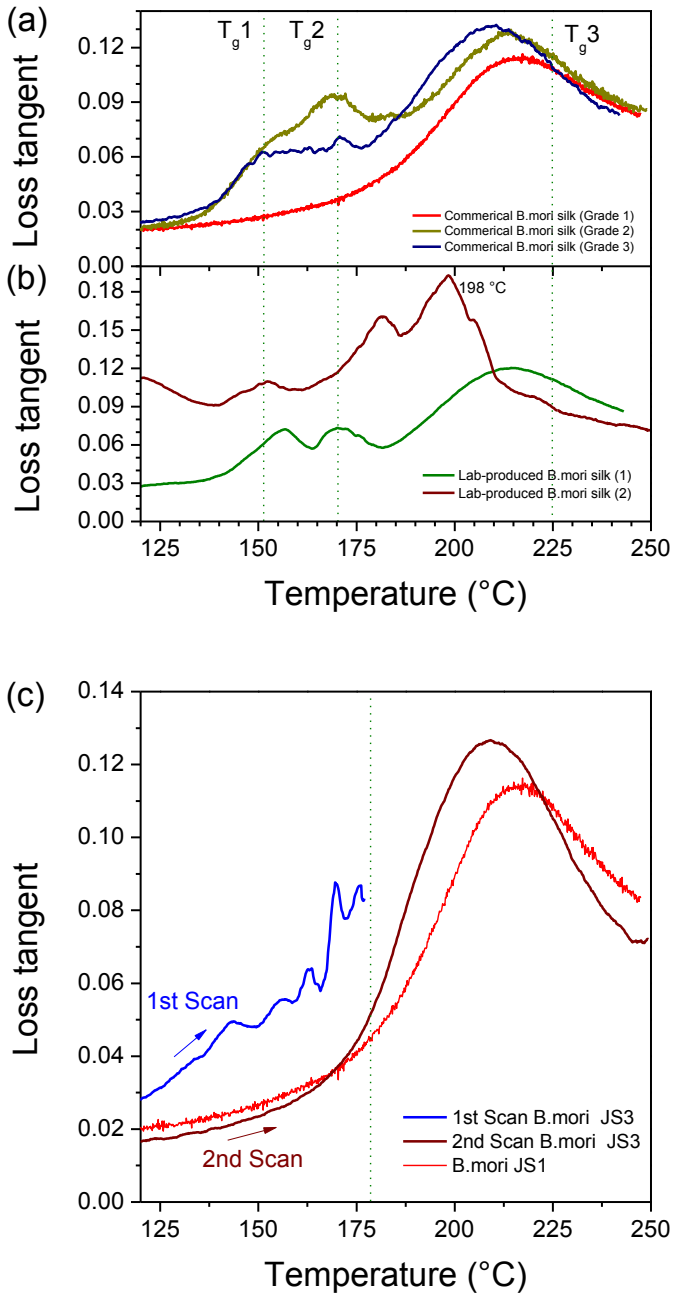

Figure 4.8 Loss tangent profiles from 3 grades of commercial silks (a), two lab-produced silks (b), and grade JS3 silk before and after annealing to 180 °C in comparison with one-scan of grade JS1 silk (c).

Figure 4.8 (a) compares temperature scans of three different commercial grades of silk, and shows that the two lower grade silks have lower temperature loss peaks roughly corresponding to two of the RSF peaks at about 155 and 170°C from Yuan [23]. Since the RSF was produced from a chaotropic solution, this suggests that the two

lower temperature transitions may be associated with more disordered structures with less intermolecular hydrogen bonding.

Figure 4.8 (b) shows the loss tangent profiles of two silks produced under controlled, but very poor, lab-rearing conditions, as outlined under methods and materials. The manipulation of rearing conditions allows us to obtain silk (1) that is similar to the commercial grade 3 silk and silk (2) that is probably more closely comparable with RSF. The peak value and peak position of the loss tangent from lab-produced *B. mori* silk (2) suggests a greater degree of disorder in the silk structure. More importantly, the two lab-produced silks illustrate the potential huge room for variability to occur in native silk structure. At this stage, how the silks were produced is less important than the observed differences between samples, and the effect of production will be discussed in the later chapter 7.

Comparing the loss tangent profiles before and after annealing to 180 °C of grade 3 silk in Figure 4.8(c), the loss peaks from 150 to 180 °C have been lost in the second scan and the main T_g peak (position and height) in the second scan does not include the lower temperature peaks. The fact that these structures can be annealed out means that thermo-mechanical treatment (remember a static load is applied during tests) through the lower-T_g dynamic transition irreversibly changes the structure of the silk. The implication is that a fraction of the lower grade silk is more disordered, but that this disorder can be removed to produce a limiting structure similar to standard commercial grade 1 silk.

Figure 4.9 shows the loss tangent profiles in a temperature scan of samples of both virgin and supercontracted spider silks [17]. For a number of runs on both silks, broad transitions through the temperature region (3) are observed that include lower

temperature loss peaks that are lost by annealing as the temperature increases through the scans. Figure 4.9 highlights a number of key features. First, the loss peak for supercontracted silk is greater than for the virgin sample, which agrees with the consensus view that supercontraction is a relaxation of metastable hydrogen bonding in highly oriented virgin dragline silk back to either random coil or helical structures [17]. The increased disordered fraction going through the glass transition then has a greater loss tangent that is proportional to the disordered fraction. Second, the strain extension of the samples under the static loading follows the loss peak profile (and the reduction in storage modulus), and the supercontracted sample extends more than the virgin sample until the silk has been stretched approximately 20% to its original pre-supercontraction length [17], from where it follows the strain profile parallel to that of the virgin sample. Thus, DMTA analysis provides useful tools to monitor effects that are important to silk behaviour.

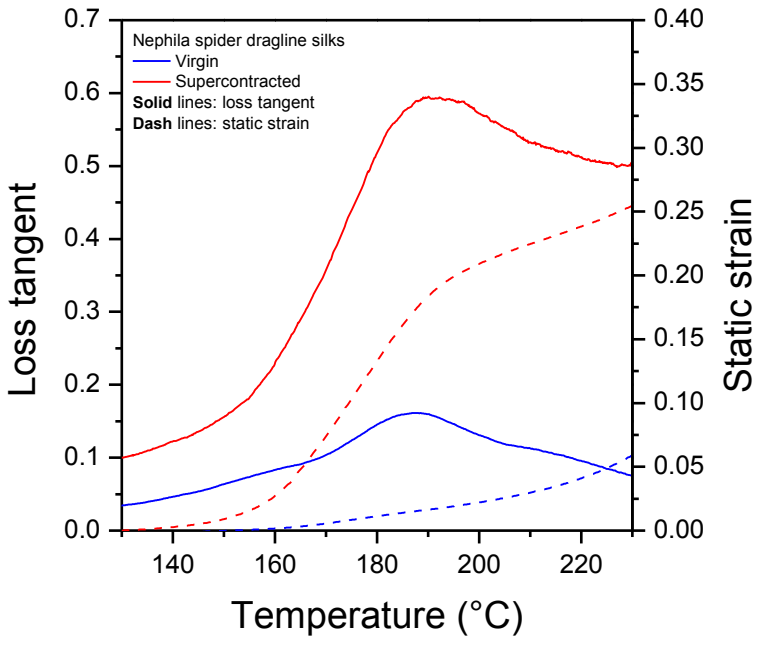

Figure 4.9 Loss tangent and shrinkage under static loading profiles from *N. edulis* dragline silks: supercontracted (a) and virgin (b).

An extension to the annealing work is to apply higher static loadings (including loadings at above the "yield" stress at room temperature) through the temperature scans. The initial idea was to explore whether mechanical loadings will affect the low-temperature transitions in silks or not. The experiments were conducted before I fully understood the thermal effect and the mechanisms for the thermally induced structural changes in silks. These results now become more a validation to the proposed theory in our publications [6, 31].

In Figure 4.10, the dynamic mechanical properties/temperature profiles from four loading-temperature scans on degummed *B. mori* silks are shown. First to look at the storage modulus, the higher static loading results in higher storage modulus if compared at the same temperature. For example, the storage modulus increased from 17 GPa at 200 MPa to 19 at 300 MPa at 25 °C. These values agree with our paper [6] on modulus under load. Another important observation is that under higher static loading the silks tended to break earlier in the temperature scan. Moreover, the high static loading seemed to suppress the low-temperature peak at -60 °C and to induce an earlier glass transition. The silk under 300 MPa could not sustain any higher temperature than 150 °C, where the glass transition starts.

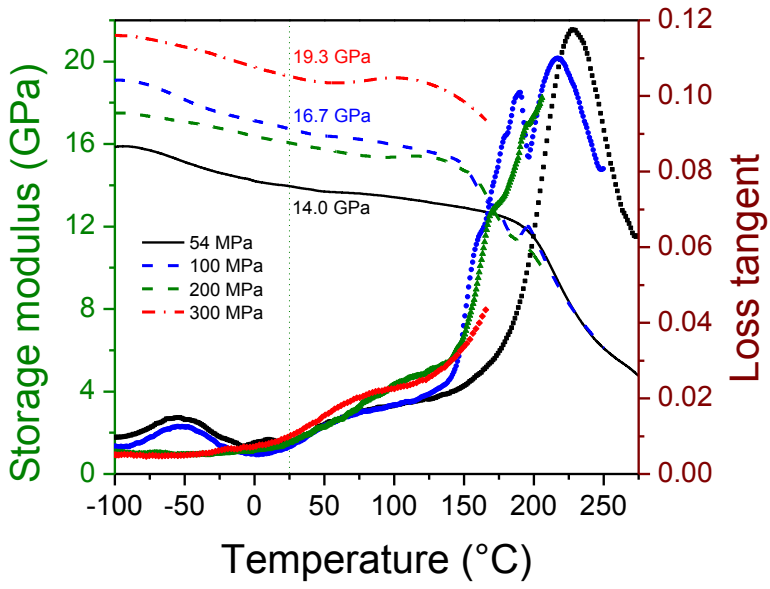

Figure 4.10 DMTA temperature scans with four static loadings on degummed *B. mori* silk fibres.

The effect of loading on the temperature scans can be explained using the order-disorder theory for silk structures. As suggested in Chapter 3, in order to sustain higher load, higher order in structure or higher storage modulus needs to be reached. Because at higher loading the disordered structures become more ordered through crystallization or orientation under the combination of heat and mechanical work, the structures which are able to dissipate energy or absorb heat are lost; therefore the whole system breaks down and reaches its failure at lower temperatures.

4.4 Discussion

4.4.1 Mechanisms for thermally induced changes in silks

It is important to note that this discussion section is attributed to the discussions with DR. Porter, and he contributed to the calculations including the equations which can also be found in his book and others [24, 25, 29], and the parameter setting for silks which can be found in our joint paper [31].

The two main sets of experimental observations on the temperature and thermal history dependence of dynamic mechanical properties of silks at lower (T < 100 °C) and higher (T > 100 °C) temperatures need to be explained quantitatively by **self-consistent** mechanisms at the molecular structural level. The objective here is, first, to show how water interacting with silk protein reduces the glass transition temperature down to -60 °C with an associated drop in storage modulus and increase in loss tangent through the transition and, second, to show how different 'dry' silk structures can have different discrete values of T_g at higher temperatures. Here in this chapter, group interaction modeling, GIM, is used to predict their highly nonlinear viscoelastic properties as a function of temperature, and more modelling details are documented elsewhere [24, 25, 29]. Application of the model to silks has shown that the mechanical properties of any silk can be predicted from its composition and fraction of "order", which is loosely identified with crystal fraction.

To generally introduce the concepts of GIM, I start with the following equations. The thermal dynamic events (glass transition for amorphous polymers or melting for crystalline polymers, for example) are predicted from the molecular parameters of the mer unit group. These parameters are the intermolecular binding energy (E_{coh}), the thermal degrees of freedom (N), and the characteristic temperature of the chain backbone (θ_1). The GIM relation for T_g (Equation 4.1) at a reference rate of 1 Hz is written in terms of the model parameters: theta temperature of skeletal mode vibrations, θ_1, the cohesive energy, E_{coh}, and the skeletal degrees of freedom, N.

$$T_g = 0.224\theta_1 + 0.0513\frac{E_{coh}}{N} \tag{4.1}$$

The next step is to calculate the change in the properties such as modulus through the thermal events. In GIM, elastic modulus reduces as mechanical energy is dissipated

through heat. The magnitude change in modulus is defined by the fraction of energy dissipated through the glass transition that is expressed as a cumulative loss tangent, tanΔ, or more specifically as the loss tangent peaks we see in DMTA plots. There is a baseline for loss tangent due to underlying thermal effects with increasing temperature. Here we only consider two states, the hydrated and dehydrated/dry silks. The reduction in modulus from one state to the other is expressed in Equation (4.2). B_e is the elastic bulk modulus, $A \approx 1.3$ GPa^{-1} is a structural term, and the fraction of disorder, f_{dis}:

$$\frac{E_{hrd}}{E_{dry}} = exp\left(-\frac{f_{dis} \times tan\Delta}{A \times B_e}\right) \tag{4.2}$$

and the cumulative loss tangent is calculated using the model parameters in Table 4.2 [24]:

$$tan\Delta = 0.0085 \frac{E_{coh}}{N} = 23 \tag{4.3}$$

Table 4.2 Parameter values for predicting T_g values using equation (1).

Transition	θ_1 (K)	N	E_{coh} (kJ/mol)	Model K (°C)
$T_{\beta 1}$	328	13.2	35.1	210 (-63)
$T_{\beta 2}$	-	-	-	Evaporation ≈ 60°C
T_{g1}	426	7.2	47.1	[18]
T_{g2}	426	7.2	48.8	430 (157)
T_{g3}	426	6.2	48.8	443 (170)
				498 (225)

The next step is to explain the specific phenomena in the results section mechanistically. Three mechanisms are proposed: protein-water glass transition to account for the low temperature loss event; simple water-loss and possibly denaturation for some silks to attribute for the room temperature to 100 °C property change; and the dry silk glass transition to attribute for the loss events at above 100 °C.

4.4.2 Protein-water glass transition

It was suggested that the low temperature loss event of proteins was associated with specific water-peptide interactions [12, 13]. Here a model hydrated peptide (alanine) structure, is shown in Figure 4.11, with the water being assumed to become part of the effective peptide mer unit, alongside the 'dry' fully relaxed peptide-peptide interaction. To distinguish from the dry silk glass transitions, the water-related loss events are referred as β-relaxations.

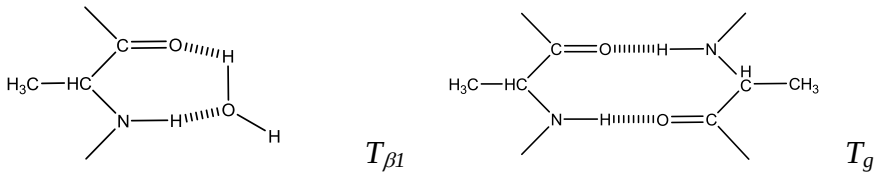

Figure 4.11 Structures of the peptide-water and peptide-peptide interactions in relation to structural transitions.

The model parameters can be assigned quite simply as shown in Table 4.2. Compared with the dry silk T_g, the increased molecular weight reduces θ_1 to 328K; the water forms strong H-bonds with the amide to prevent the two interchain H-bonds and reduce the cohesive energy by 20 kJ/mol, but increase it through the water oxygen by 6.3kJ/mol; the water adds an extra 6 degrees of freedom as a small molecule to increase N to 13.2 average. As a result $T_{\beta 1}$=-63 °C is predicted directly by equation (1) through structural parameter changes that can be attributed directly to the water interaction, and agrees well with observed values and more detailed previous quantum mechanics based simulations [12].

4.4.3 Denaturation/Dehydration

For the transition $T_{\beta 2}$ at about 60 °C, it is sufficient here to say that the water becomes mobile (perhaps also through a denaturation process in *N. edulis* silk) and evaporates [18] from the silk fibres and the modulus simply increases from hydrated to dry as water is lost. Of course, there must be detailed adjustments to the overall properties and parameters due to the changes in hydrogen bonding, but the mechanisms are clear at a semi-quantitative level. Thus, the 60 °C thermal or DMTA loss peak is not really a glass transition process, but simply a consequence of property changes due to the loss of water from the fibres.

Next is to account for the modulus change through thermal annealing. For silk fibroins, a generic value of $B_e \approx 13$ GPa has been calculated previously from the cohesive energy density [32]. Fu calculated the ordered fraction for *B. mori* silk as 0.77 [32], to give $f_{dis} \approx 0.23$ to predict $E_{hyd}/E_{dry} \approx 0.73$, such that a dry modulus of 9.2 GPa in Figure 2(a) is predicted to drop to 6.7 GPa, compared with the observed 6.3 GPa under ambient conditions. For force reeled *N. edulis* dragline, Yi suggested $f_{dis} \approx 0.15$ [33] to predict $E_{hyd}/E_{dry} \approx 0.82$, such that a dry modulus of 15.6 GPa in Figure 2c is predicted to drop to 12.8 GPa, compared with the observed 12.3 GPa. Given the uncertainty of the parameter values, these estimates for modulus change are reasonable enough with a clear physical basis to validate the general principle of the suggested mechanisms.

4.4.4 Glass transition of dry/dehydrated silk

T_g is the temperature for the onset of cooperative mobility in the disordered phase at the elastic instability point where intermolecular forces go through a maximum, or intermolecular bond stiffness tends to zero [29]. The difficulty here is we observed seemingly discrete T_g values and how to find the origin of these different values of T_g.

We start from a 'generic' or typical silk composition with a peptide sequence GAGAGS which is very representative for the *B. mori* silk as suggested by previous work [24, 25].

As shown in Table 4.2, three temperatures of T_g are predicted from a common value of θ_1 and the same average group molecular weight. The middle value T_{g2}=170 °C is that predicted for a classical amorphous polymer with all the available degrees of freedom and two hydrogen bonds per peptide group, and agrees well with the reference amorphous T_g = 177 °C value of Yuan for RSF films produced from a chaotropic solution [23]. The lower T_{g1}=152 °C transition can be associated with Yuan's 'more amorphous' structure value of 155 °C, which is attributed here to the –OH group at the end of the serin side chain forming a hydrogen bond with a main chain amide C=O group as a highly disordered structure, thereby reducing the average cohesive energy by one H-bond or 10kJ/mol in each GAGAGS segment, or 1.7 kJ/mol average per peptide. The upper limiting value T_{g3} = 225 °C is attributed to the high polarity of the amide chain segments associating strongly in a fully relaxed conformation to restrict the torsional rotation in the amide segment, thereby reducing the value of N by one per peptide, from 7.2 to 6.2 average and agrees quite well with the observed values in the range 190 to 210 °C for 'more ordered' silks.

In addition to the three core high T_g values, there must also be intermediate (again discrete) values due to energy sharing between adjacent interacting peptide groups. GIM takes each polymer group to be surrounded typically by 6 others pairwise sharing of energy, and here to list two examples of the intermediate temperature: ($2\times T_{g2}$ + $1\times T_{g3}$) = 460 K (187 °C) and ($1\times T_{g2}$ + $2\times T_{g3}$) = 479 K (205 °C), which would

complete the set of T_g loss tangent peaks observed in this work and previous on RSF [23].

4.5 Conclusions

The effect of temperature and thermal history on the dynamic mechanical properties of native silkworm and spider dragline silks has been investigated using dynamic mechanical thermal analysis (DMTA). The properties of storage modulus and loss tangent showed considerable variability between samples reared or processed in different ways. Temperature scans from -100 °C to 250 °C and cyclical scans with different upper limits (120 °C and 180 °C) on the first cycle allowed key origins of this variability to be identified and quantified to suggest structural mechanisms at the molecular level.

Both silkworm silks and spider dragline silks showed two loss peaks centered at -60 °C and +60 °C, and an increase in dynamic modulus during the first temperature scan from +25 to 100 °C through the second loss peak. However, all these features disappeared in the second temperature scan. This implies that the temperature-induced property changes below +100 °C are due simply to water loss.

The loss tangent profile through the glass transition temperature (T_g) range of a number of different dry silkworm silks was used to study contributions to silk variability in terms of molecular structures and interactions. A number of discrete loss peaks were identified in the range +150 to 220 °C and associated quantitatively using GIM modelling with different states of disordered structure with different intermolecular hydrogen bonding, which agreed with previous observations on RSF silk. Each of the lower T_g loss peaks could be removed by heating above the

corresponding T_g under the small static load in the DMTA test until a final limiting relaxed disordered state was achieved with a T_g in the range +200 to 220 °C.

Silks produced under a range of different unspecified conditions were used in this study to highlight the range and types of property and structural variability possible in natural silks. It emerged that DMTA is a sensitive and very powerful tool that can be used to link rearing and production conditions to silk quality and silk properties. Importantly, we assert that the tool can be used on both mulberry and wild silks (with their different biological functions as well as changes in molecular structure) in both fundamental research and in quality control for commercial sericulture.

4.6 References

[1] McCrum, N. G.; Read, B. E.; Williams, G., *Anelastic and dielectric effects in polymeric solids.* John Wiley & Sons: London, **1967**.

[2] Kaplan, D.; Adams, W. W.; Farmer, B.; Viney, C. Silk - Biology, Structure, Properties, and Genetics. *Silk Polymers* **1994**, 544, 2-16.

[3] Yang, Y.; Chen, X.; Shao, Z. Z.; Zhou, P.; Porter, D.; Knight, D. P.; Vollrath, F. Toughness of spider silk at high and low temperatures. *Adv. Mater.* **2005**, 17 (1), 84-88.

[4] Blackledge, T. A.; Swindeman, J. E.; Hayashi, C. Y. Quasistatic and continuous dynamic characterization of the mechanical properties of silk from the cobweb of the black widow spider Latrodectus hesperus. *J. Exp. Biol.* **2005**, 208 (10), 1937-1949.

[5] Blackledge, T. A.; Boutry, C.; Wong, S.-C.; Baji, A.; Dhinojwala, A.; Sahni, V.; Agnarsson, I. How super is supercontraction? Persistent versus cyclic responses to humidity in spider dragline silk. *J. Exp. Biol.* **2009**, 212 (13), 1981-1989.

[6] Guan, J.; Porter, D.; Vollrath, F. Silks cope with stress by tuning their mechanical properties under load. *Polymer* **2012**, 53 (13), 2717-2726.

[7] Hu, X.; Kaplan, D.; Cebe, P. b-sheet crystallinity in fibrous proteins by thermal analysis and infrared spectroscopy. *Macromolecules* **2006**, 39, 6161-6170.

[8] Hu, X.; Kaplan, D.; Cebe, P. Effect of water on the thermal properties of silk fibroin. *Thermochim. Acta.* **2007**, 461 (1-2), 137-144.

[9] Hu, X.; Kaplan, D.; Cebe, P. Dynamic protein-water relationships during beta-sheet formation. *Macromolecules* **2008**, 41 (11), 3939-3948.

[10] Motta, A.; Fambri, L.; Migliaresi, C. Regenerated silk fibroin films: thermal and dynamic mechanical analysis. *Macromol Chem Physic* **2002**, 203 (10/11), 1658-1665.

[11] Porter, D.; Vollrath, F. The role of kinetics of water and amide bonding in protein stability. *Soft Matter* **2008**, 4 (2), 328-336.

[12] Porter, D.; Vollrath, F. Water mobility, denaturation and the glass transition in proteins. *Biochimica Et Biophysica Acta-Proteins and Proteomics* **2012**, 1824 (6), 785-791.

[13] Doster, W. The dynamical transition of proteins, concepts and misconceptions. *European biophysics journal* **2008**, 37 (5), 591-602.

[14] Seydel, T.; Knoll, W.; Greving, I.; Dicko, C.; Koza, M. M.; Krasnov, I.; Muller, M. Increased molecular mobility in humid silk fibers under tensile stress. *Phys. Rev. E* **2011**, 83 (1).

[15] Plaza, G. R.; Guinea, G. V.; Perez-Rigueiro, J.; Elices, M. Thermo-hygro-mechanical behavior of spider dragline silk: Glassy and rubbery states. *J. Polym. Sci. Pol. Phys.* **2006**, 44 (6), 994-999.

[16] Fu, C. J.; Porter, D.; Shao, Z. Z. Moisture effects on Antheraea pernyi silk's mechanical property. *Macromolecules* **2009**, 42 (20), 7877-7880.

[17] Guan, J.; Vollrath, F.; Porter, D. Two mechanisms for supercontraction in Nephila spider dragline silk. *Biomacromolecules* **2011**, 12 (11), 4030-4035.

[18] Tian, K.; Porter, D.; Yao, J.; Shao, Z.; Chen, X. Kinetics of thermally-induced conformational transitions in soybean protein films. *Polymer* **2010**, 51 (11), 2410-2416.

[19] Porter, D.; Vollrath, F.; Tian, K.; Chen, X.; Shao, Z. Z. A kinetic model for thermal degradation in polymers with specific application to proteins. *Polymer* **2009**, 50 (7), 1814-1818.

[20] Magoshi, J.; Magoshi, Y.; Nakamura, S. Crystallization, liquid-crystal, and fiber formation of silk fibroin. *Appl. Pol. Symp.* **1985**, (41), 187-204.

[21] Nakamura, S.; Magoshi, J.; Magoshi, Y. Thermal properties of silk proteins in silkworms. *Silk Polymers* **1994**, 544, 211-221.

[22] Hu, X.; Lu, Q.; Kaplan, D. L.; Cebe, P. Microphase separation controlled beta-Sheet crystallization kinetics in fibrous proteins. *Macromolecules* **2009**, 42 (6), 2079-2087.

[23] Yuan, Q. Q.; Yao, J. R.; Huang, L.; Chen, X.; Shao, Z. Z. Correlation between structural and dynamic mechanical transitions of regenerated silk fibroin. *Polymer* **2010**, 51 (26), 6278-6283.

[24] Porter, D.; Vollrath, F.; Shao, Z. Predicting the mechanical properties of spider silk as a model nanostructured polymer. *The European Physical Journal E* **2005**, 16 (2), 199-206.

[25] Vollrath, F.; Porter, D. Spider silk as a model biomaterial. *Appl. Phys. A-Mater.* **2006**, 82 (2), 205-212.

[26] Shao, Z. Z.; Vollrath, F. Surprising strength of silkworm silk. *Nature* **2002**, 418 (6899), 741-741.

[27] Feldman, A.; Wachtel, E.; Vaughan, G.; Weinberg, A.; Marom, G. The brill transition in transcrystalline nylon-66. *Macromolecules* **2006**, 39 (13), 4455-4459.

[28] Atkins, E.; Hill, M.; Hong, S.; Keller, A.; Organ, S. Lamellar structure and morphology of nylon 46 crystals: a new chain folding mechanism for nylons. Macromolecules 1992, 25 (2), 917-924.

[29] Porter, D.; Gould, P. J. Predictive nonlinear constitutive relations in polymers through loss history. *International Journal of Solids and Structures* **2009**, 46 (9), 1981-1993.

[30] Cunniff, P. M.; Fossey, S. A.; Auerbach, M. A.; Song, J. W.; Kaplan, D. L.; Adams, W. W.; Eby, R. K.; Mahoney, D.; Vezie, D. L. Mechanical and thermal properties of dragline silk from the spider Nephila clavipes. *Polym. Adv. Technol.* **1994**, 5 (8), 401-410.

[31] Guan, J.; Porter, D.; Vollrath, F. Thermally induced changes in dynamic mechanical properties of native silks. *Biomacromolecules* **2013**, 14 (3), 930-937.

[32] Fu, C.; Porter, D.; Chen, X.; Vollrath, F.; Shao, Z. Understanding the Mechanical Properties of Antheraea Pernyi Silk—From Primary Structure to Condensed Structure of the Protein. *Adv. Funct. Mater.* **2011**, 21 (4), 729-737.

[33] Liu, Y.; Sponner, A.; Porter, D.; Vollrath, F. Proline and processing of spider silks. *Biomacromolecules* **2008**, 9 (1), 116-121.

Chapter 5. Humidity effect on mechanical properties of *B. mori* silkworm silks

5.1 Introduction

It is well known that solvents or plasticizers have an effect on the thermal, dielectric and mechanical properties of synthetic polymers [1-4]. For "hydrophilic" polymers, the effect of water can be so dramatic that the mechanical properties of these polymers deteriorate after exposure to water or humidity even at ambient temperatures [5-7]. It has been suggested that the solvent effect is linked to the glass transition of polymers [1, 6, 8]. With increasing solvent content, the glass transition temperature (T_g) of the polymer/solvent system decreases, and the modulus decreases once the effective glass transition conditions are reached. For example, when the humidity increases from 0% to 92%, the T_g of nylon-6 drops from 95 °C to room temperature [7]. Similarly, silk properties can be affected substantially by its hydration state, especially the mechanical properties [8-10]. This effect has been studied in detail on the quasi-static tensile properties of silks from some silk-spinning species (*Bombyx mori* silkworm, *Antheraea pernyi* silkworm and *Argiope* spider) at various temperatures [8, 11, 12].

T_g is the most important property index that links thermal properties with the macroscopic mechanical properties for polymers. Polymer and solvent are usually taken as two independent components of the system and, because solvent usually has significantly lower T_g, the T_g of polymer/solvent system will decrease. This approach works well for many simple polymer/solvent systems and the Fox-Flory model (Equation 5.1) and Group Interaction Modelling [1] are two relatively simple approaches to quantitatively understand the effect of solvent or humidity on properties of polymers.

$$\frac{1}{T_g} = \frac{W_1}{T_{g1}} + \frac{W_2}{T_{g2}} \tag{5.1}$$

For silks in the experimentally accessible range of humidity and temperatures, T_g has an approximately linear relationship with humidity, H (%), as described for *A. pernyi* silks in Equation (5.2) [12]. Here, the (external) humidity (H) is converted to the internal water fraction in the disordered fraction (the crystalline or ordered fraction does not absorb water) for use in Equation (5.1) using a linear relationship [9]. The experimental T_g of 470 K (197 °C) is used for dry *A. pernyi* silks and a consensus T_g of 140 K for water. A temperature-humidity gradient in the equation was defined for "generic" silks using parameters from the most-studied *B. mori* silk which have a "dry" T_g at 491 K and "wet" T_g at 250 K [12].

$$T_g(°\mathrm{C}) = 197 - 2.4H(\%) \tag{5.2}$$

There are various terms used in the literature regarding the effect of water, such as moisture, humidity and hydration. For clarification here, moisture and humidity usually mean the water in the air or the environment (in either condensed droplets or vaporized form), which may or may not diffuse into the materials of interest; hydration describes the state where water permeates into materials and interacts with the host materials. As mentioned earlier, a linear relationship is often assumed between the environmental humidity and the internal water fraction, which is however not always true. Relative humidity is the ratio of the partial pressure of water vapour in an air-water mixture to the saturated vapour pressure of water at a prescribed temperature. Q800 humidity accessory uses relative humidity (rH) as its control parameter and I often use the term "humidity" as an abbreviation of relative humidity in the following text.

Figure 5.1 (a) shows the operating window of humidity against temperature (the green shade) as specified for the TA Instrument humidity accessory, and the right axis shows the corresponding water fraction in disordered silk to the left axis of external humidity using reference [9]. The maximum achievable humidity at 100 °C is about 70% and the converted water fraction in disordered silk is approximately 22%. Figure 5.1 (b) shows the T_g-humidity relations from the Fox-Flory model and GIM [12], and the practical operating zone of humidity confined by the temperature range of 5-65 °C.

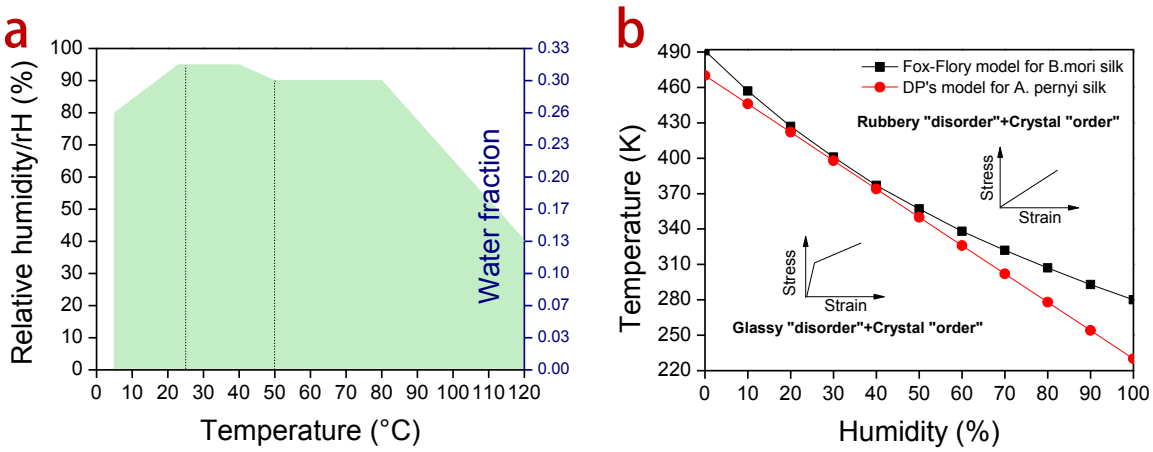

Figure 5.1 Relative humidity-temperature regime (in light green) as specified for the TA Q800 humidity accessory (a); the Fox-Flory and GIM model curves [12] (b).

In this chapter, I mainly examine the effect of humidity on both tensile properties and dynamic mechanical properties of *B. mori* silkworm silks (both raw and degummed). The tensile properties of hydrated silks are studied for the sake of comparison with literature, as well as for establishing a methodology based on our lab instrument (TA Q800 and the humidity accessory). As an interesting biological fibre, human hair was also tested for studying the same effect. The novelty of this chapter is the study of the effect of humidity on the dynamic mechanical properties of silks through the temperature-humidity scans.

In the case of spider dragline silks, the water-silk interplay is more dramatic and water is believed to play a role of more than a 'plasticizer'. Some spider draglines interact with water and become structurally, morphologically and mechanically different in a phenomenon called supercontraction [13, 14]. One key difference between *B. mori* silks and some spider silks is that supercontraction is shown to correlate to the concentrated proline fraction in spider silks [14, 15], and the effect of water on supercontractable spider silks will be explored in detail in the next chapter.

5.2 Experimental section

5.2.1 Materials

Raw and degummed *B. mori* silks: only the raw and degummed *B. mori* silkworm silks from Grade 1 cocoon, Jiangsu Province (BM-JS1) were used for tests in this chapter. As described earlier in Chapter 3, raw silks were carefully pulled from the cocoon to minimise breaking the sericin coating. Consistent with the previous sample preparations, both raw and degummed single fibres were mounted on paper frames with 5 mm gauge length, and stored in an air-tight chamber for further testing.

Human hair: the author JG's hair was used as an example of keratin fibre in comparison with silks. As described earlier in Chapter 3, her hair is Asian type with black/dark brown colour and is fairly circular in cross-sections.

It is worth mentioning that the type of glue used for fixing the fibres onto the sample holders using Loctite superglue is supposed to resist humidity and hence it is not a concern that the fibres may loosen or slip from the clamps under high humidity. One concern regarding the sample fixing methods is that sample holders are made of paper cardboard of cellulose fibres and they may absorb or release moisture when high humidity or high temperature is reached. However, since 3 psi clamping pressure was

applied between clamps and sample holders, the "water absorption" of the sample holders should be prevented. Therefore the effect of sample holders interacting with water on silk samples could be marginal.

5.2.2 Humidity tensile testing

All the tensile testing was conducted on TA Q800 with the humidity accessory. The normal furnace, which operates at temperatures up to 600 °C, was replaced by a humidity enclosure with a humidity sensor and surrounding insulation materials around the chamber. Instead of supplying dry nitrogen, dry or humid air at a prescribed temperature would be supplied in the sample chamber, as written in the user handbook. Humidity can change at a fixed rate of 2%/min and temperatures range from 5 °C to 120 °C with a maximum ramp rate of 1 °C/min.

In the humidity tensile test, silks were loaded first; and after both the temperature and the humidity had reached the target, 30 minutes of soaking time was applied before the silks were tested at a force ramp rate of 0.1 N/min until failure. 50 °C was set up as the temperature for humidity tensile tests for both raw and degummed *B. mori* silks as will be explained in the results section.

Due to the larger cross-sectional area, hair was tested at a higher force-ramp rate of 2 N/min in order to achieve a similar strain rate to that of silks (detailed explanations can be found in Chapter 3). In the hair humidity tensile tests, one hair was cycled with a small deformation strain of 0.5% each time at different humidity levels from 0% to 90% at 10% intervals. Again, the testing temperature was chosen to be 50 °C.

5.2.3 Dynamic mechanical testing with humidity control

In a normal dynamic mechanical test, temperature or time is the main variable and dynamic mechanical properties are plotted as a function of changing temperature or time. Here with the humidity accessory a new control variable, humidity, is added. It allows two new types of tests: temperature scan with varied humidity or humidity scan with varied temperature. I used only the degummed *B. mori* silks in this section of the experiment to avoid the confounding effect of the sericin interacting with humidity.

The set-up parameters for the two types of humidity dynamic tests are as follows: (1) temperature scan with varied humidity: temperature ramps from room temperature to around 110 °C at 1 °C/min after 30 minutes of equilibrium at four relative humidities of 35%, 40%, 45% and 50% (however, the actual sample humidity is actively monitored during the test, which will be shown in the results); (2) humidity scan with varied temperature: humidity ramps from 0% to about 90% at three given temperatures (20 °C, 50 °C and 80 °C) at 2%/min after 30 minutes of equilibrium after the target temperature was reached; additionally, humidity ramps were conducted from 0% to about 90% at 50 °C for silks under various static loadings (50 MPa, 100 MPa and 200 MPa).

5.2.4 Analyzing the mechanical properties

For all the tensile tests, engineering stress was calculated from the raw signal "force" using the following average areas (the detailed measurements on the three subject fibres, raw *B. mori* silks, degummed *B. mori* silks and human hair can be found in Chapter 3): 400 μm^2 for raw silks; 124 μm^2 for degummed silks; and 5200 μm^2 for human hair. For the dynamic mechanical tests, the same average areas were used for static stress and dynamic modulus calculations. It should be noted that although the

fibres would probably swell when exposed to high humidity the humidity induced changes in the cross-sectional area are not considered here in the results and analysis due to the difficulty in quantification.

5.3 Results and discussion

5.3.1 The effect of humidity on tensile properties of silks and human hair

For humidity-tensile testing and humidity-dynamic mechanical testing, choosing an optimal temperature for observing the maximum effect of humidity is important. As discussed in Chapter 4, 65 °C is the protein denaturation temperature or the onset temperature of changes of amide-water bonding [16, 17]. TA Q800 humidity accessory operates at temperatures from 5 °C to 120 °C (as shown in Figure 5.1(a)). However, to study silks in their native states, we have a limited operating temperature window between 5 °C and 65 °C. Also from the introduction and previous observations, it is known that at higher temperatures lower critical humidity values will be needed for the glass transition and the transition width could probably span a 30% humidity range. 50 °C is 25 °C apart from room temperature but also well below the denaturation temperature, so it was initially suggested as a control temperature for most tests in this chapter.

Figure 5.2 shows the low-strain tensile behaviours of a human hair from 0% to 80% humidity at 25 °C and 50 °C, and the inset shows the full range tensile profile of human hair at each temperature. In the full tensile profile in the insets, hair yields at above 100 MPa (50 °C gives lower-stress yield than 25 °C). However, the yield point varies across samples, which might also be due to the variations in the cross-sectional areas of hair samples. The hair tensile modulus decreases gradually as the humidity increases. Also comparing the two temperatures, higher temperature gives lower modulus at the same

humidity. From the hair humidity tests, it is expected that similar changes of decreasing initial tensile modulus will happen to silks.

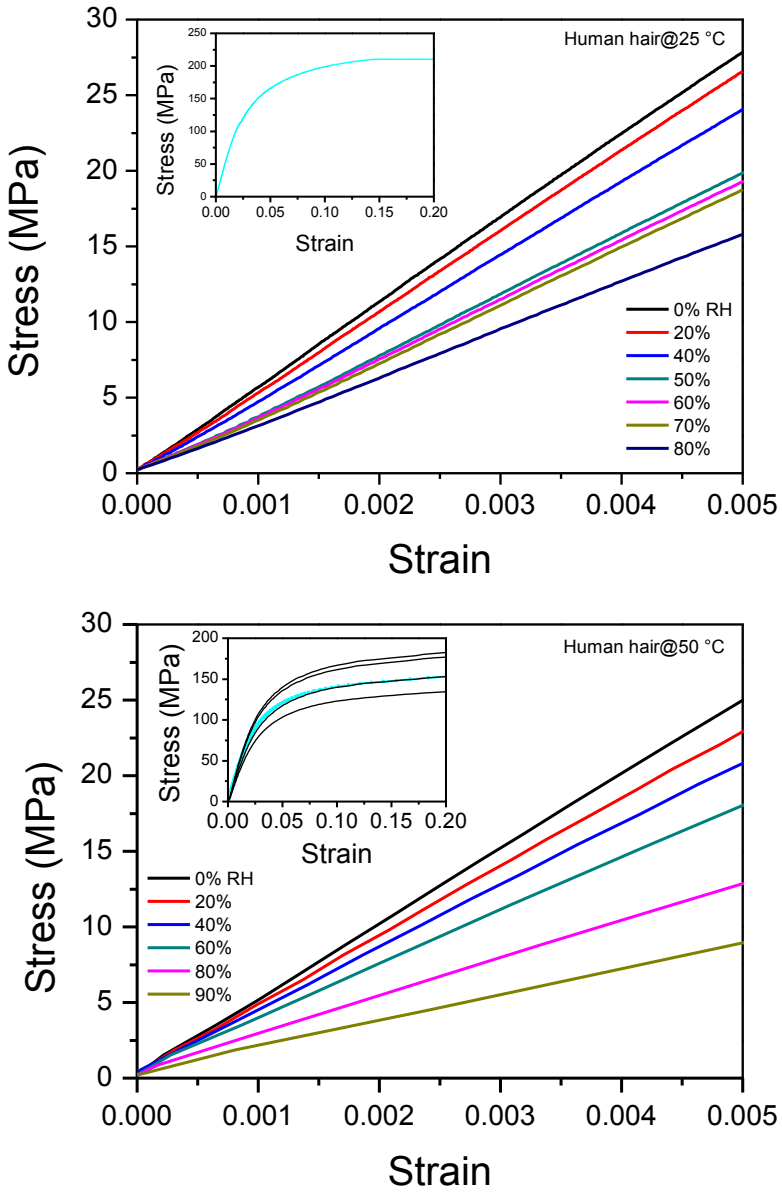

Figure 5.2 Initial stages (at strain below 0.005) of stress-strain behaviour of human hair with changing humidity from 0% to 90% at 25 °C and 50 ^{o}C. Inset shows the full stress-strain of hair at the corresponding temperature.

Figure 5.3 shows the tensile results of both raw and degummed *B. mori* silks at 50 °C at various humidities from 0% to 90%. For raw *B. mori* silks, there seems to be a gap in the tensile behaviour between humidity 50% and 60%, below which humidity the initial moduli changed in a stepwise manner. A similar post-yield modulus of about 470 MPa

at strain above 0.1 is seen across different humidity curves. At the highest humidity 90%, raw silks only show small change in the modulus (from 880 MPa at strain below 0.01 to 460 MPa at strain above 0.35), which suggests the amorphous/disordered structure of silk is yielded from the start under the combination of humidity (90%) and temperature (50 °C). The initial tensile modulus will be discussed in the next section. Figure 5.3 (b) plots the strain and stress at break with humidity. It shows a slight trend of increase in the breaking strain and decrease in the breaking stress, although the data at 20% and 30% humidity are exceptional from the general trend for unknown reasons.

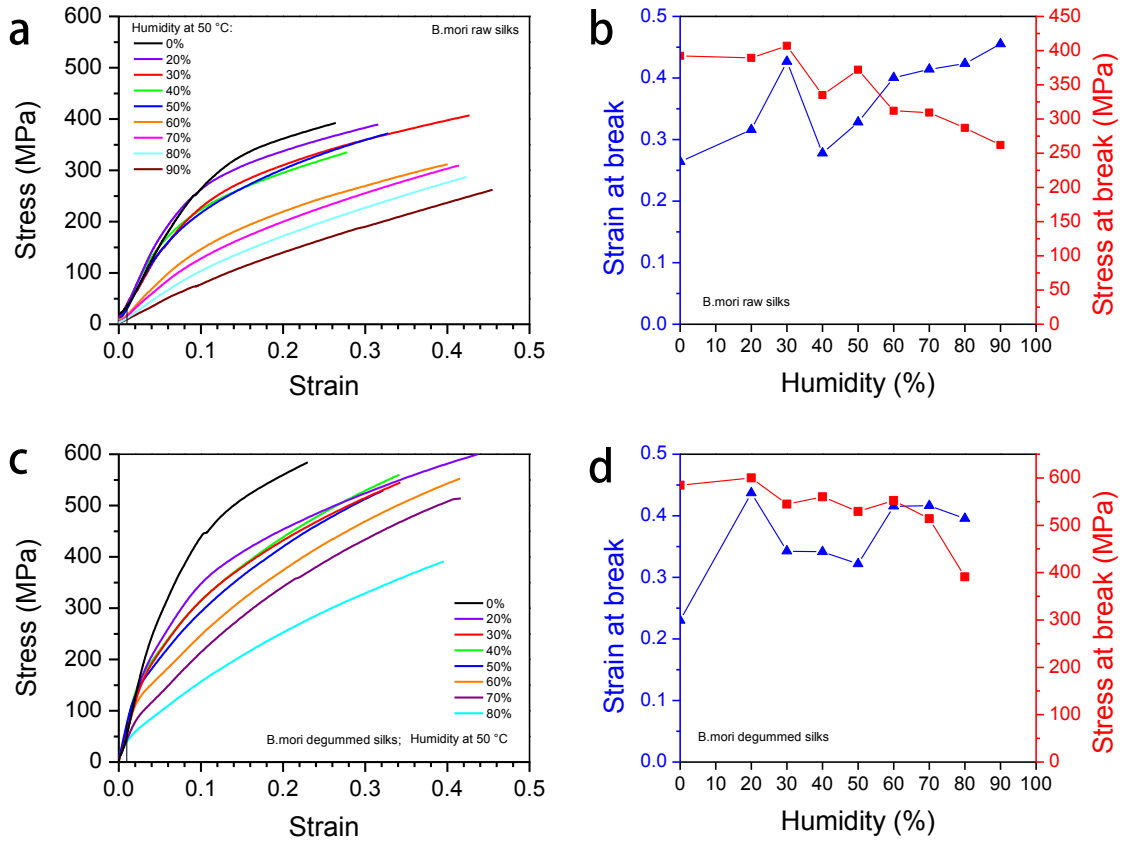

Figure 5.3 Stress-strain curves of *B. mori* silk fibres at different relative humidity at 50 ^{o}C: raw (a) and degummed (c); and the results of strain and stress at break from the left: raw (b) and degummed (d).

For degummed *B. mori* silks in Figure 5.3(c) and (d), the humidity effect on tensile behaviour is similar to that on raw silks. The stress-strain behaviour shows the following changes as the humidity increases: at 0% silks have low breaking strain and

high breaking stress; and between 20% and 50% silks have increased breaking strain and seem to maintain high breaking stress; and above 60%, the breaking strain increases further but the breaking stress starts decreasing. Again, the data at 20% humidity does not fit to the trend.

5.3.2 Quasi-static tensile modulus with changing humidity

Figure 5.4 plots the quasi-static tensile modulus of silks and hair with changing humidity at 50 °C from the stress-strain curves shown in Figure 5.3. For the error range of the raw *B. mori* silk's modulus, please refer to Table 2.1 in page 53. However, the errors for other data are not determined. The initial tensile modulus of hair changes from 5 GPa at 0%RH to less than 2 GPa at 90%RH. The gradual change of hair modulus with humidity could be due to the gradual water permeation into the hair fibre through the hard/dense cuticle. In contrast, both raw and degummed silks show more transition-type of change in tensile modulus as the humidity increases. Note here the "bump" in the curve for degummed silk may be caused by the larger variation of the modulus results under humidity. The transitional humidity lies between 50% and 70% as indicated by the green shaded area for both raw and degummed silkworm silks, which overlaps with the glass transition zone of *A. pernyi* silks [12]. It suggests the changes are induced by the glass transition of disordered silk.

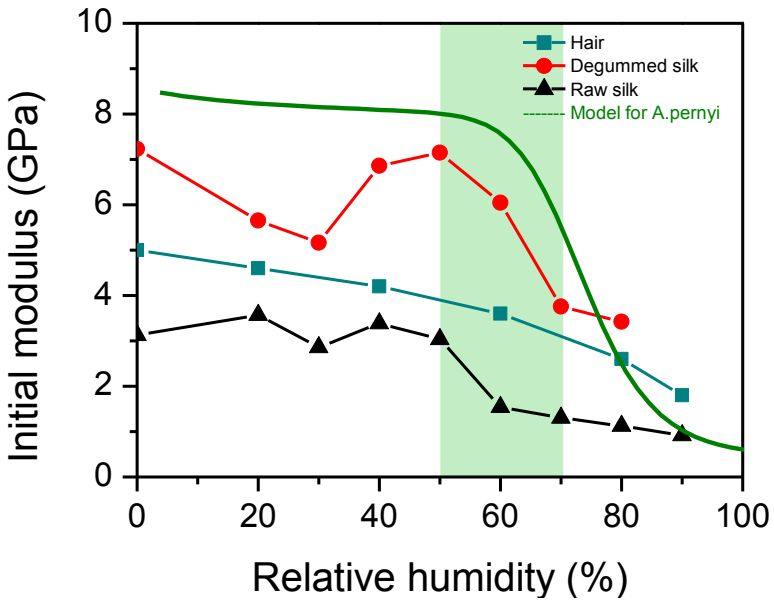

Figure 5.4 Initial modulus against relatively humidity at 50 ^{o}C for different fibres: hair, degummed silk and raw silk. A model curve for *A. pernyi* is shown in olive green [12]. Shaded area is the suggested transition zone.

From the tensile moduli at low and high humidity, it is possible to calculate the amorphous/disordered fraction in silk or the degree of order in silk structure using Group Interaction Modelling which will be discussed again in the next chapter. Taking moduli of 6.5 GPa and 3.5 GPa at 0% humidity and 80% humidity respectively at 50 °C for degummed silkworm silks, and assuming that the disordered silk is yielded at 80% humidity, the disordered fraction would be 0.34 in silkworm fibroin (the degree of order is therefore 0.66), which agrees well with the previous work [18].

5.3.3 The effect of humidity on dynamic mechanical properties of silks

Humidity scans at different temperatures

This section of dynamic mechanical testing starts with the humidity scan at three control temperatures, 20 °C, 50 °C and 80 °C, as shown in Figure 5.5. At the lowest temperature of 20 °C, the storage modulus of *B. mori* silk did not decrease with increasing humidity, but perhaps increased slightly due to the stretching of the silk

indicated by the length data (not shown), and the loss tangent was well above the conventional baseline of 0.01, suggesting high molecular mobility. At 50 °C, the storage modulus started decreasing faster at a critical humidity of 58%, where the loss tangent also started to form a broad peak. However, the peak could not complete before the test ended at humidity 80%. Finally, at 80 °C a fuller transition starting from a critical humidity of 48% with a relatively complete loss tangent peak is observed. The changes of decreasing storage modulus accompanied by a loss tangent peak suggest a glass transition mechanism, and the peak height of 0.11 suggests it is the disordered silk structure observed at 210 °C in the normal temperature scan of *B. mori* silks in the previous chapter. Note that this is the first time that the loss tangent peak height is referenced to compare the silk structure. The reason behind is a glass transition peak should ideally be a Gaussion peak with a temperature span of about 20-30 °C and the peak height is approximately proportionate to the peak area. In this thesis, I use both the peak height ($tan\delta$ at T_g) and peak area ($tan\Delta$) for comparing the degree of disorder in silks. It is also interesting to note that the storage modulus at 20 °C is the lowest among the three temperatures. It could be explained that the silks at 50 °C or 80 °C have undergone dehydration and have a "dry" modulus that is higher, as shown in Chapter 4.

To summarize this section, at low temperatures (e.g. 20 °C) the glass transition does not take place in *B. mori* silks until a high humidity of 85%; then at 50 °C when humidity increases to above 58%, both the reduction in storage modulus and the loss tangent peak suggest the glass transition of silk; finally at 80 °C, a complete glass transition process of disordered silk is captured.

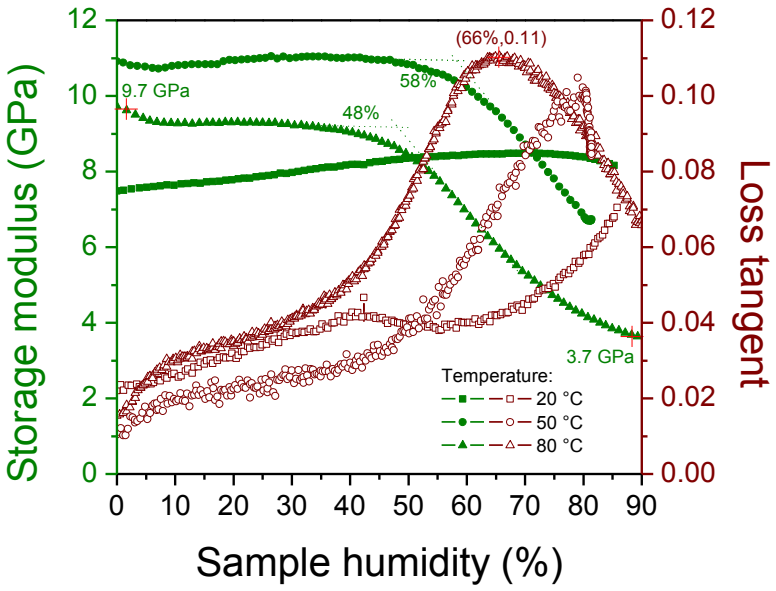

Figure 5.5 Dynamic mechanical properties of degummed *B. mori* silks, storage modulus and loss tangent, as a function of humidity at three temperatures: 20 °C, 50 °C, and 80 °C.

Loading-humidity scans at 50 °C

In addition to the normal humidity scans, loading-humidity tests were conducted to show whether loading makes any difference in the dynamic mechanical properties of silks in a humid and hot environment. Because silks soften considerably at high humidity as seen in the humidity-tensile tests and high stress especially above the yielding stress may over stretch the fibre, only three static loadings on *B. mori* silks were tested and Figure 5.6 shows the results.

Static stresses of 100 MPa and 200 MPa result in higher storage modulus regardless of the humidity. The environmental humidity does not seem to affect the values of dynamic storage modulus at the two stress levels compared with the data in Chapter 3. In agreement with the previous section, the glass transition only starts when the humidity reaches 50%. Moreover, the critical humidity (the onset humidity for the storage modulus reduction) does not appear to be affected by higher static loadings.

The loss tangent profiles for the three static loadings appear very similar through the humidity range. Loss tangent has a higher baseline as the humidity increases to be above 10% compared with that of 0.1 in the normal temperature scan in a dry environment, which suggests as more water molecules gradually permeates to silk and become mobile plasticizers they contribute to the high loss tangent. Whether water would partially become hydrogen bonded to silk is not evident here for the effect from temperature, humidity and loading is very complex, which needs further study. This agrees with previous observations on humid silks under tensile stress using neutron-scattering [19]: water does participate in the diffusive motion of humid silks. However, our study does not suggest the water mobility or diffusibility is affected by static stress at humidities below 80%. Additionally, the loss tangent at higher static stress (200 MPa) might show a slightly broader but lower peak-height peak compared with that of the glass transition observed in a normal temperature scan.

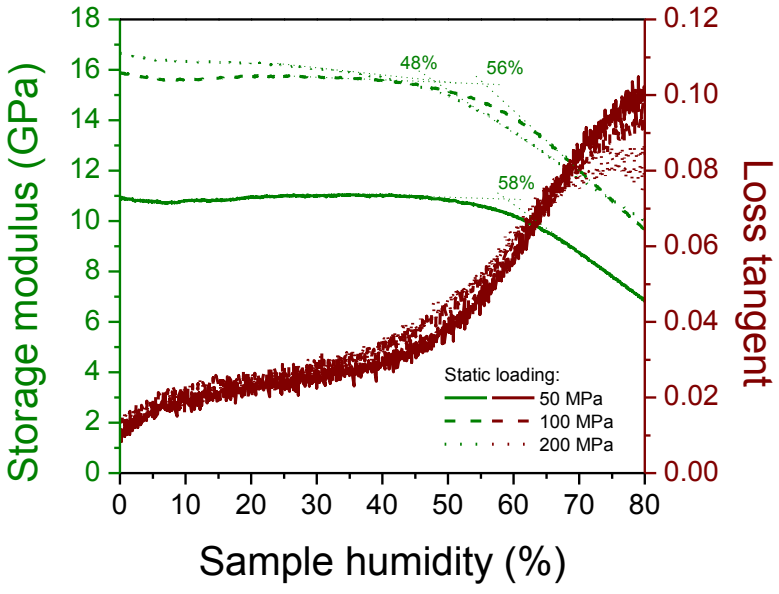

Figure 5.6 Dynamic mechanical properties, storage modulus and loss tangent, as a function of humidity for degummed *B. mori* silks at different static stresses at 50 °C.

Temperature scans at different humidities

This section of experiments sets a constant humidity and ramps temperature from room temperature to 115 °C at a rate of 1 °C/min. Figure 5.7 shows the results of one scan at humidity 54%. Following the example of discussions in Chapter 4, here three phases are also separated for the convenience of discussions according to the different changes in the properties in the top graph: (1) from 25 °C to 65 °C, the storage modulus decreases and the loss tangent increases; (2) from 65 °C to 90 °C, the storage modulus increases and the loss tangent decreases; and (3) from 90 °C to 115°C, the storage modulus decreases and the loss tangent increases again. In the lower graph, the sample sensor humidity and the static strain are shown. The static strain increases in phase (1), stabilizes in phase (2) and increases again in phase (3).

From all previous observations, it is logical to attribute the changes in phase (1) to the glass transition of disordered silk, although the modulus drop is not as much and the loss tangent plateaus at <0.1 due probably to insufficient humidity. Phase (2) shows an increase of the storage modulus with increasing temperature, a feature that can be explained by "dehydration" through the temperature scan as discussed in Chapter 4. More interestingly, phase (3) with the decrease in modulus and increase in loss seems to show a new transition.

It is worth mentioning that we expected a transition of the helical structure of silks under the combination of high temperature and high humidity. Nakamura suggested the structural transition from α-form to β-form in silk happened at 270 °C [20]. So if the helical transition did happen, the conditions would be between the glass transition of the disordered structure of silks and the melting of β-sheet crystals. Nevertheless, due to unknown control problems of the humidity accessory, the sample humidity experienced

a dramatic drop from 54% to 28% at 75-90 °C and a sharp return to the original humidity at 90-100 °C, where coincidentally we see dramatic property changes in phase (2) and phase (3). Because the humidity change alone could sufficiently explain the modulus change in these two phases: modulus increases if humidity drops, and vice versa, our hypothesis on helical-structure transition cannot be confirmed before new experiments with reliable humidity control are done.

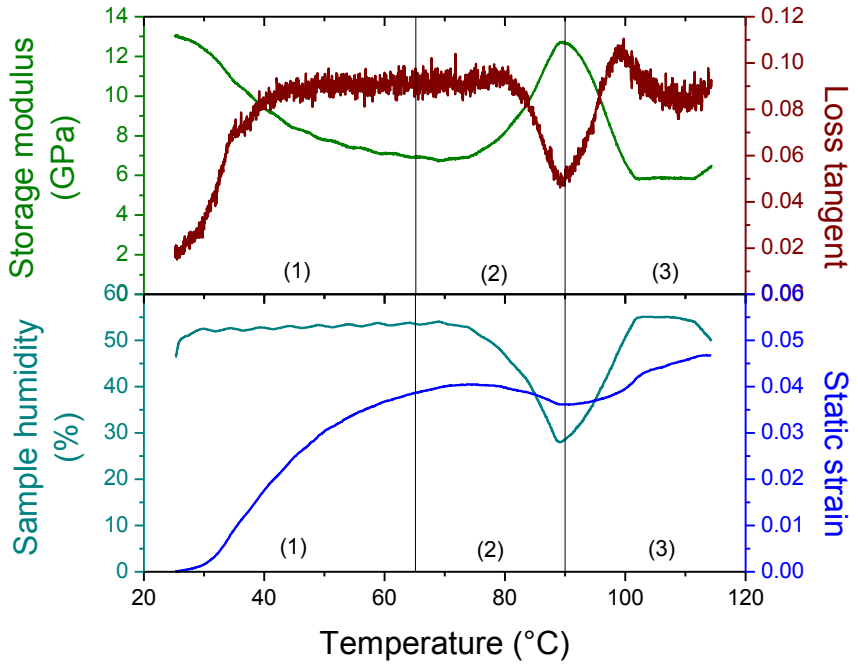

Figure 5.7 Dynamic mechanical properties of storage modulus, loss tangent and static strain of degummed *B. mori* silk fibres in a dynamic temperature scan from 25 °C to 115 °C at controlled relative humidity 52%.

The same experiment was repeated with different humidity settings. Figure 5.8 shows the results of these dynamic mechanical temperature scans at four humidities: 42%, 47%, 52% and 59%. As the humidity level increases, the gradient of loss tangent rising increases. Following the assumption of the absorbed water being mobile plasticizers, it is reasonable that the higher atmospheric water pressure, the faster water

can permeates to silk and more water would be absorbed at the equilibrium. Since the same control problem was observed for all the tests, only the property changes in phase (1) are briefly discussed here. It was found that higher humidity resulted in faster reduction in the storage modulus and a higher peak/plateau in the loss tangent.

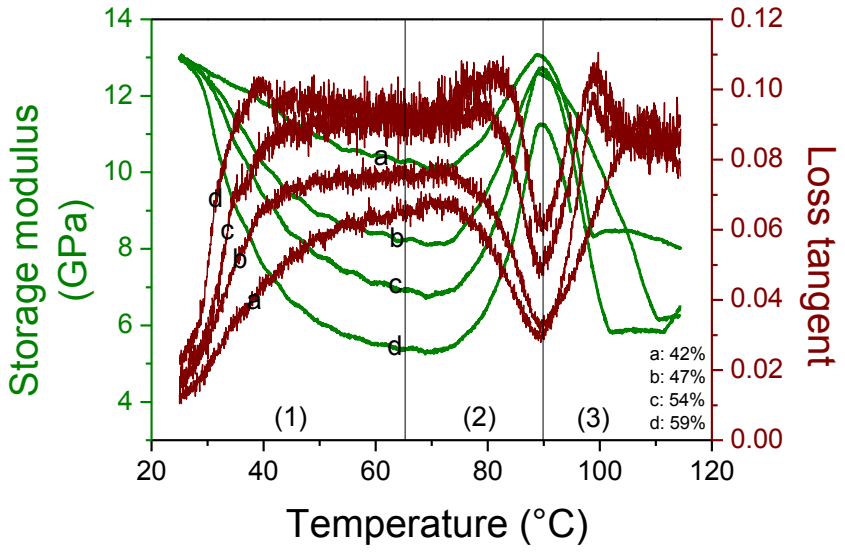

Figure 5.8 Comparing the dynamic mechanical properties at four humidities: 42% , 47%, 52% and 59%. For comparison reasons, the measured storage moduli of the four test at the starting temperature of 25 °C are scaled up to the same value of 13 GPa. Only relative changes are considered.

Despite the loss of instrumental control in the humidity at temperatures above 70 °C, the results of temperature scans in this section provide a good reference for the dynamic mechanical properties of *B. mori* silks under the conditions of certain humidity (between 40% to 60%) at each specific temperature point from room temperature up to 70 °C. As shown in Figure 5.9 storage modulus and quasi-static tensile modulus are shown as a function of both humidity and temperature. The modulus reduction is clearly shown by the data taken from the dynamic test which suggest a glass transition mechanism especially at temperature 60 °C.

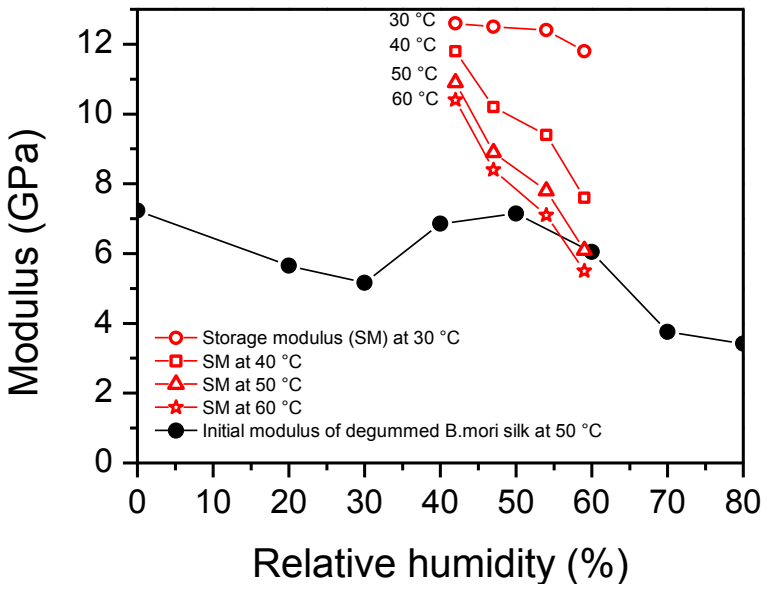

Figure 5.9 Modulus of degummed *B. mori* silks as a function of humidity and temperature: storage modulus (red symbols) from dynamic mechanical humidity test (Figure 5.8) and tensile modulus (black symbols) from quasi-static tensile tests (Figure 5.3).

5.4 Conclusions

Hydration water has an important effect on the mechanical properties and structures of silks as already discussed in Chapter 4. In this chapter, the effect of high humidity at room temperature and 50 °C was studied on both the quasi-static tensile properties of *B. mori* silks as well as the dynamic mechanical properties of *B. mori* silks. Human hair was also studied for reference as an interesting natural fibre as was used in Chapter 3.

Quasi-static tensile tests on raw, degummed *B. mori* silks and human hair were conducted only at 50 °C as a good compromise between glass transition conditions and the denaturation temperature. The initial modulus of both raw and degummed silkworm silks experience a transition-type of drop as the humidity increases to above 50%. The combined effect of humidity and temperature agrees well with previous observations on the **moisture-induced glass transition** of *A. pernyi* silks [12] and the Fox-Flory model as shown in Figure 5.1.

Three types of humidity dynamic mechanical tests were conducted on degummed *B. mori* silks to examine the effects of temperature, loading, and humidity on dynamic mechanical properties of *B. mori* silks. It is shown that higher constant temperature reduces the onset humidity for the glass transition of disordered silk and higher constant humidity reduces the glass transition temperature; and higher loading increases the structural order of silks despite the presence of highly mobile water.

However, due to an instrument humidity control problem the property changes at high humidity and temperature (90 °C) in the temperature scans with varied humidity cannot be confirmed. In order to better understand the changes and mechanisms, repeated experiments need to be done. More importantly, the reason that we did not observe more interesting transitions in *B. mori* silks is that *B. mori* silks do not contain much "meta" structures (e.g. helical structure or β–turn structure), but a high degree of β-sheet crystal. In the next chapter, spider dragline silks will be studied and extra effects or changes will be observed due to structural complexity.

5.5 References

[1] Porter, D., *Group Interaction Modelling of Polymer Properties*. Marcel Dekker: New York, **1995**.

[2] Rubin, J.; Andrews, R. D. Effect of solvent treatments on the mechanical properties of nylon 6. *Polymer Engineering & Science* **1968,** 8 (4), 302-309.

[3] Hata, N.; Tobolsky, A. V.; Bondi, A. Effect of plasticizers on the viscoelastic properties of poly(vinyl chloride). *J. Appl. Polym. Sci.* **1968,** 12 (12), 2597-2613.

[4] Laredo, E.; Hernandez, M. C. Moisture effect on the low- and high-temperature dielectric relaxations in nylon-6. *J. Polym Sci B: Polym. Phys.* **1997,** 35 (17), 2879-2888.

[5] Chapman, B. M. A review of the mechanical properties of keratin fibres. *J. Text. Inst.* **1969,** 60 (5), 181-207.

[6] Ellis, T. S.; Karasz, F. E. Interaction of epoxy resins with water: the depression of glass transition temperature. *Polymer* **1984,** 25 (5), 664-669.

[7] Miri, V.; Persyn, O.; Lefebvre, J. M.; Seguela, R. Effect of water absorption on the plastic deformation behavior of nylon 6. *Eur. Pol. J.* **2009,** 45 (3), 757-762.

[8] Plaza, G. R.; Guinea, G. V.; Perez-Rigueiro, J.; Elices, M. Thermo-hygro-mechanical behavior of spider dragline silk: Glassy and rubbery states. *J. Polym. Sci. Pol. Phys.* **2006,** 44 (6), 994-999.

[9] Agarwal, N.; Hoagland, D. A.; Farris, R. J. Effect of Moisture Absorption on the Thermal Properties of Bombyx mori Silk Fibroin Films. *J. Appl. Polym. Sci.* **1997,** 63, 401-410.

[10] Agnarsson, I.; Dhinojwala, A.; Sahni, V.; Blackledge, T. A. Spider silk as a novel high performance biomimetic muscle driven by humidity. *J. Exp. Biol.* **2009,** 212 (13), 1989-1993.

[11] Plaza, G. R.; Corsini, P.; Perez-Rigueiro, J.; Marsano, E.; Guinea, G. V.; Elices, M. Effect of water on Bombyx mori regenerated silk fibers and its application in modifying their mechanical properties. *J. Appl. Polym. Sci.* **2008,** 109 (3), 1793-1801.

[12] Fu, C. J.; Porter, D.; Shao, Z. Z. Moisture Effects on Antheraea pernyi Silk's Mechanical Property. *Macromolecules* **2009,** 42 (20), 7877-7880.

[13] Work, R. W. A comparative study of the supercontraction of major ampullate silk fibres of orb web building spiders (Araneae). *J. Arachnol.* **1981,** 9, 299-308.

[14] Liu, Y.; Shao, Z. Z.; Vollrath, F. Relationships between supercontraction and mechanical properties of spider silk. *Nat. Mater.* **2005,** 4 (12), 901-905.

[15] Liu, Y.; Sponner, A.; Porter, D.; Vollrath, F. Proline and processing of spider silks. *Biomacromolecules* **2008,** 9 (1), 116-121.

[16] Porter, D.; Vollrath, F. The role of kinetics of water and amide bonding in protein stability. *Soft Matter* **2008,** 4 (2), 328-336.

[17] Porter, D.; Vollrath, F. Water mobility, denaturation and the glass transition in proteins. *Biochimica Et Biophysica Acta-Proteins and Proteomics* **2012,** 1824 (6), 785-791.

[18] Vollrath, F.; Porter, D. Spider silk as an archetypal protein elastomer. *Soft Matter* **2006,** 2, 377-385.

[19] Seydel, T.; Knoll, W.; Greving, I.; Dicko, C.; Koza, M. M.; Krasnov, I.; Muller, M. Increased molecular mobility in humid silk fibers under tensile stress. *Phys. Rev. E* **2011,** 83 (1).

[20] Nakamura, S.; Magoshi, J.; Magoshi, Y., Thermal properties of silk proteins in silkworms. In *Silk Polymers*: Materials Science and Biotechnology, Kaplan, D.;

Adams, W. W.; Farmer, B.; Viney, C., Eds. American Chemical Society: Washington, **1994**; Vol. Symposium Series 544, pp 211-221.

Chapter 6. Supercontraction of spider dragline silks

6.1 Introduction

The tensile and dynamic mechanical properties of *B. mori* silks may deteriorate under the combination of high humidity and reduced temperature of the glass transition as shown in Chapter 5. In the case of spider dragline silks, direct contact with cold water causes a more dramatic effect– these silks shrink substantially and become less stiff. Because of the general belief that the structural organization is very different between spider silks and domesticated silks, people have not tried to make any direct comparisons between the two seemingly different phenomena. Here, I write this chapter on spider silk supercontraction in light of the observations from the previous chapter of the effect of humidity on silkworm silks, and try to find whether a general glass transition mechanism has any effect in spider silk supercontraction. A thorough literature survey was conducted to first summarize previous observations, and this was used to formulate a hypothesis about contributions to supercontraction, and finally a new method was developed to understand better the interaction between water and spider silk.

First to introduce the phenomenon of "supercontraction". On exposure to water, spider dragline silks can shrink by up to about 50% of their original stretched length. Supercontraction is an interesting phenomenon because of the very high and reproducible values of shrinkage that can be reversibly induced by cyclical loading and then unloading in the presence of water [1-3]. Supercontraction varies between dragline silks from different spider species [4, 5], and more information can be found in the introduction, section 1.2.4; however, other silk types have also been found to undergo supercontraction, albeit to a far smaller degree [6]. Supercontraction provides new

potential applications for spider silks; for example, as tunable shape memory polymers, which are of great technological interest [7, 8]. Spider silk has also been found to show torsional memory effects [9], and a recent study suggests that spider silks may give repeatable and effective performance as potential replacement for muscles [10].

Different approaches were applied to understand supercontraction and the underlying mechanisms. The silks before and after supercontraction are usually called virgin silks and supercontracted silks respectively. Supercontraction was first discussed and defined by Robert Work [1, 11-13]. Since then there has been a growing interest in spider silks and webs. More specifically, Work compared properties of virgin and supercontracted silks, made initial suggestions on the bio-functions of supercontraction, and first hypothesized that orientation changes in the silk structure before and after supercontraction [12].

Blackledge has looked at supercontraction by observing cyclical changes to the length and load under different environmental conditions of *Argiope* spider dragline silk [10, 14]. For example, virgin silks were restrained under constant length and the cyclic stress response was measured under cycles of humidity between 0% and 100%. Two different responses were reported but not related directly to structural changes, which we interpret as: first, reduced modulus of virgin silk at high humidity giving a reduction in stress under restraining load; and second, a classical supercontraction of stretched silk at high humidity to give a higher stress.

Plaza quantified 'supercontraction stress' to be ~ 60 MPa by raising the humidity up to 100% under constant length [15]. He then observed that supercontraction could be linked to the glass transition in silk by using a combination of high humidity (about 70%) and increased temperature (50°C) and showed that supercontraction occurred

under the same conditions as the reduction in modulus associated with the glass transition [16, 17]. However, there is no other reference discussing any differences in supercontraction strain using this approach relative to simply exposing spider silk to liquid water. In a different study, a quantitative structure-property model was proposed for the changes in tensile modulus through the glass transition in *A. pernyi* silk, but this was again not extended to the supercontraction effect [18, 19].

Some researchers have attributed supercontraction to relaxation of orientation in the amorphous fraction of the silk polymers. For example, Michal's work on controlled supercontraction to investigate structural mechanisms used 2D NMR techniques [20, 21]. Michal suggested that on hydration the mobile (amorphous) phase first disorientates; if more contraction is allowed then the orientation distribution of both mobile and static (crystalline) components broadens. However, the attribution of orientation alone fails to explain quantitatively the variety of supercontraction effects across spider species.

Savage showed that there were major differences in the structural organisation in the glycine-rich domains and different molecular mechanisms for elastic effects in proline-rich and proline-poor segments of hydrated spider silks [22, 23].

Boutry and Blackledge discussed the role of the two GGX and GPGG motifs in supercontraction, and argued that the GPGG motif of MaMaSp2 has evolved to enhance supercontraction effects in dragline silks, without actually differentiating between the shrinkage mechanisms in the two motifs [24].

Liu's work attributed supercontraction mainly to proline content [4, 5]. He proposed that the close link between proline and particular elastin-like motifs in spider silks affected the orientation and relaxation of these intrinsically disordered peptide segments

both during fibre formation (spinning) and during fibre performance in environmental humidity (rH), respectively. Liu's experimental measurements also showed relationships between supercontraction capability and mechanical properties. Highly stretched native dragline silks have a relatively consistent stress-strain profile with high modulus and high strength. With greater supercontraction, the stress-strain profile changes to lower modulus and higher extensibility. Since the stress-strain profile can be predicted from the structural degree of order in the silk, this allows supercontraction to be linked directly to the structure and morphology of silk.

Silks from three species of *Nephila* spiders (*Nephila clavipes, edulis* and *senegalensis)* have been used frequently in supercontraction studies. The same spider family seem to share genes for making silks, and their silks display comparable mechanical and processing behaviour [25]. *Nephila* draglines have been shown to consist of two different proteins, namely, MaMaSp1 (proline-free) and MaMaSp2 (proline-rich) [26]. Liu's work strongly suggests that the proline-rich MaMaSp2 fraction makes a substantial contribution to supercontraction. However, it is not clear how other structural components might also participate in supercontraction, or how the intrinsically disordered proline might contribute to both amorphous and crystal relaxation processes suggested by Michal [20].

Based on all the work presented above, we formulated the hypothesis that there are at least two major mechanisms to supercontraction: (i) relaxation of oriented amorphous domains in the MaMaSp1 fraction and (ii) relaxation of proline-rich metastable ordered domains in the MaMaSp2 fraction. The empirical measurements presented here and their analysis have as their objective the test of the 'two-contributions' hypothesis for super-contraction. For this, we experimentally separated the two contributory effects in

Nephila edulis dragline silk by focusing on the MaSp1 and MaSp2 protein components. Both these proteins have 'hard' blocks of about 30% molar alanine segments that form beta-sheet crystal domains and 'soft' blocks of intrinsically disordered segments with characteristic sequence components - GGX- and -GPGXX- for MASP1 and MaSp2 respectively.

It is known that immersing silk in liquid water induces full supercontraction so that both mechanisms are assumed to contribute. It was also noted that in some experiments with controlled humidity only partial supercontraction was induced and supposedly only one of the contributions was activated. In this chapter, our refined experiments will show that reproducible and stable fractions of the total supercontraction could be induced at specific combinations of stress, temperature and humidity, which corresponds well with the glass transition conditions for generic silks. This new finding leads to a new understanding upon the structures of spider silk, especially the different structural components contributing differently to the properties of silk, such as contraction and mechanical properties.

6.2 Experimental section

6.2.1 Sample preparation

Nephila edulis spider dragline silk (*Nephila* dragline silk) was collected as described in section 3.2.1. The collection of both virgin and supercontracted spider dragline silks was introduced in section 4.2.1, however, because this chapter is solely about spider silk and both supercontraction and a partial contraction, it is necessary to repeat these procedures for referencing convenience. Silks were kept at constant length and stored in a dark drawer under lab conditions (20 °C, rH 40 %) until needed for measurement.

Segments of silks were then carefully transferred from the spool to sample-holders with minimal deformation.

Virgin silks: The dragline silks directly transferred from the spool to sample holders are categorized as virgin silks.

Supercontracted silks: Virgin silks were firstly transferred carefully from the segments of a spool to dividers with a dividing distance of 25 mm. The restraining length on the dividers was then adjusted from 25 mm to 19 mm to loosen the silk before the silk was immersed in water at room temperature. The silk shrank and became tensioned under water. Further measurement of the shrinkage was conducted in a 1 mm-stepwise manner. When the silk no longer shrank in water (observed as loss of tension under an optical microscope), the silk was marked as fully supercontracted and the shrinkage was noted down. On average, all silks have a shrinkage of 6-8 mm out of 25 mm; and the supercontraction ratio is calculated as the shrinkage divided by the full original length: 24%-32%. The supercontracted silks were mounted on the paper holders without tensioning soon after the supercontraction (they were still wet). Both natural and supercontracted silks were kept restrained on paper holders in the testing room (temperature 20 °C, relative humidity < 40%) until the test starts.

Araneus diadematus (*Araneus d.*) spider dragline virgin and supercontracted silks: A fair size *Araneus d.* garden spider (body length of about 8 mm) was supplied by Dr. Thomas Hesselberg in November 2011, and draglines were identified under the microscope after the spider was immobilized on a piece of plastic foam. Then double draglines were reeled onto a segmented spool and the reeling set-up was kept the same as for reeling *Nephila e.* spider silks. As-reeled silks are virgin silks.

Virgin silks were first transferred to dividers, and then individual silks were carefully loosened and immersed in water until the silk no longer showed tightening in water, and the shrinkage was noted down. The average supercontraction ratio from 4 samples was 53%.

Argiope bruennichi (*Argiope b.*) spider dragline virgin and supercontracted silk: Two *Argiope b.* spiders from Slovenia were kindly brought to the lab by Prof. Fritz Vollrath in September 2012. The collection and preparation procedure of *Argiope b.* dragline silks was the same as described for *Araneus* and *Nephila*. The measured average supercontraction ratio from 10 samples was 56%.

6.2.2 Dimensional Measurements

Both virgin and supercontracted silks from the three spider species were carefully transferred from the spool to SEM stubs with minimal stretching, especially for supercontracted silks. Silks from different parts of the spool were sampled to obtain an average value and standard deviation for cross sectional area for stress and modulus calculations. Because spider silks have a fairly round cross-sectional shape, the diameter was directly measured from the longitudinal view at a high magnification. For supercontracted silks, the diameter was also measured. The representative SEM images of virgin spider silks can be found in Figure 3.2, Chapter 3.

Table 6.1 Spider silk dimensions and supercontraction ratios
(Diameter in μm and area in μm^2)

Spider species	Measured Diameter (MD) Virgin	MD Super-contracted	Measured Area (MA) Virgin (A)	MA Super-contracted (B)	Super-contraction ratio (SC)	Super-contracted Area by Guinea rule (B')
Nephila e.	5.7	-	25.5	-	28%	35.4
Araneus d.	4.2	6.2	13.85	30.2	53%	29.5
Argiope b.	2.4	3.6	4.5	10.2	56%	10.2

As a validation to the measured supercontraction ratio, the areas of virgin and supercontracted silks (*A* and *B*) were also compared using measured diameters; if a constant volume rule as suggested by Guinea [32] can be applied, the supercontracted silk area will be $B'=A/(1-SC)$. For the partially contracted fibres, the constant volume rule was applied to estimate the cross-sectional areas instead of measuring from SEM images.

6.2.3 Dynamic humidity scan at 50 °C

DMTA Q800 (TA dynamic mechanical thermal analysis, DMTA, Instrument) is used for both static and dynamic mechanical testing. A tailored humidity accessory was installed to control the humidity-temperature experiments as described in section 5.2.2. The resolution of temperature was 1 °C and relative humidity was 2%.

Dynamic mechanical test set up as a humidity scan on supercontracted silks (single fibre) was as follows: 50 MPa static stress, ~0.2% dynamic strain, 1 Hz frequency, 50 °C, relative humidity ramp from 0% to 90% at 1%/min rate.

6.2.4 Humidity-Contraction test

Length tests were conducted in controlled-force mode. Length and force were monitored in all the tests.

a) Temperature set

For the temperature set, virgin silks were kept under static stress of 10 MPa for a range of humidity from 0% to 90% at five temperatures 10, 25, 37.5, 50 and 70 °C.

b) Stress set

For the stress set, different static stresses from 0 MPa to 20 MPa were applied to virgin silks through changing the humidity from 0% to 90%. Silks were recycled for tensile tests.

c) Time

In order to test the effect of soaking time under high humidity on length changes, one virgin silk sample was run at 50 °C first for a humidity ramp from 0% to 70%, and then the humidity was kept constant at 70% for over 60 mins.

6.2.5 Quasi-static tensile test

Static tensile tests were conducted at a force-ramp rate of 0.05 N/min, comparable to a strain rate of 0.01 s^{-1}, at room temperature after being equilibrated in the chamber for 10 minutes under nitrogen purge. Both virgin and supercontracted samples were single fibre, double brins. The tested silks from the stress-set of humidity-contraction test were saved for tensile tests too.

6.3 Results and discussion

6.3.1 Glass transition of supercontracted silk

Figure 6.1 shows the changes of the dynamic mechanical properties of supercontracted dragline silk as a function of changes in humidity at the controlled temperature of 50°C. As the humidity increases, the storage modulus drops slowly at first and then more rapidly down to below 1 GPa when the humidity goes above 63%. The loss tangent increases as the modulus decreases before a peak at a relative humidity (rH) of 82%.

We attribute the reduction in modulus and the loss tangent peak to the glass transition in silk, which is usually observed at about 200°C at low humidity. Plaza and Fu have studied the glass transition conditions for *Araneus diadematus* dragline silk and *Antheraea pernyi* silkworm silk, respectively, using a tensile tester with an environmental chamber [16, 18]. Our measurements, using DMTA, gives comparable

results. We used supercontracted silk for this test because virgin silk contracts or supercontracts within the humidity and temperature regime (discussed below), which would interfere with the glass transition effect, where length increases rather than decreases. By using fully-supercontracted silk, we are able to isolate the glass transition effect and confirm that the combination of temperature and humidity can induce the glass transition in supercontracted *Nephila* dragline silks.

To quantify the T_g position as a critical temperature or humidity, we took the onset of the reduction in modulus by extrapolating the almost linear sections of the modulus-temperature or modulus-humidity curves both below and above the main region of curvature, as shown in Figure 6.1. It is critical to note that the link of Figure 6.1 and Figure 5.5, indicating both *B. mori* silk and *Nephila* spider silk have the similar glass transition mechanism induced by combined humidity and temperature. This is consistent with the approach of Fu [18], and is more easily correlated with shrinkage measurements than the alternative measure of using the T_g position of the loss tangent peak maximum.

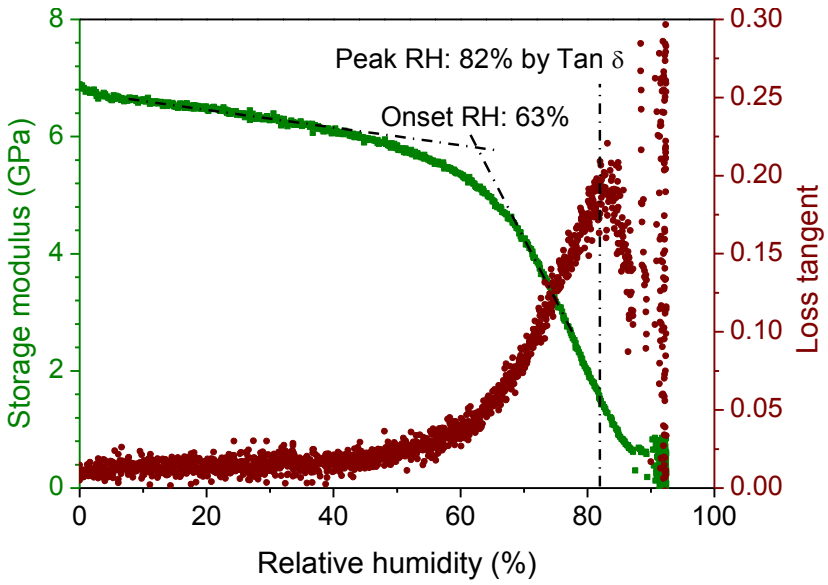

Figure 6.1 Storage modulus and loss tangent as a function of relative humidity at 50 ^{o}C and 10 MPa stress for maximally supercontracted silk.

6.3.2 Glass transition induced contraction

a) Temperature effect

Figure 6.2 (a) shows how different the contraction of virgin dragline silk is when induced at different temperatures at a stress of 10 MPa through a humidity ramp. The higher the temperature, the lower the critical humidity for the contraction in length. However, the maximum shrinkage seemed to reach a consistent plateau of about 9% at this stress, which is very different from the full supercontraction shrinkage of almost 30% with liquid water.

Figure 6.2 (b) at 50 ^{o}C shows this contraction to have a nearly identical profile as the modulus reduction curve induced by glass transition; here we note that they are opposite effects in terms of changes in length.

Figure 6.2 (c) shows our results of humidity and temperature combinations from the series of contraction tests in comparison with modeling and Plaza's experimental data for silk glass transition [16, 18]. Both our contraction data and the reference mechanical T_g points follow the same linear trend to that derived as a structure-property relation by Fu, and shows that the relation is common to different silk types and confirms and refines the suggestion of Plaza that one component of supercontraction and T_g have a common origin.

b) Stress effect

Since the shrinkage observed in Figure 6.2 is far lower than the full supercontraction shrinkage, the effect of restraining stress on T_g-contraction was investigated next. Figure 6.3 (a) shows that stress does affect the contraction, but not the onset humidity.

With lower restraining stress, the silk contracts more. With 20 MPa restraining stress, the silk only contracts 5%. When the stress goes down to 1 MPa, the shrinkage seems to reach a maximum value of 13%, which is still far lower than the full potential supercontraction. Between the lower and upper limits, the shrinkage changes linearly with stress, as shown in Figure 6.3 (b).

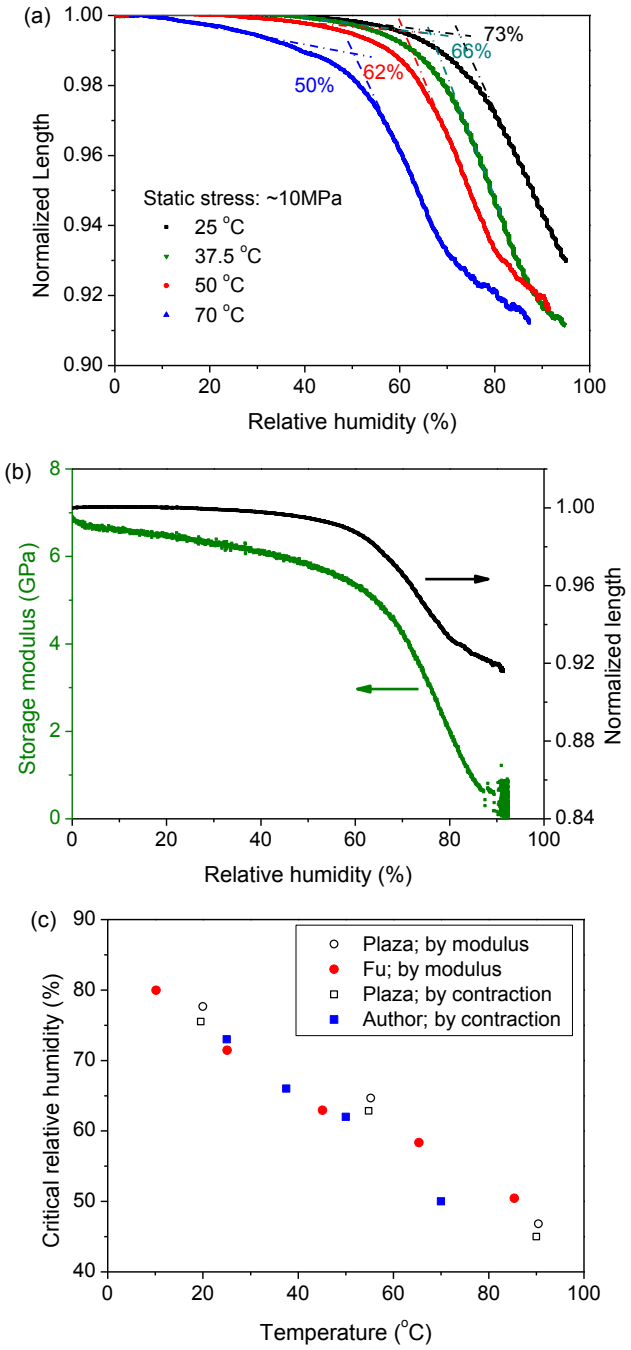

Figure 6.2 (a) Contraction tests on spider dragline silks through humidity 0%-80% at different temperatures and a constraining stress of 10 MPa. Critical RHs of transition at

different temperatures are labelled with dotted lines. (b) The modulus and contraction profiles at 50 °C through T_g have the same general form. (c) The locus of T_g points in temperature and RH is the same for contraction and modulus, with data of Fu [9] and Plaza [24] for reference.

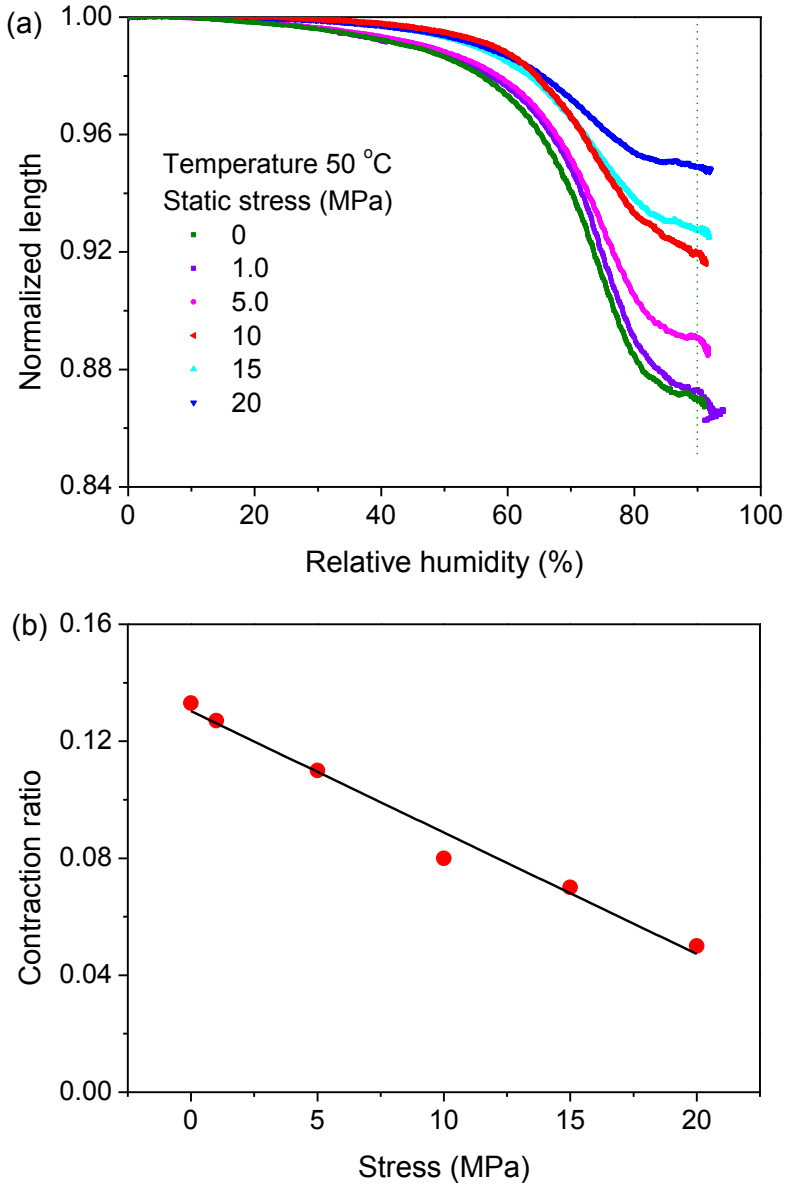

Figure 6.3 (a) Contraction of spider dragline silk through humidity at 50 °C under different static stresses. (b) Plateau T_g-contraction at 90% RH as a function of constraining stress.

c) Time effect

The silk fibres were observed to shrink more when they are held at high humidity for longer. Figure 6.4 shows how the soaking time under high humidity above the glass transition changes the final shrinkage under constant stress and temperature. Although the humidity was only 70% (just above the critical humidity of 62% at 50 °C) increased contraction of 13% is observed; and the maximal shrinkage plateaus very slowly as the soaking time continues. We attribute this time dependence to macromolecular relaxation processes through the induced glass transition and gradual permeation of water into the fibre.

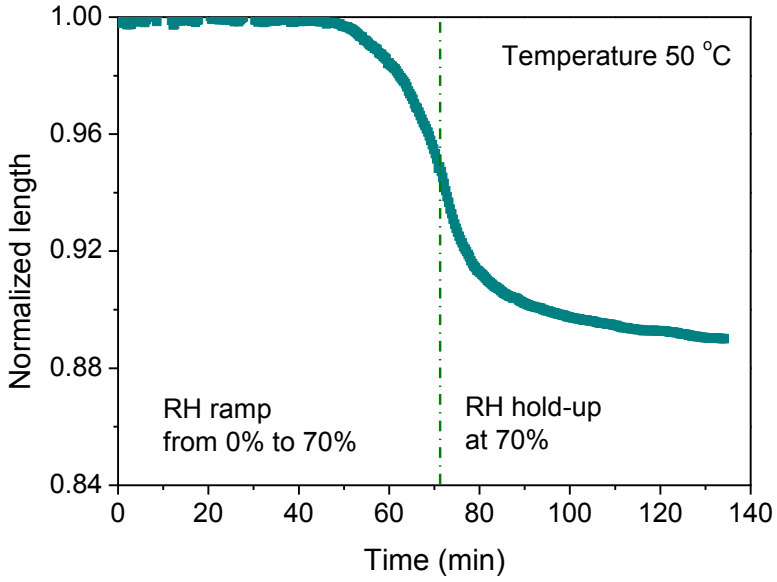

Figure 6.4 Length change as a function of time. The plot is separated into two parts: the first is the humidity increase at rate of 1%/min; and the second is the humidity held at 70%.

6.3.3 Comparing the tensile properties of T_g-contracted silks with virgin and supercontracted

Figure 6.5 shows how three T_g-contracted silks with different partial degrees of contraction at different constraining stresses have different mechanical property characteristics from both virgin and fully-supercontracted silks. They yield at a similar

strain of about 3% as the fully-supercontracted silks (conventionally attributed to the yield of amorphous polymer [27]) but develop a higher post-yield modulus, which tends towards that of the virgin silks at high strain through a relatively rapid strain hardening region. It is also important to note that both the initial tensile modulus and the yield stresses of the three partially contracted silks are higher than that of the fully-supercontracted but lower than the virgin silk, which implies an intermediate fraction of disordered structures in the partially contracted silks. I have not yet been able to repeat the T_g-contraction and stress-strain measurements on the re-stretched T_g-contracted silk fibres in order to test whether the contraction-stretching is cyclically repeatable, as observed for conventional supercontration [14]. Such tests will verify whether a specific fraction (and which) of the silk structure can be oriented and relaxed repeatedly. However, strain hardening occurs in the range of 5 to 13% strain, and suggests that this is the reorientation of the amorphous fraction that relaxes in the T_g-contraction process, since it occurs in the same strain range as the contraction shown in Figure 6.3.

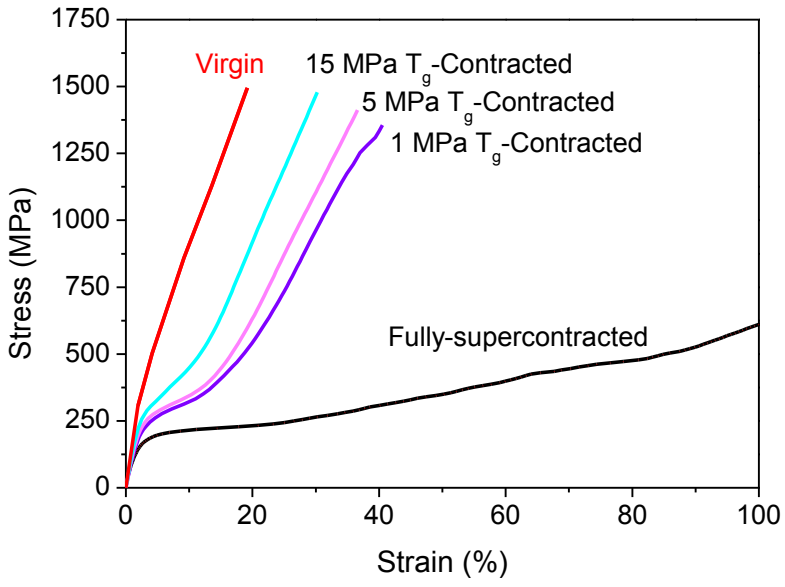

Figure 6.5 Stress-strain curves of three contracted or humidified spider dragline silks compared with virgin and fully supercontracted silks.

6.3.4 Mechanisms for supercontraction in *Nephila* spider silk and structural deconvolution

In order to analyze the observed correlations between supercontraction and the structural components for *Nephila* dragline silks, it is necessary to quantify the main structural and morphological contributions. Here we discuss a very simplified structure, in which the different domains act independent of each other. The major ampullate dragline is generally thought to consist of two main protein types: MaSp1 and MaSp2. These two principal proteins contain, for MaSp1 and MaSp2, respectively, about 30% molar of ordered/crystalline alanine blocks and about 70% of intrinsically disordered blocks with the generic sequences –GXG– and –GPGXX– [26, 28, 29].

For *Nephila* draglines, the exact fractions of MaSp1 and MaSp2 proteins is unclear from the literature, with Hinman [26] suggesting a ratio of 3:2 and Sponner suggesting higher ratios (but without making specific recommendations) [29]. If we take a generic value of 4.2% proline overall in *Nephila edulis* dragline silks [5] and 14% proline fraction in the MaSp2 fraction specifically [19], simple proportionality suggests about 30% molar MaSp2 and the –GPGXX– fraction becomes 21% molar if 70% is intrinsically disordered. Consequently, the overall fraction of –GXG– becomes 49% molar. However, the results of Liu [5] suggest that a fraction of about 20% of the silk cannot be ordered in the maximum observed ordered fraction of about 80% in all the draglines from 8 species examined in his study. Thus, the remaining –GXG– that can be oriented and ordered is estimated to be about 29% molar.

In terms of morphology, we consider the 30% alanine segments to be permanently order, PO, crystal domains that are insensitive to water or other environmental conditions [19]. The 29% –GXG– segments are conventionally associated with

disordered amorphous chains [23], which can be oriented under load and are assumed here to undergo relaxation above their glass transition temperature, and are here called meta-disorder, MD, where the term 'meta' is used to denote metastable structures that revert to a preferred lower energy state. Porter and Vollrath suggested that the 21% –GPGXX– segments can be effectively oriented and ordered under load as the torsional twists of the proline segments are pulled into line to allow the other 4 peptide segments to order and be held in place by strong hydrogen bonding [30]. This formation we will here call Meta Order, MO. For completeness, we call the 20% residual disordered fraction Permanent Disorder, PD, which might be helical 3_{10} coils, for example, as suggested by NMR [31].

In order to calculate the maximum contraction strain of each component, we need to make some estimates of the changes in dimension from oriented to contracted forms. Using the Liu data for contraction and proline content as a guide [5], we suggest that the MO fraction contracts from β-sheet to condensed sphere due to the twisting of the proline segments, with a maximum shrinkage of about 86% for the –GPGXX– blocks (estimated from the dimensions of the 30 to 35 peptide segment blocks). We further suggest that the MD fraction contracts to alpha-helix or 3_{10}-helix form with a maximum shrinkage of about 50%. We believe this assumption to be justified by the observation that the maximum observed supercontraction for *Araneus diadematus* fibres is about 56% for 14% proline or 70% –GPGXX–, which gives a maximum predicted contraction of $0.86 \times 0.7 = 0.6$. Figure 6.6 illustrates the potential change in dimensions of oriented secondary structure forms from which the maximum potential shrinkage is estimated.

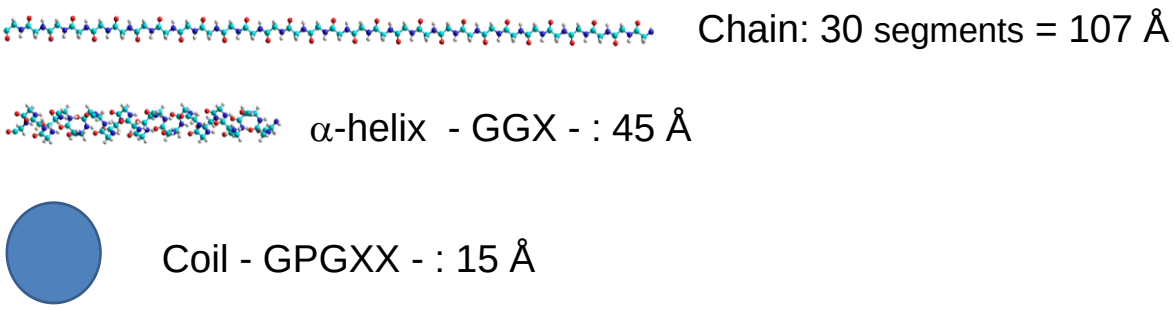

Figure 6.6 Illustration of size and shape of a polypeptide chain in three configurations.

Table 6.2 presents the predicted maximum contraction for the different components of *Nephila* dragline silk with 4.2% proline. The MD component –GXG– can contract up to 15% and the MO component –GPGXX– can contract up to 18%, for a total of 33%, which is in good agreement with published values of 0.28 to 0.33 [5]. Our dragline samples were collected at a relatively slow speed, so the observed total value of about 28% supercontraction is not unreasonable due to the lower degree of orientation [5].

Table 6.2 Suggested fractions and contributions to the supercontraction of the different structural and morphology components in *Nephila edulis* fibres.

Component	Fraction	Structure	Maximum contraction	Nephila edulis
Permanent order, PO	0.30	-An-	0	0
Permanent disorder, PD	0.20	Long side chains?	0	0
Meta order, MO	0.21	-GPGXX-	0.86	0.18
Meta disorder, MD	0.29	-GXG-	0.50	0.15

6.3.5 Supercontraction in spider silks of two other species: *Argiope b.* and *Araneus d.*

As introduced in Chapter 1, *Araneus d.* and *Argiope b.* are two other orb-weaving spiders that are commonly found in Europe, and their dragline silks have different AA sequences and supercontraction properties as shown in [4, 25]. The full supercontraction

ratio can be found in Table 6.1 from the methods section: *Araneus d.* is 53%; and *Argiope b.* silk is 56%. Comparing with the reported values of 53% and 48% for *Araneus* and *Argiope* silks [5], the relatively large *Argiope* supercontraction ratio in my results is probably due to the differences in reeling as well as the silk dimensions. As shown in the morphology Figure 6.7, the *Argiope* spider silks are very thin (diameter of only 2.4 μm), and they tend to be stretched into more ordered structures under the same reeling speed as reeling speed was shown to impact the supercontraction capability [4], therefore more MO is created, and therefore the silks would possess a larger potential for supercontraction.

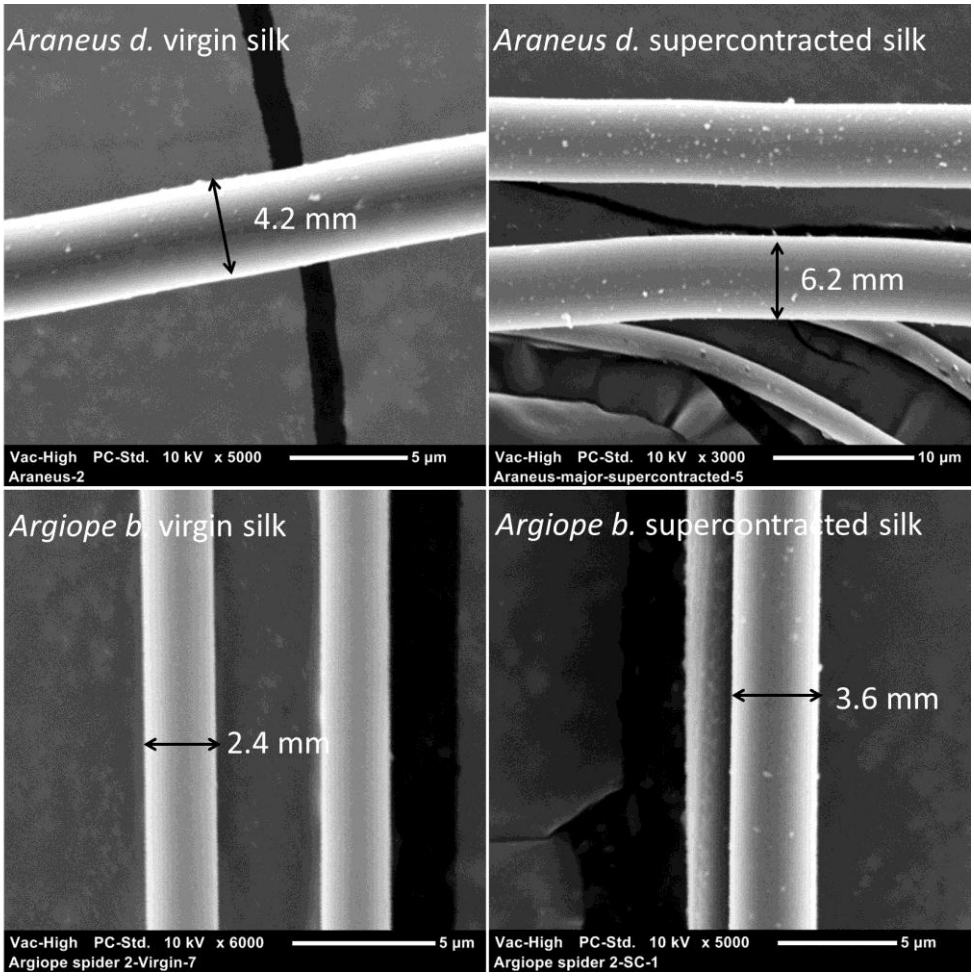

Figure 6.7 SEM images of virgin and supercontracted dragline silks from spiders *Araneus d.* and *Argiope b.*

The tensile properties of both the virgin and supercontracted draglines from the two spiders were examined, and results are shown in Figure 6.8. The moduli are only estimated from the rough trendlines of curves (red dash lines) without detailed fitting or statistical analysis. *Araneus* virgin has an initial modulus of 7.3 GPa and supercontracted has 3.0 GPa, whereas *Argiope* virgin has an initial modulus of 11.8 GPa and supercontracted has 5.3 GPa. More interestingly, the stress-strain profile of Araneus virgin silks shows a yield plateau after 3% strain, which is very similar to that of partially contracted *Nephila* silks. This suggests that *Araneus* silks might have already been contracted partially.

To follow the idea of T_g-contraction for *Nephila* dragline silk, humidity contraction tests on both virgin *Araneus* and *Argiope* silks were also conducted. As shown in Figure 6.9, *Argiope* silk has only 9% T_g-contraction, which is smaller than the ratio for *Nephila* silk. The tests on *Araneus* silks turned out to be only partially valid and no maximum T_g-shrinkage was captured, as the samples were not free to shrink fully due to insufficient distance between clamps.

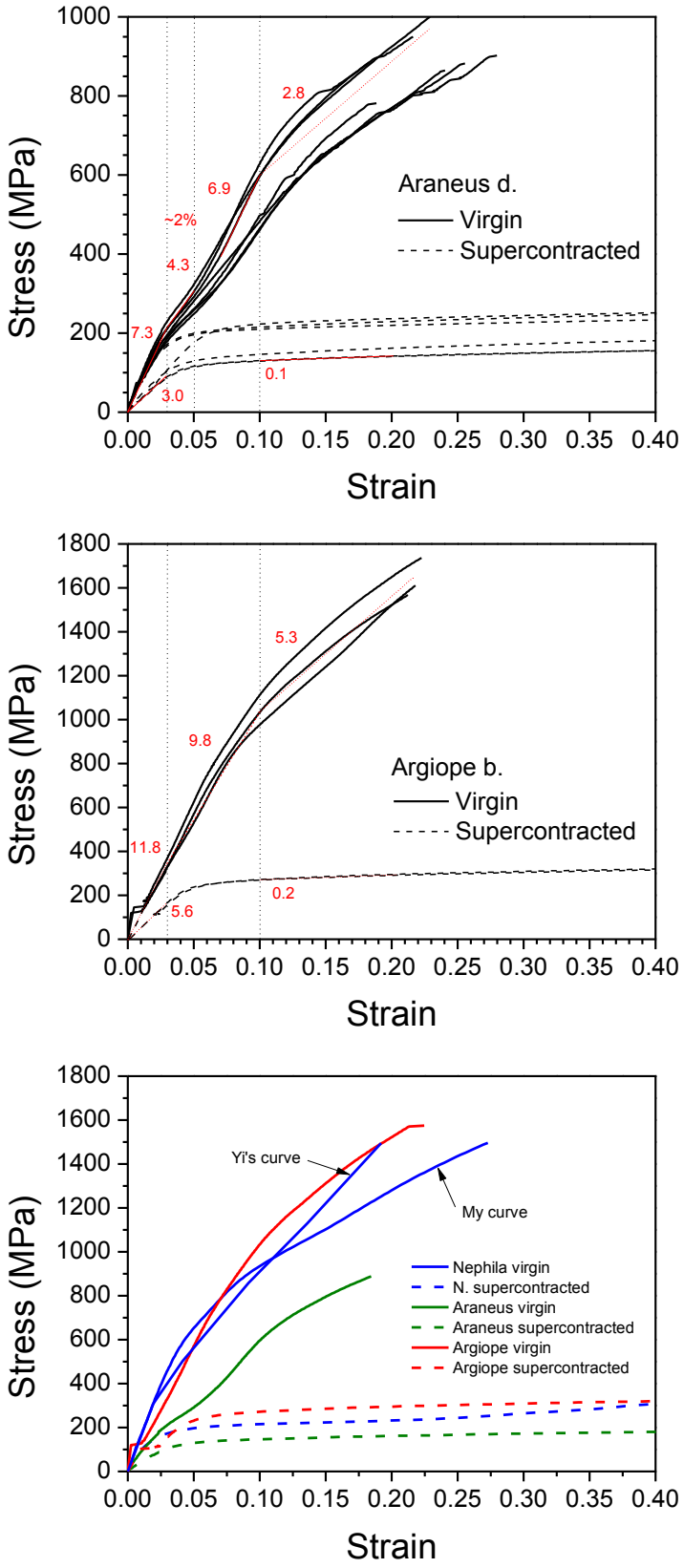

Figure 6.8 Stress-strain curves of virgin and supercontracted dragline silks from spider species: *Araneus d.* (a), *Argiope b.* (b), and the representative stress-strain curves for the three species *Araneus d.* (green) *Argiope b.* (red) and *Nephila e.* (blue). Solid lines are virgin silks, and the dashed lines are supercontracted silks.

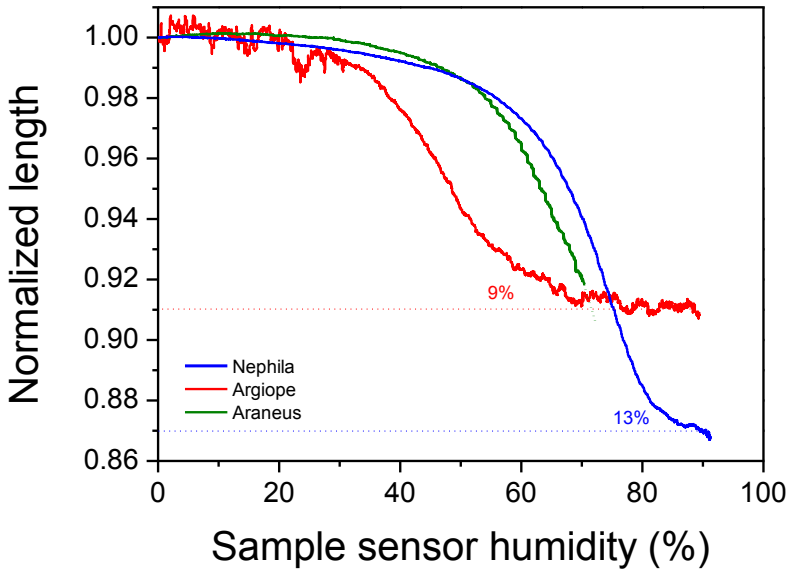

Figure 6.9 Comparison of the length contraction tests on three spider species: *Araneus d.*, *Argiope b.*, and *Nephila e*: normalized length as a function of increasing humidity at 50 °C.

6.3.6 Structural model for spider dragline silks from T_g-contraction and supercontraction

(In collaboration with Dr. David Porter.)

Although the T_g-contraction results for the two later examined spider species are still incomplete, there seems enough information available for an attempt to de-convolve the structural components in each spider silk. From GIM analysis, the modulus from tensile tests (E) and the degree of order have a quantitative relationship as detailed in Equation 6.1 [27, 32], see also section 4.4.1 for the same set of parameters in a different context. To explain the parameters here, $tan\Delta$ means the cumulative loss tangent as if the structure is fully disordered; $f_{d*}tan\Delta$ is the measured cumulative loss tangent; so that f_d can be calculated by comparing, not only the moduli Ey and E0, but also against the calculation of fully disordered $tan\Delta$ in section 4.4.1. Moreover, from the T_g-contraction ratio, proline-containing domain content and full contraction ratio, based on the same

deductive procedure established for *Nephila* silks, the fraction of meta-disorder structure and meta-order structure could be estimated to a first approximation.

$$E_y \approx E_o \, exp\left(\frac{-f_d \, tan\Delta}{A \, E_o}\right) \approx E_o \, exp\left(\frac{-50 \, f_d}{E_o}\right) \tag{6.1}$$

Take the example of *Argiope* silk. It has E_o = 11.3 GPa and E_y = 5 GPa at about 10% strain, so it is deduced that there is a permanent disordered fraction of $f_d \approx 18\%$ and the disorder is partially ordered helical (rather than random coil), since it yields at 10%. From the T_g-contraction of 9% for a helix fraction of 18% at 50% shrinkage and a total supercontraction of 48% [5] that suggests a random coil fraction of about 46% (proline fraction is about 10% for a total of ≈50% GPGXX max.). Thus, the stretched disordered fractions are 18% helix and 46% random coil for a total stretched disordered fraction of 64%.

The same methods could be adopted for resolving the structures of other spider dragline silks. We propose a universal spider silk model with four structural components, and the organization of the four components is a homogeneous distribution (obeying a simple linear additive rule). T_g-contraction could be a way to identify the fraction of meta-order structure. From Table 6.3, we find the total apparent order in spider silk structure may vary between 0.6 and 0.75; and the total fractions of meta-structures determine the capability of supercontraction. The four structural components contribute together to the overall properties of spider silks, especially mechanical properties. What is the evolutionary/survival need that has driven spiders of different species to genetically and chemically modify the fraction of each component in proteins that goes into their silks? It cannot be answered at this stage. However, in this study by clearly separating out the four typical structural components (each component possesses a set of properties) in spider silks, at least we could establish links between materials

structures and properties, quantify structural building blocks, and lay the foundation for structure-property-function relationships of biological systems.

Table 6.3 Structural de-convolution for dragline silks of three spider species

Species	SC* ratio	T_g-contraction ratio	Proline content	Permanent order (PO)	Permanent disorder (PD)	Meta order (MO)	Meta disorder (MD)
Nephila e.	28%	13%	4%	0.33	0.20	0.26	0.21
Araneus d.	53%	-	14%	0.15	0.25	0.60	-
Argiope b.	48%[5]	9%	8%	0.18	0.18	0.46	0.18

*: SC stands for supercontraction.

6.4 Conclusions

Humidity-dynamic mechanical analysis on *Nephila edulis* spider dragline silks has shown that supercontraction in this species of dragline silks has two distinct components. The first component is a contraction of maximum about 13% associated with relaxation processed through the glass transition, T_g, being induced by increasing combinations of temperature and humidity. The T_g-induced contraction is linked to the disordered component of MaSp1 protein and is linearly dependent upon the restraining stress on the fibre, and the mechanical properties of the partially contracted silk have different profile features for both native and fully supercontracted fibres. The remaining supercontraction to a total of about 30% then is linked to the intrinsically disordered proline-containing fraction of MaSp2 protein. It is important to mention the argument here to differentiate the humidity from liquid water is that at even very high humidity the water molecules are in vapour form meaning the odds of two molecules attacking the same spot in silks are much lower comparing with condensed water. However, why the full supercontraction can happen at room temperature or even below with in contact of water is not explained explicitly in any research on my view.

Mechanical analysis and supercontraction tests on dragline silks from another two spider species, *Araneus diadematus* and *Argiope bruennichi*, show that the structures of silks can be de-convoluted into four structural components as proposed for *Nephila e.* spider silk. To conclude, a structural model comprising of four structural components (permanent order, permanent disorder, meta order and meta disorder) and a linear additive organization of the structural components could be generalized for spider dragline silks with supercontraction capablities. Glass transition plays a role in the supercontraction of some spider silks where the meta-order structure is present.

6.5 References

[1] Work, R. W. A comparative study of the supercontraction of major ampullate silk fibres of orb web building spiders (Araneae). *J. Arachnol.* **1981,** *9*, 299-308.

[2] Shao, Z. Z.; Vollrath, F. The effect of solvents on the contraction and mechanical properties of spider silk. *Polymer* **1999,** *40* (7), 1799-1806.

[3] Grubb, D. T.; Ji, G. Molecular chain orientation in supercontracted and re-extended spider silk. *Int. J. Biol. Macromol.* **1999,** *24* (2-3), 203-210.

[4] Liu, Y.; Shao, Z. Z.; Vollrath, F. Relationships between supercontraction and mechanical properties of spider silk. *Nat. Mater.* **2005,** *4* (12), 901-905.

[5] Liu, Y.; Sponner, A.; Porter, D.; Vollrath, F. Proline and processing of spider silks. *Biomacromolecules* **2008,** *9* (1), 116-121.

[6] Plaza, G. R.; Corsini, P.; Perez-Rigueiro, J.; Marsano, E.; Guinea, G. V.; Elices, M. Effect of water on Bombyx mori regenerated silk fibers and its application in modifying their mechanical properties. *J. Appl. Polym. Sci.* **2008,** *109* (3), 1793-1801.

[7] Mather, P. T.; Luo, X.; Rousseau, I. A. Shape memory polymer research. *Annual Review of Materials Research* **2009,** *39*, 445-471.

[8] Xie, T. Tunable polymer multi-shape memory effect. *Nature* **2010,** *464* (7286), 267-270.

[9] Emile, O.; Le Floch, A.; Vollrath, F. Biopolymers: Shape memory in spider draglines. *Nature* **2006,** *440* (7084), 621-621.

[10] Agnarsson, I.; Dhinojwala, A.; Sahni, V.; Blackledge, T. A. Spider silk as a novel high performance biomimetic muscle driven by humidity. *J. Exp. Biol.* **2009,** *212* (13), 1989-1993.

[11] Work, R. W.; Morosoff, N. A physicochemical study of the supercontraction of spider major ampullate silk fibers. *Text. Res. J.* **1982,** *52* (5), 349-356.

[12] Fornes, R. E.; Work, R. W.; Morosoff, N. Molecular-orientation of spider silks in the natural and supercontracted states. *J. Polym. Sci. Pol. Phys.* **1983,** *21* (7), 1163-1172.

[13] Work, R. W. Viscoelastic behaviour and wet supercontraction of major ampullate silk fibres of certain orb-web-building spiders (Araneae). *Journal of Experimenal Biology* **1985,** *118* (1), 379-404.

[14] Blackledge, T. A.; Boutry, C.; Wong, S.-C.; Baji, A.; Dhinojwala, A.; Sahni, V.; Agnarsson, I. How super is supercontraction? Persistent versus cyclic responses to humidity in spider dragline silk. *J. Exp. Biol.* **2009,** *212* (13), 1981-1989.

[15] Guinea, G. V.; Elices, M.; Perez-Rigueiro, J.; Plaza, G. Self-tightening of spider silk fibers induced by moisture. *Polymer* **2003,** *44* (19), 5785-5788.

[16] Plaza, G. R.; Guinea, G. V.; Perez-Rigueiro, J.; Elices, M. Thermo-hygro-mechanical behavior of spider dragline silk: Glassy and rubbery states. *J. Polym. Sci. Pol. Phys.* **2006,** *44* (6), 994-999.

[17] Elices, M.; Plaza, G. R.; Pérez-Rigueiro, J.; Guinea, G. V. The hidden link between supercontraction and mechanical behavior of spider silks. *Journal of the mechanical behavior of biomedical materials* **2011,** *4* (5), 658-669.

[18] Fu, C. J.; Porter, D.; Shao, Z. Z. Moisture Effects on Antheraea pernyi Silk's Mechanical Property. *Macromolecules* **2009,** *42* (20), 7877-7880.

[19] Fu, C.; Porter, D.; Chen, X.; Vollrath, F.; Shao, Z. Understanding the Mechanical Properties of Antheraea Pernyi Silk—From Primary Structure to Condensed Structure of the Protein. *Adv. Funct. Mater.* **2011,** *21* (4), 729-737.

[20] Eles, P. T.; Michal, C. A. Strain dependent local phase transitions observed during controlled supercontraction reveal mechanisms in spider silk. *Macromolecules* **2004,** *37* (4), 1342-1345.

[21] Eles, P. T.; Michal, C. A. A DECODER NMR study of backbone orientation in Nephila clavipes dragline silk under varying strain and draw rate. *Biomacromolecules* **2004,** *5* (3), 661-665.

[22] Savage, K. N.; Gosline, J. M. The effect of proline on the network structure of major ampullate silks as inferred from their mechanical and optical properties. *J. Exp. Biol.* **2008,** *211* (12), 1937-1947.

[23] Savage, K. N.; Gosline, J. M. The role of proline in the elastic mechanism of hydrated spider silks. *J. Exp. Biol.* **2008,** *211*, 1948-1957.

[24] Boutry, C.; Blackledge, T. A. Evolution of supercontraction in spider silk: structure–function relationship from tarantulas to orb-weavers. *The Journal of Experimental Biology* **2010,** *213* (20), 3505-3514.

[25] Gatesy, J.; Hayashi, C.; Motriuk, D.; Woods, J.; Lewis, R. Extreme Diversity, Conservation, and Convergence of Spider Silk Fibroin Sequences. *Science* **2001,** *291* (5513), 2603-2605.

[26] Hinman, M. B.; Lewis, R. V. Isolation of a clone encoding a second dragline silk fibroin. Nephila clavipes dragline silk is a two-protein fiber. *J. Biol. Chem.* **1992,** *267* (27), 19320-4.

[27] Porter, D.; Gould, P. J. Predictive nonlinear constitutive relations in polymers through loss history. *International Journal of Solids and Structures* **2009,** *46* (9), 1981-1993.

[28] Hinman, M. B.; Dong, Z.; Lewis, R. V. Unusual Structural Features in Spider Dragline Silk. *Mol Biol Cell* **1992,** *3*, A113-A113.

[29] Sponner, A.; Schlott, B.; Vollrath, F.; Unger, E.; Grosse, F.; Weisshart, K. Characterization of the protein components of Nephila clavipes dragline silk. *Biochemistry* **2005,** *44* (12), 4727-4736.

[30] Vollrath, F.; Porter, D. Spider silk as an archetypal protein elastomer. *Soft Matter* **2006,** *2*, 377-385.

[31] van Beek, J. D.; Hess, S.; Vollrath, F.; Meier, B. H. The molecular structure of spider dragline silk: Folding and orientation of the protein backbone. *Proc. Natl. Acad. Sci. U. S. A.* **2002,** *99* (16), 10266-10271.

[32] Vollrath, F.; Porter, D. Spider silk as a model biomaterial. *Appl. Phys. A-Mater.* **2006,** *82* (2), 205-212.

Chapter 7. The "quality" of silkworm silks

7.1 Introduction

Differing from previous chapters, this final technical chapter focuses on a more practical problem of the "quality" of silkworm silks. This subject, or the specific example of grading silkworm cocoons, was introduced right at the beginning of this DPhil work, when a set of graded cocoon samples were provided from China. The question then was very simple: is the commercial grading process rather subjective or does it genuinely reflect the intrinsic structural and property differences of the cocoons and the fibres? One way to answer this question was to assess the graded cocoons and their fibres using the methodology on DMA developed for silks in this work. Here, in this introduction, the concept of silk quality is first introduced, followed by an overview of the conventional procedure for evaluating cocoon or silk quality, and concluded by a summary of further key aspects of the production and processing of silkworm silks that are related to the issues of silk quality.

Commercial *B. mori* silk as a type of luxurious textile material is highly regarded in many cultures, especially in China and India. For millennia, silks have enjoyed the reputation of the "Queen of Textiles". Lustrous, soft, colourful, comfortable, wearable, strong and "sensuous" are the typical words to describe the fabrics of silk and the special "qualities" of silk. However, these words can be translated into more scientific descriptions: *thin* fibre, *smooth* surface morphology, highly *light-reflective*, water *absorbent*, strongly dye-binding, *high strength, high toughness etc*.

On the other hand, in order to produce a silk fabric, the material has to go through a time- and energy- consuming process starting from rearing silkworms and harvesting raw silk cocoons, to processing raw silks, weaving silk fabric and marketing silk

products. In every step of this production chain, great effort is made to ensure good silk quality. The issue of the intrinsic quality of the raw silk material is so important that it affects every sector of the silk industry and the micro-economics of the silk farmers, traders and producers *etc*. However, how to evaluate and control the quality of silks effectively and efficiently is not straightforward and evaluating and controlling silk quality in a consistent manner through the whole production chain of silks does not seem to be easily achieved.

The methods to evaluate the quality of silks vary from place to place and have evolved with time. Take the example of evaluating silk quality in China. Sericulture in China has been practiced for over five thousand years[1]. Historically, producing silks was more or less an 'empirical' manual process in both rearing silkworms and classifying the raw silkworm cocoons. Today, as the biggest silk-producing country, China has developed a series of national standards for classifying fresh cocoons as well as evaluating raw silk quality since the 1950s, and the most recent standards were published in 2008 [2, 3]. The cocoon classification has evolved from the early empirical 'look and feel' approach to a more standardized procedure. For example, in classifying cocoons, 5‰ of the total weight of the cocoons are first selected and dried, then boiled and reeled, and finally an average value of the maximum length of non-broken filament is used to classify cocoons. These methods of cocoon classification are relatively simple compared with the methods of raw silk classification, which include eight different types of test (e.g. size test and tensile test). One problem with cocoon classification is that it only compares the reelability of the cocoons, but not directly the quality of the fibres drawn out of the cocoon. One initial aim of the work reported here was to examine the effect of farming by evaluating the cocoons and the fibres prior to any further processing.

There are other aspects that concern the effects of production or processing on silk quality. Some experiments have been conducted to manipulate the natural rearing and spinning conditions to see whether the cocoon or silk quality could be affected. For example, some studies revealed that the type and the sufficiency of the diet to silkworms may affect the production and hence the quality of silkworm cocoons [4, 5]. Even at the later stages of rearing when the silkworms are ready to spin, instead of natural spinning, manipulating the way silks are spun has also been evaluated. For example, force-reeling was shown to improve the tensile properties of silkworm silks and give surprising strength to silkworm silks [6]. Different from the natural spinning process, the use of reconstituted silk fibroin (RSF) to make artificial silks has been attempted numerous times [7-9]. However, it has not yet produced any useful 'synthetic' silk fibres to match natural silk fibres. Given the complexity of the problem, I only focus here on a few factors that can be examined directly from the available samples from different collaborators, and aim to qualitatively understand various effects during production, processing and storage on silk quality. These effects include genetic varieties, ageing, force-reeling, manipulated rearing conditions and spinning from reconstituted silk fibroin.

To complement the understanding of silk quality from practical sericulture and the silk textile industry, I try here to correlate silk quality with the silk structure and morphology. On the one hand, structure and morphology determine material properties and functions and, on the other hand, the silk structure could be interpreted using dynamic mechanical thermal analysis (DMTA), as demonstrated in Chapter 3, Chapter 4 and Chapter 5. Now the motivation for this work is clear: can silk quality be correlated with the silk structure? Is DMTA and mechanical analysis able to differentiate silk structures subject to different processing histories?

7.2 Materials and methods

7.2.1 Materials

Three grades of cocoons and silks

Three different quality cocoons (pupae removed) from Jiangsu Province, China were provided by Prof. Yaopeng Zhang from Donghua University, China. They were produced during the same period, June 2010, and pupae were removed immediately upon collection. Three cocoon samples (one for each grade, named as G1, G2 and G3) were randomly chosen for experiments and analysis. The rough outer layer of each cocoon was removed before taking the fibres from the middle of the cocoon shell for mounting. Raw silk fibres (silk baves with sericin coating) were manually gently pulled out from the middle layer of the cocoon. The pulling of the fibres inevitably causes some breaking-up of the sericin coating. However, with care, minimal damage to the sericin-fibroin bonding was maintained.

Defective cocoons from Zhejiang Province

Six types of cocoons with different defects were produced in Zhejiang Province, China and provided by Prof. Yaopeng Zhang from Donghua University, China. These cocoons were only used for demonstrating cocoon morphology and defects, and no silks were drawn out for testing.

Silks from lab-reared silkworms under controlled rearing and spinning conditions

Two types of cocoon silks from lab-reared silkworms were provided by Dr. Chris Holland and Catherine Offord. The silkworms were under controlled environmental conditions during rearing and spinning. The detailed description of the methods has not

been published; therefore in this work the two silks are labelled simply as: lab-produced (1) and lab-produced (2).

Force-reeled silks

Four types of force-reeled *B. mori* silks from different silkworms and different reeling conditions were provided by Beth Mortimer. The ready-to-spin silkworms were first paralysed before reeling, the method of which can be referred to in [10]. The silk labels and reeling conditions are as follows: the initial reeling speeds from the silkworms are kept constant at 18-20 mm/s; W1 (air-reeled) was force-reeled in air without post-draw; W27 was post-drawn under water and stored under ambient conditions without tension; W30 was post-drawn under water and stored under ambient conditions with tension; W39 was also post-drawn under water and stored in dry and cold conditions.

Aged silks: the 1853 silk

Two types of *B. mori* silks stored for different periods of time are used to evaluate the effect of ageing. The first silks labelled as 1853 silk were received as a gift from Dr. Chris Graham to Professor Fritz Vollrath. The silks most likely originated from China and were collected and transported by Dr. Graham's ancestor to England in 1853. The second silks (labelled as 2004 silk) were initially obtained from China in 2004, and have been stored in the lab since under ambient conditions.

Artificially wet-spun silks from reconstituted silk fibroin (RSF)

Artificial silk fibres from reconstituted silk fibroin were provided by Wang Qin from Fudan University, China. The RSF spinning dope was obtained by dissolving silk fibroin in ionic liquid AmimCl following the procedure described in [11].

All silks were carefully mounted onto the sample holders using Loctite superglue. Sample-holders are card frames, designed for the DMA tension clamp and cut by laser cutter with precision. The cross-sectional area for each silk was measured as described in the following SEM section.

German research booklet

A research booklet in German was provided by Professor Fritz Vollrath that dates back in 1940s. This research booklet contains valuable information on the tensile properties of a group of silks from different genetic strains of silkworms. The data was translated by the author into modern units and reanalysed.

7.2.2 Cocoon morphology, weight and size

Photographs of the three cocoons (G1, G2 and G3) were taken using a Panasonic camera in order to compare features of their appearance such as colour and contamination. The size was measured from the photographs; and the weight was measured on a lab balance.

7.2.3 SEM characterization on silk morphology

Images of the morphological features of both cross-sections and surfaces of the above-introduced silks were taken on a Scanning Electron Microscope (Jeol Neoscope JCM-5000). For most silks, a magnification of 1,000 times was used for cross-sectional shots. Image analysis of the cross-sectional areas was done using ImageJ (protocol provided by lab members). An average area from this analysis for each grade of silks (G1, G2 and G3) was then used for calculating the stress and modulus in mechanical analysis. For the 1853 silk, similar image analysis was conducted to obtain an average cross-sectional area. For the force-reeled silks, the average areas for each type were provided by Beth Mortimer. For the RSF silks, due to large variation between samples,

individual cross-sectional area was assigned for stress calculation. For the lab-produced silks, only dimensionless loss tangent is discussed here and no areas were measured.

7.2.4 (Quasi-static mechanical) Tensile testing

Quasi-static mechanical tests, or tensile tests, were conducted in controlled-force mode on a TA Q800 instrument instead of the Instron. 5mm gauge length was used for all mechanical tests, including dynamic tests. The "end effect" is not taken into account here as the thickness/length ratio is very small with a 5 mm gauge length. Tests were set up using the following parameters: force-ramp rate of 0.1N/min; room temperature 25 °C; and relative humidity of below 50%. Approx. 15 specimens were tested for each grade of the three grades, and the sample size for other silks will be mentioned in the corresponding section. For all other silks, the same parameters were applied for tensile tests.

7.2.5 Dynamic mechanical thermal analysis: Temperature scan

Dynamic mechanical tests were also conducted on the TA DMA Q800 using the following settings: temperature ramps from -100 to 250 °C at 3 °C /min, 0.02 N static load for G1, 1 Hz frequency, 0.2% dynamic strain (equivalent of ~15 MPa dynamic stress at 25 °C). Samples were all equilibrated at 30 °C for 10 mins under nitrogen purge (to remove the excess moisture from the specimens).

A cyclical temperature test was conducted on G1 silks using the same settings as above: the first scan was from -100 to 120 °C, and then the second scan was from -100 to 250 °C after cooling to -100 °C at -10 °C /min. Another cyclical temperature scan (annealing test) was conducted on G3 silk with the first scan to a maximum temperature of 180 °C.

7.3 Results and discussions

7.3.1 Comparing the cocoon morphology, size and weight

In the Chinese cocoon industry, visual inspection on the size and weight of the cocoons is the first step for classifying cocoons according to the "silk reeling and testing manual" (http://www.fao.org/docrep/x2099E/x2099E00.htm). The optical photographs of three grades of cocoons from Jiangsu Province and six "B" grade cocoons from Zhejiang Province are shown in Figure 1. The top grade cocoons (G1) from Jiangsu are selected for the normal silk industry; G2 are second class but good enough for the normal silk industry; while G3 cannot be used for normal silk industry. "B" grade cocoons from Zhejiang Province are defective cocoons that cannot be processed normally during degumming and reeling and are discarded from the fine silk industry. Different defects dominate in these defective cocoons. For example, B1 is classified as imprinted and B2 is classified as yellow cocoon contaminated by silkworm body fluid. Here, I will focus on the three Jiangsu grades that represent a wide range of cocoon quality.

To compare the colour/contamination of the three grades, as shown in Figure 7.1, cocoon G1 and G2 are both white without contamination, while cocoon G3 is discoloured or yellowish. The size of cocoon G1 is 4.3cm by 2.5cm, much bigger than that of G2 (3.6cm by 2.0cm) and G3 (3.6cm by2.1cm). Moreover, the weight of G1 is 0.51g, heavier than that of G2 (0.29g) and G3 (0.33g).

Jiangsu Prov. Zhejiang Prov.

Figure 7.1 Photos of various grade cocoons from Jiangsu and Zhejiang Province, China.

From these visual features of the cocoons, it may be concluded that the top grade cocoons are cleaner, bigger cocoons that tend to produce whiter and more fibres per cocoon.

7.3.2 Morphology of raw silk fibres

On top of the cocoon morphology, it is more interesting to look into the morphology of silk fibres of different grade since the fibres are what make a silk fabric. As shown in Figure 7.2, silk fibres from G1 have more regular cross-sectional shapes (triangular or bone-shaped), and the two brins of a bave are well wrapped by sericin with little exposure of individual brins; while theG2 and G3 fibres are not coated evenly by sericin, and the spread or coating thickness of sericin varies a lot around and along the fibre, which can also be seen from the longitudinal view in the last column of Figure 7.2. In addition, for G2 and G3 silks, there are perhaps more cracks on the interfaces between sericin and fibroin and more holes in the fibre cross-sections. The ‘cracks’ in G2 and G3 are defects and may cause early failure in mechanical testing. From the results of SEM cross-sectional measurements shown in Table 7.1, it is found that the top grade G1 silks are the thickest and the low grade G2 and G3 silks are thinner.

It may be concluded from the silk fibre morphology that the low grade silks are more vulnerable to breakage due to the uneven coating of the sericin during the raw silk

reeling. Moreover, because the lower grade silks tend to be thinner, they would break more easily when subjected to the same level of stretching force. For example, the breaking force for G3 is 0.103 N compared with that of 0.159 N for G1.

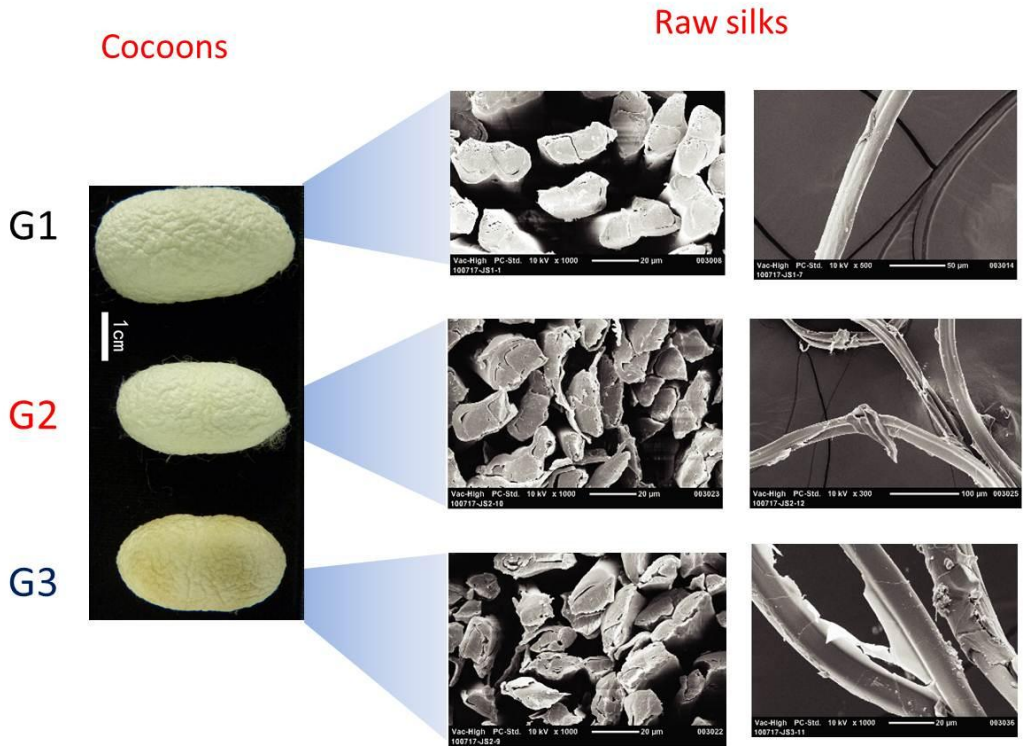

Figure 7.2 Photographs of the three cocoon grades are on the left, SEM images of the cross-sections are in the middle column, and surface/longitudinal views of the raw silks taken from the middle layer of the cocoons are shown on the right.

Table 7.1 Cross sectional areas of silks from three grades

Cocoon grades	Mean of cross section areas (μm^2)	Sample size (n)
G1	401±50	33
G2	334±31	25
G3	270±34	29

7.3.3 (Quasi-static) Tensile performances of silk fibres

To further examine the tensile properties of the three grades of silks, quasi-static tensile tests were conducted and the results are compared here. Figure 7.3 shows the stress-strain curves of the three grades, about 15 silk samples tested for each grade. Table 7.2 summarizes the results. In general, G3 has a larger variability in the tensile

performance compared with G1 and G2. For example, the breaking strain and stress of G3 has a larger standard error of 8% and 13.6% respectively. Two-sample t-tests were conducted for significance test on each property index among the three grades. The initial moduli of G1 (4.95 GPa) and G2 (5.15 GPa) silk fibres are significantly higher than G3 (3.59 GPa); and the post modulus of G1 (796 MPa) is significantly higher than G2 (664 MPa) and G3 (635 MPa). However, the breaking energy of G1 is lower than that of G2 or G3, which may be attributed to the increased breaking strain for G2 and G3, whereas the breaking stress remain at a similar level across the three grades. This increased energy is usually a sign of increased disorder in the molecular structure.

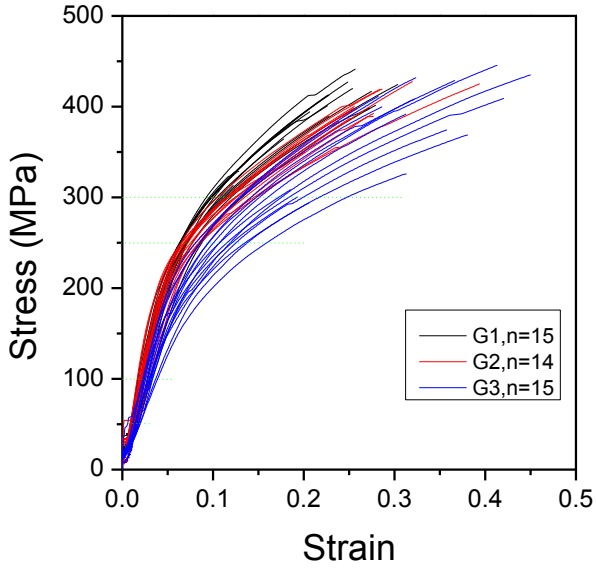

Figure 7.3 Stress-strain curves of 3 grades of *B. mori* silks (from the middle layer of cocoons.

Table 7.2 Results of stress-strain curves of three grades of silks

Grades	Initial modulus (GPa)[a]	Post modulus (MPa) [b]	Breaking strain (%)	Breaking stress (MPa)	Breaking energy (J/cm^3)
G1	4.95±0.75	796±99	23.1±5.0	397±36	64.8±19.1
G2	5.15±1.10	664±61	26.8±5.7	392±32	76.4±21.0
G3	3.59±0.80	639±101	32.1±8.1	382±52	88.1±31.1
p-value (null hypothesis: $\mu_1 = \mu_2$)	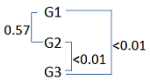	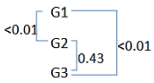	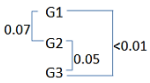	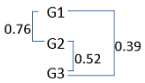	

[a]: Instead of strain limits, initial modulus are calculated using stress limits, between 50MPa and 100MPa (because of the stress-control basis of DMA and the unbending process of B.mori silks before straightening).
[b]: Post modulus are calculated using stress limits of 300MPa (G1 and G2) or 250MPa (G3) and breaking stress.

7.3.4 Dynamic mechanical thermal analysis of silk fibres

Can the quality of silks be revealed in a DMA temperature scan? To first review the previous findings in Chapter 4 (refer to section 4.3.3 and Figure 4.5), in a temperature scan both storage modulus and loss tangent of *B. mori* silks change as a function of temperature. From room temperature upwards, there are two main features in the changes: first, the storage modulus increases with a high loss tangent at temperatures from 50 to 100 °C; second, the storage modulus decreases and is accompanied by a strong loss tangent peak between 150 and 250 °C. The two events are caused by water loss and the glass transition of the "dry" silk structure, respectively [12]. The magnitude of both events could be related to the silk structure and now it needs to be proved whether this could be further linked to silk quality. Here, I focus only on the event of the "dry" silk glass transition.

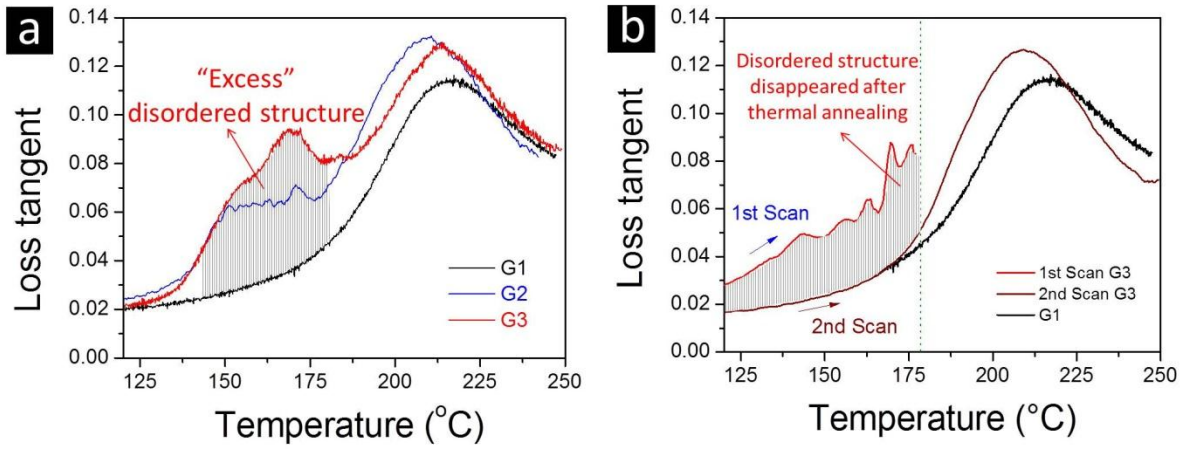

Figure 7.4 (The figures are reused from Chapter 4, Figure 4.8) DMTA temperature scans of the three grades G1, G2 and G3 (a); the annealing temperature scan to 180 °C of G3 (b). Shading indicates processes due to disorder effects that can be removed by annealing.

The dimensionless loss tangent of each silk grade is compared in Figure 7.4(a) in the temperature range of 120 to 250 °C, where the "dry" silk glass transition takes place. It is clear that G2 and G3 silks show more loss peaks between 151°C and 170°C which are absent for G1. As also discussed in section 4.3.5 in Chapter 4, these "excess" loss peaks in this temperature region are associated with more disordered structures, which also appear in reconstituted silk fibroin films and other poorly reeled silks [13]. This implies that G2 and G3 silks have more "disorder" in their structures than G1.

It is also noted that the "excess" loss peaks below the main glass transition peak at 220 °C are not exact in position and magnitude for different samples of the low grade silks, which was due to the different combinations of disordered structures and interactions in different silks, as explained in the paper [12]. This may pose questions addressing whether this method is reliable to be applied widely in the practical silk industry, and how to quantify the "disordered" structures for larger scale silks.

In exploring the thermal stability of the "excess" disordered structures in low grade silks, as shown in Figure 7.4(b), it was observed that these disordered structures can be

annealed out through a temperature treatment up to 180 °C. The explanation is that the combination of heat and mechanical energy can effectively increase the mobility of the molecules and relax the structures into more ordered forms. This implies that the low grade silks could be improved in quality to match the top grade silks through thermal mechanical treatment. Further studies need to also consider the economic balances of the heat treatment versus the total production of poor grade silks.

To summarize the sections on evaluating the three grades of *B. mori* silks, various tests including cocoon morphology, raw silk morphology, silk tensile performance and silk dynamic mechanical analysis were performed. The observations on both cocoon and silk morphology agree with the industrial standards: bigger and whiter cocoons with thicker and even silks are classified as top grade. More importantly, from the quasi-static and dynamic mechanical analysis, it is revealed that low quality silks possess more disordered structures, which can be indicated in the "dry" silk glass transition region in a DMTA temperature scan. This establishes a clear link between silk quality and silk structure (degree of order/disorder).

7.3.5 Assessing various effects on silk quality

a) Genetic variations

Since sericulture was invented in China, different varieties of silkworm genetic strains have been carefully selected and preserved through generations as precious genetic resources. However, how do the silks vary in terms of properties produced by different genetic strains? The German research booklet from 1940 of our collection may answer this question. In this research, silks from 15 genetic strains of silkworms with four treatments were tested using a simple tensile testing set-up. Although there was no recording of the detailed stress-strain curves, the breaking stress and strain for each type

of silks were recorded, and re-analysed by me. Figure 7.5 shows the results from the dry/raw silks of the 15 strains. The mean breaking stress of 15 strains is 555 MPa with a standard deviation of 20.1%, and the mean breaking strain is 26.1% with standard deviation of 2.5%. It is noted that in this Figure the breaking stresses for all the dry/raw silks are higher than my results in Table 7.2, together with however relatively high breaking strains too, which couldn't be explained here without enough information on the experimentation of the old results. In general, it is not obvious which genetic strain possesses superior tensile properties to the others. However, the treatment (e.g. degumming and wetting as shown in Figure 7.5 bottom row) makes a great difference to the tensile properties. Degumming removes the "softer" component of sericin from the fibres (bave) and results in stronger fibroin fibres (individual brins); and wetting, consistent with the effect of humidity studied in Chapter 5, makes the silk less strong but more extensible. Although temperature scans on the 15 strains of silks could not be performed, it may still be concluded that the effect of genetic variation is not a great concern for good mechanical properties of silks.

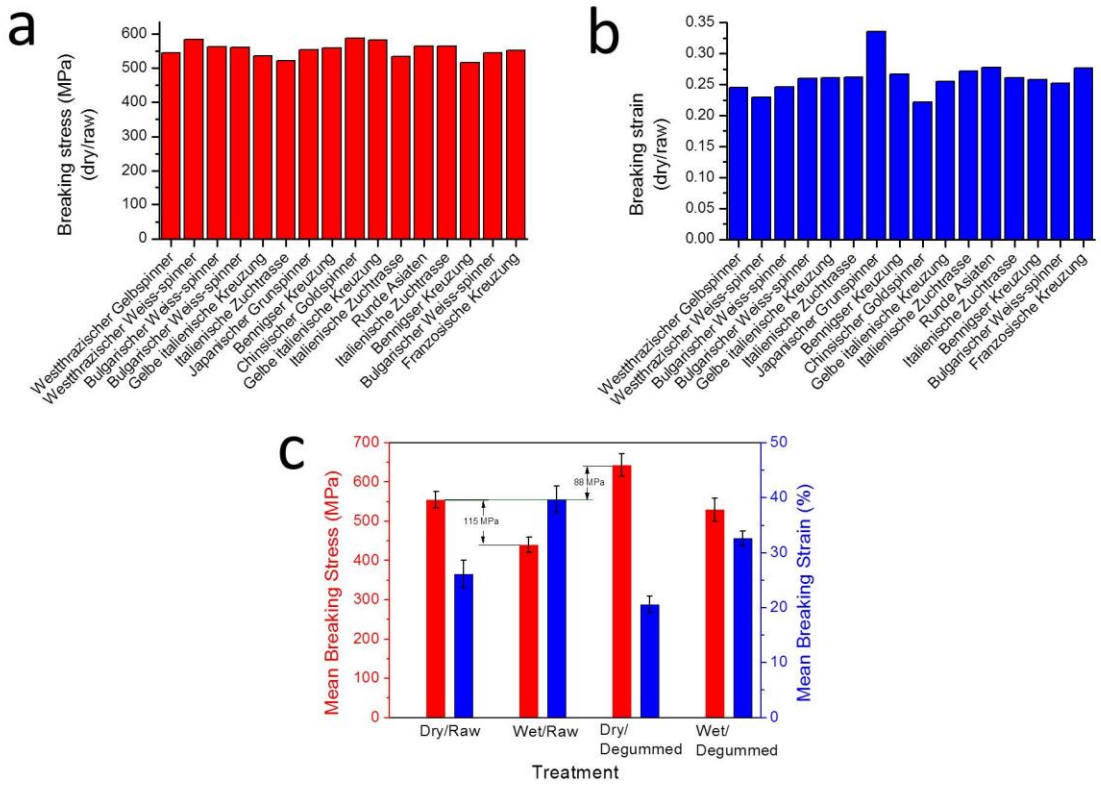

Figure 7.5 Breaking stress (a) and breaking strain (b) from tensile tests on 15 strains of *B. mori* silks; and comparison of the average tensile properties of 15 strains from four treatments (c).

b) Force-reeling

Force-reeling is a method that draws silks forcibly from silkworms or spiders at a controlled speed instead of letting worms spin the silk naturally. According to many studies, force-reeling could change the silk structure and properties, depending on the reeling speed and environmental conditions [14, 15]. However, there is no consensus whether force-reeling gives better mechanical properties than naturally spun silks.

Four force-reeled silks were provided for this study. Figure 7.6 compares the mechanical analysis of two silks, W1 force-reeled in air and W27 force-reeled under water. Figure 7.6 (a) shows that the air-drawn silks have much larger glass transition loss peak, which corresponds to more a disordered structure compared with the normal cocoon silk. Figure 7.6 (b) shows that the air-drawn silks are brittle and have much

lower toughness than the normal cocoon silk. In contrast, the water-drawn silks (W27) in Figure 7.6 (c) and (d) have much smaller loss peaks of glass transition and the tensile performance before annealing is very similar to that of normal cocoon silk.

Comparing the two silks W1 and W27, it suggests that post-drawing silks under water helps to develop a silk structure that is less coagulated or disordered, closer to the natural silk structure. The mechanism for this is that by using the water bath the glass transition conditions for disordered silk structures are met when post-drawing can effectively orient the already mobile molecular structures. However, it is not yet clear what are the best conditions to produce better silkworm silks through force-reeling. As shown in Figure 7.7, the four examples of force-reeled silks represent a wide range of silk structures, and the two extreme examples are the air-reeled W1 and that reeled under water W27. The three silks (W27, W30 and W39), all reeled under water, do not show a consensus in their structures, which means there should be other unknown factors during force-reeling that affect the silk structure. It suggests that more work needs to be done in order to produce force-reeled silkworm silks with consistent structure and properties.

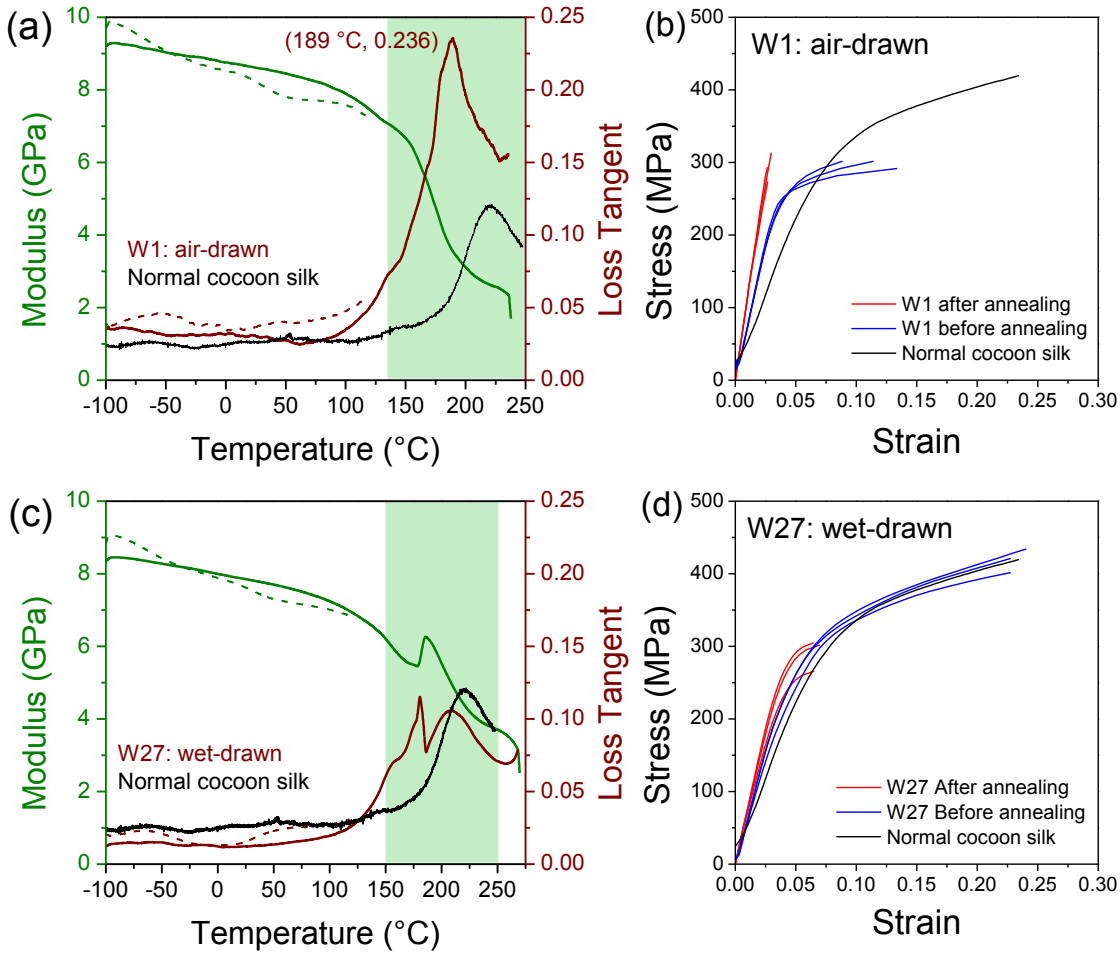

Figure 7.6 Dynamic mechanical thermal analysis (temperature scan) and tensile tests on two force-reeled silks: W1 and W27. In (a) and (c), the dashed lines show the first scan and the solid lines show the second can, and shade highlights the broader "dry" silk glass transition region; and in all plots, the performance of normal cocoon silk is compared.

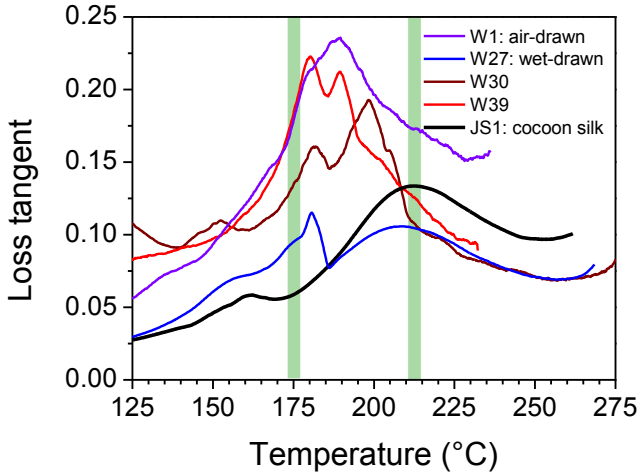

Figure 7.7 Temperature scans on four force-reeled silkworm silks in comparison with normal cocoon silk. The two lines highlight the RSF T_g at 175 °C and the normal silk T_g at 220 °C.

c) Ageing

One interesting aspect of silk quality is whether it deteriorates with time. Methods based on the chemical composition or isotopes for evaluating the age of silk textiles are often used in conservation and archaeology [16, 17]. Here, I focus on the mechanical properties and structure of silks due to the effect of ageing.

One sample is an aged raw silk from 1853, originally produced in China. As shown in Figure 7.8, the silk appears slightly yellow, which might suggest a normal ageing process, where cross-linking or degradation, has taken place. The longitudinal view of silk fibres shows uneven coatings of sericin and the cross-sectional view shows most fibres contain two brins bonded by sericin, which implies these silks were raw silks obtained just through reeling without any further processing.

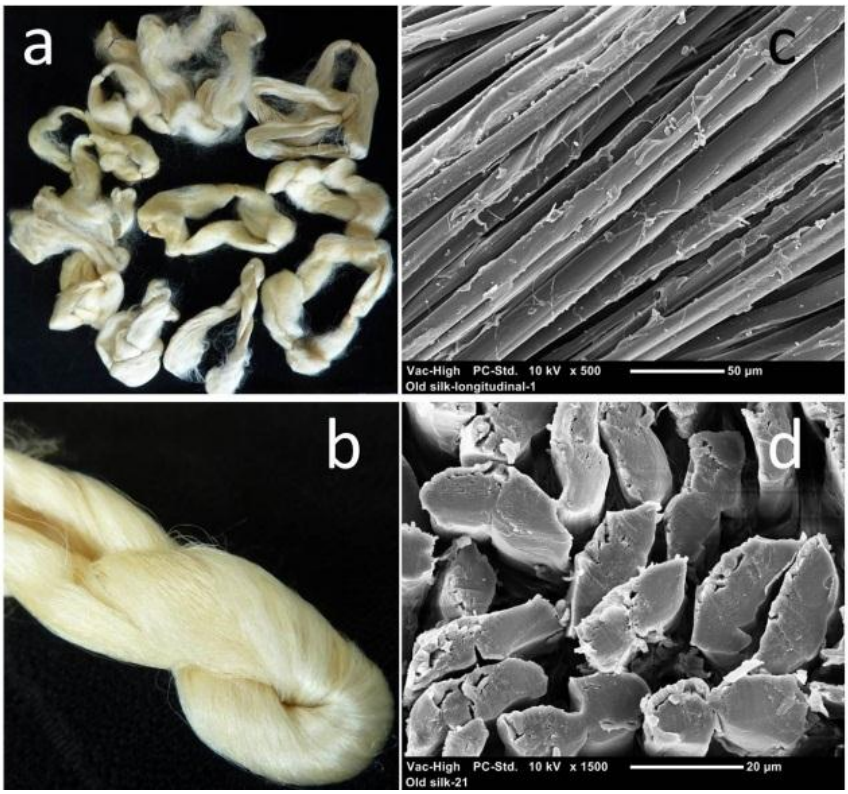

Figure 7.8 Yarns of the 1853 silk (each yarn has a folded length of about 20 cm) and the SEM morphology including the longitudinal and cross-sectional views of the silk. The scale bars are 50 μm in (c) and 20 μm in (d).

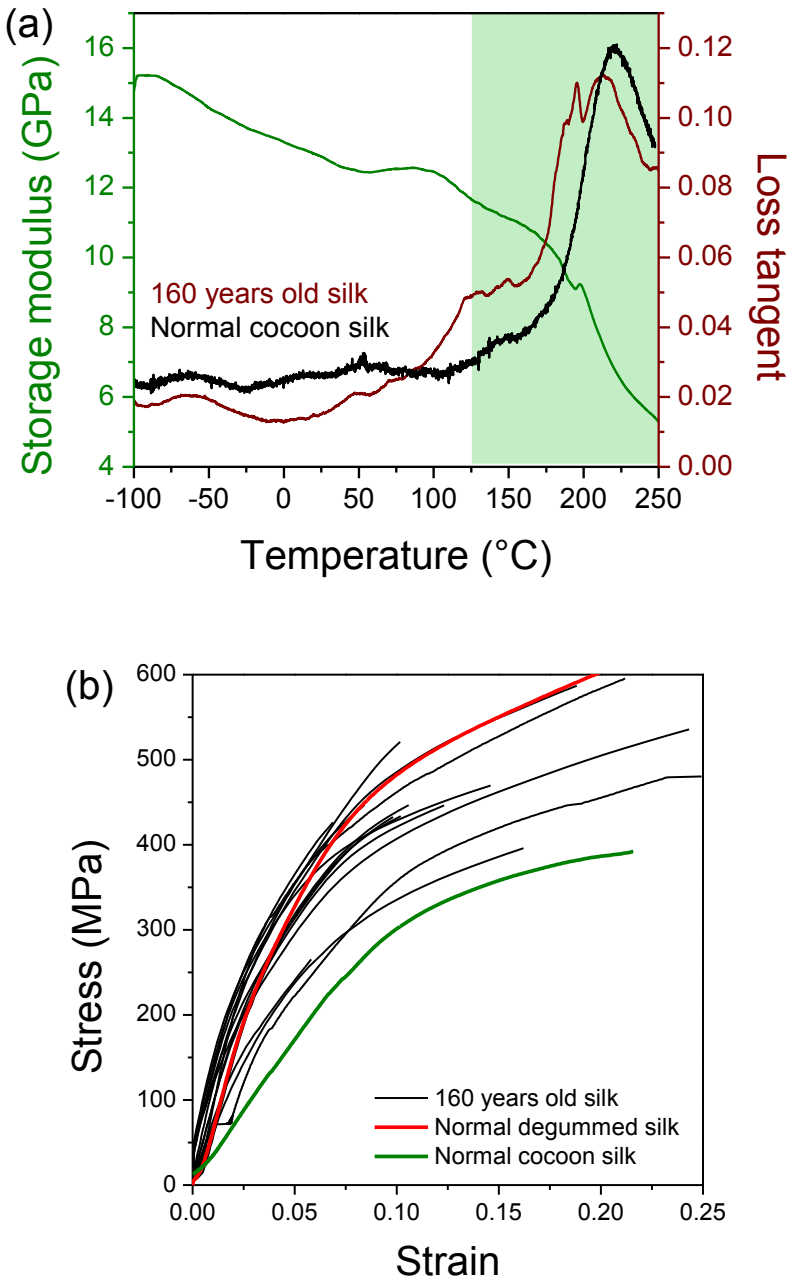

Figure 7.9 Dynamic mechanical temperature scan and tensile tests on the 1853 silk.

In Figure 7.9 (a), dynamic mechanical analysis on the 1853 silk shows the T_g peaks shift to lower temperatures, which suggests the packing of the disordered structure in the silk becomes less tight. However, the total area of the disordered peaks does not

seem to increase after a storage period of 160 years. The storage modulus of 13 GPa is high, given that the silk is raw. The observations on the loss tangent and the storage modulus do not seem to agree since one (loss) suggests the order of the structure is maintained and the other (storage) suggests the "order" is increased.

The stress-strain performance in Figure 7.9 (b) is highly varied for the 1853 silk (especially the three samples that are out of the normal range). However, the general trend suggests that the silk becomes stiffer compared to the fresh cocoon silks and the stiffness matches that of the degummed silk.

Cross-linking and gradually losing hydration could be two explanations for the increase of storage modulus and stiffness in both dynamic and quasi-static mechanical performances. Over the course of time, the reactive groups in silk could be cross-linked, for example, by UV light or oxidation, although we suspect the silk has been stored in a desk drawer before being discovered. Moreover, the water molecules which mediate between the silk chains are gradually expelled, so that the chains become close enough to be cross-linked. The low loss tangent in the low temperature range from -100 °C to 100 °C in the aged silk is consistent with the higher storage modulus at room temperature and may be due either to lower levels of bound water, or to crosslinking reactions between peptide side chains that immobilise those more dynamic segments of the silk protein chain. Unfortunately, the results presented here do not allow us to specify any mechanism.

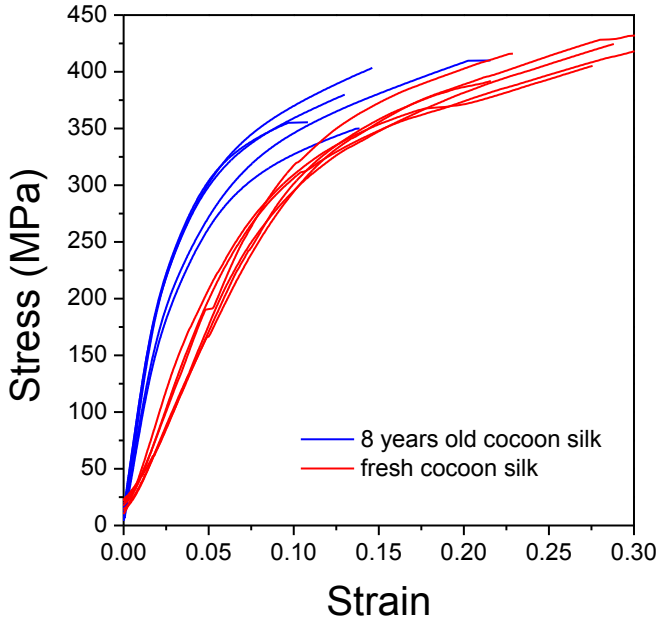

Figure 7.10 Stress-strain curves of two differently aged silks: fresh and the 2004 silk.

Another comparison test was performed on fresh cocoon silks and an aged silk from 2004. Figure 7.10 shows that the 2004 silk becomes stiffer; a similar trend to the 1853 silk. It is interesting to note that this Figure is very similar to Figure 4.5 (b), and it is as if the aged silks went through heat treatment and lost the hydration water. Therefore, it is suggested here that, under normal atmospheric conditions, the silk structure does not simply increase in local structural order, but loses the hydration water and may also undergo inter-chain crosslinking with time. This may provide valuable information for fabric preservation and conservation, for example, the ancient silk robes.

d) Impact of manipulated environments during rearing and spinning

In sericulture, there are huge regional differences in the quantity and quality of cocoon production due partly to varied climates and environments. Silk manuals [18] often say that appropriate temperatures and humidities with good ventilation are important for silkworm rearing at different stages and are essential for producing good

quality silks. However, how do these conditions matter to the mechanical properties of silk fibres?

Figure 7.11 compares two lab-produced silks under different (and implied quite extreme) controlled environmental conditions during rearing and spinning with the normal cocoon silk. It is found that although these manipulated silks have more low-temperature T_g losses suggesting more disordered structures, the overall structure of the two examined silks does not seem to diverge as far from the normal cocoon silk structure as those extreme examples of force-reeled silks. It may be concluded that the environmental conditions during rearing and spinning are not a priority concern for controlling the mechanical properties of silkworm silks.

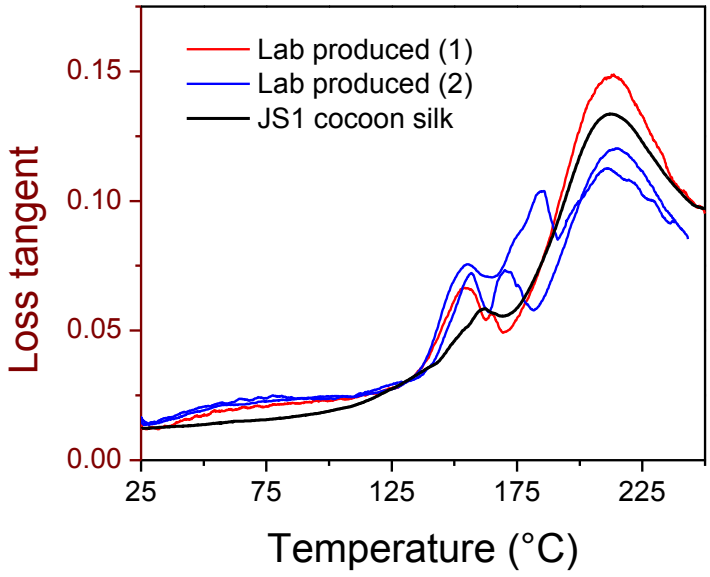

Figure 7.11 Comparing the loss tangent profiles of two lab-produced silks with the normal cocoon silk.

e) RSF: artificial spinning

To spin a good artificial silk has been one of the ultimate goals of silk science and technology. First of all, a stable artificial silk solution with a good *spinning index* or *spinnability* [19,20] has to be in place. Dissolving silks using lithium bromide, and

through deionizing to make an aqueous solution is the common way to obtain concentrated RSF solution. Qin *et al* [11] used ionic liquid AmimCl to dissolve silks and made new RSF solutions that show excellent viscosity profiles, comparable with the natural dope. The artificial silk fibres spun from this solution would be expected to achieve better mechanical properties than other synthetic analogues.

Nevertheless, the first attempt at artificial spinning from this ionic liquid RSF solution does not show success. As shown in Figure 7.12, the silk fibres do not form circular or dense cross-sections. Instead, the fibres show holes and voids. This morphology is not favoured for a strong and tough fibre. Figure 7.13 shows the fibre has a large T_g peak at 190 °C, which suggests the structure is highly disordered and the degree of disorder was suggested by my colleague Dr. Porter to be 0.5-0.6 using group interaction modelling; the tensile tests confirm that these silk fibres are more similar to other artificial silk fibres and clearly different from natural silks. By the first look, Figure 7.13 is alike the stress-strain curves of virgin and supercontracted spider silks, e.g. in Figure 6.8. However, I do not propose that these two systems of order/disorder share the same structural mechanisms. One simple reason is that supercontracted spider silks can be mechanically stretched back to become virgin silks, but a RSF fibre has not yet to be found to possibly become a natural *B. mori* silk through stretching.

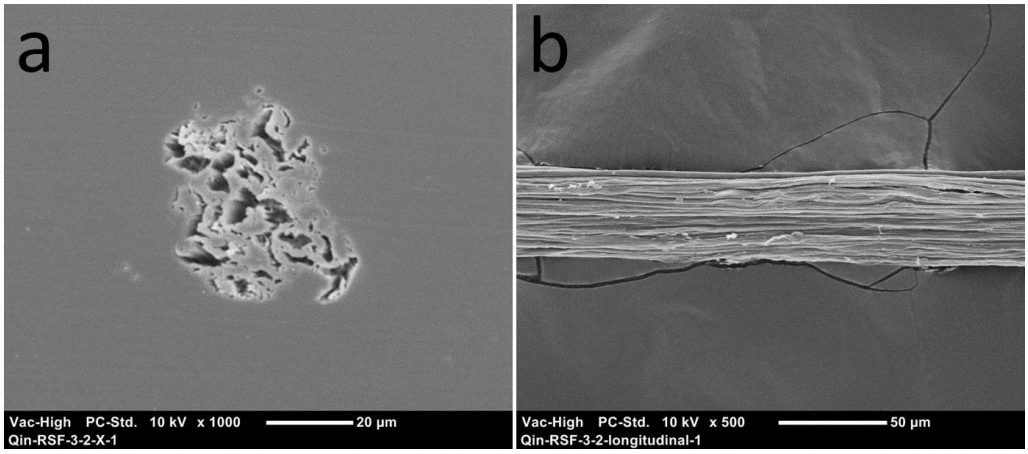

Figure 7.12 Cross-sectional and longitudinal views of artificial fibres made from ionic liquid RSF solution.

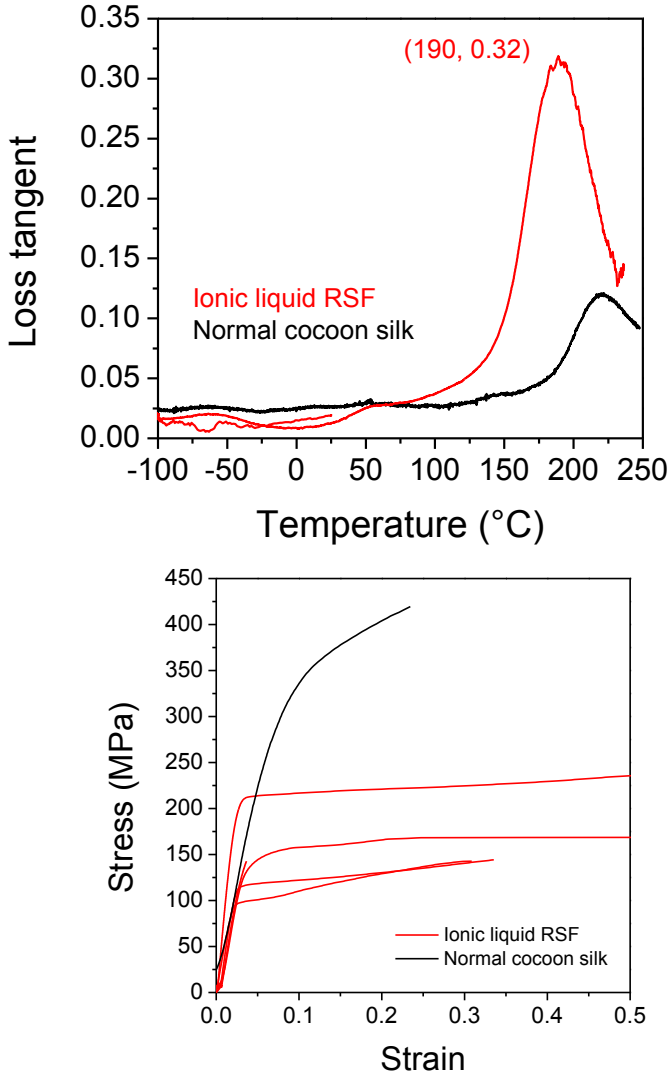

Figure 7.13 Dynamic mechanical temperature scan and tensile tests on artificial silk fibres made from AmimCl-RSF solution.

7.3.6 The quality of silks

To sum up the study of the three grades of cocoons and raw silks, it is found that low quality silks are characterised by more lower-temperature T_g peaks below the major T_g at about 220 °C, which are indicators of more structural disorder. Here it is worth mentioning again the link between the experimental measurements of loss tangent and the calculation of structural disorder using the relationships developed by GIM (refer to section 4.4.3 and 6.3.6). Using this link between silk quality and structural disorder in silk structures, various effects during natural or unnatural silk production are then evaluated. As summarized in Figure 7.14, force-reeling and RSF feedstock produce two extremely "bad" example silks, which show large degrees of structural disorder, which may be classified as "unnatural". Other factors including genetic varieties, controlled rearing conditions and storage for periods of time are shown to affect the silk structure within a "natural" range. Therefore, in terms of producing good quality silks, it may be suggested that the two more essential effects are the feedstock solution and the spinning process.

In addition, it is demonstrated that mechanical analysis, especially dynamic mechanical thermal analysis, allows the determination of the structural disorder of silks which could be useful for silk quality evaluation. Therefore, I propose that DMTA would be an effective tool for both quality evaluation and quality control in the silk industry.

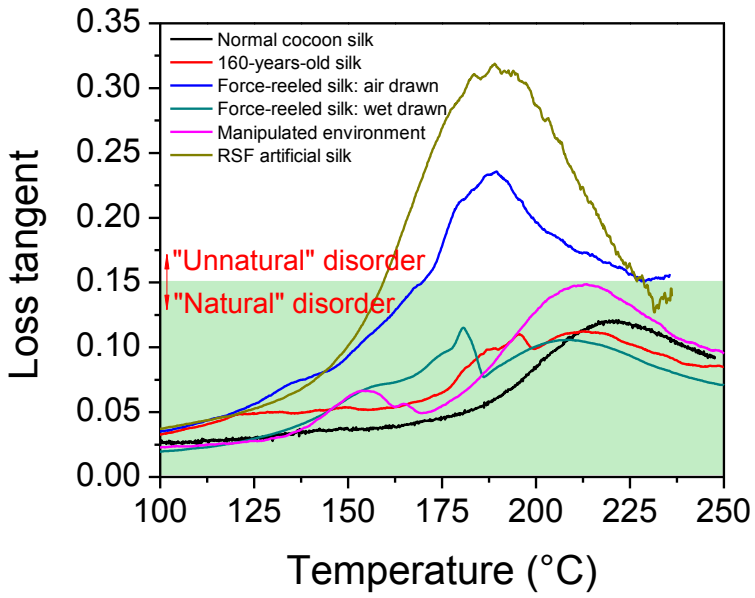

Figure 7.14 Comparing the loss tangent profiles of silkworm silks subject to various effects. The shaded area distinguishes the two generalised levels of "natural" and "unnatural" structural disorder.

7.4 Conclusions

This chapter presents a wide range of *B. mori* silks and discusses the relationship of silk quality and the silk structure. Using both quasi-static tensile testing and dynamic mechanical thermal analysis, the mechanical properties and the structures of raw silk fibres for the three cocoon grades were examined, and the low grade or low quality silks were shown to have a more disordered molecular structure, which could be "annealed out" using thermal mechanical treatment.

By establishing these links between silk quality and structural disorder, it was possible to evaluate more effects including genetic varieties, ageing, force-reeling, environmental rearing and artificial spinning. The results suggest that control over the feedstock and the spinning process is crucial for producing a good quality silk fibre with "natural" structural disorder. In addition, DMTA is proved to be a sensitive and

effective tool for evaluating the quality of silks and the effect of silk rearing as well as processing.

7.5 References

[1] Schoeser, M., *Silk*. Yale University Press: New Haven, Conn.; London, 2007.

[2] General Administration of Quality Supervision, I. a. Q. o. C.; China, S. A. o. t. P. s. R. o., Mulberry silkworm fresh cocoons. Standards Press of China: Beijing, China, 2008; Vol. GB/T15268-2008.

[3] General Administration of Quality Supervision, I. a. Q. o. C.; China, S. A. o. t. P. s. R. o., Testing method for raw silk. Standards Press of China: Beijing, China, 2008; Vol. GB/T 1798-2008.

[4] Cappellozza, L.; Cappellozza, S.; Saviane, A.; Sbrenna, G. Artificial diet rearing system for the silkworm Bombyx mori (Lepidoptera: Bombycidae): effect of vitamin C deprivation on larval growth and cocoon production. *Appl. Ent. Zool.* **2005,** *40* (3), 405-412.

[5] Ito, H.; Muraoka, Y.; Yamazaki, T.; Imamura, T.; Mori, H.; Ichida, M.; Sumida, M.; Matsubara, F. Structure and chemical composition of silk proteins in relation to silkworm diet. *Text. Res. J.* **1995,** *65* (12), 755-759.

[6] Shao, Z. Z.; Vollrath, F. Materials: Surprising strength of silkworm silk. *Nature* **2002,** *418* (6899), 741-741.

[7] Zhou, G. Q.; Shao, Z. Z.; Knight, D. P.; Yan, J. P.; Chen, X. Silk Fibers Extruded Artificially from Aqueous Solutions of Regenerated Bombyx mori Silk Fibroin are Tougher than their Natural Counterparts. *Adv. Mater.* **2009,** *21* (3), 366-370.

[8] Yao, J.; Masuda, H.; Zhao, C.; Asakura, T. Artificial Spinning and Characterization of Silk Fiber from Bombyx mori Silk Fibroin in Hexafluoroacetone Hydrate. *Macromolecules* **2002,** *35* (1), 6-9.

[9] Ha, S.-W.; Tonelli, A. E.; Hudson, S. M. Structural studies of Bombyx mori silk fibroin during regeneration from solutions and wet fiber spinning. *Biomacromolecules* **2005,** *6* (3), 1722-1731.

[10] Vollrath, F.; Woods, A. Paralysation of silkworm larvae. 2011.

[11] Wang, Q.; Yang, Y.; Chen, X.; Shao, Z. Investigation of Rheological Properties and Conformation of Silk Fibroin in the Solution of AmimCl. *Biomacromolecules* **2012,** *13* (6), 1875-1881.

[12] Guan, J.; Porter, D.; Vollrath, F. Thermally induced changes in dynamic mechanical properties of native silks. *Biomacromolecules* **2013,** *14* (3), 930-937.

[13] Yuan, Q. Q.; Yao, J. R.; Huang, L.; Chen, X.; Shao, Z. Z. Correlation between structural and dynamic mechanical transitions of regenerated silk fibroin. *Polymer* **2010,** *51* (26), 6278-6283.

[14] Perez-Rigueiro, J.; Elices, M.; Llorca, J.; Viney, C. Tensile properties of silkworm silk obtained by forced silking. *J. Appl. Polym. Sci.* **2001,** *82* (8), 1928-1935.

[15] Ortlepp, C. S.; Gosline, J. M. Consequences of forced silking. *Biomacromolecules* **2004,** *5* (3), 727-731.

[16] Moini, M.; Klauenberg, K.; Ballard, M. Dating silk by capillary electrophoresis mass spectrometry. *Anal. Chem.* **2011,** *83* (19), 7577-7581.

[17] Becker, M. A.; Magoshi, Y.; Sakai, T.; Tuross, N. C. Chemical and physical properties of old silk fabrics. *Studies in conservation* **1997,** *42* (1), 27-37.

[18] Wu, P.-c.; Chen, D.-c., *Silkworm rearing*. FAO: 1988.

[19] Holland, C.; Terry, A. E.; Porter, D.; Vollrath, F. Natural and unnatural Silks. *Polymer* **2007,** *48*, 3388-3392.

[20] Holland, C.; Vollrath, F.; Ryan, A. J.; Mykhaylyk, O. O. Silk and Synthetic Polymers: Reconciling 100 Degrees of Separation. *Adv. Mater.* **2012**, 24 (1), 105-109.

Chapter 8. Concluding remarks

8.1 Thesis summary

This DPhil project set out with the goal to study the complex structure and properties of natural silk fibres using the analytical technique, dynamic mechanical thermal analysis (DMTA). The starting hypothesis was: DMTA can 'reveal' the structure-property relationships of silks. However, in spite of the long history of DMTA use in polymer and fibre science, it was not clear exactly how this project could be done, or more specifically, what experiments were going to be performed?

Like many research projects, this thesis does not quite reflect the actual process of exploration that led to the relatively clear sections that present results and conclusions. The reader can refer back to the conclusions and more substantial findings from each chapter. Here, I briefly review the experimental work of the thesis in an alternative and more realistic 'try-and-see' chronological order and try to condense the most important findings into a few clear sentences and illustrations, as taken from the Table of Contents graphics for the three core papers derived from this work.

The work both started and finished by grading the quality of silkworm cocoons and silks, which demonstrated: first, that the specific DMTA instrument in our laboratory can be relied on for both quasi-static and dynamic mechanical analyses on the very *thin* silk fibres; second, that these analyses can provide valuable quantitative information on the structure and properties of highly complex silk fibres that constitute the commercially important term "quality", which is essentially qualitative and often highly subjective.

The first methodology problem was the effect of loading on silk structure and properties. To evaluate the effect of static loading on silks was not purposely planned as separate work, but evolved with the need to set-up a dynamic test over the range of conditions experienced by silk; from low stress levels where fibre 'waviness' is important to post-yield stresses where plastic flow is dominant. Similar to the first grading work, the 'surprising' observations on the static loading effect were not explained until much later as they were correlated with observations on thermal and mechanical annealing of lab-produced poor silks and high rate tests by other group members. In summary, natural silks stiffen under stress through structural changes, particularly post-yield, where the elastic modulus appears to reduce significantly in conventional quasi-static tensile tests, as shown schematically in Figure 8.1.

The second major problem was the humidity effect on *B. mori* silks and spider dragline silk supercontraction. It was not expected that the humidity accessory on the Q800 instrument would provide interesting results such as the T_g-contraction effect. However, in a series of tests over the whole project, humidity effects gradually emerged as a key capability for understanding silk structure and properties. The important findings were that silk loses water once heated to above 100 °C and that spider silk supercontraction can have two independent structural mechanisms, as illustrated in Figure 8.2 below.

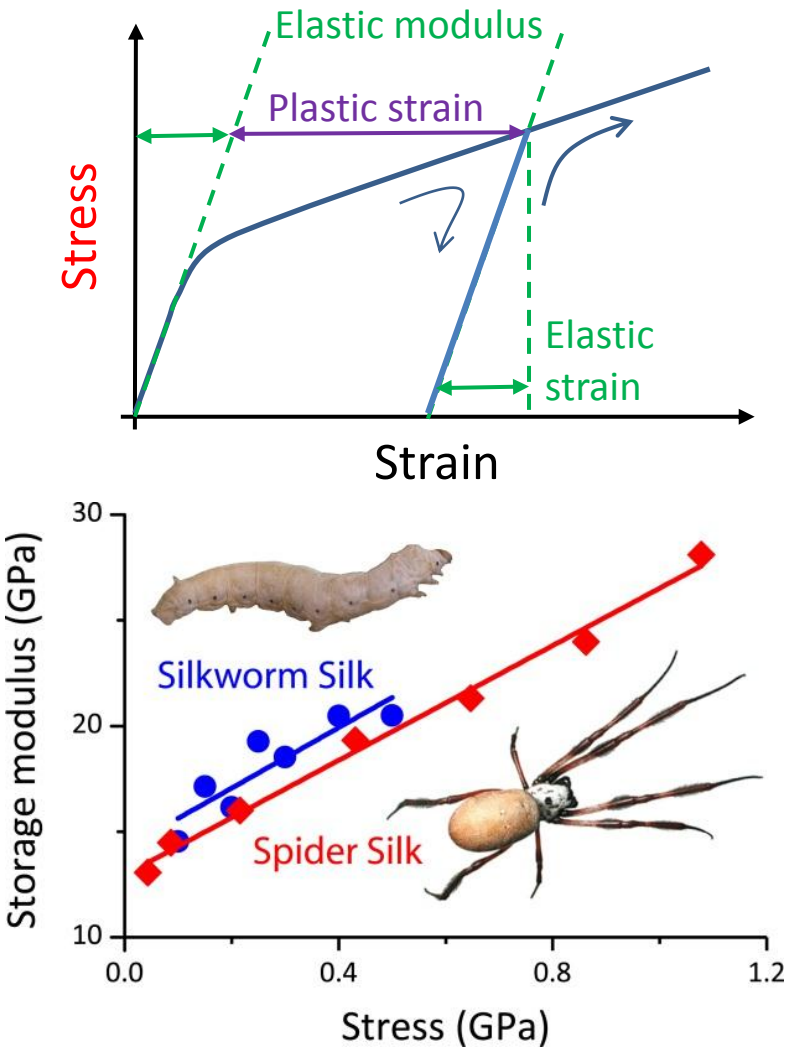

Figure 8.1 Stress effect on modulus of silks (refer to section 3.4 and [1]).

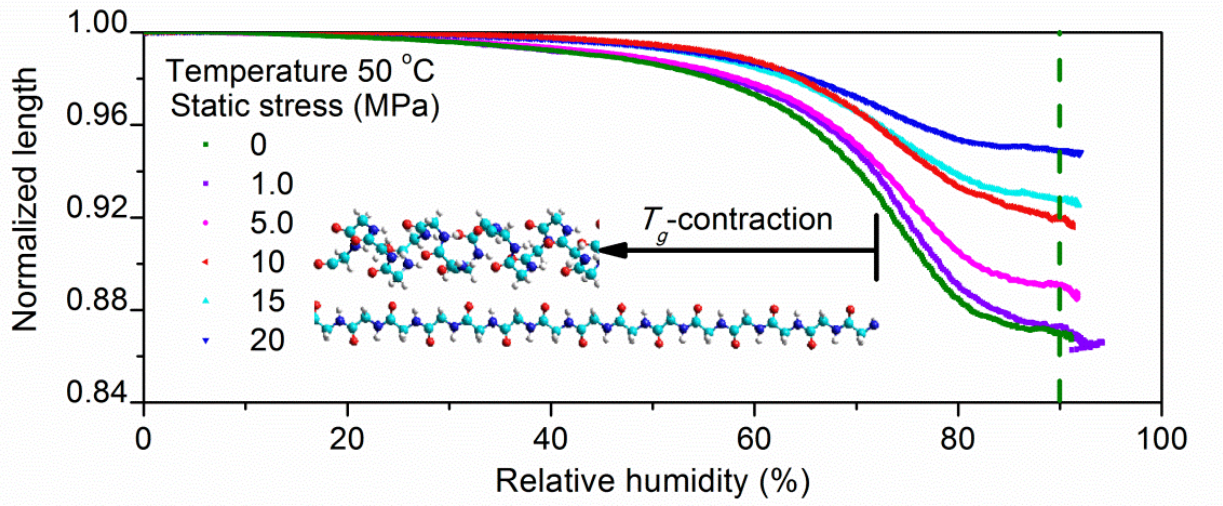

Figure 8.2 T_g-contraction (as one contribution to supercontraction) of different degrees under series of stresses [2].

The third and final core problem was the thermal and thermal history effect on silks. The thermally induced changes in silk structure such as water loss and change of T_g with higher temperatures and stresses looked superficially straightforward, as illustrated in Figure 8.3. However, because of the complication of all factors, especially water and heat, finding a consistent explanation through the whole temperature range took quite some time. There were also experiments that were very time-consuming but turned out to be 'not as informative' or straightforward, such as repeated temperature scans with increasing static load. I admit that there is a lot more analysis that could be potentially done from these complicated but valuable results. It was only towards the end of this project that this aspect of the silk quality issue was revisited and explored. The main overall finding in this area was that the T_g of the disordered structure in natural silk is 220 °C and other lower $T_g s$ suggest greater degrees of disorder (different hydrogen bonded secondary protein structures) and contribute to lower silk quality.

Thus, the work presented in this thesis evolved as a gradual refinement of ideas and techniques over a range of different complementary problems and effects, both within the project itself and through dialogue with colleagues working on parallel projects where DMTA observations could provide important new insights.

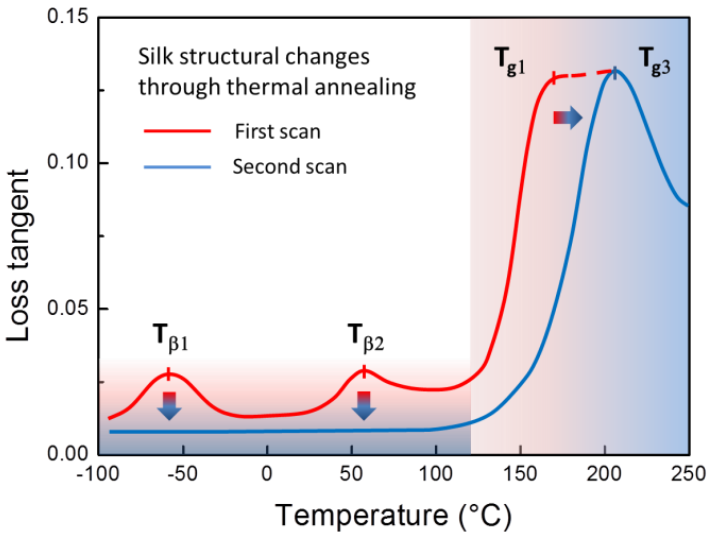

Figure 8.3 Thermal and thermal history effects on natural silks [3].

8.2 General discussion

Throughout this thesis, the quasi-static and dynamic mechanical properties of two natural silks have been examined using a consistent methodology, which is the first general contribution of this work to the field. On top of the mechanical properties, the structure of silks has been a key focus of this work.

Silks are semi-crystalline polymers, as many people already have seen over decades of analysis [4, 5]. However, as it was discussed in the introduction, a two-phase model is too simple to explain the much more complex behaviour of silks and the potential for many different protein secondary structures. In this work, we propose a structural model for silks in section 6.3.6 that contains four different generalised morphological and structural components: permanent order, meta-disorder, meta-order, and permanent disorder. Also, keeping the model simple for many natural silks, the components are isotropic and their contributions to properties are additive. Moreover, these components could be associated with specific secondary structures under defined stress and/or thermal environments. For example, meta-order could be a temporary β-sheet region

formed by the stretched out chains that contain stretched proline segments (intrinsically disordered according to many studies), which shrinks back to disorder in contact with water. The varied composition of the four components gives silks versatile microscopic structures and macroscopic properties. Here in Figure 8.4, we illustrate this simple idea of a silk structural model with two examples, *B. mori* silkworm silk and *Nephila edulis* major ampullate dragline silk. The calculation of the morphological fractions can be referred to [6] and Chapter 6. Note that our total order (permanent order and meta-order) is not the equivalent of conventional crystallinity. It is clear that *Nephila* spider silk has more meta-structure than *B. mori* silk, which makes *Nephila* spider silk more flexible and responsive to the changing environment.

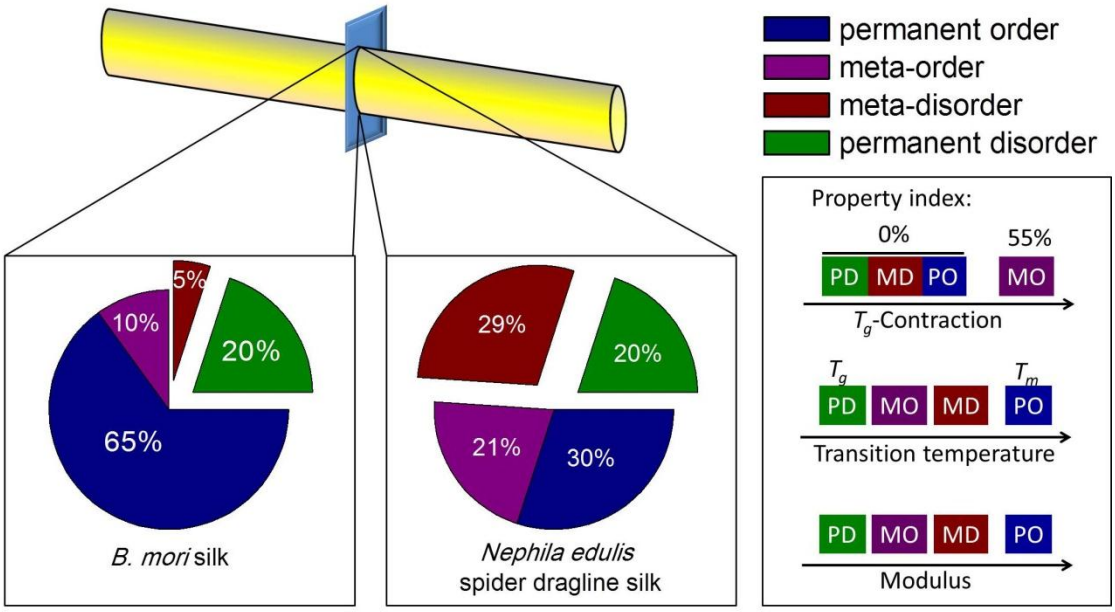

Figure 8.4 Structural decomposition for *B. mori* silk and *Nephila edulis* spider dragline silk using a four-component model.

As also suggested in Figure 8.4, the properties for each structural component could be solved by conducting careful experiments, e.g. T_g-contraction, dynamic mechanical thermal analysis, and tensile tests. However, there may be other important techniques

that could be implemented to solve the structural model further. For example, future experiments that directly follow on from this structural model will be: (1) study the solvent effect on the structure and properties of silks using DMA with the solvent immersion bath in the Q800, and try to deconvolve the structural components of silks, especially the meta-structures; and (2) probe the silk structures in a spectrometer (for example, Raman Spectroscopy) with in-situ control of stress and temperature (ideally with dynamic control too), and try to find more evidence on the structure of silks under load, as well as to extend the findings of this work on structure-property relationships for natural silks.

My approach to decompose the structure of silks is to detect the change in silk *properties* that is induced by the structural changes under heat, stress *etc*. Dynamic mechanical analysis is a powerful tool that resolves each structural component by differentiating energy storage and dissipation, or capturing a characteristic change in length as the components are stretched. In addition, although my methods based on DMA have been developed for thin semi-crystalline fibres, especially those with complex structures, they could also be adapted for materials with other morphologies (for example, membranes or powders). Therefore, this approach of deducing material structure from properties using tools such as dynamic mechanical analysis could be extended to understand more biopolymers and biomaterials.

To conclude, my work has demonstrated that the silk structure and properties can be examined and interpreted via a consistent methodology based on mechanical analysis, and more specifically dynamic mechanical analysis (DMA).

8.3 References

[1] Guan, J.; Porter, D.; Vollrath, F. Silks cope with stress by tuning their mechanical properties under load. *Polymer* **2012,** *53* (13), 2717-2726.

[2] Guan, J.; Vollrath, F.; Porter, D. Two mechanisms for supercontraction in Nephila spider dragline silk. *Biomacromolecules* **2011,** *12* (11), 4030-4035.

[3] Guan, J.; Porter, D.; Vollrath, F. Thermally induced changes in dynamic mechanical properties of native silks. *Biomacromolecules* **2013,** *14* (3), 930-937.

[4] Termonia, Y. Molecular Modeling of Spider Silk Elasticity. *Macromolecules* **1994,** *27* (25), 7378-81.

[5] Simmons, A. H.; Michal, C. A.; Jelinski, L. W. Molecular orientation and two-component nature of the crystalline fraction of spider dragline silk. *Science* **1996,** *271* (5245), 84-87.

[6] Fu, C.; Porter, D.; Chen, X.; Vollrath, F.; Shao, Z. Understanding the Mechanical Properties of Antheraea Pernyi Silk—From Primary Structure to Condensed Structure of the Protein. *Adv. Funct. Mater.* **2011,** *21* (4), 729-737.